Fraunhofer MEVIS

JACOBS UNIVERSITY

Automated Medical Image Processing Using Efficient Shape Descriptors: Principles and Applications

by

Lei Wang

A thesis submitted in partial fulfillment
of the requirements for the degree of
Doctor of Philosophy
in Computer Science

Approved Dissertation Committee

Prof. Dr. Horst K. Hahn Jacobs University Bremen - Fraunhofer MEVIS
Prof. Dr. Lars Linsen Jacobs University Bremen
Prof. Dr.-Ing. Dorit Merhof RWTH Aachen University
Jun.-Prof. Dr. Christian Hansen Otto-von-Guericke University Magdeburg

Date of Defense: May 22, 2017

Computer Science & Electrical Engineering

Statutory Declaration

Family Name, Given/First Name	Wang, Lei
Matriculation number	20331576
What kind of thesis are you submitting: Bachelor-, Master- or PhD-Thesis	PhD-Thesis

English: Declaration of Authorship

I hereby declare that the thesis submitted was created and written solely by myself without any external support. Any sources, direct or indirect, are marked as such. I am aware of the fact that the contents of the thesis in digital form may be revised with regard to usage of unauthorized aid as well as whether the whole or parts of it may be identified as plagiarism. I do agree my work to be entered into a database for it to be compared with existing sources, where it will remain in order to enable further comparisons with future theses. This does not grant any rights of reproduction and usage, however.

This document was neither presented to any other examination board nor has it been published.

German: Erklärung der Autorenschaft (Urheberschaft)

Ich erkläre hiermit, dass die vorliegende Arbeit ohne fremde Hilfe ausschließlich von mir erstellt und geschrieben worden ist. Jedwede verwendeten Quellen, direkter oder indirekter Art, sind als solche kenntlich gemacht worden. Mir ist die Tatsache bewusst, dass der Inhalt der Thesis in digitaler Form geprüft werden kann im Hinblick darauf, ob es sich ganz oder in Teilen um ein Plagiat handelt. Ich bin damit einverstanden, dass meine Arbeit in einer Datenbank eingegeben werden kann, um mit bereits bestehenden Quellen verglichen zu werden und dort auch verbleibt, um mit zukünftigen Arbeiten verglichen werden zu können. Dies berechtigt jedoch nicht zur Verwendung oder Vervielfältigung.

Diese Arbeit wurde noch keiner anderen Prüfungsbehörde vorgelegt noch wurde sie bisher veröffentlicht.

Lei Wang
Würzburg, September 2017

Acknowledgment

First of all, I am grateful to my supervisors, Prof. Dr. Horst K. Hahn and Prof. Dr. Lars Linsen, who have always trusted and supported me during the composition of this thesis. My special thanks also direct to Prof. Dorit Merhof and Prof. Christian Hansen. Without their visionary guidance and steering, valuable comments and discussions, generous support and inspiration, this thesis would not be accomplished.

Due to the fact that this dissertation is a collection of my scientific works that cover a broad spectrum of several fundamental image processing topics, many colleagues, partners and friends have contributed their own efforts. I would like to give my sincere gratitude to all my colleagues in Fraunhofer MEVIS. MEVIS is such a great institute where my scientific thinking and attitudes were fostered. Since the thesis has covered several research domains focusing on breast cancer diagnosis and liver disease treatment, I am thankful to the "MEVIS Breast Group", namely Dr. Markus Harz, Fabian Zöhrer, Dr. Hendrik Laue, Dr. Tobias Böhler and Dr. Joachim Georgii. Their knowledge about the clinical background of breast cancer diagnosis and treatment helped me a lot for developing methodologies. Meanwhile, I will share my gratitude to Mohammad Razavi for his wonderful work in the implementation of computer-aided diagnostic tools dedicated to breast lesion classification. Without his accurate implementation and rigorous evaluation, my ideas will not be proved to be practical. I also appreciate the collaboration with my colleagues of "MEVIS Liver Group", namely Dr. Hans Meine, Dr. Christian Hansen, and Dr. Stephan Zidowitz during the development of liver surgery planning tools.

Other clinical and industrial partners deserve my gratitude as well. For instance, Dr. Michael Kohnen (Stryker, Germany) shared me with plenty of inspiring ideas in the project of femur head segmentation. Dr. Albert Gubern-Merida, Dr. Tao Tan, Dr. Bram Platel, Dr. Ritse Mann and Prof. Nico Karssemeijer from diagnostic image analysis group at the Radboud University Nijmegen have contributed a lot to the collaborative projects of breast cancer diagnosis, especially providing substantial amount of medical image data and manual annotations plus comparison studies. Dr. Julia Müller from Mediri and her evaluation study to compare the performance of the nipple detection algorithm should also be credited.

Last but not least, I would like to express my sincere gratitude to my family, my wife Jingyan, my father Juncheng, my mother Yafen and my lovely daughters Leonie and Fenja. Without their unconditional supports, I would not be able to reach here.

Abstract

This thesis focuses on the development of fast and automated methods for detecting and segmenting anatomical structures in various modalities of medical imaging using efficient shape descriptors. The identification and delineation of these targeted objects are fundamental steps for further computer assisted applications, such as surgery planning, surgery interventional guidance, computer-aided detection and diagnosis or information fusion.

First of all, a brief introduction of fundamental topics in medical image processing will be given, including segmentation, registration, detection and classification. Common techniques and methodologies used in these domains are generally reviewed. Then, a review of shape descriptors that are commonly used in medical image processing is conducted. The review will categorize these techniques with respect to different dimensions, such as complexity, efficiency, degree of user interactions and sensitivity to parameters, etc. Afterwards, to demonstrate how these shape descriptors are applied in each individual clinical task, several segmentation, registration, classification and detection tasks, where a variety of shape descriptors serve as the mainstay, will be described in detail. Specifically, the tasks consist of the segmentation of femur heads in fluoroscopic images using a Gabor-based Hough shape descriptor, the segmentation and registration of breasts in magnetic resonance images, the detection of nipples in 3D breast ultrasound images and the segmentation of liver vessels in multi-phase computer tomography images using a variety of Hessian-based shape descriptors. Meanwhile, a computer-assisted diagnostic tool dedicated to breast lesion classification is proposed, on the basis of a series of sphere packing shape descriptors. For each task, clinical background will be first explained, and the state-of-the-art techniques that attempted to resolve the problem will be reviewed.

Contents

1

Introduction

Object segmentation, detection, registration, and classification serve as fundamental topics of research activities in medical image processing. These image processing techniques have different goal and focus. Various techniques and algorithms have been proposed to tackle the challenges within these tasks. In this chapter, a brief review of different techniques for each of the topics will be given. Then, methodologies based on shape descriptors that are commonly used in these research fields will be reviewed.

1.1. Basic Medical Image Processing Activities

1.1.1. Segmentation

The purpose of segmentation is to partition an image into multiple segments and delimit the boundaries of target objects as precise as possible. As the most fundamental medical image processing procedure, a semi- or full-automatic segmentation technique is usually required to quantitatively analyze the targeting anatomical structures in clinical applications. For instance, clinical relevant parameters can be extracted from a segmented lesion to assist diagnosis or monitor treatment response. With the development of advanced computer graphics techniques, a 3D visualization of medical imaging data is required, where segmentation of different tissues are favored, so that they can be visually differentiated with different viewing properties. Additionally, applications such as computer-aided diagnosis (CAD), surgery planning and guidance, and image fusion and registration, etc, usually involve segmentation tasks.

Many segmentation techniques have been reported in last several decades. These techniques can be categorized into edge-based, region-based and shape-based methods. Edge-based methods focus on delineating the boundaries that enclose the target objects, while region-based techniques try to segment the area that the target objects occupy. These algorithms take into account the spatial connectivity of voxels. Edge-based methods search for inhomogeneity indicating object boundaries, and region-based methods search for continuous

regions of voxels with homogeneous properties. The former are typically based on boundary indicator functions such as the magnitude of the image gradient, which is either directly used in the edge detection methods, e.g. Canny edge detector, or integrated into the energy functions of the optimal boundary searching method, e.g. active contours [1]. Many region-based segmentation methods can be expressed in terms of region growing, in which an initial set of regions are grown until the stopping criterion is met. Common stopping criteria are to grow until all neighbors exceed certain dissimilarity, or until all voxels are assigned to a region.

The success of both edge-based and region-based techniques relies on the extent of intensity contrast presented in images. The problems caused by the presence of low contrast may be overcome in two ways. First, additional user interactions can be employed, for instance by placing more markers, or by offering methods for segmentation editing that are independent of the segmentation algorithm itself [2]. Second, more domain knowledge or assumptions can be incorporated. An intermediate approach is to employ stronger smoothness assumptions, which may effectively prevent not only jagged contours, but also leakages that are only connected through some voxels. A typical method using explicit smoothness assumptions is active contours, originally introduced by Kass et al. [1] (also called snakes). Here, an initial contour (e.g., a circle or sphere near the object of interest) is moved over time (evolving), iteratively minimizing an energy functional that typically has two main terms: an external energy that is minimal near boundaries (based on a boundary indicator function) and an internal energy that penalizes strong curvature and "jaggedness" of the contour. Intuitively speaking, the external energy lets the contours snap to visible boundaries, while the internal energy prevents leakages and implausible corners (regularization). The contour can be represented explicitly as a polygonal structure with support points that move over time, or implicitly as the zero level set [3] of a function that is positive inside the object and negative outside. Explicit representations are simple to implement and efficient to update, but care has to be taken when moving support points to prevent extremely uneven sampling distances or topological problems like self-intersections, if local movements are globally inconsistent with the contour's fixed topology. These problems are elegantly prevented with level set [4], but level set functions are much difficult to update efficiently, which makes level set approaches slow in general. Both approaches need a good initialization and may get stuck in local minimal.

While the above methods perform iterative optimization of contours, graph cuts have become very popular as a tool for immediate, global optimization. The graphs are typically based on the voxel grid, i.e. every voxel is a node and connected with its neighbors via weighted edges that are used for edge-preserving regularization (with stronger connections between similar voxels). Auxiliary nodes (e.g. source or sink nodes) and edges can be used to encode prior probabilities or additional energy terms. For instance, algorithms that find a minimum cut through such a graph by computing the maximum flow from source to sink nodes have been extensively studied [5]. An advantage of graph cuts in magnetic resonance imaging (MRI) context is that the formalism can be applied to higher dimensional images (e.g., 4D time series) equally well. In medical image computing, most segmentation tasks can be broken down to binary problems with foreground and background classes, thus the limitations of

graph cuts with respect to multi-class problems can be ignored. The price for being able to find global optima is that only certain energy functions can be expressed this way [6].

Methods with explicit and strong representations of prior knowledge used most commonly are atlas- and shape-based segmentation techniques. Atlas-based segmentation was originated in the application of brain segmentation [7] and was then improved later in [8]. The basic principle is to register an image with known, confirmed labeling (e.g. manually segmented), called an atlas, to a similar new input image to be segmented. However, instead of using just one labeled image, an atlas can be constructed by combining several images by co-registration. Alternatively, several atlases may be used, selecting one based on image similarity, or fusing the labels of several relevant atlases, e.g. by majority voting. An overview of atlas-based segmentation methods is given in [9]. Understandably, the efficiency of these approaches depends on the registration algorithms used to align the reference segmentations, on the quality of the atlases (low intra- and inter-observer variance), and on the validity of the chosen atlas for the case at hand. Different atlas-segmentation strategies were compared in [10], showing that approaches that combine multiple registration steps yield better results than a single registration.

An alternative approach that is designed for exploiting prior domain knowledge is shape-based method that utilizes models of a prototypical shape (mean shape), as well as typical modes of variation [11] in order to hypothesize plausible object boundaries in areas of missing contrast. Active contours using statistical shape models are called active shape models (ASM), and can be further extended into active appearance models (AAM) by treating the appearance (voxel intensities) in the shape with the same statistical framework. Shape models may show a stronger bias towards shapes seen in the training set, while smoothness assumptions often imply a comparable bias towards a simple shape such as a sphere.

1.1.2. Registration

Image registration is often used as a preliminary step in other image processing applications. It is the process of transforming different sets of data into one coordinate system where the considered target objects are aligned spatially. Registration process fixates one image (reference image) and calculates the transformation that maps another image (moving image) onto the reference image. Misalignment of the target objects in reference and moving images may occur due to the image acquisition in different imaging modalities, such as computer tomography (CT), MRI, or ultrasound imaging, etc. Images taken in different modalities have different imaging parameters that result in different intensity levels, contrast, resolution, voxel spacing and field of view. Fusion of the information brought by multiple modalities can improve the accuracy of screening, diagnosis, treatment, intervention and therapy monitoring. Therefore, there is a huge clinical need that register the target objects appeared in different modalities of medical imaging, especially in the age of rapid development of digital imaging techniques. Another important application scenario of registration is to remove the motion artifacts caused by patient movements, such as physical movement or breathing. The motion artifact normally affects the quality of time series image sequences acquired in a specific modality. For instance,

severe motion artifacts can lead to enormous difficulties to extract functional features from dynamic contrast enhance MRI (DCE-MRI), which serves as the most important diagnostic image sequence of breast cancer. To remove motion artifacts, registration between different time sequences becomes critical during the interpretation of breast DCE-MRI.

Registration techniques can be classified into rigid and non-rigid categories. Rigid registration only allows for rigid transformations, such as translation, rotation, and scaling, which can be represented by a transform matrix. On the other hand, non-rigid registration allows for non linear transform represented by a deformation field that has the same size with reference image. The deformation field encodes the mapping vector from moving image to the reference for each single voxel. Solving rigid or non-rigid registration is the process of optimizing the parameters of transformation matrix or deformation fields, such that the difference between reference and moving images is minimized. Commonly used difference metrics include sum of squared differences (SSD), normalized gradient field (NGF) or mutual information (MI). To assure a smooth transform, a variety of regularization items are taken into account in the optimization function, such as elastic, diffusive and curvature constraints.

1.1.3. Detection and Classification

Object detection aims to only locate the position of the target instead of a complete delineation of its region, which means it does not require a precise depiction of its covered region, but focuses on its existence of location. On the other hand, object classification is the process of classifying the objects into different categories. For instance, many computer-aided detection (CADe) and diagnosis (CADx) techniques are designed to detect and classify the lesions into benign and malignant types. Another important category of methods not mentioned yet is the ones based on classification or clustering. The simplest example would be thresholding, which can be seen as a classifier rating each voxel just by its scalar value. Since this does not take spatial connectivity into account, it typically leads to implausible results, with isolated voxels being assigned to a different class than all of their neighbors. There are many ways to improve on this. Apart from the typical morphological post-processing for closing small holes or removing tiny components of the segmentation mask or a pre-processing of the image such as smoothing, it is possible to improve the classifier in two ways: First, instead of only looking at the value of a single voxel, multiple local image features can be extracted such as gradient magnitude, curvature measures, eigenvalues of the Hessian, or texture features, and composed into a feature vector. Second, a state-of-the-art classifier can be trained on a set of training samples and then used to assign class labels or probabilities (e.g. for a fuzzy segmentation result) to each voxel's feature vector. It should be stressed that the feature vector contains information about the local neighborhood, which allows the classifier to learn how to prevent single voxels from being assigned with wrong labels, so that post-processing becomes unnecessary. Clustering refers to unsupervised learning and is applied if there is no training data available. This is similar to techniques for finding automatic thresholds such as Otsu's method [12] or Gaussian mixture model, but again may use more complex features than just a single voxel value. In general, well-known clustering algorithms such as k-means or FCM are

only applied in feature space, and segmentation is derived by looking at connected components of the resulting label regions. However, it is also possible to augment the feature vector with the voxel position, in order to produce more spatially connected clusters. This is the basic idea of the mean shift approach, the name of which refers to the cluster centers (means) being iteratively moved (shifted) towards better representatives of image regions [13]. A probabilistic interpretation of classification in feature space treats the segmentation labels as random variables with a certain probability distribution, where conditional probabilities and Bayesian theorem relate class probabilities and voxel values. This setting is the basis for Markov random fields [14], a formalism for coupled random variables, which allows for an elegant probabilistic integration of the spatial neighborhood in a digital image for regularization.

1.2. Shape Descriptors

Although these different image processing techniques have different intents, they are highly related to each other in a sense that normally one replies on the performance of another to improve the overall accuracy. For instance, a prior segmentation of the target objects in multiple data sets can dramatically improve the registration accuracy by enforcing the registration strength only on the targets. A detection can be applied first to identify the location of the targets, which will facilitate subsequent segmentation procedures that require a precise initialization. Classification is the process of classifying target objects into different categories. For instance, a major application of classification is to differentiate the lesions into benign or malignant types. Classification techniques normally require an accurate segmentation of the objects to extract the morphological or functional features. In the following sections, typical shape descriptors will be introduced to reveal their advantages and effectiveness in accomplishing particular image processing applications.

In this dissertation, we put our focus on the efficient shape descriptors that were utilized in the applications of object segmentation, registration, detection and classification. These techniques leverage the advantages of the shape priors of the targeting objects, which allows for automatic recognition of a specific shape pattern. Normally, to describe a specific shape pattern for each voxel is quite computationally expensive. Therefore, the efficiency of a shape descriptor matters in practice. The shape descriptors introduced in this dissertation are designed with an intent to keep the balance of performance and complexity. Fulfilling the limited time requirement in daily clinical routine is one of the key factors that we concern during the development of each solution. These shape descriptors are versatile to differentiate variant shape patterns, such as sheet, blob, tube, line, sphere, etc. By accumulating simplified shape descriptors, complex shapes can be depicted as well. Shape discrimination techniques can be used in all the fundamental image processing topics introduced above. In the following section, a review of commonly used shape descriptors, such as active shape index, Hough transform and Hessian-based filters, etc., will be given.

1.2.1. Hessian Shape Descriptors

Filters related to the second derivative of an image are typically used for enhancing structures with different geometrical shapes, such as tube, sheet or blob. The calculation of these filters are normally based on the analysis of Hessian matrix. Hessian-based filters are quite versatile to differentiate different shape structures and have been utilized in many medical image analysis applications, for instance, the pectoral muscle segmentation leveraging a sheet-like object enhancement filter [15], the multi-scale line enhancement filter [16], and the vesselness filter proposed by Frangi et al [17].

Given a 3D image $I(x, y, z)$, the Taylor expansion in the neighborhood of a voxel $V_0(x_0, y_0, z_0)$ can be derived as following:

$$I(V_0 + \delta_s) \approx I(V_0) + \delta_s^T \Delta_{V_0,s} + \delta_s^T H_{V_0,s} \delta_s \tag{1.1}$$

where the difference vector δ_s indicates a small change of position near to V_0 at scale s, $\Delta_{V0,s}$ is the gradient vector for V_0 at the scale of s and $H_{V_0,s}$ represents the Hessian matrix computed at V_0 with the scale of s. The elements of Hessian matrix are the second order partial derivatives with respect to x, y, and z:

$$H(V_0) = \begin{pmatrix} H_{x,x}(V_0) & H_{x,y}(V_0) & H_{x,z}(V_0) \\ H_{y,x}(V_0) & H_{y,y}(V_0) & H_{y,z}(V_0) \\ H_{z,x}(V_0) & H_{z,y}(V_0) & H_{z,z}(V_0) \end{pmatrix} \tag{1.2}$$

Based on the linear scale space theory introduced by Florack et al. [18], the second order derivative of Gaussian kernel at scale s convolving with image $I(V_0)$ will derive the Hessian matrix at V_0. For instance, the following equation allows for computing the second order derivative with respect to x at scale s.

$$I_{xx}(V_0, s) = \left(\frac{\partial^2}{\partial x^2} G(V_0, s) \right) \times I(V_0) \tag{1.3}$$

where $G(V_0, s)$ is the Gaussian kernel at scale s. The second derivative of G builds a probe kernel that measures the contrast difference between inside and outside the region defined by $[-s, +s]$, as depicted in Fig. 1.1.

The eigen values and eigen vectors of $H(V_0)$ encode the local shape variations at V_0. Denoting the eigen values and eigen vectors of $H(V_0)$ as $\lambda_1, \lambda_2, \lambda_3$ and e_1, e_2, e_3, the eigen vectors corresponding to the largest and smallest eigen values represent the directions that attain the maximum and minimal second derivative variation. The third eigen vector points to the direction that is orthogonal to the others, as depicted in 1.1. Since the objects with different shapes are attributed with different variations along the eigen directions, the patterns of eigen values are capable of describing different shape structures. Assuming the eigen values are sorted based on their absolute values and fulfills the relation $|\lambda_1| \leq |\lambda_2| \leq |\lambda_3|$, the patterns associated with different shapes can be summarized in Tab. 1.1.

Taking the advantages of different eigenvalue patterns, to design a dedicated filter that is capable of enhancing a particular 3D shape structure is straightforward. For instance, a sheet-like object filter was introduced by Wang et al. to segment pectoral muscle boundaries [15],

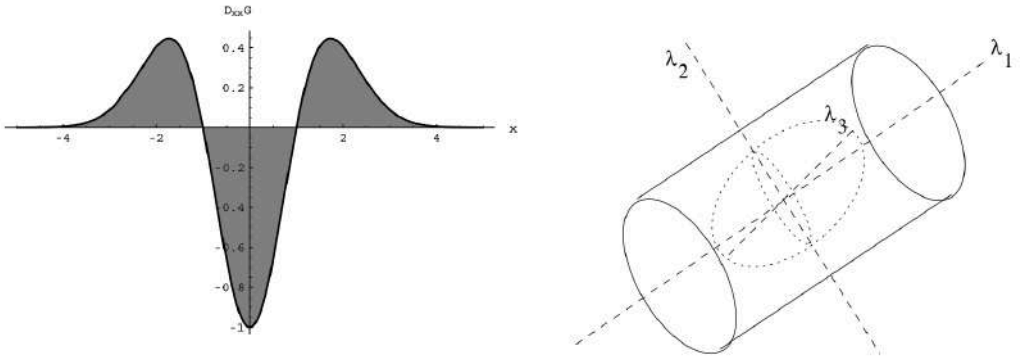

Figure 1.1: *Left*: the second derivative of Gaussian kernel with $s = 1$. *Right*: the principle directions corresponding to each eigenvalue of H [17].

Table 1.1: Eigen value patterns corresponding to different shape structures in 3D (H=high, L=low, N=noisy, usually small and can be positive or negative, +/- indicate the sign of the eigenvalue. Bright and dark indicate that the structures appear as brighter or darker than surroundings.) [17].

λ_1	λ_2	λ_3	shape structures
N	N	N	noisy, no preferred direction
L	L	H-	sheet-like structure (bright)
L	L	H+	sheet-like structure (dark)
L	H-	H-	tube-like structure (bright)
L	H+	H+	tube-like structure (dark)
H-	H-	H-	blob-like structure (bright)
H+	H+	H+	blob-like structure (dark)

a so-called vesselness filter was proposed in [17] to enhance vascular structures, a tube-like filter was used to detect nipples in breast ultrasound images [19].

1.2.2. Shape Index

Volumetric shape index and curvedness introduced by Koenderink have been widely used in describing and differentiating topological shapes of objects [20]. Particularly in the applications of CADe and CADx, for instance, the characterization and detection of polyps in colon CT images [21], the detection of small-size pulmonary nodules in helical CT images [22], or detection of specific landmarks such as fiducial markers scanned in medical images [23].

The computation of volumetric shape index and curvedness of an image point (voxel) is based on its curvatures associated with a local iso-intensity surface that passes the point. Classical surface curvature measures, such as the Gaussian and the mean curvature at a voxel of a surface, are not very indicative of depicting local shapes, as they combine the two principal curvatures as a single measurement. It would be more informative to depict different shapes using both principal curvatures. However, a single shape indicator rather than a pair of numbers is more favored and practical to use. Moreover, a reliable shape indicator should preferably not depend on the size, i.e. the amount of curvature. Considering these preferences and constraints, the volumetric shape index and curvedness were designed to fulfill these requirements [20]. The curvedness is a positive number that specifies the amount of curvature, whereas the shape index is a number in the range of $[0, 1]$ and is scale invariant. For a given voxel v, denoting the two principal curvatures as the κ_1 and κ_2, the shape index S and curvedness C of v can be computed by following equations:

$$S(v) = \frac{1}{2} - \frac{1}{\pi} arctan \frac{\kappa_1(v) + \kappa_2(v)}{\kappa_1(v) - \kappa_2(v)} \tag{1.4}$$

$$C(v) = \sqrt{\frac{\kappa_1(v)^2 + \kappa_2(v)^2}{2}} \tag{1.5}$$

Different shape index values represent different local shape structures: cup, rut, saddle, ridge or cap. In Fig. 1.2, the shapes with different shape indices are mapped to a unit circle spanned by unit curvatures κ_1 and κ_2, where an one to one mapping between distinct shapes and shape index values is illustrated, such as cup ($S = 0.0$), rut ($S = 0.25$), saddle ($S = 0.5$), ridge ($S = 0.75$) and cap ($S = 1.0$). Negative shape index represents the same shape indicated by its corresponding positive value, but with opposite orientation. Basically, one can use a value in range of $[0, 1]$ to indicate all distinct shapes. Any value between $[0, 1]$ corresponds to a unique shape. One of the key advantages of shape index is that continuous variation of index value reflects the smooth transition from one shape to another. For instance, the dome shape with $S = 0.875$ is the transient shape from ridge ($S = 0.75$) to cap ($S = 1.0$). Moreover, for medical image processing, the shape index can be computed for any voxels of the image, without explicitly extracting the iso-surface passing the voxels.

The complementary curvedness indicates the amount of curvature for each voxel, ranging from $[0, +\infty)$. A unique shape index value correlates to a unique shape, whereas the corre-

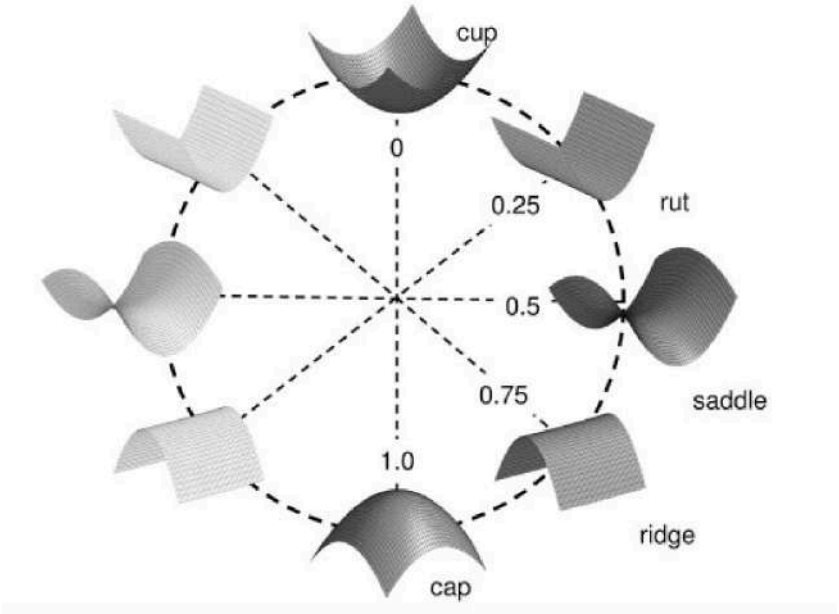

Figure 1.2: Illustration of distinct shapes and corresponding shape index values [21].

sponding curvedness expresses the extent how this specific shape is curved. Curvedness 0 is an extreme case implying no curvature presented, which means the shape is decayed into a plane. However, by increasing the curvedness value, the shapes with the same shape index will keep unchanged, but the extent of curvature will be increased, as illustrated in Fig. 1.3.

1.2.3. 3D Zernike Descriptors

Moment-based shape descriptors have been exploited broadly for image retrieval [25], pattern recognition [26], object recognition [27], and shape matching [28]. A compact numerical expression of moment-based shape features enable rapid comparisons. Moments such as 2D/3D Zernike moments are based on the theory of orthogonal polynomials [29], which allow descriptors to be constructed to an arbitrary order with some redundancy. It is also possible to reconstruct the object from its moments with quality determined by the number of terms used [26, 30].

The Zernike polynomials were introduced by Frits Zernike in 1934 [31]. Historically, Zernike introduced a set of orthogonal-normalized (Orthonormal) radial polynomials primarily dedicated to optical applications [32]. Later, the Zernike functions were used to to define Zernike moments of 2D images [29] (see Fig. 1.4 for 2D Zernike terms). More recent works used 3D Zernike moments to derive robust invariant descriptors of 3D images and/or objects and perform image/object reconstruction from a finite set of 3D Zernike moments [32].

The Zernike functions $Z_{nl}^{m}(r)$, are base functions that are constructed to form an orthonormal set over the unit ball (i.e. $0 \leqslant r^2 \leqslant 1$, $r^2 = x^2 + y^2 + z^2$). They are based on the familiar spherical harmonics, $Y_l^m(\theta, \phi)$ which θ and ϕ are the standard angular spherical coordinates. The spherical harmonics can be described as [33]:

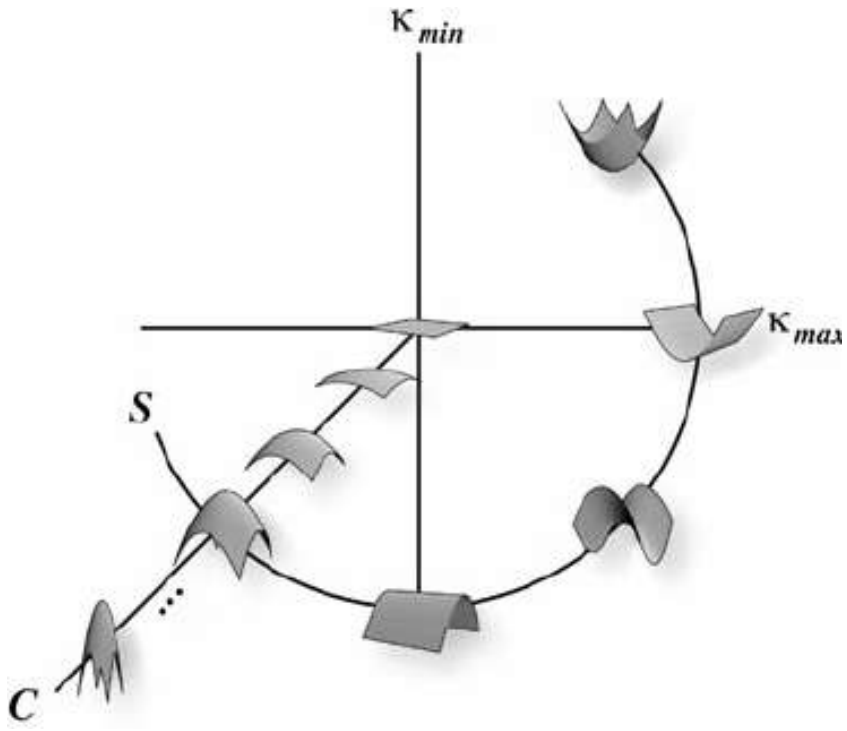

Figure 1.3: Illustrate the change of shapes when changing shape index and the change of curvature extent when changing curvedness values [24].

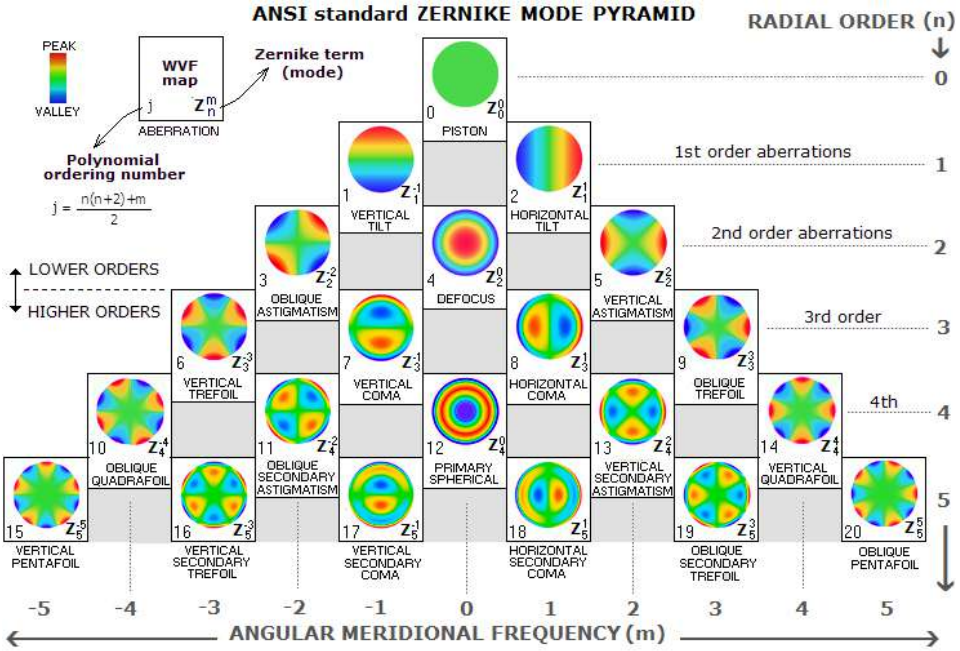

Figure 1.4: Graphical illustration of top 20 Zernike terms as a pyramid. Zernike terms (Z_n^m) expansion pyramid is a function of term's radial degree (or order) n and azimuthal frequency m. It is the basis for classifying aberrations as lower ($n \leq 2$) and higher-order ($n > 2$) in ophthalmology. Associated Zernike terms and names of aberrations; the so called $j - number$ (commonly referred as mode), the polynomial ordering number, is dependent on n and m, determining the position of the term in the Zernike terms' expansion. (Figure taken from www.telescope-optics.net)

$$Y_l^m(\theta,\phi) = N_l^m e^{im\phi} P_l^m(cos\ \theta) = N_l^m \left(\frac{x+iy}{\sqrt{x^2+y^2}}\right)^m P_l^m(\frac{z}{r}) \tag{1.6}$$

The normalization factor N_l^m is given by:

$$N_l^m = \sqrt{\frac{2l+1}{4\pi}\frac{(l-m)!}{(l+m)!}} \tag{1.7}$$

and $P_l^m(cos\ \theta)$ is the *associated Legendre polynomial*.

The *3D Zernike Descriptors* are series expansion of an input 3D function, which allow rotation invariant and compact representation of a 3D object that is considered as the 3D function. The mathematical foundation of the *3D Zernike Descriptors* was laid by Canterakis [34]. Later, Novotni and Klein [35] applied them to 3D object retrieval. Below is a brief mathematical derivation of them. For detailed derivations and discussions, refer to the literatures [34, 35].

The 3D Zernike functions are defined as follows [33]:

$$Z_{nl}^m(r) = \sum_{v=0}^{k} q_{kl}^v r^{2v} e_l^m(r) \tag{1.8}$$

with the following definitions for parameters:

$$\begin{gathered} e_l^m(r) = r^l Y_l^m(\theta,\phi),\ k = (n-1)/2, \\ q_{kl}^v = \frac{(-1)^{k+v}}{2^{2k}}\sqrt{2l+4k+3}\binom{2k}{k}\binom{k}{v}\binom{2(k+l+v)+1}{2k}/\binom{k+l+v}{k} \end{gathered} \tag{1.9}$$

The coefficients q_{kl}^v are chosen to ensure orthonormality over the unit ball; they can also be written in terms of n as follows:

$$q_{nl}^v = (-1)^{\frac{n-1}{2}+v}\sqrt{2n+3}\frac{\Gamma\left[\frac{3+l+n}{2}+v\right]}{v!\,\Gamma\left[1+\frac{n-1}{2}-v\right]\,\Gamma\left[\frac{3}{2}+l+v\right]} \tag{1.10}$$

where $\Gamma[x]$ is the complete Gamma function. The Zernike functions, therefore, are a 3D generalization of the spherical harmonics (see Fig. 1.5), which are only orthonormal on the surface of the unit ball [33].

Two instances of Zernike functions for $(nl) = (53)$ and $(nl) = (82)$ can be seen in Fig. 1.6. It shows the iso-amplitude surface for the real part of the Zernike function for each individual function, at an amplitude level equal to 0.1.

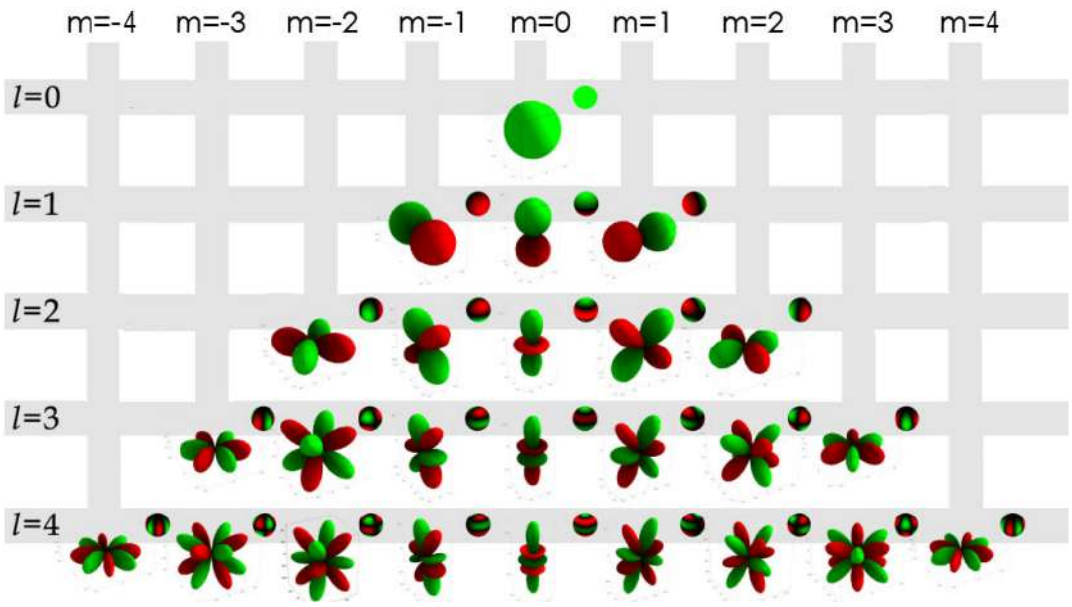

Figure 1.5: The 3D spherical harmonic basis. Visual representations of some of the first real spherical harmonics. **Green color** represents positive function values and **red color** represents where it is negative. The distance of the surface from the origin indicates the value of $Y_l^m(\theta, \phi)$ in angular direction (θ, ϕ). (Figure taken from www.quora.com)

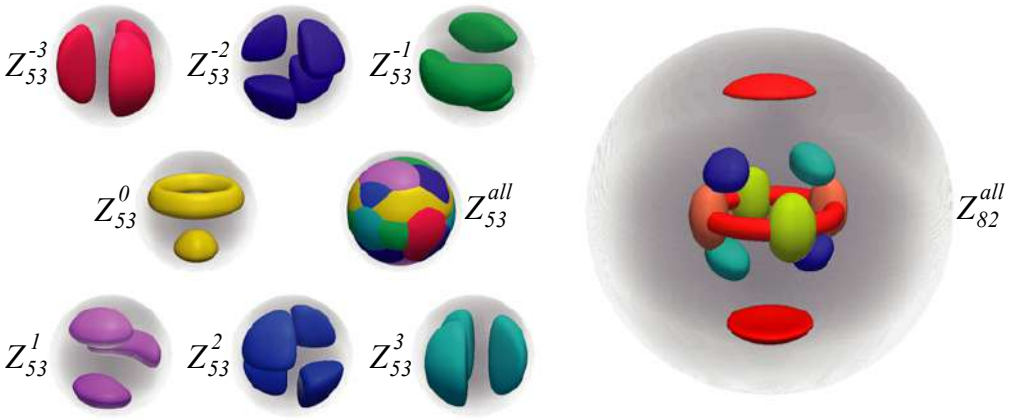

Figure 1.6: Example visualizations of selected 3D Zernike functions Z_{53}^m and Z_{82}^m. The gray halo around each function represents the embedding sphere. (Figure taken from [33])

Note that, as Zernike functions are defined over the unit ball, to compute the moments using them, the object has to be scaled down to be fitted inside the unit ball before the computation [33].

1.2.4. Sphere Packing Shape Descriptors

Sphere Packing

Sphere packing is filling an object with a set of non-overlapping spheres. It has diverse applications in various fields of scientific and engineering, including automated surgical treatment planning, investigation of processes such as sedimentation, compaction and sintering, powder metallurgy for 3D laser cutting, cutting different natural crystals, and so forth. Polydisperse sphere packing is a new and promising data representation for several fundamental problems in computer graphics and virtual reality such as collision detection and deformable object simulation. Polydisperse means that the radii of the spheres can be an arbitrary real number [36].

Here, it is tried to broaden the usages of sphere packing algorithm and utilize it to classify an object (which here is the breast lesion), using its shape features. In this work, an extended version of sphere packing algorithm, called *Protosphere*[1], which is a GPU-assisted prototype guided sphere packing algorithm. The Protosphere is inspired by machine-learning techniques and uses a prototype-based greedy choice to extend the idea of Apollonian sphere packing [36]. For an arbitrary given object, it starts with the largest possible sphere that fits in the object. It iteratively inserts new spheres, under the constraints that first, they must not intersect the already existing ones and second, they be completely contained inside the object [37].

The Protosphere algorithm was introduced in 2010 by Weller and Zachmann [37] and was extended by Teuber et al [36]. It is able to efficiently compute a space filling sphere packing for arbitrary container objects and object representations (polygonal, NURBS, CSG, etc.) under the only precondition that it must be possible to compute the distance to the object's surface from any point. This packing is achieved by successively embedding the largest possible sphere into the object [36].

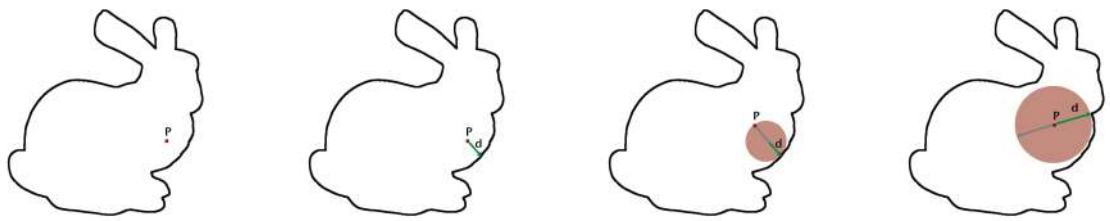

(a) (b) (c) (d)

Figure 1.7: Sphere packing prototype convergence visualization. (a) placing the prototype P randomly inside the object; (b) calculating the closest point on the surface and the distance d; (c) moving P away from the closest point; (d) repeating this until the prototype converges. (Figure taken from [36])

[1]Protosphere: A GPU-Assisted Prototype Guided Sphere Packing Algorithm for Arbitrary Objects http://cgvr.cs.uni-bremen.de/research/protosphere [Accessed on 6 September 2015]

Consider the largest sphere s inside O, the surface of a closed and simple object in 3D. Obviously, s touches at least four points of O, and there are no other points of O inside s. This implies that the center of s is a *Voronoi Node (VN)* of O. Consequently, the *Apollonian* filling can be formulated as an iterative computation of the VNs of the objects hull O plus the set of all spheres existing so far. To compute the *Voronoi Diagram (VD)* they approximate the VNs by placing a single point, *the prototype*, inside the object and let it move away from the object's surface in a few iterations. By choosing a clever movement, the prototype converges automatically towards a VN (see Algorithm 1, which is taken from [36]). The last step of the algorithm guarantees that, after each single step, p is still inside the object, because the entire sphere around p with radius $\|p - q_c\|$ is inside the object.

Moreover, moving p away from the border, into the direction $(p - q_c)$, leads potentially to bigger spheres in the next iteration. Usually, $\epsilon(t)$ denotes a cooling function that allows large movements in early iterations and only small changes in the later steps. This process is parallelized and uses a set of prototypes that are allowed to move independently instead of inserting just a single prototype, which might end up in a local optimum rather than of converging toward the global optimum.

Algorithm 1 Sphere packing prototype converge.

```
1: procedure convergePrototype (prototype p, object O )
2:     place p randomly inside O
3:     while p has not converged do
4:         q_c = arg min {||p − q|| : q ∈ surface of O }
5:         choose ε(t) ∈ [0, 1]
6:         p = p + ε(t) · (p − q_c)
7:     end while
8: end procedure
```

In order to apply sphere packing to the binary lesion segmentation (see Fig. 1.8(a)), at first, it is converted to a mesh geometric object (see Fig. 1.8(b)), then I let Protosphere pack it with arbitrary number of spheres (here, 4000 is chosen as the maximum number of spheres inside any lesion object) (see Fig. 1.8(c)). In the following section, a couple of advantageous shape features are elicited from the internal spheres to create a samples dataset for classifier.

Volume-Radius Histogram

The histogram of volume-radius feature provides an estimate for the proportion of the volume covered by spheres with a specific radius range. Some experimental observations are done on the alignment and structure of internal packed lesions:

- Benign lesions in comparison to malignant ones have a more regular shape mostly with oval or round form. According to the principal essence of the sphere packing algorithm, which initially tries to occupy as much proportion as it can with the biggest sphere possible, it is found out that the majority of their internal space is filled with a few

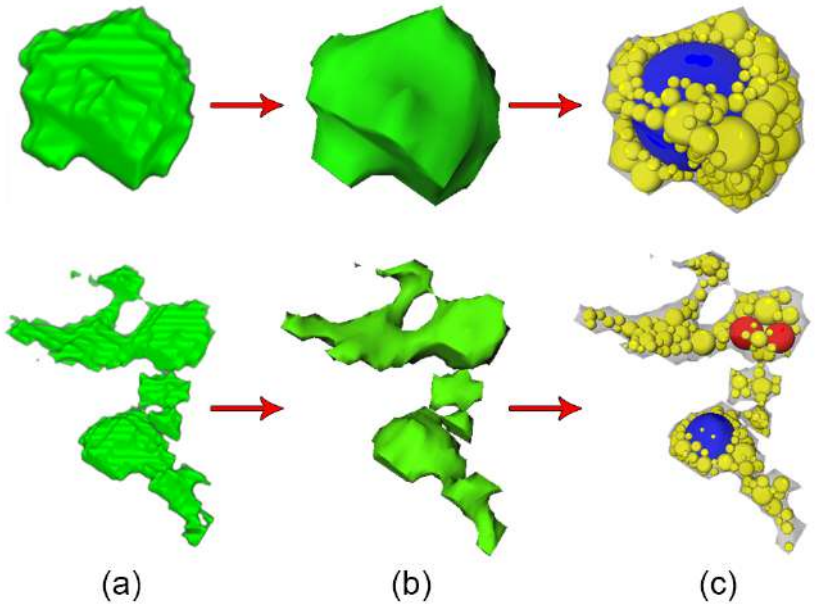

Figure 1.8: Sphere packing of the lesion 3D volume. Top shows an example of benign lesion. Bottom shows an example of malignant lesion. (a) is the binary volumetric segmented of the lesion; (b) is converted lesion volume into a 3D mesh geometry; (c) is the lesion packed with 200 spheres (the spheres color is size based and is only for better differentiation in visualization).

number of very big spheres and the rest is occupied by smaller ones with considerable differences in size.

- On the contrary, in malignant lesions, there is no such regularity: most of their volume is occupied with middle size spheres and the rest are either big ones or small ones which are scattered along the shape.

Therefore, a histogram can be created such that on the x-axis lies radius of the spheres and the y-axis is the summation of spheres' volumes with radius between two bins. An arbitrary number of bins in x-axis can be considered to form the radius range of spheres. On the y-axis, the values represent the amount of lesion's volume occupied by spheres with a particular radius range.

Figure 1.9 shows two examples of the mentioned histogram for benign lesions (on top) and two examples for malignant lesions (on bottom). By collecting the corresponding value to each radius range on x-axis, a feature vector of an arbitrary number of features can be extracted from this method. This is one of the feature vectors needed to generate the samples dataset for the classifier.

1.2.5. Other Shape Descriptors

In computer vision, pattern recognition and image retrieval, many other shape descriptors have been developed to characterize general or specific shapes mainly in 2D. Some of these descriptors can be extended to describe 3D shapes, but with additional computational efforts. Belongie et al. introduced a generic shape descriptor called *shape context* [38]. For each point

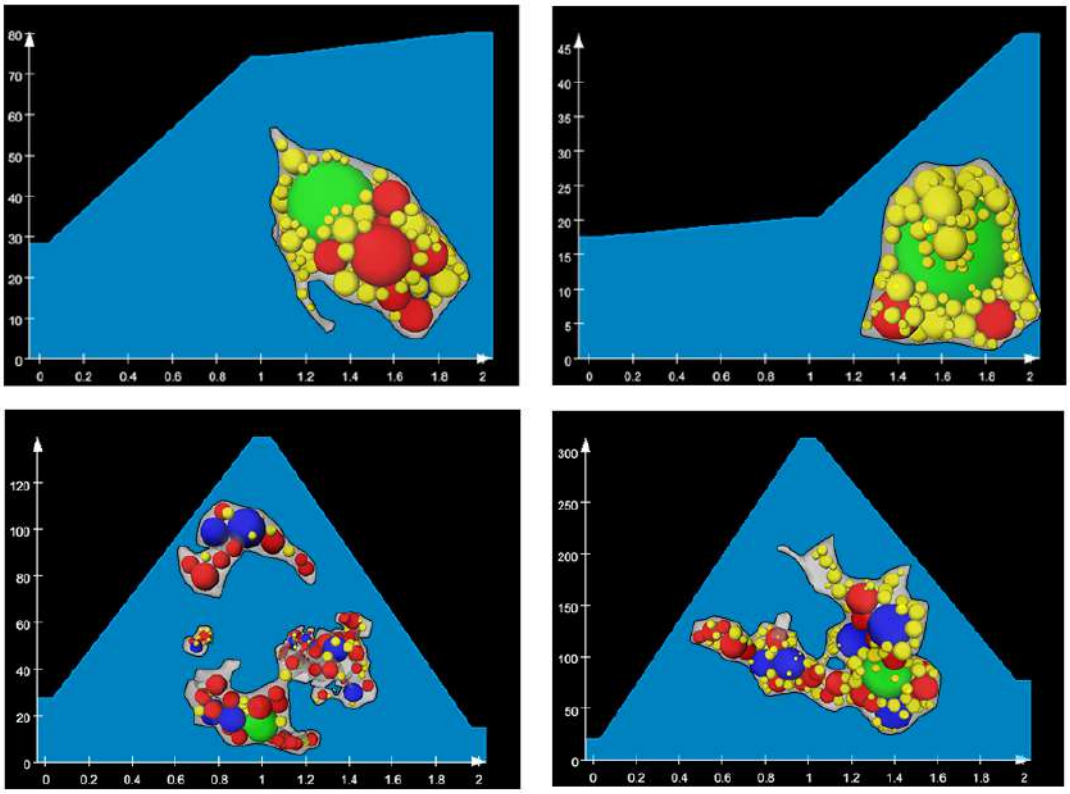

Figure 1.9: The Volume-Radius histogram from the objects packed with 200 spheres of two examples of benign (on top), and two examples of malignant lesions (on bottom). The difference between histogram shapes can be seen here, according to the different distribution pattern of sphere sizes. In benign lesions most of the object is filled with spheres having a big radius; in malignant lesions middle size spheres occupy most of the internal space. The color of spheres is based on size and is only for better differentiation in visualization.

on a 2D shape boundary, the **shape context** captures the distribution of relative positions to all other neighbors, which are encoded in a 2D log-polar histogram with one dimension representing the polar angle distribution, and the other dimension indicating the polar radius distribution. The histogram is computed for each single point sampled on object boundary (see Fig. 1.10). One of the key advantages of *shape context* is the invariance to standard deformations, such as translation, rotation and scaling, due to the usage of relative position correlation. Moreover, the similarity of two shapes can be measured by computing the distance between their corresponding *shape context* distributions (see Fig. 1.10(h)). In case the number of sample points is not equal, dummy nodes with constant matching cost will be added to each point set, by which the robustness of the algorithm can be even improved.

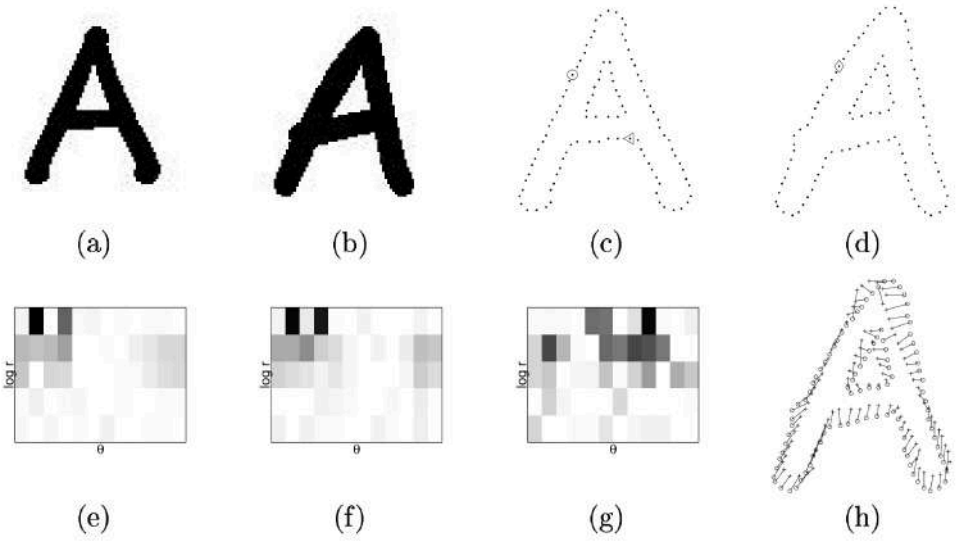

Figure 1.10: Illustration of *shape context*. (a, b) two original "A" letter shapes. (c, d) sampled boundary points. (e-g) log-polar histograms encoding the shape distribution on the points indicated by circle, rhombus and triangle. (h) correspondences found between points on two shapes.

The definition of *shape context* allows for an easy extension from 2D to 3D shape characterization. However, as the number of voxel increases, the computational expense is dramatically elevated, due to the fact that the dimensionality of histogram will be larger. Therefore, the *shape context* descriptor is mainly adopted in the applications of computer vision, pattern recognition, and image retrieval that deal with 2D images. The same limitation also applies to other commonly used 2D shape descriptors ranging from moments and Fourier descriptors [22] to Hausdorff distance and the medical axis transform [39]. Considering the substantial amount of data coming with 3D medical images with much higher spatial and temporal resolutions, these technique might perform with lower efficiency.

Another category of shape descriptors is constructed on basis of Hough transforms, which are commonly used to describe the regular shapes that can be expressed mathematically by analytic functions, such as line, circle, and sphere [40]. To extend its applicability, Chiu et al. developed a fast and generalized Hough transform algorithm that can depict any arbitrary

shapes [41].

1.3. Outline of the Dissertation

To demonstrate the applicability and efficacy of the shape descriptors, several practical medical image processing tasks are introduced with comprehensive algorithm description and rigorous evaluations. The adoption of a specific shape descriptor is based on the characteristic of each task, in the purpose of making the proposed solution applicable in real clinical routine, which means that both the performance accuracy and efficiency have to be guaranteed.

This dissertation is organized as following: chapter 2 presents the first task aiming to automatically segment the femur heads in 2D fluoroscopy images using Gabor-based Hough transform. The precise delineation of the femoral heads in a number of 2D fluoroscopic images can be used to reconstruct 3D position of the relevant anatomy that provide valuable guidance information for surgeons. The implemented method is used in a surgical guidance software to improve the positioning accuracy of the instruments in orthopedic surgeries operating on femur bones.

The second task is to develop a fully automated algorithm to segment breasts in magnetic resonance imaging, which is introduced in chapter 3. In this task, a solution leveraging Hessian-based shape descriptor is designed. Since MRI has become more prevalent in breast cancer screening and diagnosis due to its high sensitivity, many computer-aided detection and diagnosis works were developed, where a breast segmentation is critical for the success of these systems. One of the successful applications taking advantages of automatic breast segmentation is the follow-up registration of breast MR images, which is also presented in this chapter.

The application of shape descriptors in object classification is given in chapter 4. In this task, breast lesions found in MR images are classified into benign and malignant types with the help of machine learning techniques. Prominent shape descriptors such as sphere packing related features show their great penitential in distinguishing tumor malignancy.

In the field of object detection, chapter 5 illustrates a task attempting to automatically detect nipple position in automated 3D breast ultrasound (ABUS). The nipple is recognized as important landmarks in breast images. Its position can be used in a variety of computer assisted applications, such as cross-modality registration from ABUS to mammography and MRI. The detection algorithm developed will be further enhanced by testing with a substantial amount of datasets. The detection algorithm utilizes again a Hessian-based shape descriptor that can capture the most prominent characteristic of the shadowing effect adhere to the nipple.

In chapter 6, a comprehensive framework for liver vascular segmentation in multi-phase CT images is introduced, which will be integrated into a liver surgery planning software. The work is sponsored by an industrial project collaborated with Siemens medical solution sector, Erlangen. The aim of this tool is to provide a virtual resection planning environment that optimizes the surgery outcomes. The segmentation of vessels (hepatic vein, portal vein and hepatic arteries) in the liver is a critical procedure of this tool, which directly influences the

decision-making of resection planes. A semi-automated segmentation framework is designed for this task to fulfill the accuracy and efficiency defined in this project.

Basically, the outline of each specific task consists of clinical background, related state-of-the-art techniques, description of proposed solution and quantitative performance evaluation. At the end, major conclusions, comments and further improvement ideas are summarized in chapter 7.

2

Femur Head Segmentation Using Gabor-based Hough Transform

Acknowledgment

This work was the results of a collaboration with an industrial partner, which financed the project and delivered the results into a commercial product of bone surgical navigation system. The main contributor of this work is Dr. Michael Kohnen (Stryker, Germany), who has kindly shared many valuable and inspiring ideas and comments. He also supported a lot in the evaluation of the method by providing a large scale of test images and categorizing them into three groups based on the image quality. Moreover, without the guidance and support of Prof. Dr. Horst Hahn, this work will not achieve its success in terms of performance and efficiency.

Publications

The algorithm description, implementation, and evaluation of this work were published in the following scientific paper:

- **Wang L**, Kohnen M, Friman O, Hahn HK (2011) Fast automated segmentation of femoral heads in fluoroscopic X-ray images. In: IEEE Int. Symp. Biomed. Imaging (ISBI), pp. 984–988.

2.1. Introduction

To fixate a fractured femur bone, nails and screws must be implanted in orthopedic surgery which is usually performed under fluoroscopic intra-operative X-ray tracking, where the two dimensional projection images have to be interpreted by the surgeons to get an estimation of the three dimensional anatomy (see Fig. 2.1). In fluoroscopic tracking for fractured femur bone fixation, a precise identification of the femoral head provides valuable guidance for positioning the implant instruments such as nails and screws. The precise localizations of the femoral heads in a number of 2D fluoroscopic images can be used to reconstruct 3D position of the relevant anatomy that provide valuable guidance for improving positioning accuracy. The fluoroscopic images are generally acquired with a C-arm device in two standard orientations (Fig. 2.11), i.e., Anterior-Posterior (AP) and Medio-Lateral (ML), and typically exhibit low signal-noise ratio, non-uniform intensities and textures, occlusions, as well as weak and spurious edges. The task of extracting the femoral contour automatically is therefore fairly difficult. Noise, occlusions and weak edges challenge the task of automatically segmenting the femoral head. In this work, a fast and fully automated method to precisely delineate the femoral head in fluoroscopic X-ray images is presented. The proposed method comprises two stages. First, a candidate circle detection stage using a set of curved Gabor filters and a Gabor-based Hough transform is applied to estimate a few candidate circles approximating the femoral head. Second, a fine circle determination stage extracts the target circle from the candidates by analyzing the anatomical features of the femoral head and its spatial relation to the acetabulum. The validity and robustness of the method were tested on a set of 1184 fluoroscopic images from different vendors.

2.2. Related Works

Most of the analysis of femur heads is carried out in the context of other medical imaging modalities, such as CT [42–44] and MRI [45]. The task of segmenting femur heads in fluoroscopic images is quite specialized and more challenging, because the regions delineated by femur head boundaries present high non-uniformity in both intensities and textures. However, through an intensive literature review, several works focusing on the analysis of femur bones have been found. Among these techniques, model-based approaches are commonly used to extract the contours of femur bones in X-ray images [46–50].

Generally, these automatic or semi-automatic [49] methods construct either 2D [46, 47] or 3D [48, 50] generic models, initialize or project the models in the 2D X-ray images, analyze and extract the prominent features of the bone structures, and register the projected model onto the X-ray images. The geometrical models used in these works have to be built in a training stage, which requires a large amount of training samples. Typically, a post-processing refinement step using active contour [46, 50] or level set [47] algorithms is applied. These methods were only tested on AP views and will encounter difficulties on ML view images because the initialization, projection, and registration steps of model-based methods are highly subject to the viewing direction. Moreover, the involvement of non-rigid registration [48, 50] makes the methods computationally expensive, which makes them hardly applicable in real

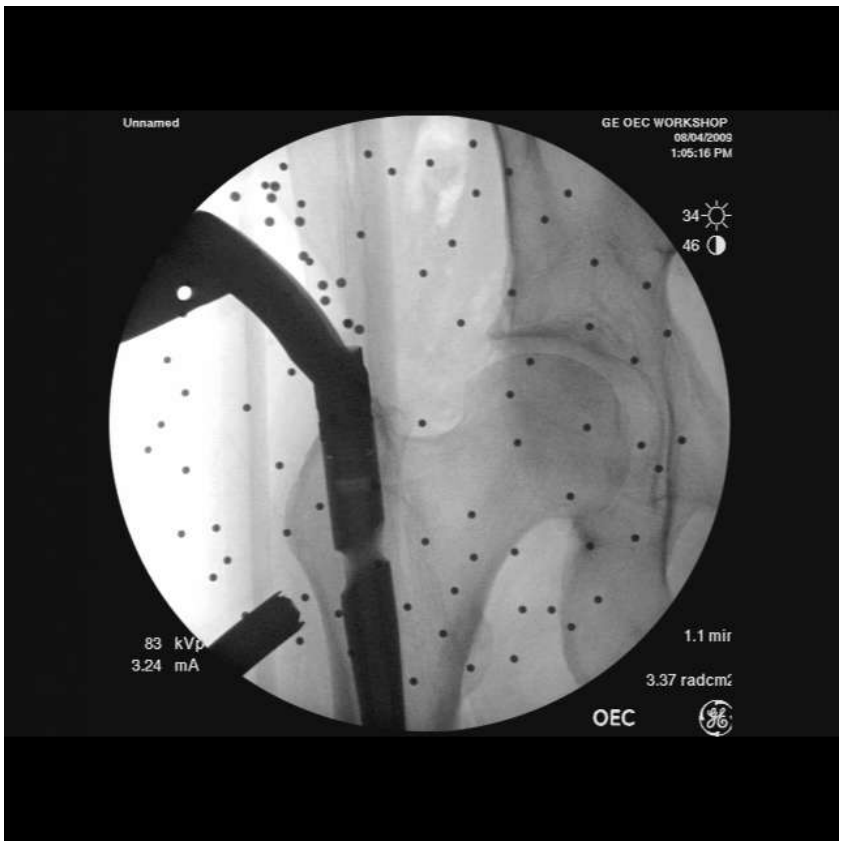

Figure 2.1: A typical fluoroscopic X-ray image acquired during hip-joint surgery by C-Arm device.

time surgical routines.

To fulfill the performance and time constraints, in this work, a fast and automated method for precisely extracting the circular contours of femoral heads in both AP and ML views is developed. The method takes advantages of an efficient shape descriptor, Gabor-based Hough transform. The investigation of the sphericity of the femoral head ensures the reliability and feasibility to model the femoral head contour as a circular object in the 2D projection image [51]. The proposed method comprises two stages. First, a set of curved Gabor filters and a Gabor-based Hough transform are applied to estimate a few candidate circles. Second, the target circle from the candidates is extracted by analyzing the anatomical features of the femoral head and its spatial relation to the acetabulum. The joint consideration of the acetabular boundaries makes the method more robust.

2.3. Methods

The proposed segmentation procedure can be subdivided into two main stages: *candidate circle detection* and *fine circle determination*. A schematic overview of the detection workflow is depicted in Fig. 2.2.

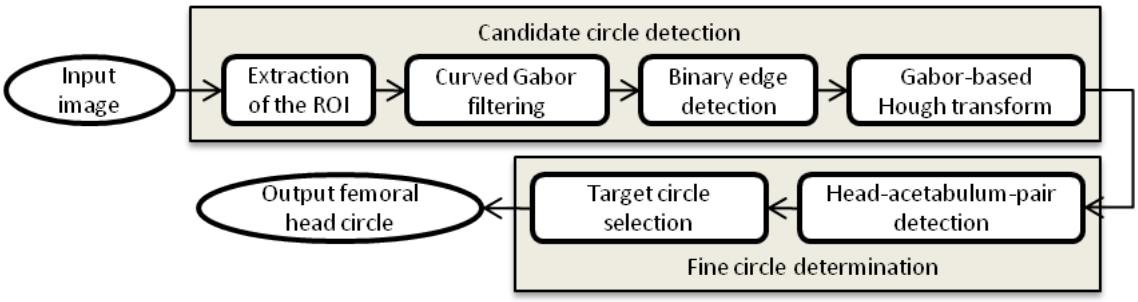

Figure 2.2: The overall work-flow of the proposed method.

2.3.1. Candidate Circle Detection

In the candidate circle detection stage, a region of interest (ROI) indicating all potential femoral head projections on the X-ray image is estimated at first. Then, a set of curved Gabor filters is applied to the ROI to extract the magnitudes and the directions of edge structures. The extracted and classified edges are utilized to build a 3D Hough space with the occurrence probabilities of circular objects within a predefined radius range. In the Hough space, a number of candidate circles with roughly estimated center positions and radii can be found. Details follow below.

Extraction of the ROI

The ROI is a rectangular box tightly bounding all possible projections of the femoral head in the X-ray image. During the intraoperative navigation, the 3D position of the nail as well as the trajectory of the proposed or implanted screw are known. Figure 2.3 illustrates the known geometric relations of implanted nail, screw and potential femoral head search space. The possible projected area of the femoral head can be found based on several measurements, i.e., the femoral head radius, the distance from the femoral head center to the screw hole. After investigating 636 CT datasets acquired from different sites worldwide in our training database, the following measures were extracted:

- Femoral head radius range: $r \in [17.63, 29.36]$mm
  with mean=23.49mm and standard deviation=1.95mm
- Distance from head center to screw hole:
  $d \in [43.67, 76.31]$mm

From these observations, a number of extremal femoral head projected positions are computed for the AP and ML views, and the bounding box delimiting these projections serves as the ROI, see Fig. 2.4.

Moreover, to keep the parameters and other measurements applied in the succeeding detection algorithms invariant to the resolution of ROI, the ROI is transformed into a standard image where the mean femoral head has always a radius specified with a fixed number of pixels, see Fig. 2.5 and 2.7. In the standard image, the possible radius range of the projected

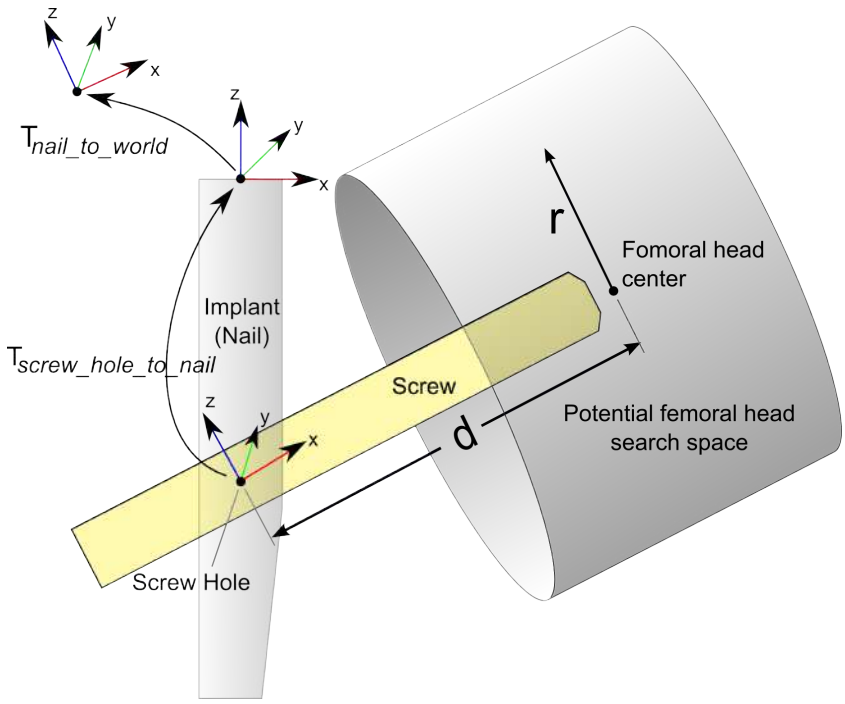

Figure 2.3: The geometric relations of implant nail, screw, femoral head and world coordinate, by which the possible projections of the femoral head can be estimated.

femoral heads in the transformed ROI can be derived, which is $r \in [57, 103]$ pixels. Consequently, a reverse transformation is required to place the detected circle in the transformed ROI back to the original image.

Curved Gabor Filtering

To extract the edges of the femoral head, we introduce a bending kernel that deforms the standard Gabor filter into a curved shape with a defined radius. The curved kernel allows the Gabor filters to enhance curved edge structures and inhibit other forms. The extended Gabor kernel is defined as follows:

$$g(x, y; \lambda, \theta, \psi, \sigma, \gamma, r) = \exp\left(\frac{x''^2 + \gamma^2 y''^2}{2\sigma^2}\right) \cos\left(2\pi \frac{x''}{\lambda} + \psi\right) \tag{2.1}$$

$$\text{where } x'' = x' \cos\theta + y' \sin\theta, y'' = -x' \sin\theta + y' \cos\theta \tag{2.2}$$

$$\text{and } x' = l - x, y' = \begin{cases} -\varphi \cdot r, & y \geq 0 \\ \varphi \cdot r, & y < 0 \end{cases}$$

$$\text{with } l = \sqrt{(x-r)^2 + y^2}, \varphi = \arccos\left(\frac{x-r}{l}\right) \tag{2.3}$$

Equations 2.2 and 2.3 are designed to rotate and bend the original Gabor kernel. In this work, the size of the curved Gabor kernel is 27×27 pixels, and the parameters and their settings are as follows:

- λ represents the wavelength of the cosine factor, and is set to $\lambda = 5.0$ pixels.

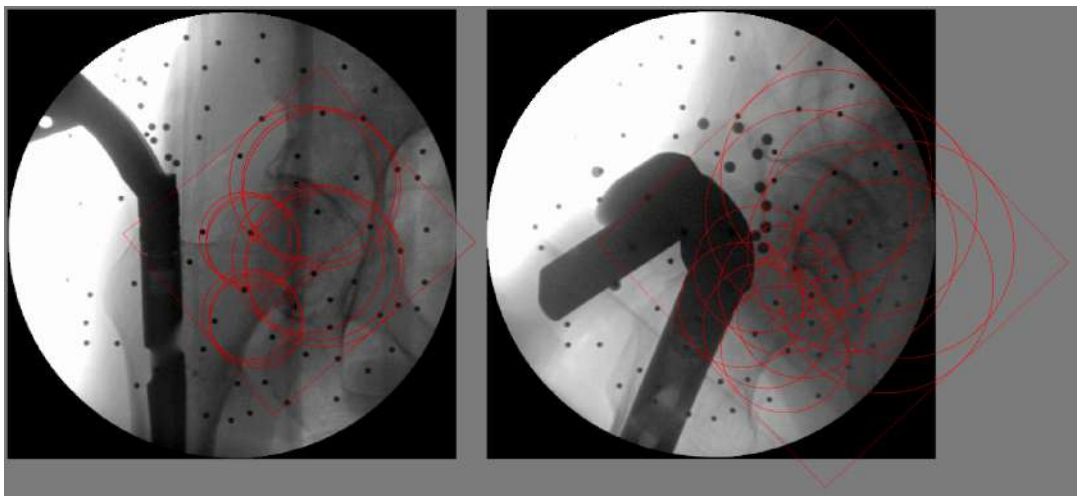

Figure 2.4: The estimated ROI that includes all possible projections in AP (left) and ML(right) views.

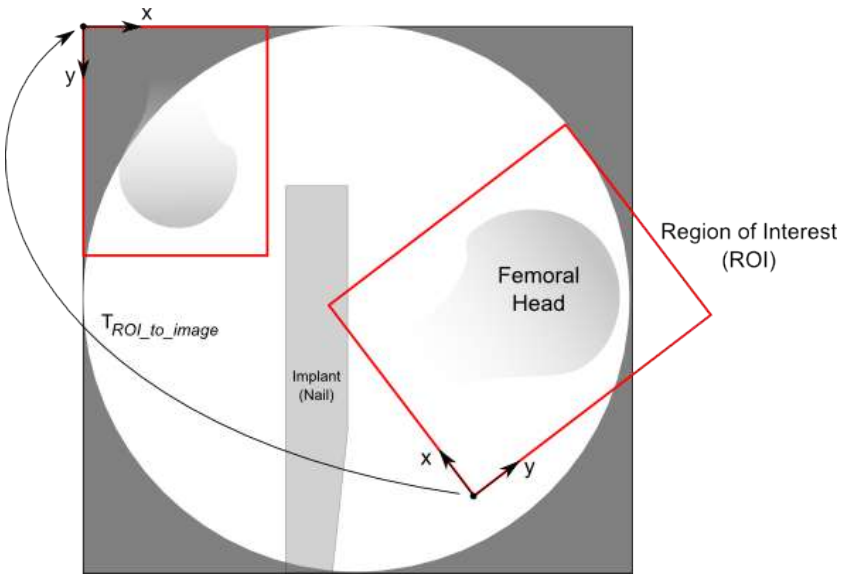

Figure 2.5: The transformation of ROI into the standard image.

- θ represents the orientation of the kernel. In total, 72 orientations (5.0 degree increment within $0° - 360°$) are chosen, generating a filter set.
- ψ is the phase offset which is set to $\psi = \pi/2$.
- σ is the standard deviation of the Gaussian envelope which should be adapted to the wavelength. Hence, $\sigma = \lambda/6$ is chosen.
- γ is the spatial aspect ratio, which specifies the ellipticity of the Gabor function and is set to $\gamma = 0.18$.
- r is set to the average radius of the femoral head : 80 pixels, corresponding to about 23.5mm.

Three examples of extended Gabor filter templates in different orientations are visualized

in Fig. 2.6. The highest response of the orientated Gabor filter set and corresponding orientation are recorded in separate amplitude and orientation images, which will be used in the succeeding steps of the algorithm.

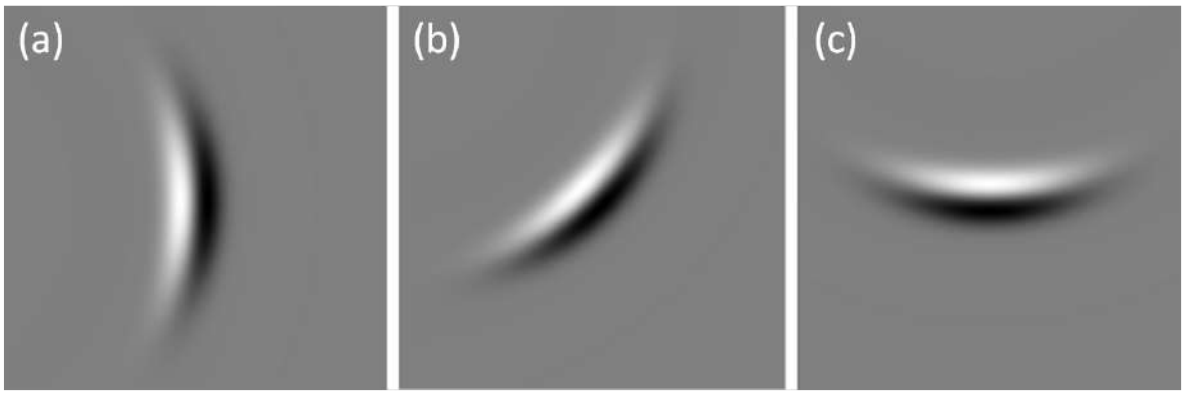

Figure 2.6: Extended Gabor filters with different orientations: (a) $\theta = 0$, (b) $\theta = \pi/4$, (c) $\theta = \pi/2$.

Binary Edge Detection

Based on the outputs of the Gabor filters, i.e., the amplitude and orientation images, a Gabor-based edge detector is developed to yield a binary edge distribution. To this end, we replace the gradient and direction measurements used in the original Canny edge detector with the amplitude and orientation responses of the Gabor filters. This concept enables the edge detector to react accurately on all visible boundaries of the femoral head, see Fig.2.7.

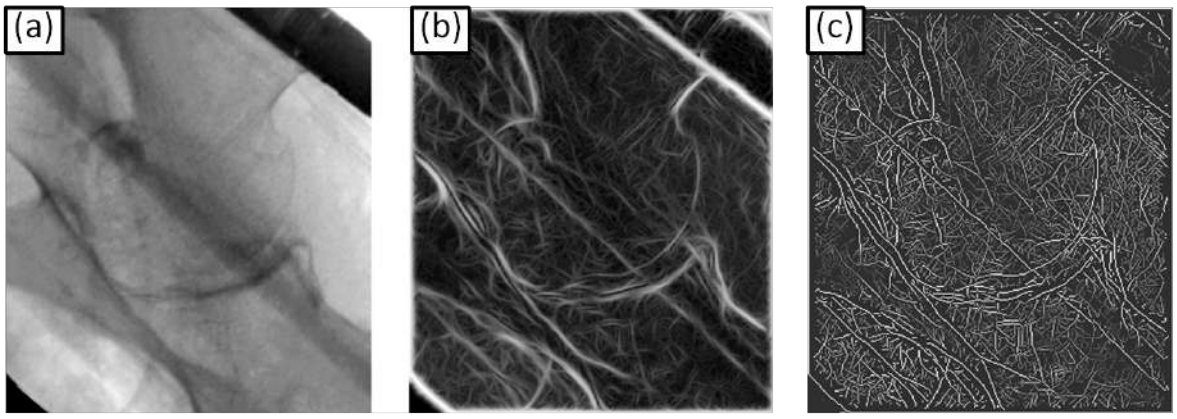

Figure 2.7: Thin edge detection: (a) Transformed ROI. (b) Amplitude response of Gabor filters. (c) The detected thin edges.

Gabor-based Circular Hough Transformation

The Hough transformation is an efficient and robust algorithm for detection of circular shape objects [40]. In 3D Hough space, each coordinate $\{c_x, c_y, r\}$ represents a circle with center $\{c_x, c_y\}$ and radius r. The Gabor-based Circular Hough transformation implemented in this work extends the original Hough transformation by integrating the output response of the Gabor filters. Only the edge pixels in Fig. 2.7(c) contribute to build the 3D Hough parameters

space. The calculation of the Hough space has two steps: the radius discretization and the center accumulation. As mentioned earlier, the possible radius range in the transformed ROI is $r \in [57, 103]$ pixels. A step size of 2 pixels is chosen for the discretization. For each radius, each detected edge pixel emanates along its gradient direction a *diffused anisotropic spot* at a distance determined by the radius. The anisotropy is needed to take the uncertainty of the estimated gradient direction into account. All the diffused spots generated by the edge pixels are accumulated to find the center positions of circles with the current radius. The iteration through all the radii within the range assembles a 3D Hough space depicted in Fig. 2.8. Finally, a number of circle candidates are obtained by exploring the highest local maxima in the 3D Hough space (see Fig. 2.9).

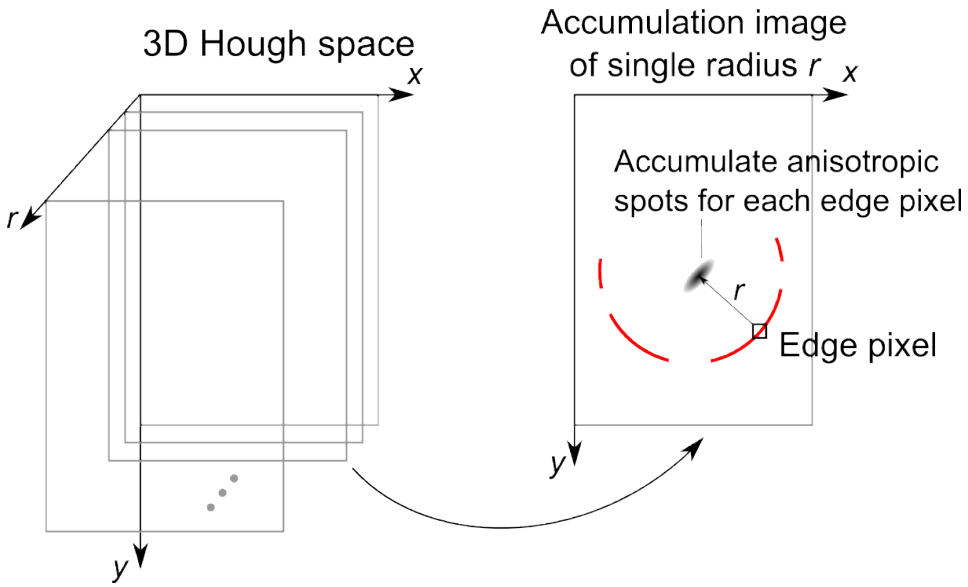

Figure 2.8: The computation of the 3D Hough space indicating center and radius and the accumulation of diffused anisotropic spots emanated from the edge pixels to locate centers of circles.

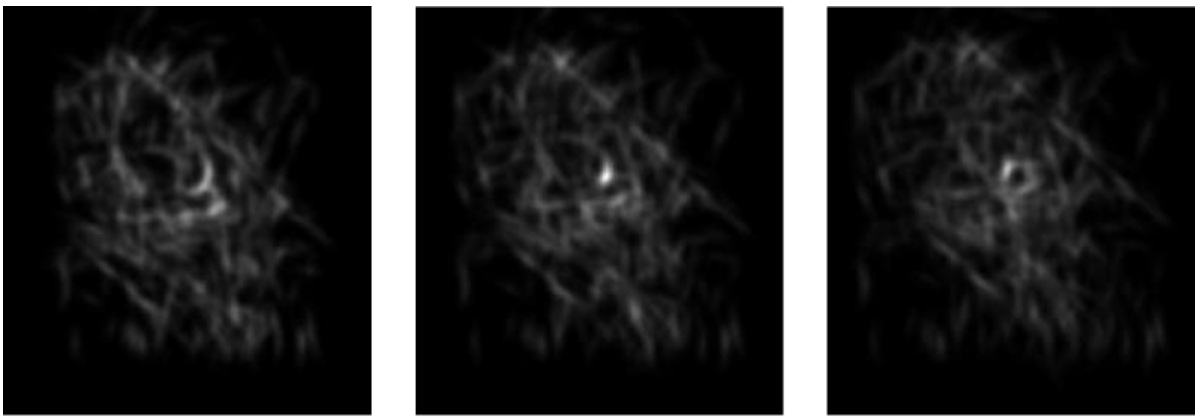

Figure 2.9: The accumulated circle probability map computed with respect to different radius r.

2.3.2. Fine Circle Determination

The fine circle determination stage aims to fine tune the candidate circles and determine the true femoral head. In many cases, the candidate circle with the highest accumulation value is not necessarily the femoral head but other neighboring circular anatomical structures, e.g., the acetabular boundaries. Moreover, the true candidate circle delineating the femoral head offers only an approximate center position and radius that needs to be fine adjusted.

Head-acetabulum-pair Detection

In this step, a *head-acetabulum-pair* that comprises the femoral head and the acetabular boundary circles is detected for each candidate circle. Based on the anatomical relation of the femoral head and the acetabulum, an acetabular circle in the proximity of the femoral head circle can be found, see Fig. 2.11. Hence, in the area where the true candidate circle is located, a head-acetabulum-pair can be detected. The joint consideration of the acetabulum provides more reliable characteristics, e.g., the gradient amplitudes, orientations, and the spatial relation of both femoral head and acetabular circles, that help to select the true candidate circle. Moreover, it can prevent the acetabular circle to be erroneously recognized as part of the femoral head circle.

The edge pixels contributing the accumulation to the center of each candidate circle in the Hough space are the feature points. The purpose of tracing the feature points is to find the head-acetabulum-pair by a RANSAC circle fitting algorithm [52]. For each candidate circle, the femoral head feature points are traced in a search area that has a ring and arc shape, see Fig. 2.10(a). The radius range of the ring search area is defined by multiplying two factors, i.e., 80% and 120%, to the candidate radius. An optimally fitted femoral head circle is achieved by adopting the RANSAC algorithm to the sought feature points. The RANSAC algorithm randomly selects three valid points to compose a circle. The supporters to the current circle are the feature points that it passes through within a given margin. The circle with the most supporters is revised with a least square fitting procedure to output the fitted femoral head circle. The acetabulum feature points can be acquired based on the fitted femoral head circle in the same manner, see Fig. 2.10(b). Subsequently, the RANSAC algorithm is employed again to the acetabulum feature points so that an optimally fitted acetabulum circle can be generated. Finally, the two fitted circles formulate a *head-acetabulum-pair*, which will be evaluated in the target circle selection step.

Target Circle Selection

The previous step results in several head-acetabulum-pairs. The additional consideration of the acetabular circle improves the robustness of the method because it prevents the interference between the femoral head and the neighboring acetabulum. The qualities of both circles are scored by investigating their prominent characteristics: the number of supporters of each circle in RANSAC, the consistency of the gradient directions of the image pixels at the border with the normals on the boundary circle, and the gradient amplitudes. The final score of each candidate pair is a weighted sum of the femoral head and acetabular qualities. The candidate with the highest score is picked as the detection result.

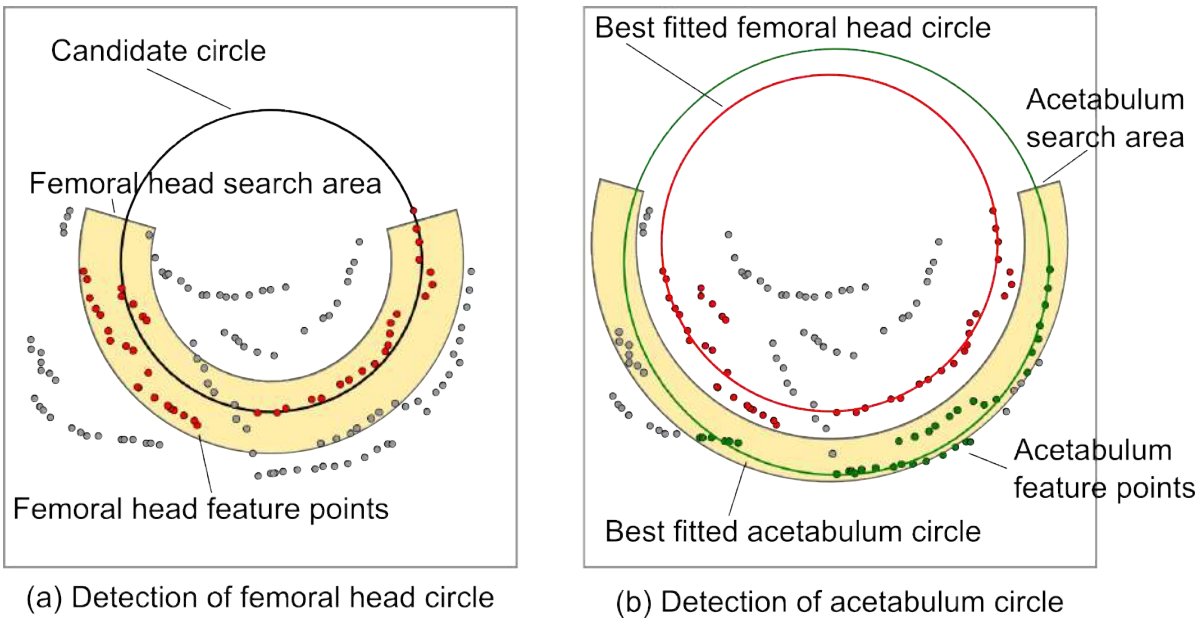

Figure 2.10: Trace the feature points and detect the fitted circle for (a) femoral head boundary and (b) acetabular boundary.

2.4. Results and Quantitative Evaluations

To quantitatively assess the performance of the proposed method, a test dataset comprising 1184 fluoroscopic images with 719 AP views and 465 ML views was used for evaluation. Test data were not used for the algorithm development. The size of the test images were 640×480 pixels. The referenced ground truth was obtained by manually annotating the center position and the radius of the femoral head. Moreover, the test images were ranked into normal, moderate and difficult categories, see Fig. 2.12, based on the image qualities, e.g., the level of noise, the percentage of the visible femoral head edges, the occlusion caused by the implants. The ground truth circles were established in a four-eye-principle as manual femoral heads were observed by a second person.

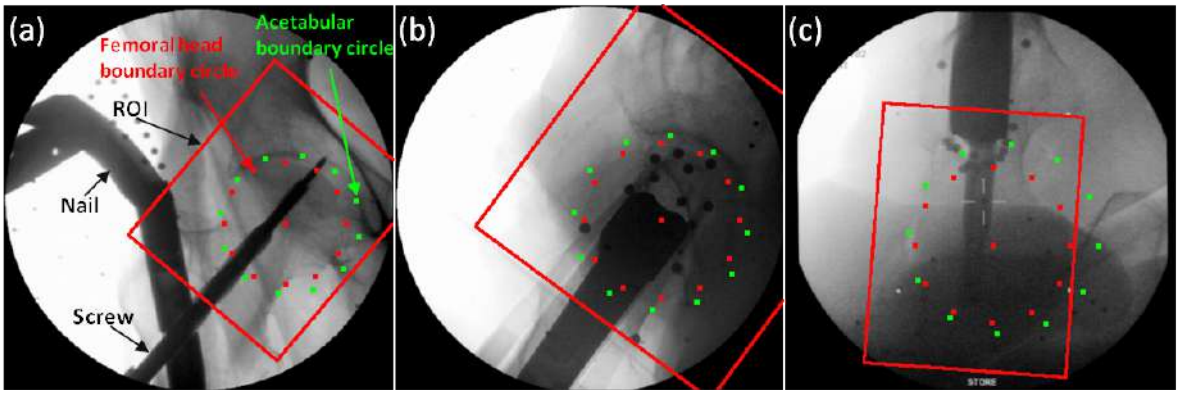

Figure 2.11: The demonstration of the extracted ROI (red box), the detected femoral head circle (red dots) and the acetabular circle (green dots) for the test image in category (a) normal (AP view), (b) moderate (ML view), and (c) difficult (ML view).

The method was implemented in C++ using OpenMP based parallelization for the computational expensive parts [53]. The average computational time per case was 2.04 seconds in a Intel Core2 Duo 2.2GHz CPU. Compared with the ground truth circle, the overall error distance was the summation of the center deviation and radius difference. A detected circle with an error distance lower than 2 pixels was considered to be accurate. Table 2.1 summarizes the number of images in each category and the detection rates. From the statistical results, the detection rate for all test images was 80%, and for normal and moderate categories it was 91.4%. Note that the high detection rate of 98.5% was achieved in the normal category. The proposed method performed with a low detection rate in difficult category, because the difficult category enclosed the extremely challenging cases for which even a human observer may have difficulties to determine the femoral head precisely. In this category, only a little parts of the femoral heads are visible with faint edges and enormous noises due to low exposure. In addition, the existing superimposed structures, e.g., the implants, the pelvis, and the surgical tools, may occlude the femoral head in the projected images. More representative examples were shown in Fig. 2.13 and 2.11 to demonstrate the performance of the method.

Category	Count	Detected	%
Difficult:	206	53	25.7
Moderate:	308	234	76.0
Normal:	670	660	98.5
All:	**1184**	**947**	**80.0**

Table 2.1: The evaluation results.

2.5. Discussion

This contribution presents a fast and fully automatic method for extracting femoral head contours in fluoroscopic X-ray images. The proposed method comprises two stages: First, a candidate circle detection stage estimates a few candidate circles approximating the femoral head using a set of curved Gabor filters and a Gabor-based Hough transform. Second, a fine circle determination stage extracts the target circle from the candidates by analyzing the anatomical features of the femoral head and its spatial relation to the acetabulum. The joint consideration of the acetabular circle enables the method to cope with some hard cases where the femoral head is very close to acetabulum, thus, improves the detection performance significantly. The quantitative experiments showed that the proposed method attained excellent and satisfactory performance for the images with normal and moderate qualities, respectively. Though the extremely poor quality of difficult category degraded the performance of the method, the overall detection performance has been proven to be reliable for a large number of clinical data sets, and the proposed method is to be integrated in a commercial product.

During the development of this method, it has been noticed that most of the related works have focused on the extraction of femur heads imaged in other modalities, such as CT [42–44] and MRI [45]. Therefore, it is quite hard for us to compare the performance against

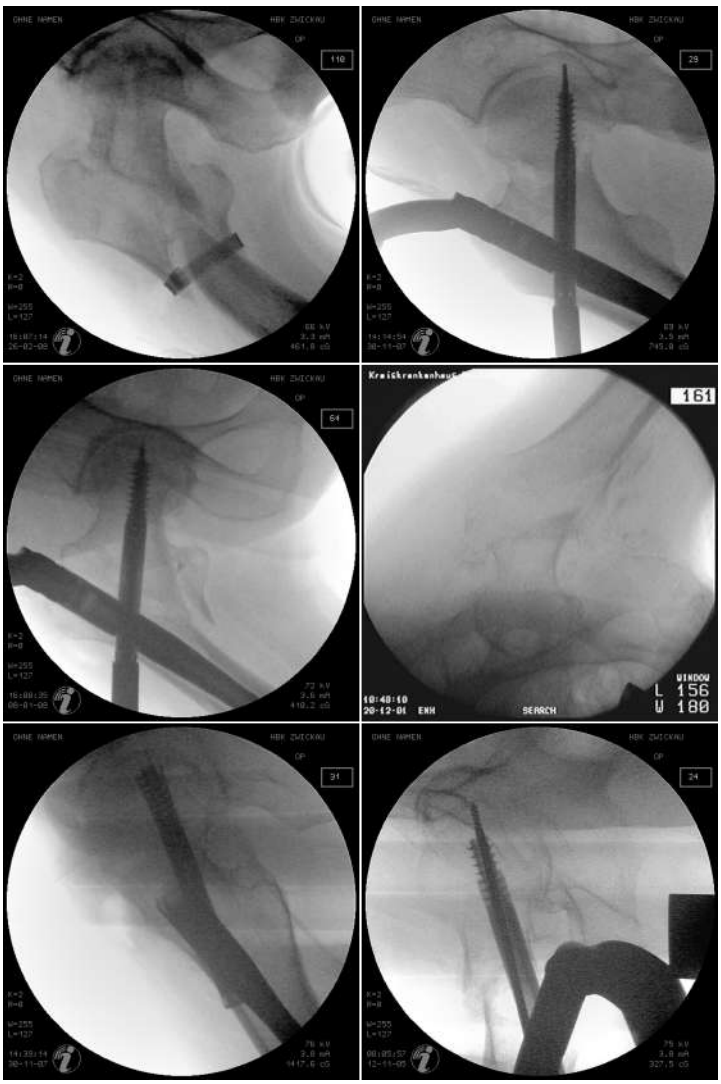

Figure 2.12: Example input images in category normal (first row), moderate (second row), and difficult (third row).

other techniques. Shape-model based approaches were commonly used in dealing with the same challenges in CT images [46, 48]. The construction of shape models for pathological patients is complicated and error-prone, because larger shape variation of the femur bone can be observed due to pathological change. Additionally, considering the fluoroscopic images are acquired intra-operatively, the computational efficiency is prioritized higher than the accuracy. Hence, the speed of the proposed technique fits in this task better than other techniques. Certainly, it has to be mentioned that the method might fail when the femur head presents with extremely lower contrast, or there are substantial other irrelevant circular structures in the images.

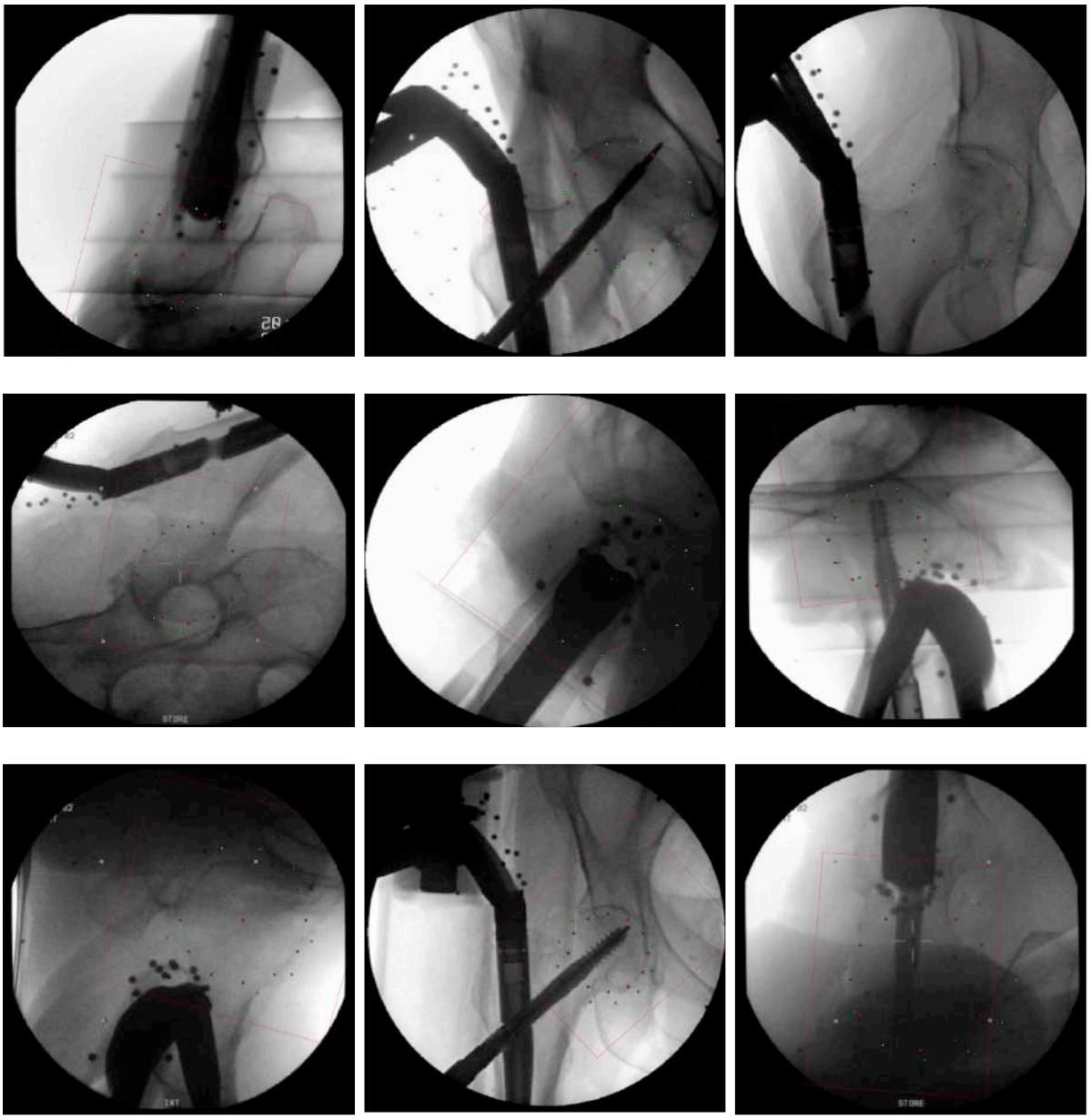

Figure 2.13: More results examples selected from normal (top row), moderate (middle row) and difficult (bottom row) groups.

3

Breast Segmentation in MRI: Methods and Applications

Acknowledgment

The HAMAM project (Highly Accurate Breast Cancer Diagnosis through Integration of Biological Knowledge, Novel Imaging Modalities, and Modelling) was launched in 2008 under the 7th Framework Programme for Research, and was successfully finalized in 2012 [1]. The development of breast tissue segmentation is under the financial support of HAMAM project. I would like to give my sincere gratitude to my colleagues in MEVIS: Dr. Ola Friman, and Prof. Dr. Horst Hahn, who have supported with many inspirations and ideas during the initial construction, evaluation and optimization of this method. Besides, the works of Dr. Tatyana Ivanovskaya (Greifswald, Germany) who has contributed to improve the method and extended its application in the fields of bias-field correction in breast MR images. Additionally, I am also grateful to the work of Mohammad Razavi, who has assisted me to evaluate the algorithm by extending the test dataset plus his wonderful works of breast parenchyma segmentation and breast lesion classification, where breast tissue segmentation was used as a fundamental step. Moreover, I would like give my gratitude to Dr. Albert Gubern-Merida (Nijmegen, Netherlands) and Dr. Yago Diez (Girona, Spain) and Dr. Susanne Diekmann for their contributions to organize reader studies and compare the methods introduced in this chapter with other approaches in terms of accuracy and efficiency.

Publications

The algorithm description, implementation, and evaluation of breast tissue segmentation in MRI were published in the following scientific papers:

- **Wang L**, Filippatos K, Friman O, Hahn HK (2011) Fully automated segmentation of the

[1] http://www.eibir.org/projects/fp7-projects/hamam/

pectoral muscle boundary in breast MR images. In: SPIE Med. imaging. pp. 796309-796309-8.

- **Wang L**, Platel B, Ivanovskaya T, et al. (2012) Fully automatic breast segmentation in 3D breast MRI. IEEE Int Symp Biomed Imaging (ISBI) pp. 1024-1027.
- **Wang L**, Chitiboi T, Meine H, et al. (2016) Principles and methods for automatic and semi-automatic tissue segmentation in MRI data. Magn Reson Mater Physics, Biol Med 29: pp. 95-110.
- Gubern-Merida A, **Wang L**, Kallenberg M, et al. (2013) Breast segmentation in MRI: quantitative evaluation of three methods. In: SPIE Med. imaging. pp 86693G-86693G-7.

The applications that internally used breast segmentation, such as the breast current-prior registration, motion artifact quantification, breast fibroglandular tissue segmentation, bias field correction and breast deformation model construction, have been published in the following papers:

- **Wang L**, Strehlow J, Rühaak J, et al. (2015) A fast alignment method for breast MRI follow-up studies using automated breast segmentation and current-prior registration. In: SPIE Med. imaging. 9413, pp. 941334-941334-8.
- **Wang L**, Gubern-Merida A, Diaz O, et al. (2015) Automated assessment of motion in breast MRI to assess study quality and prevent unnecessary call-backs. ECR 1-10.
- Diez Y, Gubern-Merida A, **Wang L**, et al. (2014) Comparison of methods for current-to-prior registration of breast DCE-MRI. Breast Imaging: 12th International Workshop (IWDM), pp. 689-695.
- Razavi M, **Wang L**, Gubern-Merida A, et al. (2015) Towards accurate segmentation of fibroglandular tissue in breast MRI using fuzzy c-means and skin-folds removal. ICIAP 2015.
- Ivanovskaya T, **Wang L**, Hegenscheid K, Völzke H (2015) Sliding Level Set-Based Boundary : Fully Automated Dense Breast Segmentation in Native MR Mammograms. MICCAI BIA Workshop 1-8.
- Ivanovska T, Laqua R, **Wang L**, et al. (2014) A Level Set Based Framework for Quantitative Evaluation of Breast Tissue Density from MRI Data. PLoS One 9:e112709.
- Ivanovska T, **Wang L**, Laqua R, et al. (2013) A fast global variational bias field correction method for MR images. In: 2013 8th Int. Symp. Image Signal Process. Anal (ISPA), pp. 667-671.
- Harz MT, Georgii J, **Wang L**, et al. (2012) Efficient Breast Deformation Simulation. Work Virtual Real Interact Phys Simul, pp. 117-126.

3.1. Breast Segmentation with Sheet-like Shape Descriptor

3.1.1. Introduction

Breast cancer is the most commonly diagnosed cancer disease among women and a major cause of death. X-ray mammography is conventionally used for screening and diagnosis of breast cancer. However, due to its well-known limitations in the cases of imaging dense or postoperative breasts, Dynamic Contrast Enhanced breast MRI (DCE-MRI or breast MRI more generally) is regarded as an invaluable complementary tool [54]. In recent years, MRI is increasingly used as an important tool in the detection, diagnosis, staging and therapy monitoring of breast cancer [55, 56]. The key benefits of breast MRI are its high sensitivity in detecting breast carcinoma and the ability of depicting cancers that are occult on mammography, ultrasound, and clinical breast examinations [57]. Thus, it is recommended as an additional screening modality of breast cancer to mammography in selected population groups with elevated risk, especially the group of high-risk patients with BRCA 1 & 2 gene mutations or dense breasts [58].

To standardize the interpretation procedure of reading breast MRI, the Breast Imaging Reporting and Data System (Bi-RADS) was developed by the American College of Radiologists as a standard to rate the level of suspicion of breast MR findings [59]. In this reporting system, not only the characterization of lesions is included, but also their position and distance to other relevant anatomical structures such as the nipples, the skin and the pectoral muscle. For instance, the distance between posterior breast masses and pectoral muscle can be used to assess the extent of the disease in patients suspected to have tumor invasion into the underlying muscle [60].

Since breast MRI serves as an invaluable tool in the clinical work-up of patients, many works focusing on computer-aided diagnostic methods and tools have been developed aiming to assist the radiologists and physicians in automatic reporting, density analysis, breast tumor detection and diagnosis [61–63]. Normally, precise segmentation of relevant anatomical structures such as breast region and fibroglandular tissue are required. For CAD systems, breast segmentation serves as a fundamental step in pre-processing to avoid analyzing irrelevant structures, such as air-background and the thoracic organs including heart, liver and lung. For instance, a good segmentation of breast in MRI is essential for a CAD system to improve its efficiency and accuracy by eliminating false positives in thoracic region, which are normally enhanced in DCE-MRI as well. Other clinical applications that might use breast segmentation are breast density measurement, lesion detection and automatic reporting. The previous clinical studies show that the distance between the posterior breast lesions and the pectoral muscle can be used to assess the extent of the disease. To enable automatic quantification of the distance from a breast tumor to the pectoral muscle, a precise delineation of the pectoral muscle boundary is required.

However, the segmentation of breast in MRI is not an easy task. Common imaging artifacts, such as intensity inhomogeneity, ghosting and aliasing effect, and the large variation of anatomical detail and different imaging protocols, such as axial, sagittal or coronal acquisition, still pose challenges to this segmentation task. Generally, the task of breast segmentation

can be subdivided into two major modules, the breast-air boundary and the pectoral muscle boundary segmentation.

3.1.2. Related Works

Methods that have been reported for semi- or fully automated breast segmentation in MRI can be categorized into contour-based, region-based and atlas-based approaches.

Normally, the contour-based approaches segment the breast in two steps: the identification of breast-air boundary and pectoral muscle boundary. The former boundary separates the air-background and breast region, while the latter boundary separates the pectoral muscle and breast region. A slice-by-slice pectoral boundary detection algorithm was proposed in [64], consisting of edge enhancing and linking steps, for breast segmentation in sagittal view. Milenkovich et al. applied a technique to search for the shortest path with a novel cost function using edge map derived from Gabor filters [65]. Giannini et al. recently introduced a method that used Otsu's thresholding for breast-air boundary detection and identified pectoral muscle boundary by investigating the gradient characteristic of pectoral muscle slab [66].

Region-based methods include the work by Koenig et al., who presented a thresholding-based algorithm to detect the breast region [67]. Nie et al. combined fuzzy c-mean classification, B-spline fitting and dynamic searching to segment breast, where the aortic arch was initialized by users as a landmark [68]. Lin et al. proposed a semi-automated technique using Canny edge detection, combined with Bezier curve fitting and k-means clustering [69]. The segmentation of pectoral muscle boundary was started from the central slice and propagated superiorly and inferiorly to the other slices. Ivanovska et al. applied a level-set based technique to simultaneously correct the inhomogeneity artifacts and segment the breast. Thereafter, the breast region was extracted, and possible leakages into the chest-wall were corrected using the information from neighboring slices [70, 71].

Atlas-based approaches have been drawn much attention on breast segmentation in MRI. The prior shape knowledge of the targeted objects is normally encoded into a set of atlas. When a new input image is given, the atlas images will be registered on to the input image, and the target object will be segmented through a voting process. Ortiz and Martel presented a method based on 3D edge detection refined with probabilistic atlas of the breast [72]. Khalvati et al. proposed a multi-atlas segmentation algorithm, which uses phase congruency maps to create breast atlas that is robust to intensity variations. The atlas constructed with one MR sequences can be used to segment the breast from both intra- and inter-sequences [73]. To exclude the body from the breast, Gubern-Merida et al. applied a probabilistic atlas-based method [74], which contained information of pectoral muscle, lungs, heart, thorax, and breast tissue.

Unlike other methods that normally require the detection of anatomical landmarks, such as aortic arch [68] or sternum [74] which might not be always imaged in different MR sequences, or a large scale of training set [73, 74], the method that we have implemented is fully automatic and does not rely on the presence of landmarks. A quantitative performance comparison will be given in the evaluation section, which proves that the proposed approach is capable of

achieving comparable performance, while it dramatically reduces the computational efforts.

3.1.3. Materials and Methods

In this chapter, we propose a novel solution for breast segmentation in MR acquisitions based on Hessian shape descriptors, which does not require any anatomical landmarks. The approach is partially inspired by the work of Sato el al. [16], Frangi et al. [17] and Descoteaux et al. [75], who used Hessian-based filter for segmenting tube-like structures. It is specially designed for processing non-fat suppressed breast MRI, where fatty tissue has a high intensity level compared to parenchyma and pectoral muscle. The method is based on the key observation that the pectoral muscle and breast-air boundaries exhibit smooth sheet-like surfaces in 3D, which can be simultaneously enhanced by a Hessian-based sheetness filter [17]. The enhancement strength of the designed Hessian-based filter correlates with the shape and contrast information of the structures, which means that structures with non-specific shapes and lower contrast will be suppressed. The overall framework consists of four major steps: enhancement of the sheet-like structures, segmentation of the pectoral muscle boundary defining the lower border of the breast region, segmentation of the breast-air boundary delimiting the upper border of the breast region, and breast extraction which eventually captures the area of breast tissue.

The schematic overview of the entire segmentation work-flow is depicted in Fig. 3.1, and the details of each major step are described in the following sections.

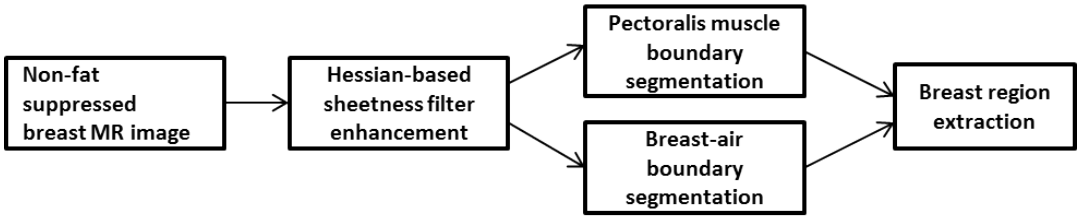

Figure 3.1: The workflow of the proposed method.

To validate the proposed method, the segmented breast boundaries of 84 breast MR images, acquired in five different sites with variant imaging protocols, were compared to the manual segmentation. An average distance of 2.56mm with a standard deviation of 3.26mm was achieved.

Hessian-based Sheetness Filter

As introduced in 1.2.1, Hessian-based filters have been widely employed to analyze the local structures of 3D images. The relation between the Eigenvalues of the Hessian matrix helps to differentiate several specific geometrical structures of a 3D image, such as blob-like, tube-like or sheet-like objects [75]. Descoteaux et al. proposed a sheetness measure used for enhancing bone structures [76]. Each voxel was given a score ranging from 0 to 1, representing the likelihood that it is located in a sheet-like surrounding neighborhood. Three ratios, R_{sheet}, R_{blob}, R_{noise} were designed in their work to highlight sheet-like structures, eliminate blob-like and noisy structures and slightly preserve the tube-like structures. In this work, we focus

on enhancing sheet-like structures and eliminating all other structures. Hence, we choose a somewhat different and simplified measure constructed by two ratios, whose behavior is investigated [76] as in Table 3.1

Table 3.1: Theoretical properties of the ratios defined for the sheetness measure assuming the Eigenvalues sorted in $|\lambda_1| \geq |\lambda_2| \geq |\lambda_3|$.

Defined ratios	sheet-like	tube-like	blob-like	noise
$R_{sheet} = \lvert\lambda_2\rvert/\lvert\lambda_1\rvert$	0	1	1	undefined
$R_{noise} = \sqrt{\lambda_1^2 + \lambda_2^2 + \lambda_3^2}$	λ_1	$\sqrt{2}\lambda_1$	$\sqrt{3}\lambda_1$	0

Ultimately, with the help of these two ratios, we define the sheetness measure:

$$S = \begin{cases} 0, & \text{if} \quad \lambda_1 = 0, \\ \exp\left(\frac{-R_{sheet}^2}{2\alpha^2}\right)\left(1 - \exp\left(\frac{-R_{noise}^2}{2\beta^2}\right)\right) & \text{otherwise,} \end{cases} \tag{3.1}$$

where the parameters α and β control the sensitivity of each ratio to the measure. As suggested, in this work, α and β are set to 0.5 and half of the maximum R_{noise} respectively [16]. The sheetness measure S is scaled from 0 to 1. More specifically, its maximum will theoretically be assigned to the sheet-like local structures and all other structures will be scored with low scores. As a second derivative filter, the defined Hessian-based filter results in a zero-crossing on the target boundaries (step edges) and maximal response on both upper and lower sides of the edges. By differentiating the sign of the largest eigenvalue, only the voxels enhanced on the dark region are kept.

Pectoral Muscle Boundary Segmentation

The identification of the pectoral muscle boundary is necessary when separating the irrelevant thoracic organs from the breast tissue. The method first generates a region of interest which covers the pectoral muscle by selecting a specific range of gradient directions of the enhanced sheet-like structures. Then, a vector-based connected component filter, which takes the eigenvectors into considerations, is employed to further segment the pectoral muscle boundary more accurately. In addition, the method is capable of handling cases where the parenchyma is quite close to the pectoral muscle in dense breasts.

The pectoral muscle boundary to be segmented in the 3D breast MR images is a dark step-edge structure (see Fig. 3.2(a)) rather than a pure manifold plane. Applying a second derivative Hessian-based sheetness filter results in a zero-crossing at exactly the boundary edge, meanwhile negative (on breast) and positive (on pectoralis) side-lobes on each side of the boundary, where the eigenvalues with maximal magnitudes possess opposite signs and roughly equal quantity (see Fig. 3.2(b)). However, considering the fact that the voxels in the positive side-lobe, which can be adequately close to the boundary by carefully setting the scale of the filter, exhibit roughly the same eigenvalue patterns as the ones in a sheet-like object, these boundary-proximal voxels can still be enhanced and segmented by defining a sheetness filter like what people did to segment sheet-like structures.

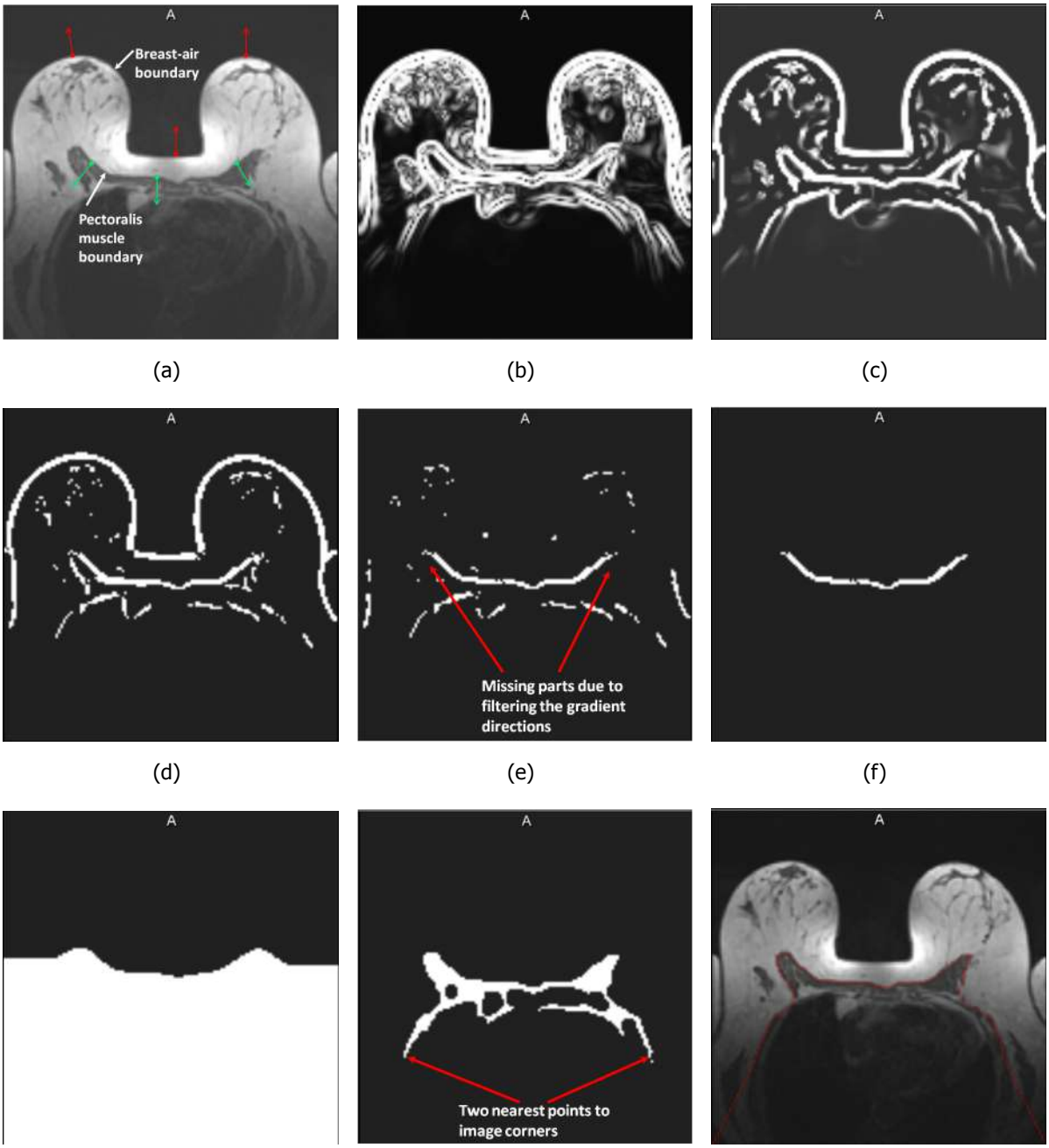

Figure 3.2: The segmentation workflow. (a) A representative image slice indicating the breast-air boundary and the pectoral muscle boundary (by white arrows), and the gradient directions of their example voxels labeled by red and green arrows respectively. (b) Response of the sheetness filter with positive and negative side lobes on each side of boundary edge. (c) Erase the negative side-lobe. (d) Threshold the sheetness score. (e) Remove the breast-air boundary. (f) Extract the main part of pectoral muscle using connected component filter. (g) Generate a mask (ROI) through the main part of pectoral muscle. (h) Apply the sheetness filter within ROI and threshold the scores followed by a vector-based connected component filter. (i) Extract the boundary contour of the pectoral muscle and stretch it to the corners (in red) overlaid with input image.

The segmentation workflow comprises four key steps, preprocessing, detecting the region of interest of the pectoral muscle, enhancing and segmenting the pectoral muscle, and extracting and refining the pectoral muscle boundary. The parameters of all used filters were tested to be robust.

Preprocessing

To reduce the computational efforts and compute the Hessian matrix in a fixed scale for all input images, the input images are resampled subject to an isotropic voxel spacing $2.5\text{mm} \times 2.5\text{mm} \times 2.5\text{mm}$. The scale of the second order derivative of a Gaussian kernel, which is used for computing the Hessian matrix, is set to be 2.5mm such that after applying the sheetness filter, the positive side-lobe lying on the pectoralis would adequately be close to the boundary. The negative side-lobe generated by the sheetness filter can be easily erased by explicitly constraining the sign of the eigenvalues with maximal magnitude to be positive (see Fig. 3.2(c)).

Detecting the Region of Interest

After assigning and thresholding the sheetness scores with a threshold value 0.6, only the highly enhanced structures, such as breast-air and pectoral muscle boundaries, are left (see Fig. 3.2(d)). The exclusion of the breast-air boundary is essential, because it will be enhanced by the sheetness even stronger than the pectoral muscle boundary, which confounds the connected component filter to select the breast-air boundary as the largest component (see Fig. 3.2(d)). Notice that most voxels proximal to the breast-air boundary and the pectoral muscle boundary possess roughly opposite gradient directions (see Fig. 3.2(a)). Hence, we conduct a gradient direction filtering process by selecting the voxels whose gradient directions point roughly from image top to bottom (indicated by green arrows in Fig. 3.2(a)). Here, the scale parameter of the first derivative Gaussian kernel used to compute gradient vector is set to be 2.5mm. Consequently, most parts of the breast-air boundary are eliminated, whereas a few parts of pectoral muscle are also jeopardized (see Fig. 3.2(e)). Afterwards, a 3D connected component filter is applied, and the main parts of the pectoral muscle are extracted by selecting the largest component (see Fig. 3.2(f)). Even though the extracted main parts are incomplete due to the filtering process of gradient directions, they reveal the coarse location of the pectoral muscle and can be used to generate a mask image that labels the ROI of the pectoral muscle (see Fig. 3.2(g)).

Enhancing and Segmenting the Pectoral Muscle

Once the ROI of the pectoral muscle is identified, the designed sheetness filter scores each voxel again inside the ROI with a value scaling from 0 to 1. A sheetness-score-threshold is set to be 0.5 in this step, which has been tested to be robust through a large number of experiments. Usually, some unwanted sheet-like anatomical structures, such as the boundaries of the lung in thorax and the splitting planes between the arm and body, are enclosed in the ROI and thus enhanced by the Hessian-based filter as well. To eliminate them, a 3D vector-based connected component filter is exploited to investigate both the geometrical connectivity and the consistency of the eigen-directions of the segmented objects. Voxels with acute alteration of the vector direction are regarded as isolated and excluded. Here, the uniformed eigenvec-

tor associated with the largest eigenvalue is examined in the filter, and the distance threshold is set to be 0.1, which means the two neighbor voxels will be determined to be connected if the dot production of their eigenvectors is larger than 0.9. Finally, the largest connected component with maximal number of voxels is selected as shown in Fig. 3.2(h).

Extracting and Refining the Pectoral Muscle Boundary

Firstly, the holes or gaps of the segmented object are filled and bridged by a connection cost filter followed by a morphological closing filter with scale of $3 \times 3 \times 3$ both for dilation and erosion [77]. To fetch a neat and complete pectoral muscle boundary, we employ a surrounding filter to obtain the outer contours of the segmented object. To extend the resulted outer contour to the image corners, two nearest points on the contour to the bottom-left and bottom-right corners are searched out respectively (see Fig. 3.2(h)), and they are linked to the corresponding corners by drawing two line segments. Finally, the segmented boundary contour overlaid with the original image is demonstrated in Fig. 3.2(i).

Breast-air Boundary Segmentation

Breast-air boundary segmentation is not a trivial task due to artifacts that can appear in MR images, such as the presence of aliasing artifacts and fiducial markers, which might cause failure of intensity based methods. In addition, the absence of one breast due to mastectomy surgery might also challenge the model based methods (see Fig. 3.3).

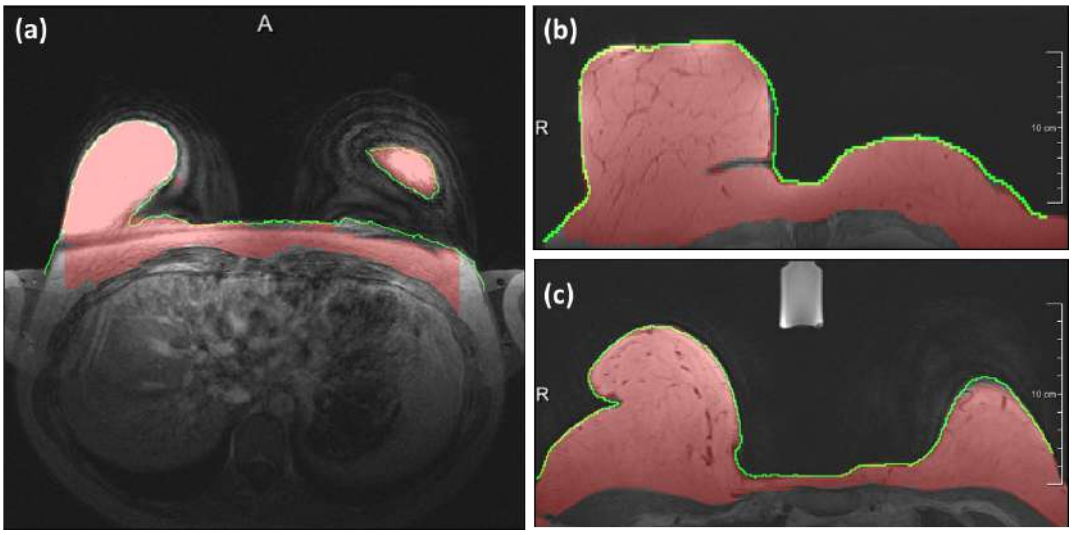

Figure 3.3: The artifacts and challenges presented in breast MRI, overlaid with the segmented breasts (red masks), and the reference breast-air boundaries annotated by a radiologist (green contours): (a) Presence of aliasing artifacts (ghost shadow). (b) Absence of the left breast. (c) Presence of fiducial markers.

Compared to the response of the pectoral muscle boundary, the breast-air boundary is enhanced even stronger by the sheetness filter, which obtains a sheetness score mostly higher than 0.9, due to the high contrast between air and breast tissue. The mask of the pectoral muscle segmented in the previous step can remove the thoracic region of the Hessian filter response, which facilitates the segmentation of the breast-air boundary (Fig. 3.4(a)(b)). By thresholding the remaining enhanced structures with a minimum threshold of 0.8 on S,

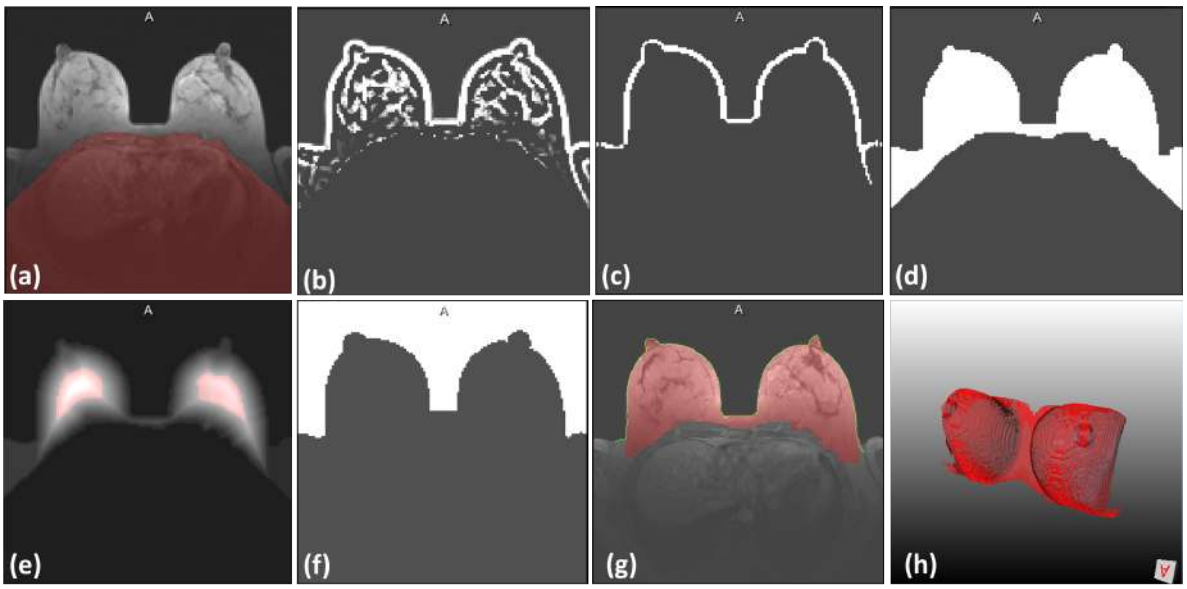

Figure 3.4: The breast-air segmentation and the breast extraction: (a) Original input overlaid with pectoral muscle segmentation (red mask); (b) Masked Hessian filter response where breast-air boundary is highly enhanced; (c) Breast-air boundary segmented with connected component and morphological filters; (d) Initial breast tissue segmentation using segmented breast-air and pectoral muscle boundaries; (e) Seed voxels (encoded in red) extracted from distance transform image of the initial segmentation; (f) Air background detection based on the initial segmentation; (g, h) 2D and 3D demonstration of segmented breast tissue.

unwanted objects slightly enhanced inside the breast can be filtered out. Then, a 3D vector-based connected component algorithm is applied to extract the largest connected component, which is the breast-air boundary (Fig. 3.4 (c)). The algorithm takes the eigen directions of the voxels into consideration and inspects the connectedness with not only spatial connectivity but also the consistency of the eigen directions. This enables the algorithm to isolate the attached parenchyma from the breast boundary. Another observation is that the segmented breast-air boundary normally has a thickness larger than one single voxel resulting from the scale of the Hessian filter. However, by properly setting the scale, the segmented boundary can be acquired sufficiently close to the true boundary. In this work, the input image is down-sampled with an isotropic voxel size of 2.5mm, and the scale parameter of the Hessian filter is set to 2.5mm (1 voxel) as well.

Final Breast Tissue Segmentation

The segmented breast-air and pectoral muscle boundaries delimit the upper and lower borders of the breast tissue, which already allows for capturing an initial segmentation of the breast tissue (Fig. 3.4(d)). However, in extreme inferior slices where the visible breast tissue is not directly connected to the body (see Fig. 3.3(a)), the connected component algorithm may lose the breast tissue. In addition, the local misalignment of the detected pectoralis and breast-air boundaries may cause the breast tissue extraction to deviate locally from the true borders. To cope with this issue and refine the breast tissue segmentation in local areas, an intensity based region growing algorithm is adopted, working on the basis of the initial breast segmentation.

Firstly, the seeds of the region growing are automatically identified by analyzing the distance transform image of the initial breast segmentation (Fig. 3.4(e)). The voxels with high distance transform values are distributed around the geometric center of the initial segmentation. More specifically, we choose the voxels above the 70 percent quantile of the histogram of distance transform values as the seeds (encoded in red overlay in Fig. 3.4(e)) . Secondly, three constraints are implemented to ensure that the region growing propagates within the breast and prevent leakages into the thorax and air. The detected pectoral muscle and breast-air boundaries are superimposed to the original input and the intensities of the covered voxels are set to zero, aiming to block the growing process. In addition, the intensity level of the air background is investigated by first segmenting the air region using a ray tracing technique, where the rays are emitted from the top of the image and travel downwards until hitting the segmented breast-air boundary (Fig. 3.4(f)), and then analyzing the intensity histogram. The lower threshold of the region growing is safely set as the mean of this histogram plus three times the standard deviation. The region growing process makes the assumption that the breast parenchyma possesses higher intensities than air background. However, in a few rare cases, where the patient suffered from surgical biopsy or tumor resection, the operated sites might exhibit similar low signals as the background, which results in a few small-scaled holes or cavities inside the breast uncovered by region growing. Since these cavities are surrounded by fatty tissue, they can be easily recovered by hole-filling techniques, such as morphological closing and connection cost filters. Ultimately, the segmentation result of the region growing is demonstrated in 2D (Fig. 3.4(g)) and visualized in 3D (Fig. 3.4(h)).

3.1.4. Evaluations

Since pectoral muscle boundary segmentation is the main challenging part of the entire breast segmentation workflow, we established a separate experiment to test its performance. Afterwards, the performance of entire breast segmentation is tested with more test images. In the end, the proposed method is bench-marked with two atlas-based methods in an extra comparison study.

Evaluation of Pectoral Muscle Boundary Segmentation

The breast DCE-MR images were acquired in three acquisition protocols, T1-weighted coronal, T1-weighted axial, and T2-weighted axial. The test data set includes 30 independent non-fat suppressed MR images (none were used during algorithm development) acquired from 30 different female patients, 10 from each imaging protocol. The method operated on pre-contrast breast DCE-MR images, and the processing time for the image with maximum resolution ($512 \times 512 \times 70$) was about 6 seconds using a 3.07 GHz Intel CPU and a GeForce gtx285 graphics card.

To evaluate the method quantitatively, two ground truth sets were built for the test set as shown in Fig. 3.5(a)(c). The pectoral muscle boundaries were manually annotated by two independent radiologists, such that the inter-observer variation could be maximally decreased. The radiologists annotated every 2 to 8 slices depending on the available slice number to make sure that at least 15 equally distributed slices were annotated for each image as shown in Fig.

3.5(b)(d). To precisely evaluate how well the segmented boundary surface (see Fig. 3.5(f)) matched the ground truth contours, especially in the parts of the pectoral muscle, the distance between the points on the ground truth contours and their corresponding paired points on the segmented pectoral contours (Fig. 3.5(e)) was measured. For each point on the ground truth contour, its paired point on the segmented pectoralis contour was defined as the one with the least distance to it. The sum distance was computed over all these point pairs for all slices that have been annotated in the ground truth. Ultimately, the average distance was calculated by dividing the sum distance with the count of the point pairs.

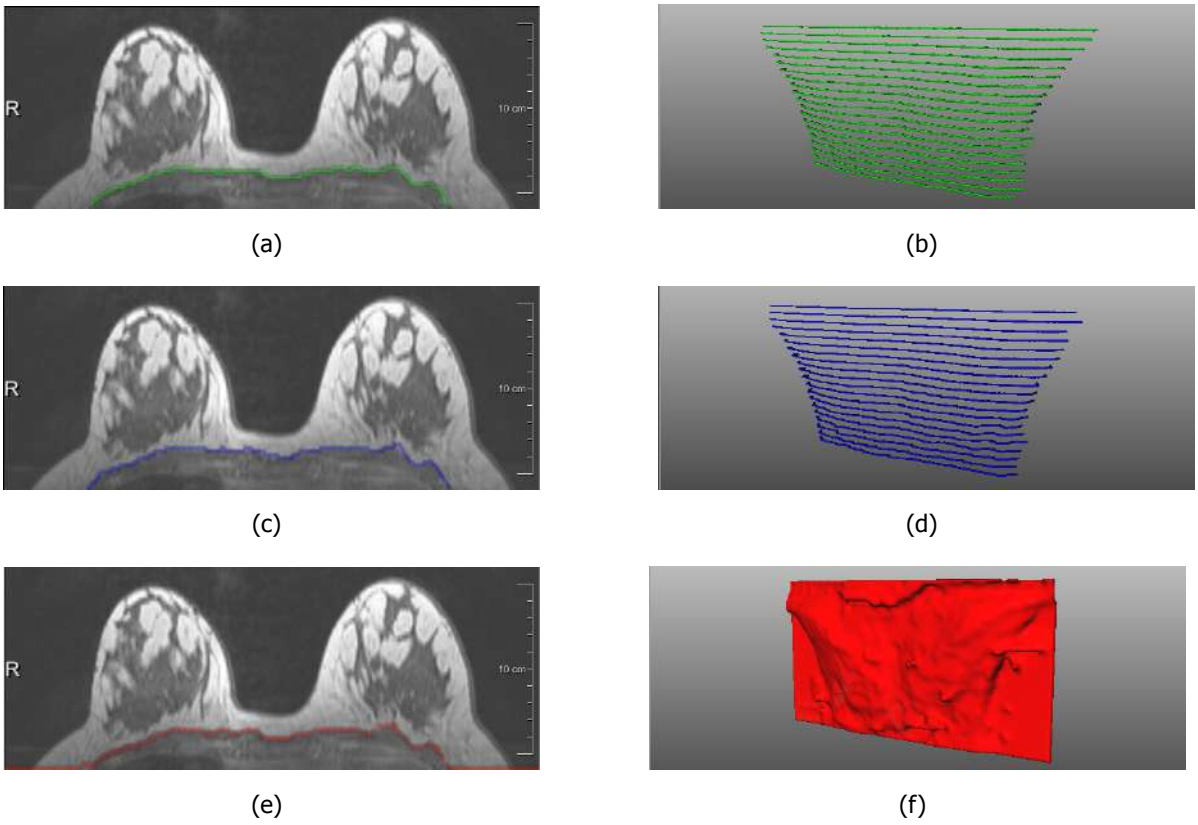

Figure 3.5: The ground truth and the segmentation results. (a) A representative contour (the green contour) annotated by the first radiologist overlaid with input image. (b) The 3D visualization of the contours of the ground truth image annotated by the first radiologist. (c) The contour (the blue contour) annotated by the second radiologist for the same input image. (d) The 3D visualization of the contours of the ground truth image annotated by the second radiologist. (e) The segmented contour (red contour) of the boundary between breast and pectoralis muscle. (f) The 3D visualization of the segmented surface of the boundary between breast and pectoralis muscle.

Table 3.2 lists the sum distances, the counts of the point pairs, the average distances, and the imaging protocols for all 30 images in the test data set. Considering the voxel space, all the distances were given in millimeter and measured twice for both databases of the ground truth. From the table, it can be observed that the maximal average distance between the ground truth contours and the segmented surfaces was 2.471 mm, whereas the minimum was 0.546 mm. The mean value of all average distances measured for both ground truth datasets was 1.434 mm, and the standard deviation was 0.4661 mm. The aberration has no clinical

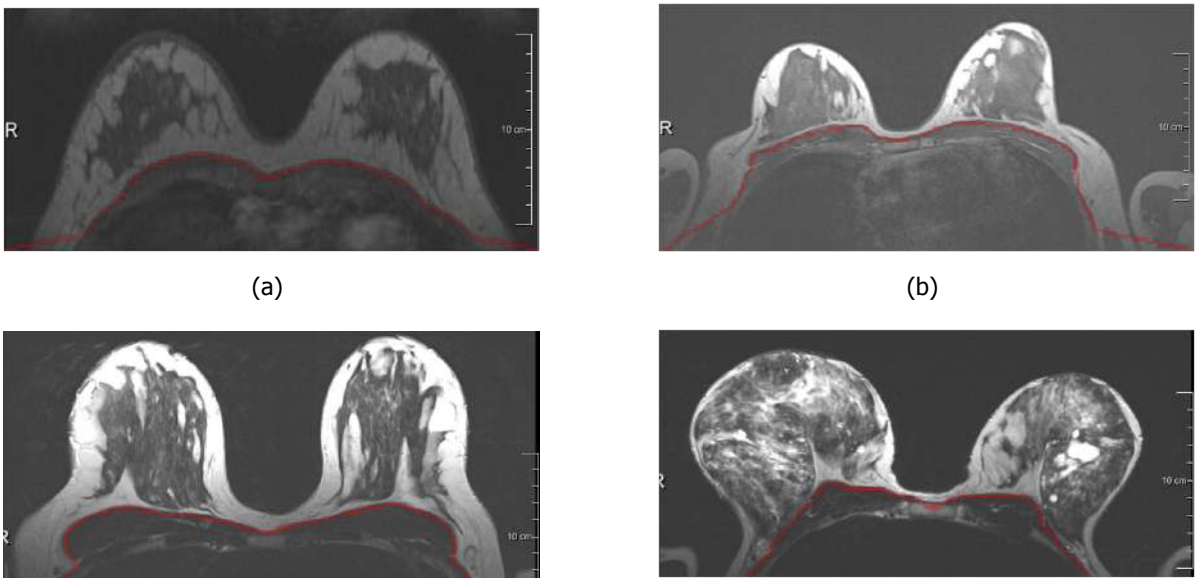

(a) (b)

(c) (d)

Figure 3.6: The reformatted axial view of the segmented pectoralis boundaries (red contours) of four extreme dense breasts in different imaging protocols: (a) T1-weighted coronal, (b) T1-weighted axial (c)(d) T2-weighted axial.

significance when measuring the distance from the posterior breast lesions to the pectoral muscle. The segmentation task becomes more challenging for the extreme dense breasts, because the large amounts of breast parenchyma can be very close to the pectoral muscle and exhibit approximately the same intensity level. The vector-based connected component filter can prevent the segmented pectoral muscle boundary from passing the boundary of the breast parenchyma by constraining the acute variations of the vector directions. Figure 3.6 gives some successful segmentation for extreme dense breasts in different imaging protocols. To further demonstrate the performance of our approach in clinical application, two more boundary surfaces of the segmented pectoral muscles selected from the test data set are visualized in 3D as shown in Fig. 3.7, where the silhouettes of the breast tissues and the lesion masses are rendered, and the distances from the lesion masses to the pectoral muscle surfaces are measured and presented as well.

Evaluation of Overall Breast Segmentation

To evaluate the performance of the presented method, a test data set enclosing 84 non-fat suppressed breast MR images was collected. The test images were acquired in five different hospitals with different imaging protocols, i.e., T1-coronal, axial, sagittal, T2-axial. Only the pre-contrast images were processed for dynamic contrast enhanced images. The image resolution varied from $256 \times 256 \times 64$ to $512 \times 512 \times 80$ with different voxel sizes. The reference segmentations were manually annotated by an experienced radiologist. For each test image, two individual reference contours, delineating the pectoral muscle boundary and the breast-air boundary, were annotated, and the combined contours were used as the reference boundaries of the breast. Considering the resolution and slice numbers of the data, the radiologist

Table 3.2: The statistical results of the quantitative evaluation.

	Ground Truth 1			Ground Truth 2			
No.	Sum(mm)	Count	Average(mm)	Sum(mm)	Count	Average(mm)	Protocol
1	2285.63	4189	0.545626	2398.81	4245	0.565092	T1-axial
2	5850.96	4295	1.36227	9153.61	4773	1.91779	T1-axial
3	6491.42	5477	1.18522	6500.38	5513	1.1791	T1-axial
4	5624.79	4543	1.23812	5394.09	4529	1.19101	T1-axial
5	6422.99	5035	1.27567	5595.71	4964	1.12726	T1-axial
6	6528.05	4663	1.39997	5947.65	4587	1.29663	T1-axial
7	3009.71	4367	0.689193	2843.58	3909	0.727445	T1-axial
8	7219.68	4896	1.47461	6496.56	4861	1.33647	T1-axial
9	5058.85	5162	0.980017	5780.14	5287	1.09327	T1-axial
10	5198.9	4179	1.24405	4091.21	3793	1.07862	T1-axial
11	8848.55	5065	1.747	9324.09	5123	1.82004	T1-coronal
12	5746.51	3541	1.62285	6012.54	3509	1.71346	T1-coronal
13	8978.29	4091	2.19464	7823.37	3925	1.99322	T1-coronal
14	7514.22	4127	1.82075	7152.3	4142	1.72677	T1-coronal
15	6830.65	2764	2.47129	6522.88	2710	2.40697	T1-coronal
16	4010.04	2574	1.5579	4082.54	2617	1.56001	T1-coronal
17	9151.6	4218	2.16965	8226.05	4136	1.98889	T1-coronal
18	6976.92	4404	1.58422	7461.65	4293	1.7381	T1-coronal
19	4884.94	4634	1.05415	5178.55	4692	1.1037	T1-coronal
20	5920.8	4134	1.43222	5372	4133	1.29978	T1-coronal
21	13215.7	6445	2.05053	6468.75	5496	1.17699	T2-axial
22	5072.41	5504	0.921587	5520.89	5525	0.999256	T2-axial
23	4979.34	5873	0.847836	4661.12	5822	0.800605	T2-axial
24	5919.46	5733	1.03252	6459.2	5658	1.1416	T2-axial
25	6490.37	5233	1.24028	9634.28	5291	1.82088	T2-axial
26	16073.9	10093	1.59258	15263.6	9928	1.53743	T2-axial
27	7246.87	5899	1.22849	8915.37	5786	1.54085	T2-axial
28	4592.27	4866	0.943746	4756.82	5113	0.930339	T2-axial
29	14415.8	7236	1.99223	15449.8	7164	2.15659	T2-axial
30	26187.9	12381	2.11517	25402	12343	2.05801	T2-axial

annotated the breast-air and pectoral muscle boundaries for every second to eighth slice to make sure that at least 15 equally distributed annotated slices were provided. The processing time for the image with maximum resolution was about 10 seconds using a 3.07 GHz Intel CPU and a GeForce gtx285 graphics card.

The boundary contours of the breast-air and the pectoral muscle were extracted from the segmented region of the breast. We measured the distances from the reference contours to the segmented contours in the slices where reference contours exist. The distance from each voxel in the reference contour to the segmented contour was measured, and the mean, standard deviation, and maximum of the distance error of each test image were computed. In addition, an average overlap rate, defined as the percentage of the reference voxels whose distance error was less than a tolerance threshold of 3mm, was evaluated.

Two experiments were carried out to validate the segmentation accuracy of the pectoral muscle and the breast-air boundaries by comparing to the corresponding reference bound-

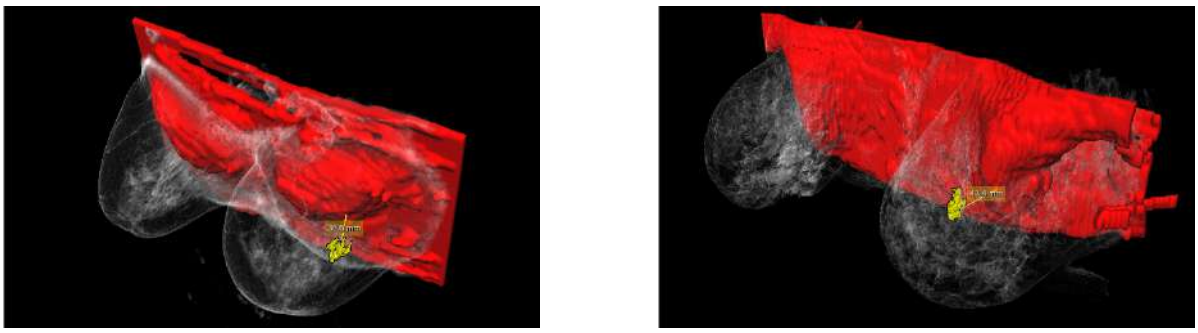

Figure 3.7: Two example visualizations of the segmented surfaces of the pectoral muscle (red plane) and the lesion masses (yellow entities) overlaid with the silhouettes of the breast tissues. The distances from the lesion masses to the pectoral muscle surfaces are measured and presented with yellow line segments.

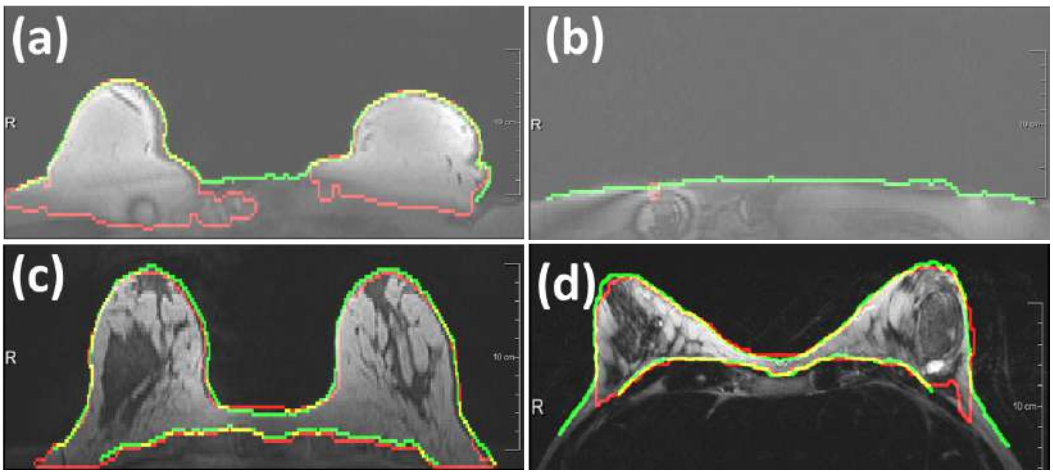

Figure 3.8: The segmented pectoralis and breast-air boundaries (red), the reference contours (green), the overlap contours (yellow).

aries, respectively. Moreover, the accuracy of the segmented breast boundaries was assessed by comparing to the reference boundaries of the breast in the third experiment. Table 3.3 lists the average values of the evaluation metrics obtained in each experiment for all test images. From the test, it is observed that the pectoral muscle boundary possessed higher accuracy than the breast-air boundary, with a lower mean distance error and standard deviation. For the entire breast boundary, the method achieved a mean distance of 2.56mm with a standard deviation of 3.26mm. The overlap rate reached 87% on average. The relatively larger average maximum distance recorded as 33.56mm resulted from the deviations in the extremely inferior slices, where for instance the segmented breast-air boundaries were isolated while the radiologist annotated a continuous reference breast-air boundary crossing the muscles (Fig. 3.8(a)), no breast tissue volume was presented while the radiologist annotated a continuous reference pectoral muscle boundary (Fig. 3.8(b)). To demonstrate the results, two segmented breast boundaries for dense breasts are illustrated in Fig. 3.8(c)(d), and the segmented breast masks of the forenamed challenge cases are shown in Fig. 3.3.

Boundary	Mean(mm)	Std(mm)	Max(mm)	O.R.
Pectoralis	1.99	2.66	22.16	0.92
Breast-air	2.81	3.22	30.47	0.84
Breast:	**2.56**	**3.26**	**33.56**	**0.87**

Table 3.3: The average values of the evaluation metrics validating the segmentation accuracy of the pectoral muscle boundary, breast-air boundary and both (the breast boundary), where O.R indicates overlap rate.

Performance Comparison with Other Methods

In [78], Gubern-Merida et al. has independently compared the performance of our method with other two approaches based on probabilistic atlas [79] and multi-atlas [80]. Both atlas-based methods use 27 fully manually segmented MR scans to build the atlas and a dedicated registration framework based on a sternum landmark to segment the body area. The schematic overview of probabilistic atlas approach is depicted in Fig. 3.9, while the workflow of multi-atlas based approach is delineated in Fig. 3.10.

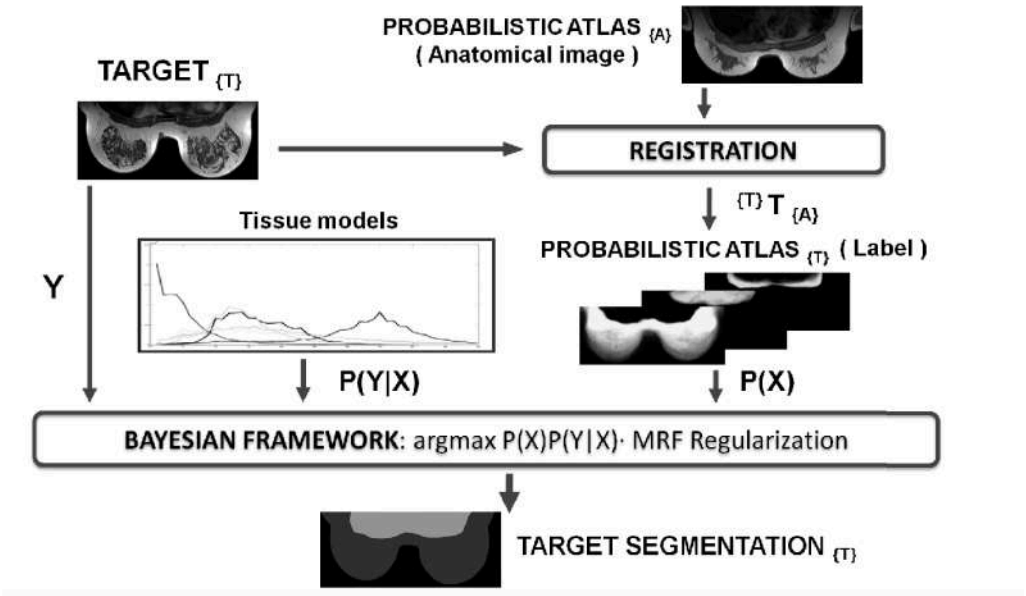

Figure 3.9: Probabilistic atlas breast segmentation approach overview [79].

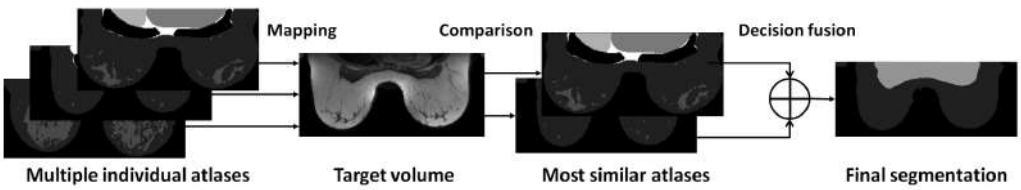

Figure 3.10: Multi-atlas breast segmentation approach overview [80].

Materials and Metrics

In this study, a data set enclosing 52 pre-contrast coronal T1-weighted MR breast scans

obtained from 52 different patients is collected. The cases were acquired from 2003 to 2009 at the Radboud University Nijmegen Medical Centre. Reference segmentation of pectoral muscle and dense tissue reference segmentation were collected for all the data sets. Figure 3.11(a) shows an example of the reference segmentation for dense tissue and pectoral muscle.

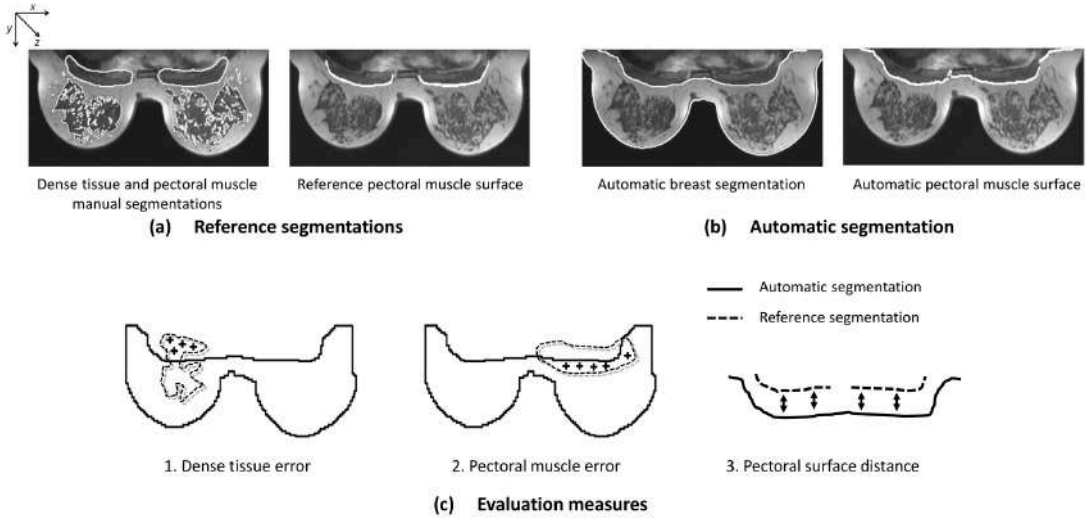

Figure 3.11: Evaluation of breast segmentation in MRI: overview of material and evaluation measures used.

For evaluation, three different measures were defined to precisely quantify the errors that have the most negative impacts when breast segmentation is utilized in CAD systems. We have chosen different measures compared with the ones used in previous sections, because more tissue types were labeled for this test data set. These measures are illustrated in Fig. 3.11(c):

1. The dense tissue error refers to the percentage of dense tissue voxels of the reference segmentation that are not included in the breast segmentation.

2. The pectoral muscle error refers to the percentage of pectoral muscle voxels of the reference segmentation that are included in the breast segmentation.

3. The pectoral surface distance refers to the distance between the manually annotated and automatic determined surface of the pectoral muscle.

Comparison Results

All 52 test cases were segmented by the probabilistic, the multi-atlas and the sheetness-based breast segmentation approaches. Figures 3.12(a), (b) and (c) show box-plots for each evaluation measure. Table 3.4 summarizes the median and the interquartile range of each method with respect to the evaluated measures. Figure 3.14 shows nine segmented examples. An extreme dense breast presented in Fig. 3.14(b) is a difficult case, since a large part of the pectoral muscle is connected to the dense breast tissue. In terms of percentage of missed dense tissue, the sheetness-based method obtained significant better performance than atlas-based methods (p-values < 0.05, two-sided paired Wilcoxon test). With respect to the pectoral muscle error, the multi-atlas method significantly outperformed the other approaches (p-values

< 0.05, two-sided paired Wilcoxon test). It is observed that the sheetness-method commits a relatively larger pectoral muscle error. One of the reasons is that the sheetness-based method chooses to delineate the inner boundary of pectoral muscle, which means at least the boundary voxels of pectoral muscle will be erroneously accounted as pectoral error (see Fig. 3.13). Finally, in terms of pectoral surface distance, the probabilistic approach obtained significant better performance than others (p-values < 0.05, two-sided paired Wilcoxon test). In terms of precision (variance of pectoral surface distance), all the approaches obtained similar scores (p-values > 0.05, Barlett test of variances). Nine minutes, 3 hours and 20 seconds were the approximate computation times to segment the breast of an MR image using probabilistic, multi-atlas and sheetness-based approaches, respectively.

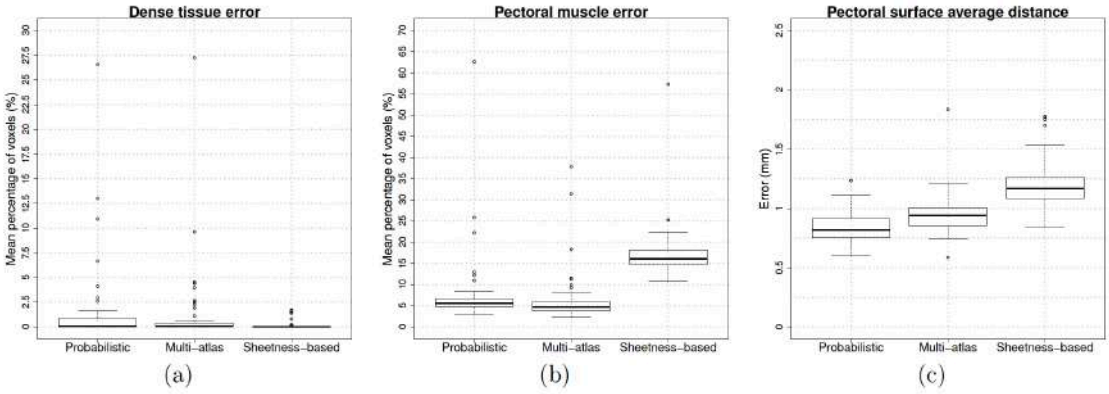

Figure 3.12: Boxplots of evaluation measures for probabilistic, multi-atlas and sheetness-based breast segmentation methods: (a) percentage of reference dense tissue voxels that are not included in the breast segmentation, (b) percentage of reference pectoral voxels that are included in the breast segmentation and (c) pectoral muscle surface distance in mm.

Table 3.4: Median and interquartile range (25th percentile - 75th percentile) for the evaluation measures.

Method	**Dense tissue error** (%)	**Pectoral error** (%)	**Pect. surface distance** (mm)
Probabilistic [79]	0.071 (0.011 – 0.880)	5.566 (4.773 – 6.663)	0.820 (0.749 – 0.913)
Multi-atlas [80]	0.087 (0.021 – 0.350)	4.697 (3.846 – 5.885)	0.940 (0.854 – 1.007)
Sheetness-based	0.005 (0.000 – 0.021)	16.072 (14.999 – 18.188)	1.167 (1.084 – 1.265)

3.1.5. Discussion

In this work, a novel step-wise method to segment the breast tissue in non-fat suppressed breast MR images is presented. The method is fully automatic without the requirements of the prior information and tuning parameters. The proposed method is based on exploring the second derivative information of the 3D image interpreted by the Hessian matrix. The idea behind the method is the key observation that the voxels proximal to the pectoral muscle and breast-air boundaries exhibit roughly the same eigenvalue patterns as a sheet-like object in 3D, which can be enhanced and segmented by a specially designed Hessian-based sheetness filter. To erase some unwanted enhanced structures inside the thoracic cavity, a vector-based

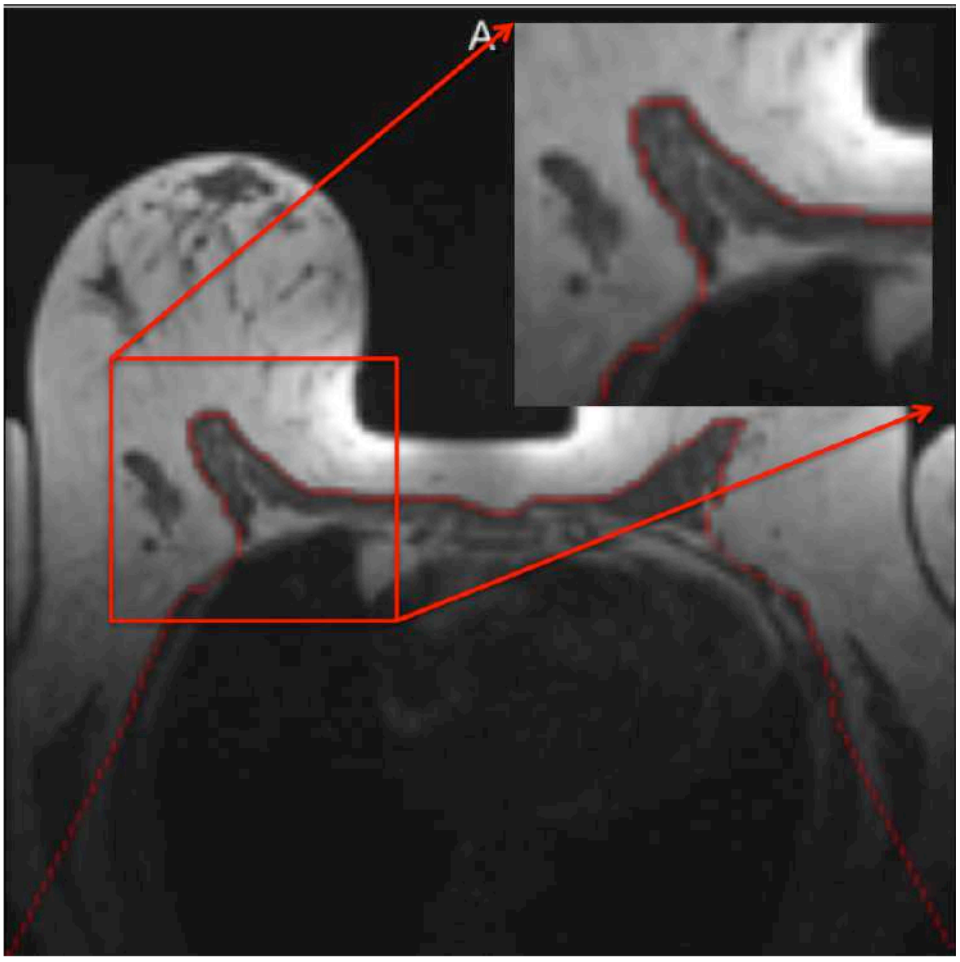

Figure 3.13: Illustration of the pectoral muscle boundary identified by sheetness-based method. The pectoral muscle boundary contour is placed on the inner side of pectoral muscle.

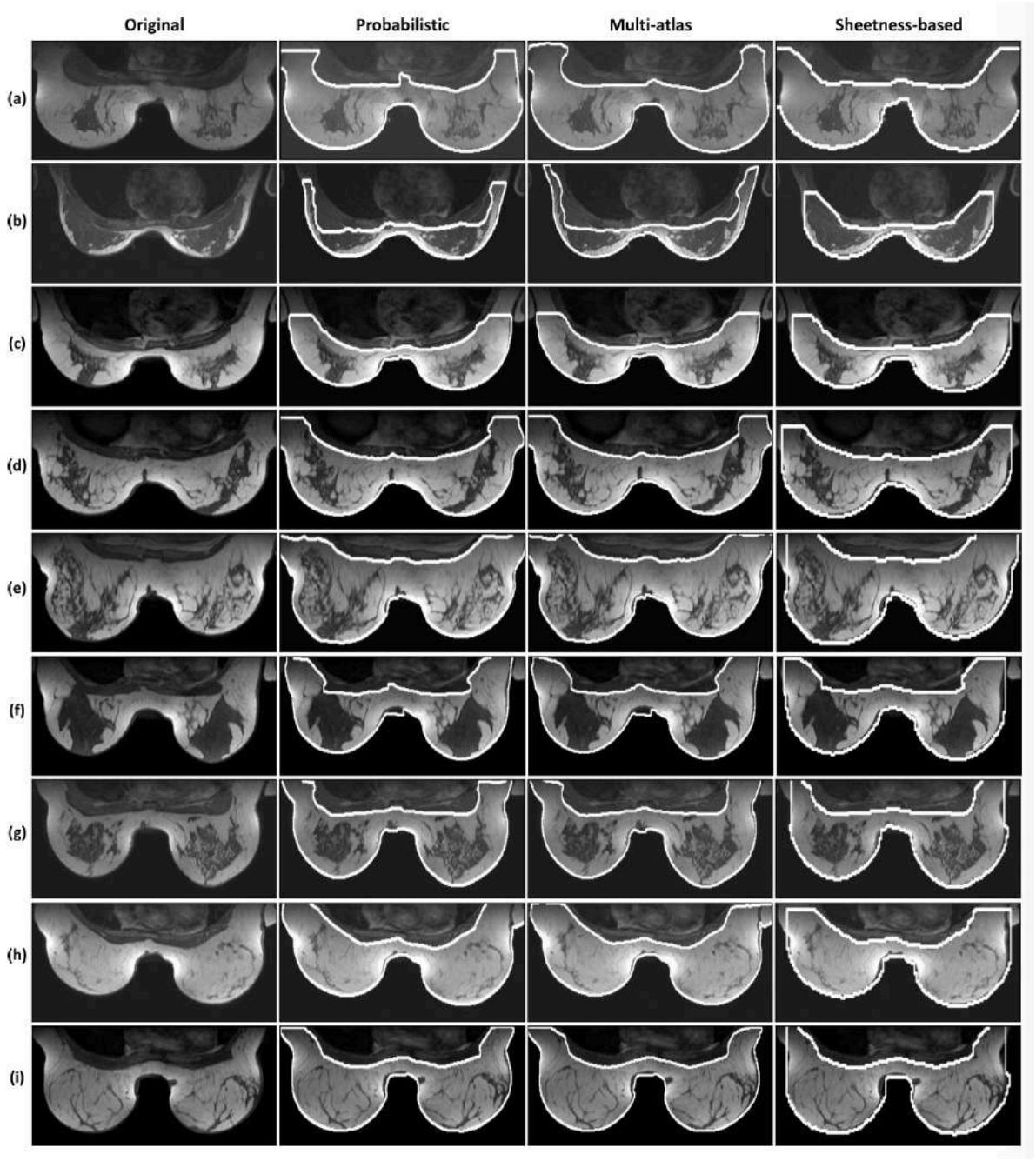

Figure 3.14: Breast segmentation examples: axial slices from 9 different MR scans segmented by the three evaluated methods.

connected component filter is applied. In the refinement stage, the completely connected contours of the pectoral muscle boundary are identified. By analyzing the test results, the designed Hessian-based sheetness filter was proven to be an accurate and robust tool for enhancing the breast-air and the pectoral muscle boundaries. The automatic initialization of the seed points and the analysis of the lower threshold of the proposed region growing technique have proven their robustness on the clinical data.

To quantitatively evaluate the performance, two experiments were conducted. First, to access the accuracy of pectoral muscle boundary segmentation, the proposed method was evaluated with a test set including 30 breast DCE-MR images with variant degrees of difficulties and alterations acquired in three imaging protocols. Two radiologists manually annotated the pectoral muscle boundary contours independently and built two data sets of the ground truth. The method was quantitatively evaluated by measuring the average distances between the segmented pectoral muscle boundary surface and the annotated surfaces in each ground truth, and the statistics showed that its mean value was 1.434mm with the standard deviation of 0.4661mm.

Second, to test the performance of overall breast segmentation method, a further extensive test including 84 data sets was carried out to assess the performance of the algorithm. The boundaries of the extracted breast region showed a high alignment with the reference contours annotated manually with an overlap rate of 87%. The performance comparison study has shown that the proposed method significantly outperform other two atlas-based methods in term if computational efficiency, while achieving comparable segmentation quality.

The advantages of this method can be summarized as follows:

- Computationally efficient.
- No prior knowledge is required.
- No training stage is required.
- No pre-assumptions of landmarks that have to be presented in the image.
- Robust against the non-fat suppressed MR images acquired with different scanners and protocols.

The disadvantages of this method have to be mentioned as well. Current version is limited to be applicable only for non-fat suppressed MR images. Other images such as fat-suppressed images will be failed. The isotropic down-sampling step in pre-processing stage can result in fuzzy segmentation boundaries for pectoral muscle and breast-air. For the pectoral muscle segmentation, it is not clinically certain where the pectoral muscle boundary should end. The way that the extracted boundary is extended to the corner of the image is determined empirically after carrying out experimental test. As mentioned in previous sections, the proposed algorithm might fail in the most anterior or inferior slices where heavy aliasing artifacts are often observed. Addition efforts that might improve the segmentation performance include the optimization of significant parameters of the presented pipeline, such as the thresholds of the sheetness filter response and the administration of parallel computing schemes.

3.2. Applications of Breast Segmentation: Longitudinal Registration

3.2.1. Introduction

In this section, a typical application that leverages the benefits of breast segmentation is presented, which is the automated registration of longitudinal breast MRI. As mentioned in previous section, MRI has been recommended in breast cancer screening for high-risk women. Compared to other imaging modalities such as mammography or ultrasound, MRI achieves higher sensitivity of detecting intraductal and hereditary cancers with a comparable specificity to mammography [81]. Recent findings indicate that the inclusion of prior MRI in breast MRI reading reduces the rate of false positives associated with initial breast cancer MRI screening [82].

In breast cancer screening for high-risk women, follow-up MR images are acquired with a time interval ranging from several months up to a few years. Adding prior studies to screening will inevitably increase the reading time and workload of clinicians. Prior MRI studies may provide additional clinical value when examining the current one and thus have the potential to increase sensitivity and specificity of screening. Therefore, quickly interrogating suspicious findings in both current and prior MR studies is requested in the screening routine. Automatic spatial linking of suspicious findings with the help of registration algorithms is desired. However, a reliable alignment method between follow-up studies is not a trivial task. Tremendous deformation of breasts are expected in follow-up studies due to the differences in breast compression and positioning. Moreover, various scanners and imaging protocols may be applied between imaging intervals producing different intensity values and different field of views. As shown in Fig. 3.15, strong deformation of breast tissue and misaligned skin boundaries are observed in current and prior MR scans. Moreover, the volumetric and anatomical change resulting from breast surgeries poses further challenges to registration algorithms.

In this work, we present a fast and robust spatial alignment framework, which combines automated breast segmentation and current-prior registration techniques in a multi-level fashion. Given a specific location in the current study, the aim of this work is to find the corresponding location in the prior study with sufficient accuracy and computational efficiency. First, fully automatic breast segmentation is applied to extract the breast masks that are used to obtain an initial affine transform. Then, a non-rigid registration algorithm using normalized gradient fields as similarity measure together with curvature regularization is applied. A total of 29 subjects and 58 breast MR images were collected for performance assessment. To evaluate the global registration accuracy, the volume overlap and boundary surface distance metrics are calculated, resulting in an average Dice Similarity Coefficient (DSC) of 0.96 and root mean square distance (RMSD) of 1.64 mm. In addition, to measure local registration accuracy, for each subject a radiologist annotated 10 pairs of markers in the current and prior studies representing corresponding anatomical locations. The average distance error of marker pairs dropped from 67.37 mm to 10.86 mm after applying registration. In the end, the performance of our proposed framework is compared with the work presented by Böhler et al. [83].

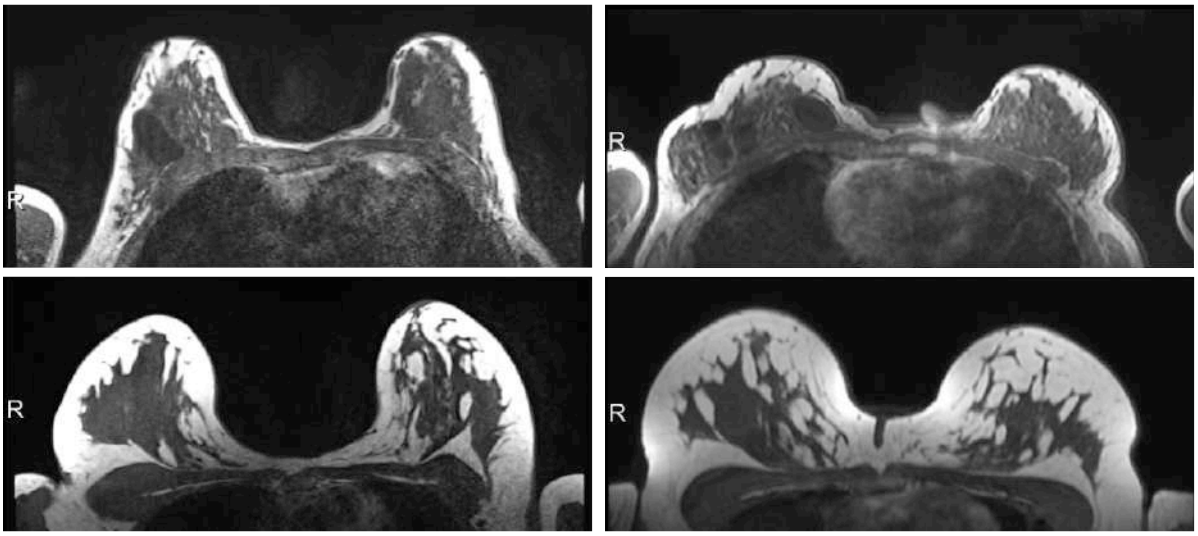

Figure 3.15: Illustration of strong deformation between current (left) and prior (right) MR studies of two subjects (top and bottom rows) with a time interval of one year. The deformation is attributed to different compression and positioning of breasts and dissimilar imaging views: current studies were acquired in axial view, while prior studies were taken in coronal view (reformatted to axial view for comparison purposes).

3.2.2. Related Work

Several current-prior registration methods have been proposed to deal with breast MRI follow-up studies. Roose et al. devised a coupled registration method that integrates a biomechanical model and iteratively updates boundary conditions. It combines elastic properties of the tissue with a matching of the enclosed surfaces, namely the skin and chest-wall surfaces. However, only three data sets acquired with the same scanner in a short time interval were used for evaluation [84]. Therefore, limited deformations introduced by different subject positioning were tested. Böhler et al. suggested a two-phase registration framework to align current and prior MR volumes. First, left and right breasts are separated and registered individually using an affine transform. Then, the deformation fields obtained for left and right breasts are stitched together and applied to the prior volume to achieve a rough alignment. Finally, a non-rigid registration was adopted to further register the deformed prior volume onto the current one [83]. Diez et al. adopted three commonly used registration algorithms on breast MRI follow-up studies, including Affine, SyN and Demons [85]. The reported landmark distance errors of these methods were over 25 mm, indicating that directly applying established registration algorithms without adaptions for this task may fail.

3.2.3. Materials and Methods

The overall framework contains three steps. Firstly, breasts in both current and prior studies are automatically segmented. Secondly, the obtained breast masks are aligned with an affine transform to estimate a rough alignment which serves as an initial transform for subsequent non-rigid registration step. Thirdly, the segmented breast volumes are registered with a non-rigid registration algorithm producing a final deformation field. The proposed registration scheme is inspired by the works of Rühaak et al. [86], which uses the discretize-then-optimize

paradigm in a multilevel Gauss-Newton optimization framework [87]. A schematic overview of the entire workflow is given in Fig. 3.16.

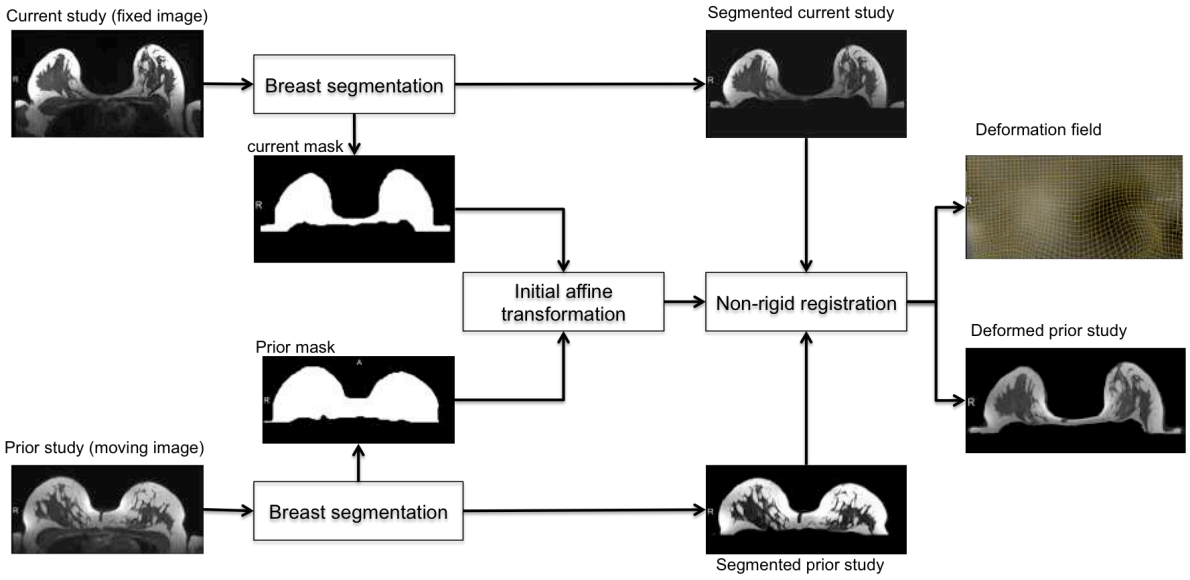

Figure 3.16: Overview of the registration workflow by illustrating intermediate segmentation and registration results.

Automatic Breast Segmentation

Different acquisition views normally cover different portions of the organs in thorax such as lung and heart in breast MRI. Images acquired in axial views may cover the entire body in imaging fields, whereas coronal and sagittal views cover fewer organs which can mislead registration processes to register the organs that are present in one image but absent in the other. To enforce registration process focusing on breast regions, automated breast segmentation is required.

We adopt the fully automatic breast segmentation method presented in section 3. The task of breast segmentation in MR images is subdivided into two steps: pectoralis and breast-air segmentation. The key observation of this method is that pectoral muscle and breast-air boundaries exhibit smooth sheet-like surfaces in 3D, which can be simultaneously enhanced by a Hessian-based sheetness filter. The method consists of four major steps: enhancing sheet-like structures, segmenting pectoralis muscle boundary that defines the lower border of breast region, segmenting breast-air boundary that delimits the upper border of the breast region, and extracting the region between the breast-air and pectoralis boundaries which finally captures the area of breast tissue as shown in Fig. 3.17.

Affine Pre-registration

Breast deformation between current and prior MR studies can be substantial, thus a good initialization is critical for the success of subsequent non-rigid registration step. Breast masks achieved in segmentation step are used to derive an initial guess of deformation field. First, centers of gravity of the masks are aligned with each other to derive an estimation of transla-

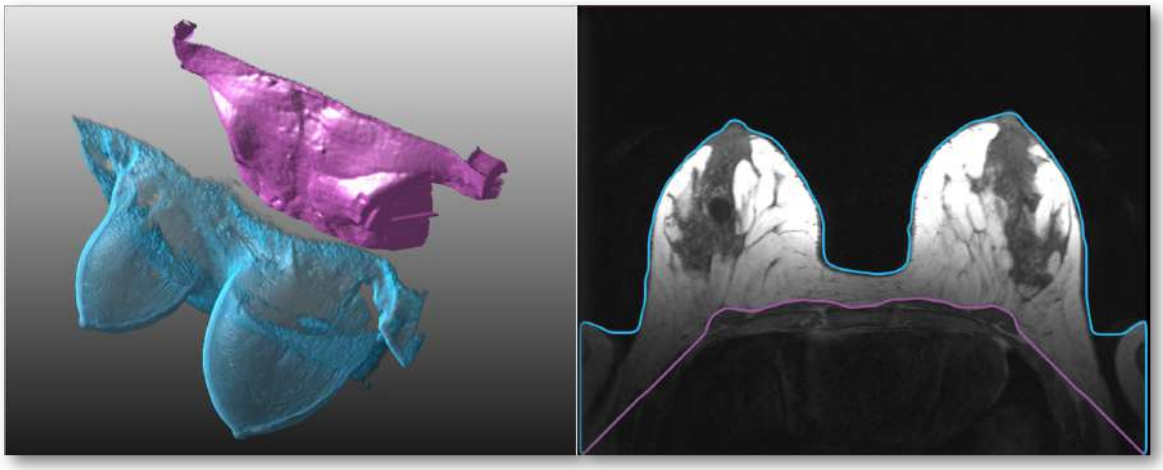

Figure 3.17: Demonstration of the segmented breast-air (in blue) and pectoral muscle (in purple) boundary surfaces in 3D (left) and 2D (right).

tion. Then, an affine transform using Sum of Squared Differences (SSD) similarity measure is estimated, which roughly positions both images together as shown in Fig. 3.18. The obtained affine transformation is used to initialize the subsequent non-rigid deformable registration process.

Deformable Image Registration

In deformable image registration, a common approach consists of formulating the registration problem as an objective function J that is to be minimized [88]. Typically, J is built up by an image similarity measure D and a regularizer S that penalizes unwanted transformations. Let $F, M : \mathbb{R}^3 \to \mathbb{R}$ denote the fixed (or reference current) and moving (or template prior) image with compact support in domains $\Omega_F \subseteq \mathbb{R}^3$ and $\Omega_M \subseteq \mathbb{R}^3$, respectively. For a transformation $y : \Omega_F \to \mathbb{R}^3$, the objective function in our model is composed of two parts:

$$J(y) = D(F, M(y)) + \alpha S(y). \tag{3.2}$$

The weighting factor $\alpha > 0$ balances between data fit and deformation regularity. Due to possibly long intervals between examinations, follow-up studies are likely acquired with changed protocols or even different scanners. This imposes problems for registrations using solely intensity-based similarity measures. Hence, we employ the edge-based Normalized Gradient Fields (NGF) similarity measure [89] which was designed to cope with such varying intensities. We use the following variant as proposed in [86]:

$$D(F, M(y)) := \int_{\Omega F} 1 - \left(\frac{\langle \nabla M(y(x)), \nabla F(x) \rangle_\eta}{\|\nabla M(y(x))\|_\eta \|\nabla F(x)\|_\eta} \right)^2 \mathrm{d}x \tag{3.3}$$

with

$$\langle f, g \rangle_\eta := \sum_{j=1}^{3} f_j g_j + \eta^2 \text{ and } \|f\|_\eta := \sqrt{\langle f, f \rangle_\eta} \tag{3.4}$$

for $f, g \in \mathbb{R}^3$. The parameter $\eta > 0$ is used to suppress the influence of gradients stemming from image noise. For transformation regularization, we employ the curvature regularizer as presented in [90]:

$$S(y) := \frac{1}{2} \int_{\Omega F} \sum_{j=1}^{3} \|\Delta(y_j - y_j^{\text{kern}})\|^2 \, \mathrm{d}x. \tag{3.5}$$

The curvature regularizer penalizes second derivatives of the deviation of y from a given transformation y^{kern}, leading the algorithm to favor smooth deformations. We set y^{kern} to the result of the affine-linear pre-registration step. All results presented in this work were calculated with a fixed parameter setting of $\alpha = 2.5$ and $\eta = 100$.

Moreover, we enforce the registration focus on the breast region by employing the pre-computed breast masks. Irrelevant structures, such as chest, lung and heart are masked out and have thus no influence on the registration. The objective function J is optimized with the L-BFGS Newton-type optimization algorithm [91]. The computation is embedded in a multi-resolution framework for both the images and the deformation, see [86] for details. The occurring objective function derivatives are calculated in a fully matrix-free manner that allows for a fast, memory-efficient, and parallel computation [92]. The alignment of breast volumes driven by affine transform and deformable registration is given in Fig. 3.18, where the deformed breast masks of the prior study are also shown.

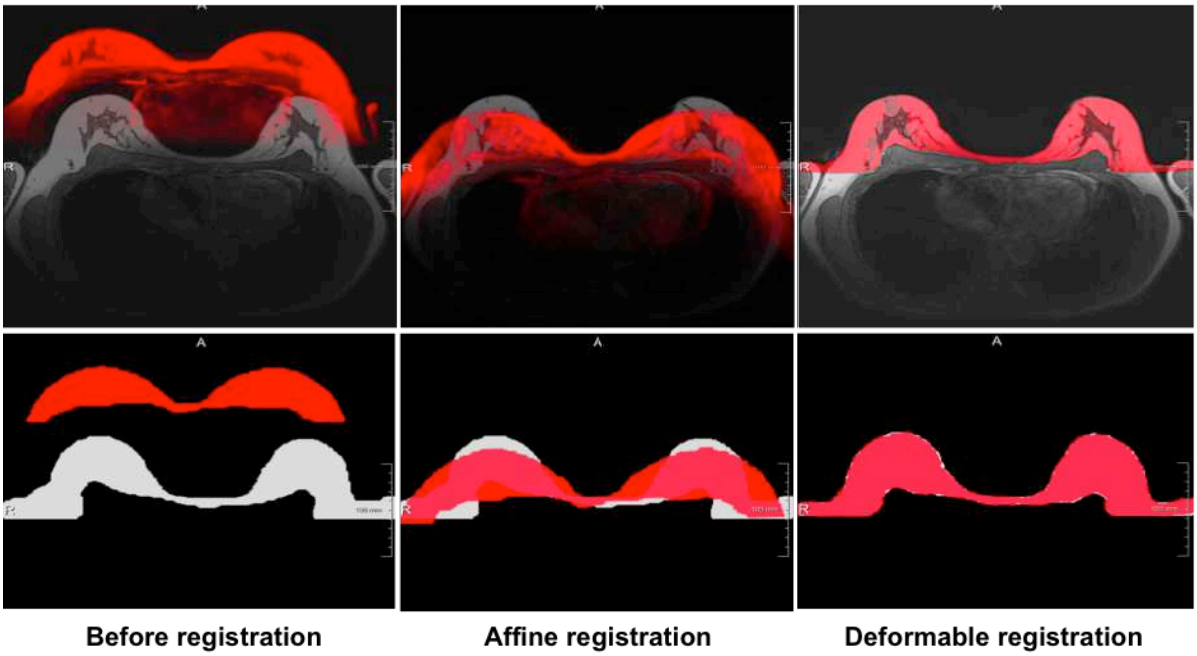

Figure 3.18: Illustration of affine transform and deformable registration: current and prior studies before applying registration (left column), after initial affine transformation (middle column) and after deformable registration (right column). The top row depicts the alignment between fixed image (current study) and moving image overlaid in red (prior study). The bottom row shows boundary alignment between fixed (in white) and moving (in red) masks.

3.2.4. Results and Evaluations

Data Sets

A collection of 29 individual subjects with 58 breast dynamic contrast enhanced MRI (DCE-MRI) follow up images were acquired from a screening program running in Radboud University Medical Center (Nijmegen, Netherlands). For each subject, two consecutive follow-up MRI studies with a time interval of 1 year were available. Current MRI examinations were performed in 2011 with a 3 Tesla Siemens scanner (MAGNETOM Skyra), with a dedicated breast coil (CP Breast Array, Siemens, Erlangen). Subjects were scanned in prone position and transversal view with following imaging parameters: $448 \times 448 \times 160$; slice thickness: 1 mm; voxel spacing: 0.8036×0.8036 mm; flip angle: 20 degrees; repetition time: 5.03 ms; echo time: 2.06 ms.

Prior MRI examinations were performed in 2010 with a 3 Tesla Siemens scanner (MAGNETOM Trio) with the same breast coils. However, subjects were scanned in prone position and coronal view with following imaging parameters: $384 \times 192 \times 160$; slice thickness: 1 mm; voxel spacing: 0.9375×0.9375 mm; flip angle: 13 degrees; repetition time: 735 ms; echo time: 2.39 ms. Current and prior DCE-MRI scans have 5 and 6 time points, respectively. Pre-contrast images were used for registration in this work. Images of two subjects were shown in Fig. 3.15.

Evaluation and Comparison

Three metrics were used to quantitatively evaluate alignment accuracy of the proposed method: Dice Similarity Coefficient [93] (DSC), boundary distance error (BDE) and landmark distance error (LDE). Dice similarity coefficient validates the volumetric overlap between deformed breast of prior studies and breasts of current studies. Higher registration accuracy should deliver better overlapping ratio.

Moreover, agreement of breast-air boundaries and pectoral muscle boundaries are of great interest for investigation, because it measures how well the breasts with different compression and shapes coincide after performing registration. Hence, we define the metric of boundary distance error as the distance between the boundary surfaces of current and deformed prior breasts.

DSC and BDE are able to quantify the consistencies of breast volumes and boundaries. However, the registration accuracy of breast parenchyma tissues inside the breasts can not be reflected directly by DSC and BDE. The most direct way to quantify the alignment quality of internal breast parenchyma tissue is to annotate a few corresponding landmarks in both current and prior studies and measure their distances after deformation. Therefore, an experienced radiologist manually identified salient anatomical landmarks on each pair of current and prior studies for all subjects. The radiologist tried to spread the landmarks through entire breast volumes. More specifically, landmark pairs were manually annotated by investigating subtracted images. Afterwards, all landmarks were visually validated on axial, sagittal and coronal planes. Nipples were marked in all breast volumes, while prominent vessels and glandular tissue margins were annotated when they occurred in both current and prior studies. As a result, a total of 10 pairs of corresponding landmarks were set for each current-prior pair

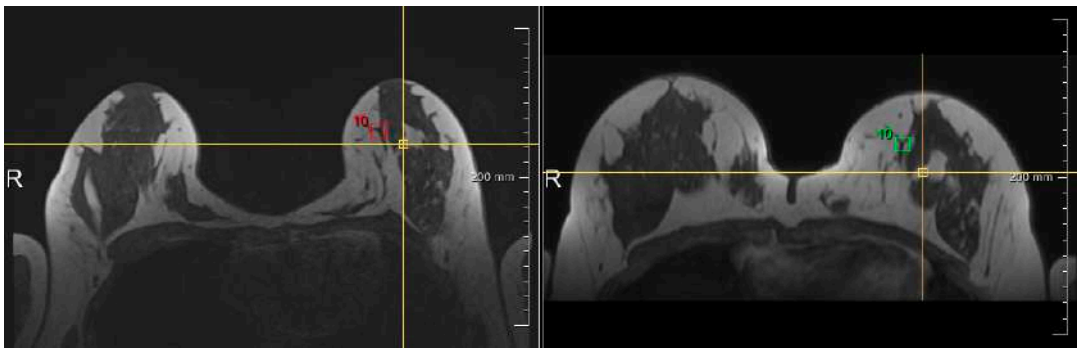

Figure 3.19: Pair-wise landmarks annotated in the original current (red markers in left) and prior (green markers in right) studies. The markers with the same label indicate the corresponding locations annotated in 3D. When a cursor is placed near the red marker labeled with 10 (in left), its corresponding cursor position calculated by registration is shown (in right).

(see Fig. 3.19).

Markers annotated in a prior study were deformed onto the corresponding current study, and the distance between deformed landmarks and fixed landmarks was computed. The landmark distance error (LDE) is defined as the averaged distance of all pairs of landmarks annotated for a subject, given in the following equation:

$$\text{LDE} = \frac{\sum_{i=1}^{n} \text{dist}(L_i^c, D(L_i^p))}{n} \tag{3.6}$$

where L^c and L^p are the current and prior markers; D refers to the deformation transform; n is the number of marker pairs. All distances refer to the root mean square distances (RMSD). Regarding computational expense, the average computation time per volume was 24.55 seconds for breast segmentation and 7.33 seconds for registration on a machine with a 3.2GHz Quad-Core CPU and 12 GB RAM.

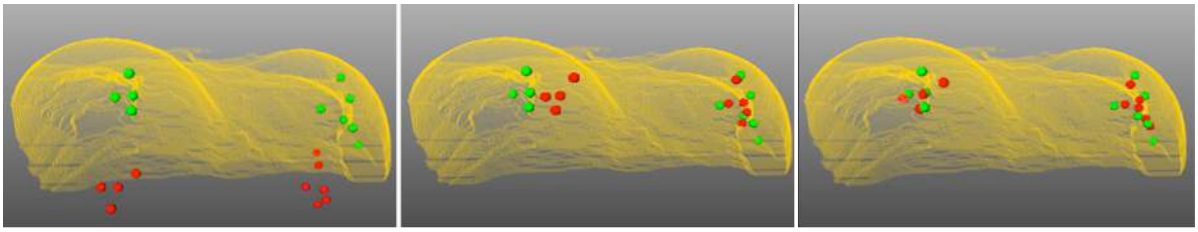

Figure 3.20: Annotated landmarks for current study (red) and prior study (green) aligned by affine transform and deformable registration. For visualization purpose, the breast volume of prior study is rendered in yellow.

Böhler et al. has developed a non-rigid registration approach that can be applied in current-prior registration [83]. This method uses a slightly different approach to registration. It begins by rigidly registering each of the two breasts (left and right) independently. However, after this step the method combines the two deformations obtained into a single deformation field. The two rigid deformations are combined using Thin-Plate-Splines interpolation. Subsequently

Table 3.5: Measuremens statistics and performance comparison with the method presented in by Böhler et al. [83].

Measurements	No registration	Proposed method	Böhler's method
Mean of DC	0.17	0.96	0.81
Stddev of DC	0.08	0.008	0.05
Mean of BDE (mm)	57.65	1.64	8.53
Stddev of BDE (mm)	18.16	0.73	2.57
Mean of LDE (mm)	67.37	10.86	15.74
Stddev of LDE (mm)	29.52	5.56	7.98

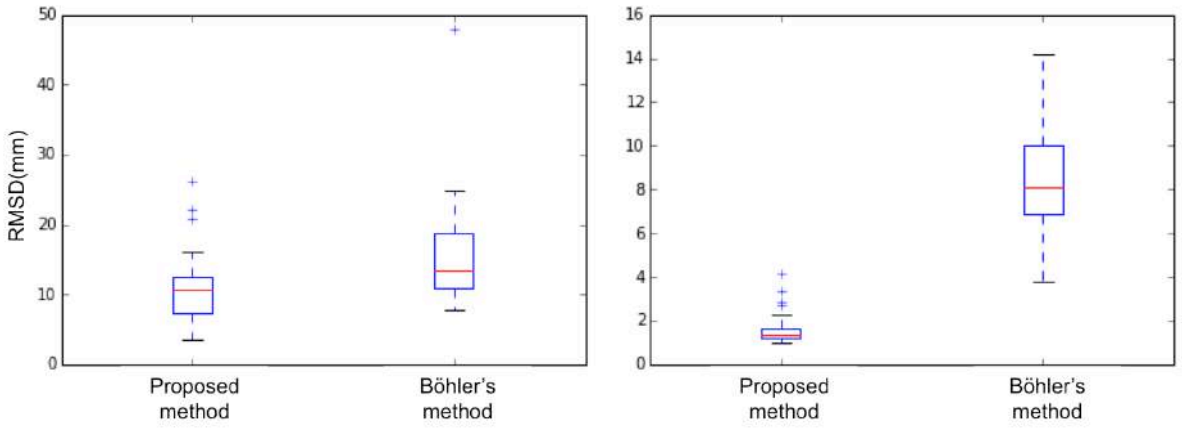

Figure 3.21: Boxplots of landmark distance error (left) and boundary distance error (right) for proposed method and Böhler's method.

a deformable registration step is performed with the images that combine the two breasts.

In comparison with the method implemented by Böhler et al., statistical results, including mean and standard deviation (mean $\pm$ stddev), of each metric when applying different methods are listed in Table 3.5. Values obtained without registration are also calculated. The results showed that the proposed method achieved higher accuracy in terms of volume overlap (DC: 0.96 ± 0.008), boundary alignment (BDE: 1.64 ± 0.73) and internal parenchyma tissue correlation (LDE: 10.86 ± 5.56). To show the alignment accuracy of landmarks, the deformed landmarks of a prior study when applying affine transform and deformable registration are visualized in Fig. 3.20. Notice that the prior landmarks progressively approach the current landmarks. Moreover, the BDE and LDE calculated for all subjects are plotted in Fig. 3.21.

Further Comparison with Other Methods

Methods to Compare

In this evaluation study, we have independently compared the performance of Böhler's method again other popular registration frameworks.

First of all, we considered Affine registration. This method provides comparison grounds for other registration results and is also used as an initialization step by the two non-rigid methods evaluated. This method was implemented using the Insight Toolkit (ITK) libraries. Affine (and in some cases Rigid) registration methods are used because they are fast and produce images that are artifact-free [94]. Although these methods are very convenient for some applications, they are global in nature (a single motion is applied to the whole of the image). This characteristic makes it difficult for them to account for local variations [95].

The second registration method studied in this work is SyN, which is part of the Advanced Normalization Tools (ANTs) package and uses bi-directional diffeomorphism [96]. These bidirectional diffeomorphisms do not need to distinguish between target and source images thus enhancing their application scenarios.

We also studied a b-spline based method. Specifically, we considered the ITK implementation of [97], which uses cubic b-splines. The second one was Nifty Reg, which provides faster convergence as well as the possibility of improved running time by running in the GPU [98].

Another type of methods studied were demons-based methods. First we used the ITK implementation of the classic algorithm (based on Thirion's demons [99]) using multi-resolution. Second, we used the diffeomorphic variant CITE AYACHE. This paper reformulated the original idea by formalizing the original demons optimization (identified from now on as "DEM") as an optimization procedure over the space of displacement fields. This reformulation allowed the authors to show how Thirion's formulation, although apparently very different to the classical registration pipeline based on an interpolator, an optimizer and a measure to be optimized, could be fit to a similar schema based on SSD minimization. Among the three variants presented (according to the deformations allowed in deformation field space), for this study and for the sake of concreteness, we decided on using the additive one. Notice how methods using the same working principle might differ greatly in their implementation details, initialization parameters or even optimization functions, so they do not always produce similar results.

We also included the DRAMMS method [100]. This is a general-purpose non-rigid reg-

istration algorithm that, as opposed to all the other algorithms studied is not solely based on intensity values. As its authors claim, DRAMMS bridges the gap between intensity and landmark-based methods. This is achieved by assigning a rich set of Gabor attributes to each voxel and then computing a non-parametric transformation. The correspondences between voxels in this transformation are determined by a function named "mutual saliency" that aims at giving more weight in the transformation to more distinctive voxels. These two concepts, attribute matching and mutual saliency, play the role that similarity metrics do for most registration methods.

Finally, we also included the method developed during the HAMAM European project by Böhler et al. [83] (noted as "HAMAM" in this study).

Data Set

In this comparison study, 31 breast T1-weighted DCE-MRI studies were collected in the Radboud University Nijmegen Medical Centre (Netherlands). For each patient, a pair of DCE-MRI studies was available: a DCE-MRI exam acquired in 2011 (current) and a DCE-MRI exam acquired in 2010 (prior). Breast MRI examinations were performed in coronal or transverse orientation on either a 1.5 or 3 Tesla Siemens scanner (Magnetom Avanto, Magnetom Skyra or Magnetom Trio).

Similar to the previous test, for evaluation purposes, landmarks were placed in all pairs of DCE-MRI volumes by a radiologist with expertise in breast imaging. Each annotation consisted of two corresponding points, each of which was placed on each of the volumes composing the DCE-MRI pair. Notice how correspondence of landmarks is a key factor, so if a particular anatomical structure was only visible in one of the scans it was not used for landmark placement. Annotations were manually performed by comparing time points, and subtracted images. Annotations were visually validated on axial, sagittal and coronal planes. This process already yielded some insight in the difficulties faced by registration methods. For example, differences in the position of patients during image acquisition (prone or supine) made the placing of landmarks challenging. Technical differences in the acquisition process or physiological changes also added to these problems. Concerning the placement of landmarks, nipples were marked in all cases. Vessels and fat/glandular tissue margins were also placed whenever possible. A total of 10 pairs of corresponding landmarks were set for each DCE-MRI pair.

Evaluation Results

Figure 3.22 presents results for the landmark distance criterion (in mm). The box-plot shows how all methods managed to improve the distance values before registration (BEF column). Specifically, distance was reduced 30% by the best methods.

Rigid registration obtained satisfactory results although far from the better performing methods (differences were observed to be statistically significant for SyN and HAMAM). Best overall results were obtained on average by the HAMAM method although they were very close to those obtained by SyN (32.61mm and 33.17mm, respectively). The performance of the HAMAM method against that of the classical demons method (DEM column) was also studied. Specifically, the HAMAM methods obtained better results than the classical demons method (the differences were found to be statistically significant).

Based on the results of this independent study, we can conclude that the method developed by Böhler achieved the best performance over others. The previous experiment has proved the proposed method outperformed Böhler's method (see Table 3.5), therefore, we can conclude the proposed method was able to obtain better performance over all methods that were tested in these two experiments.

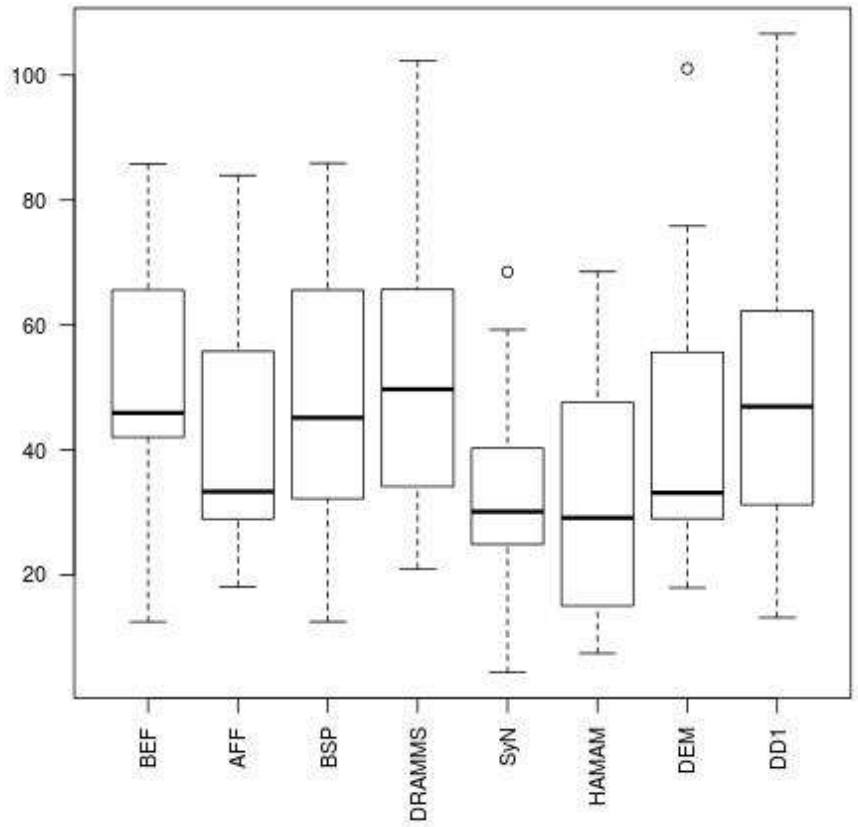

Figure 3.22: Results of landmark distance.

3.2.5. Summary

In this section, we developed a fully automated spatial alignment framework in application of registering breast MRI follow-up studies. The proposed framework combines segmentation and registration techniques, which run efficiently with acceptable time requirements for clinical applications. The proposed method requires no user interactions and achieves higher accuracy in terms of the evaluated metrics. Landmark distance error allows for a precise quantification of registration accuracy associated with breast parenchyma tissues, where breast lesions are expected to be observed. Therefore, spatial linking of lesions in current and prior studies becomes feasible by using the proposed registration method.

Additionally, since we perform breast segmentation ahead of registration, our method delivers a reasonably higher agreement in breast boundaries and volumetric overlapping. How-

ever, errors produced in segmentation will influence registration process as well. Experiments of automatic breast lesion linking in follow up pairs of MRI examinations and the dedicated user study were conducted and proved its robustness and applicability in practice. Future work includes incorporating breast parenchyma segmentation into registration step, which will potentially further improve alignment accuracy of inner parenchyma tissues.

3.3. Application of Breast Segmentation and Current-Prior Registration

If we apply the techniques of breast segmentation and current-prior registration together, it can derive practical solutions for many application scenarios. In the following sections, three representative applications are briefly introduced to demonstrate the practical usage.

3.3.1. Motion Detection and Quantification in Breast MRI

Introduction

Dynamic contrast enhanced (DCE) MRI is used for breast cancer screening examinations for women of high risk for developing breast cancer. Motion caused e.g. by muscle relaxation or coughing during image acquisition can reduce the interpretability of breast MRI. For scans with strong motion, it might be necessary to repeat the scan, but in typical screening workflow, this is only detected by the radiologist when the woman has already left the clinic. As a consequence, the woman might need to be recalled for a repeated scan. In this work, a fully automated tool based on image-processing is proposed to detect and quantify motion for unambiguous scan quality evaluation before the woman leaves the clinic.

Materials and Methods

Data Set

The breast MRI data set was provided by Radboud University Nijmegen Medical Centre (RUNMC) and extracted randomly from original breast cancer screening data. In total, 491 screening exams acquired with the current screening MR protocol of RUNMC from 449 patients were supplied. An expert radiologist manually annotated the clinical image data concerning motion artifacts focusing on the high resolution images of time point t0 (pre-contrast) and t1 (first post-contrast), as these were assumed to be representative for the whole data set. The motion artifact was categorized in four classes: no (1), mild (2), moderate (3), or severe (4) motion. For simplification, the classification was transformed into a two class categorization. Cases were considered ”positive” if they showed moderate or severe motion. The rating results are shown in Fig. 3.23. Generally, in this text, ”positive” refers to an image showing the considered artifact, while ”negative” indicates that the image is not affected by this artifact, which means that these two terms do not refer to any diagnostic outcome concerning lesions or tumors.

Automated Detection of Motion

As the standard DCE breast MRI protocol takes several minutes, it is quite possible that the woman moves slightly during the examination. As shown in Fig. 3.24, motion between time 0 (pre-contrast as t0) and the following sequences (post-contrast as t1,...,tn) leads to blurred maximum intensity projections (MIPs), as they are based on the subtraction of t0. As only the motion between t0 and t1 was rated by the radiologist, we only consider t0 and t1 as a simplification in this first approach.

To quantify the motion artifact between t0 and t1 (not within one single acquisition), prominent edges delineating the boundary contours of parenchyma, skin and pectoral muscle were detected in both t0 and t1 studies (see Fig. 3.25(a)) using the method introduced in Section 3.1. Irrelevant motion that occurred in the thorax, such as heart, lung or liver motion, was excluded by a fully automatic breast segmentation, which confines edge detection only to the inside of the breast region. Due to the administration of contrast agent and the consequent enhancement of previously faint structures, normally more edges would be captured in t1 compared to t0 using identical parameter settings for edge detection (see Fig. 3.25(b)). We adopted the Canny edge detection algorithm using a Gaussian smoothing kernel with sigma of 1.5 mm (resolution of the images in transversal plane is $0.8\text{mm} \times 0.8\text{mm}$). To speed up processing, we only focused on the 10 central slices instead of the entire volume, based on the observation that most noticeable motion occurred in these slices and thus, the motion captured here revealed the extent of motion artifact of the entire difference image.

Motion of corresponding breast tissue structures appearing between t0 and t1 results in deformation of their boundaries, thus the deformation of edges can be used to quantify motion strength. In practice, both linear and non-linear deformed edges were demonstrated. Therefore, a simple distance measure between the two sets of detected edges was not suitable to reflect the motion extent, since it was quite difficult to align the two edge sets and find accurate edge pairs for distance calculation (see Fig. 3.25(c)).

To cope with the alignment problem, we employed the fast and non-rigid registration method with a volume preservation constraint introduced in Section 3.2, aiming to register t1 (moving image) onto t0 (fixed image). The obtained deformation field had the same resolution as t0 (see Fig. 3.25(d,e)). A 3D deformation vector was assigned to each single voxel in t0 representing the direction and magnitude (strength) of the motion occurred in that voxel. The magnitude of the deformation vectors of all the edge voxels detected in t0 was saved to a list, which encoded the motion strength along edges (see Fig. 3.25(f)). Then, a histogram was generated from the magnitude list and a set of features was extracted from the histogram as follows:

- Mean
- Standard deviation
- Peak
- Maximum
- Q25: quantile corresponding to of 25% of the distribution

- Q50: quantile corresponding to of 50% of the distribution
- Q75: quantile corresponding to of 75% of the distribution
- Q90: quantile corresponding to of 90% of the distribution
- Average on top range: the average of magnitudes in range [Q50, Max]

Finally, these features were used for training a Random Forest (RF) classifier [101], which served as a decision maker to predict whether a test case had moderate/severe motion artifact or not. In Fig. 3.25 and 3.26, the motion detection results are shown for the two cases we previously demonstrated in Fig. 3.24 (a) with motion and (b) without motion. The average motion strength measured for the case with a motion artifact shown in Fig. 3.25 was 1.21 mm, which means on average the edge voxels were deformed by 1.21 mm, leading our classifier to make a positive decision. For the case without a motion artifact, the average motion strength shown in Fig. 3.26 was 0.21 mm, resulting in a negative decision by our classifier. In both figures, the areas with strong motion are marked by red squares, where one can observe larger deformation magnitude in the positive case (see Fig. 3.25(e)), while for the negative case, the deformation magnitude is much lower (see Fig. 3.26(e)).

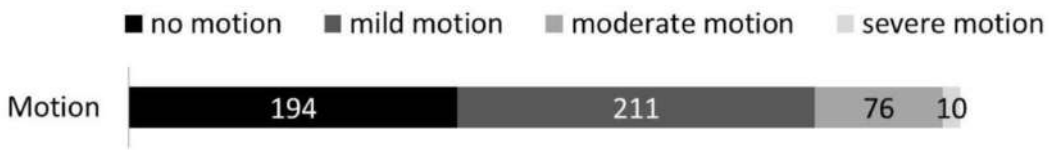

Figure 3.23: Incidence and degree of motion artifact in the considered data set as rated by an expert radiologist.

Results

To evaluate the performance of the motion classifier, 10-fold cross validation at patient level was applied to objectively report prediction accuracy. Test results presented as receiver operating characteristic (ROC) curve and statistical measures are depicted in Fig. 3.27. By selecting 0.5 as the classification threshold, it was shown that the classifier obtained a high specificity of 0.965, which means 391 out of 405 cases were classified correctly as showing no-motion. A sensitivity of 0.535 (46 out of 86 moderate and severe cases were detected correctly) with low false positive rate (0.035) was achieved. Moreover, if we intended to further decrease the false positive (FP) rate, elevating the classification threshold to 0.67 would achieve a fairly good (low) FP number as 6, while keeping true positive (TP) number as high as 36. The overall area under the ROC curve was 0.834.

Representative FP and false negative (FN) cases are demonstrated in Fig. 3.28 and 3.29, respectively. The FP case shown in Fig. 3.28 was rated by the radiologist as 2 (mild motion), and the mean motion strength evaluated by the method was 2.76 mm. The reason of inconsistency between expert annotation and method prediction might be that the criteria of judging motion artifact is different. Despite of a relatively strong motion in the image, the

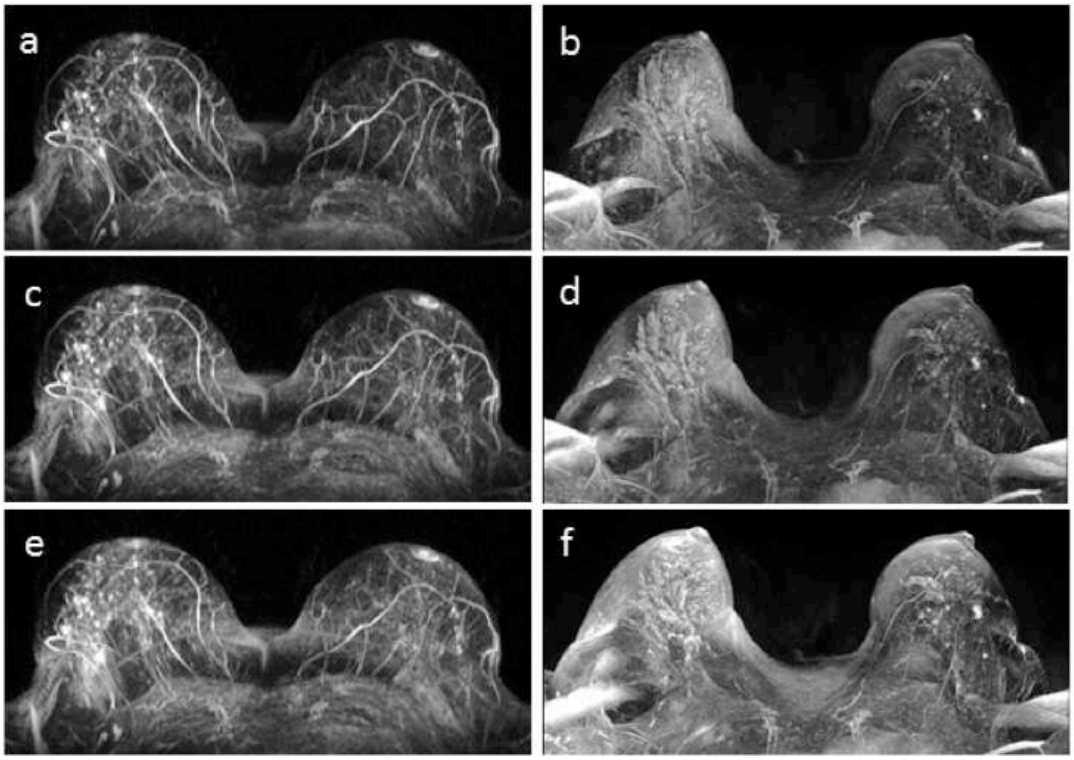

Figure 3.24: Maximum intensity projection images of the difference images (a, b) t1 – t0, (c, d) t2 – t0, (e, f) t3 – t0, of the same woman. Left column represents a case without motion and right column with moderate motion, especially in the right breast (left in the image).

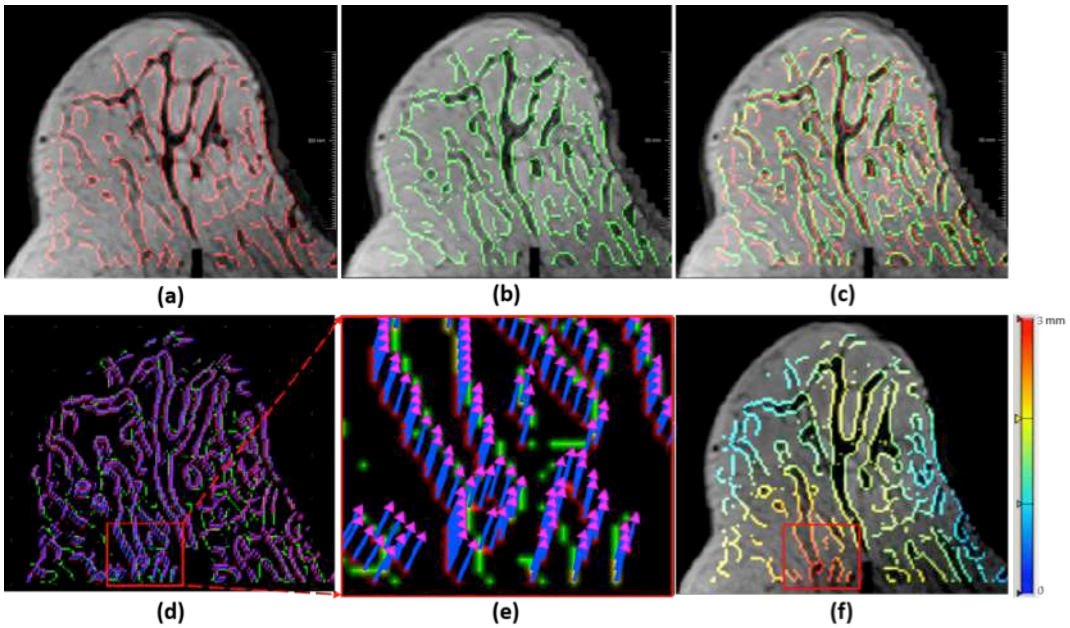

Figure 3.25: Illustration of motion quantification for the positive case shown in Fig. 3.25(right column). Its average motion strength is 1.21 mm. Detection scheme: (a) detected edges in t0 (red contours); (b) detected edges in t1 (green contours); (c) detected edges in t1 (green) overlaid with edges in t0 (red); (d) visualization of deformation vectors showing correspondence between edges in t0 and t1; (e) magnified view of the deformation vectors in the red square in (d); (f) color map of deformation magnitude (displacement in mm) calculated for edge voxels in t0, red correlates with strong motion.

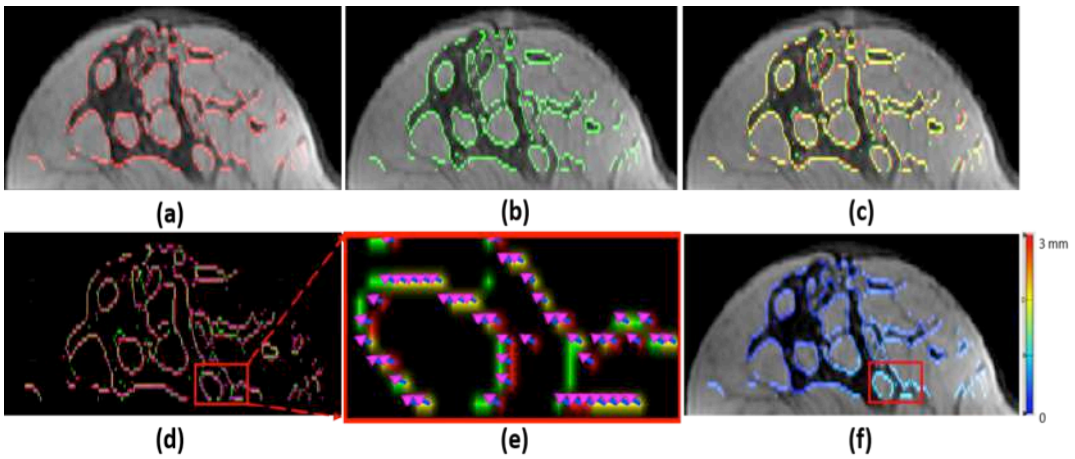

Figure 3.26: Illustration of motion quantification for the negative case shown in Fig. 3.25(left column). Its average motion strength is 0.21 mm. Detection scheme: (a) detected edges in t0 (red contours); (b) detected edges in t1 (green contours); (c) detected edges in t1 (green) overlaid with edges in t0 (red), yellow indicates perfect alignment of both; (d) visualization of deformation vector showing correspondence between edges in t0 and t1; (e) magnified view of the deformation vectors in the red square in (d); (f) color map of deformation magnitude (displacement in mm) calculated for edge voxels in t0, blue correlates with weak motion.

ultimate judgment made by the radiologist is to investigate whether the motion can impede subsequent diagnosis. The same reason might account for the inverse relation between manual annotation and automatic classification. The FN case shown in Fig. 3.29 was rated as 3 (moderate motion) by the radiologist, but the mean motion strength evaluated by the algorithm was only 0.5 mm. The inconsistency might be caused by the fact that the area, where even mild motion was detected, is quite important for diagnosis, which leads to a higher rating by human observer. Further improvements might face this challenge.

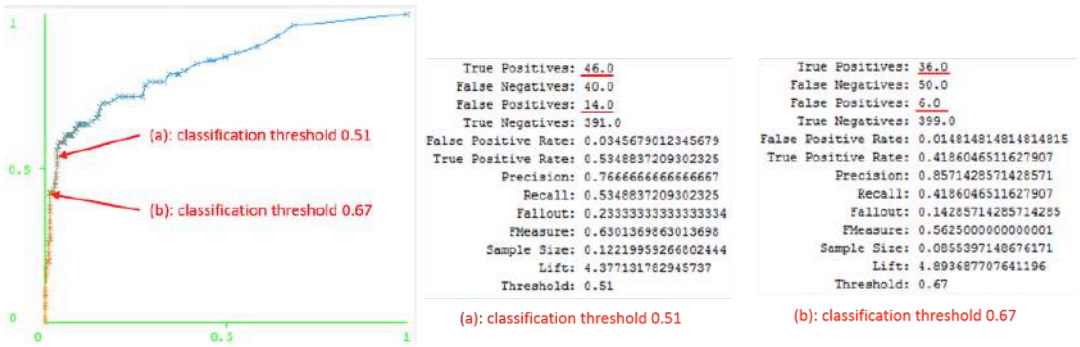

Figure 3.27: Classification accuracy obtained by 10-fold cross validation: ROC curve (left); classification accuracy with classification threshold of 0.51 (middle text block) and 0.67 (right text block).

3.3.2. Automatic Spatial Linking of Breast Lesions

In breast cancer screening for high-risk women, inclusion of prior MRI examinations can increase screening specificity. However, interpreting and correlating breast lesions across longitudinal 4D MRI data is time consuming. Therefore, automatically linking the lesions detected

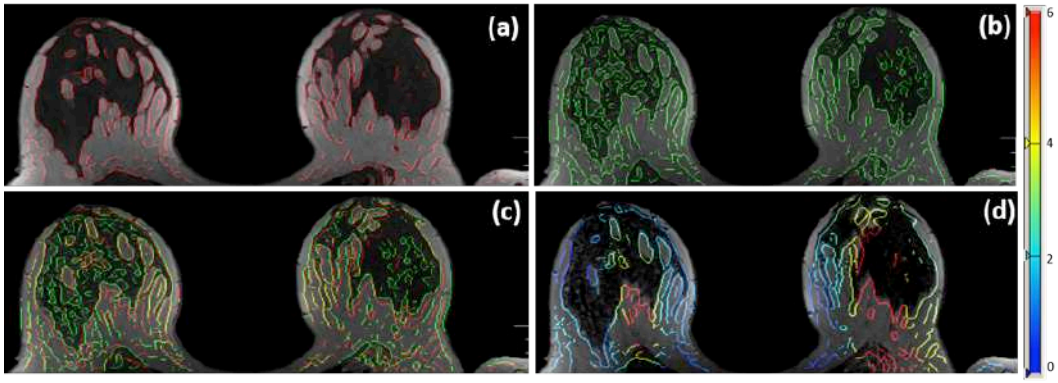

Figure 3.28: A FP example: (a) detected edges in t0 (red contours); (b) detected edges in t1 (green contours); (c) detected edges in t1 (green) superimposed with edges in t0 (red), and yellow represents completely overlaid contours; (d) color map of deformation magnitude (deviation in mm) calculated for edge voxels in t0, and red correlates with strong motion.

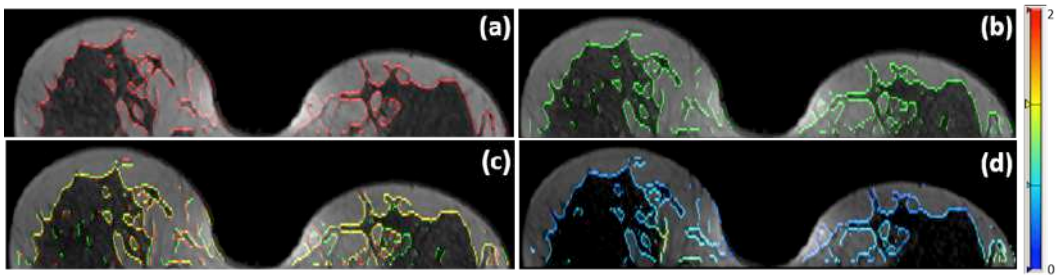

Figure 3.29: A FN example: (a) detected edges in t0 (red contours); (b) detected edges in t1 (green contours); (c) detected edges in t1 (green) superimposed with edges in t0 (red), and yellow represents completely overlaid contours; (d) color map of deformation magnitude (deviation in mm) calculated for edge voxels in t0, and blue correlates with weak motion.

in breast MRI follow-up examinations is required for the development of a computer-aided diagnosis system to quantify characteristic changes of the lesions. In this experiment, we evaluated the registration method on the application of automatic linking of lesions detected in breast MRI follow-up studies.

From 51 subjects participating in a MRI screening program, we collected 102 dynamic contrast enhanced MRI images, forming 51 pairs of follow-up studies. Current and prior examinations were acquired in different scanners with a time interval of one year, using transversal and coronal views, respectively. One experienced radiologist manually placed 71 pairs of markers, indicating the center locations of 71 pairs of lesions found in both current and prior studies.

Automatic lesion linking is achieved by registering current and prior MRI examinations using the non-rigid registration framework that we have proposed (see Section 3.2). Based on the deformation fields obtained by registration, markers labeling the lesions in the current image were transformed to the prior image frame, where the distance between the transformed markers and the markers originally labeled in prior images was computed. The average distance error was 9.6 ± 9.3 mm. The proposed system is potentially applicable to automatically link the lesions detected in a CAD system to investigate the characteristic changes. The software prototype and the linking accuracy are illustrated in Fig. 3.30.

3.3.3. Computer-aided Breast Lesion Localization

In this study, we evaluated a computer-aided lesion tracking system by comparing the time cost for localizing lesions in follow-up scans with and without tracking aid. The tracking aid system is based on the registration technique introduced in Section 3.2. From a MRI screening program, we collected 83 women with 83 pairs of current and prior DCE-MRI images including a total of 111 enhanced breast lesions. These 166 DCE-MRI scans were acquired in different scanners with a time interval of one year using different imaging protocols.

A dedicated workstation visualizing current and prior MR scans in two separate axial viewers was used. Two reading sessions were defined. In the first session without computer aid, for each pair of follow-up scans, lesions were automatically indicated in the current study. Then, the reader sought and localized the corresponding lesions in the prior study. In the second session tracking aid was activated. When a lesion in the current scan was indicated, the system automatically navigated the cursor in the prior scan to the tracked location of the lesion. The reader manually adjusted the cursor if it was incorrect. The time since the lesion was indicated in the current scan until the reader identified it in the prior was recorded in both sessions.

An experienced radiologist (R1) and a radiologist in training (R2) performed the two reading sessions with one day break in between. The time of each reader spent on localizing lesions with and without computer aid was compared.

As a result, the two readers succeeded to identify all the lesions in prior studies with and without the use of the tracking tool. Average localization time without tracking aid was 14.5 ± 13.4 and 20.8 ± 11.1 seconds for R1 and R2, respectively. Average localization time with tracking aid was 7.5 ± 7.8 and 11.0 ± 6.6 seconds for R1 and R2, respectively. The statistical result is summarized in Fig. 3.31. The computer-assisted tracking tool led to significant

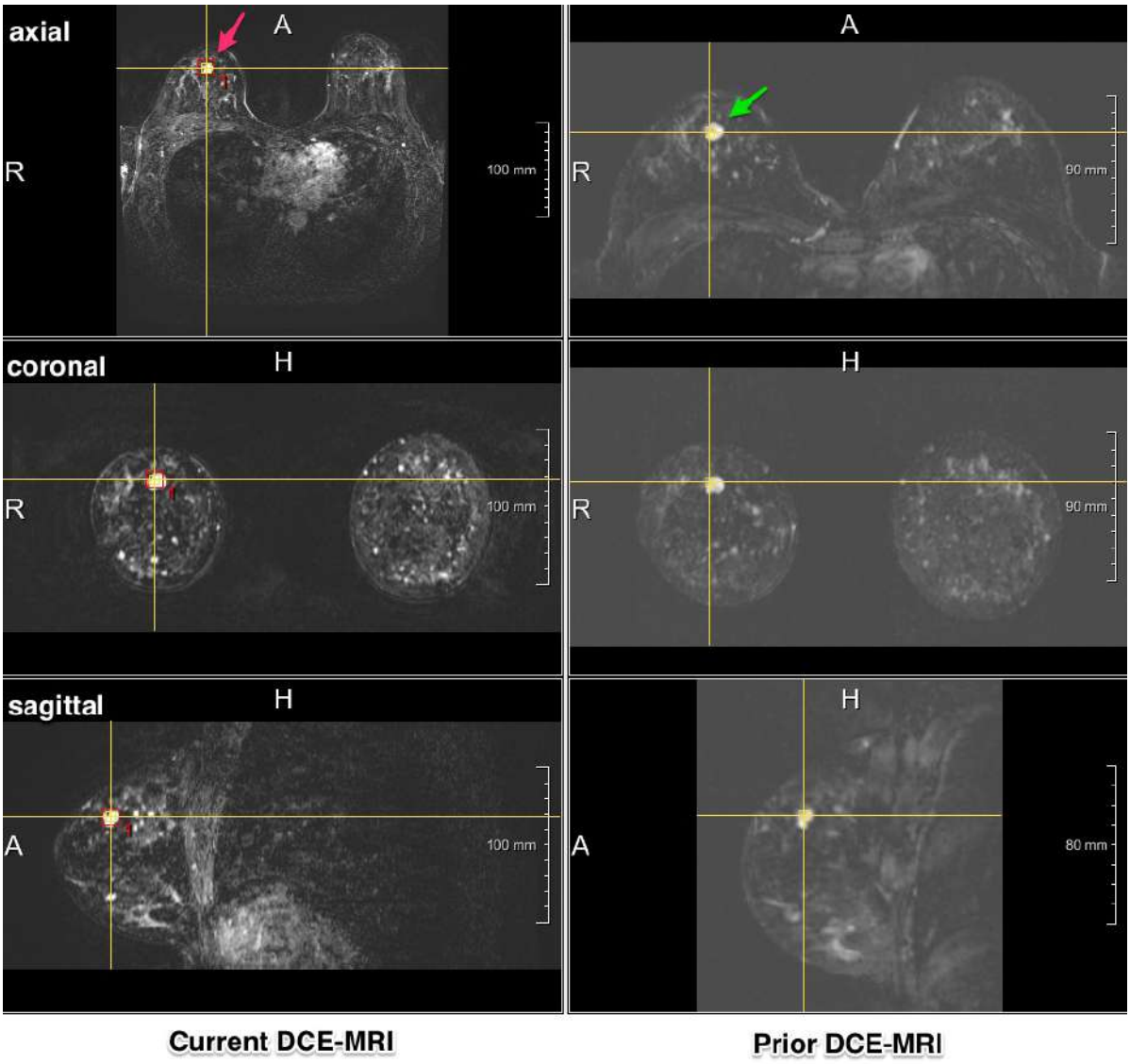

Figure 3.30: Illustration of lesion tracking results. Current and Prior subtraction images are visualized on left and right viewers in axial, coronal and sagittal planes. For the lesion indicated in current study (red arrow), its position in prior study (green arrow) is automatically given by the tracking system.

reduction of the time cost for lesion localization in breast MRI follow-up studies. The software prototype used in this study is given in Fig. 3.32.

Localization time cost (unit: seconds)	Reader 1		Reader 2	
	No assist	Assist	No assist	Assist
Mean	14.5	7.5	20.8	11
Standard Deviation	13.4	7.8	11.1	6.6

Figure 3.31: Statistical results of the time cost spent by two readers with and without computer aids.

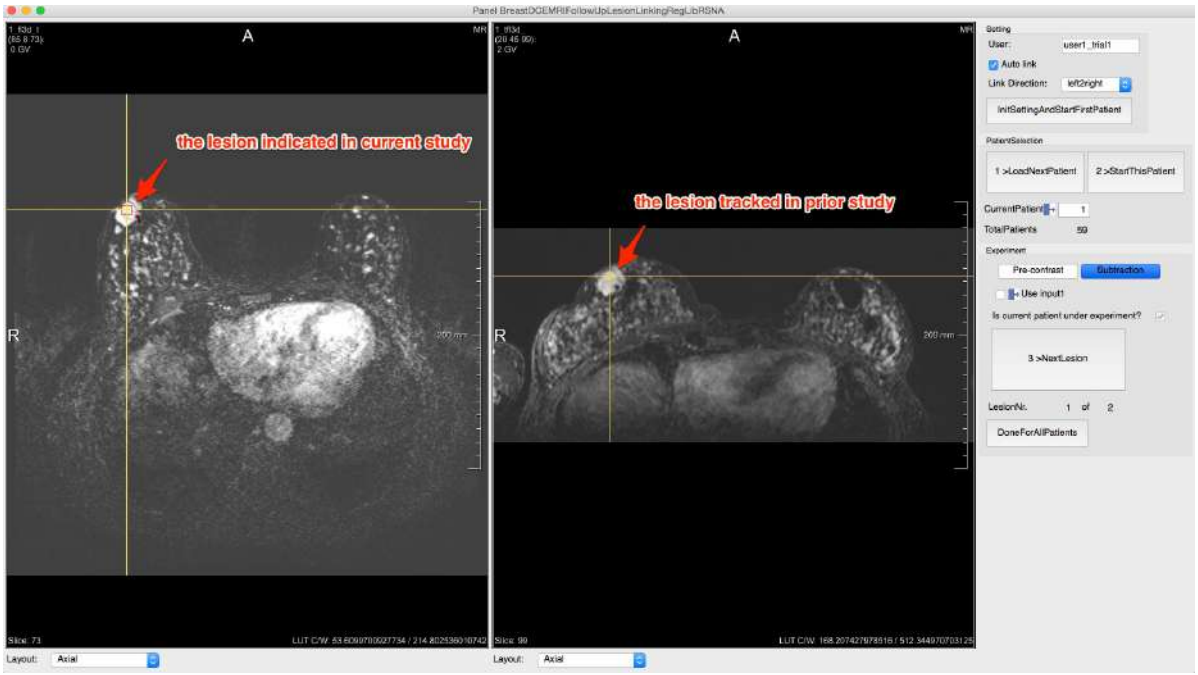

Figure 3.32: A snapshot of the workstation with tracking aid. Current and prior subtraction images are visualized in left and right viewers. For the lesion indicated in current study, its position in prior study is automatically given by the tracking system.

3.3.4. Summary

In this section, we listed several successful applications that take the advantages of the developed segmentation and registration techniques. In the application of motion detection and quantification, an automated approach for motion detection in breast DCE-MR images was presented. Based on the manually annotated data set, the algorithm showed to extract meaningful features that allow a robust automatic classification. Such a system can be used

to trigger an alert after acquisition to warn the technician that the study quality is too low. This would allow re-scanning the women shortly after the first scan, thus preventing unnecessary call-backs. In the applications of automatic lesion spatial linking, we have proved how the developed tools assist the radiologists in reading current and prior breast MRI studies by increasing the efficiency of lesion interpretation work flow. We believe more application can be definitely explored.

4

Breast Lesion Classification Based on Sphere-packing Shape Descriptors

Acknowledgment

The ASSURE project is supported by the European Union under the 7th Framework Programme for Health Research, and started in December 2012. The project is coordinated by the Radboud University Nijmegen Medical Centre, which was successfully finalized in December 2015 [1]. The development of breast lesion classification is under the financial support of ASSURE project.

I would like to give my sincere gratitude to my colleagues in MEVIS: Dr. Markus Harz and Dr. Handrik Laue, who have supported me to understand the clinical background and the machine learning techniques such as random forest classifier and the evaluation criteria commonly used in the assessment of classifier performance. Additionally, I am also grateful to the work of Mohammad Razavi, who has assisted me to implement and evaluate the algorithm by extending the test data set. Moreover, i would like give my gratitude to Dr. Albert Gubern-Merida (Nijmegen, Netherlands) and Dr. Tao Tan (Nijmegen, Netherlands) for their support to deliver the medical image data for testing purposes.

Publications

The algorithm description, implementation, and evaluation of this method were published in the following scientific papers:

- **Wang L**, Harz M, Boehler T, et al. (2014) A robust and extendable framework towards fully automated diagnosis of nonmass lesions in breast DCE-MRI. IEEE Int Symp Biomed Imaging (ISBI). doi: 10.1109/ISBI.2014.6867826

[1] http://www.assure-project.eu/

- Razavi M, **Wang L**, Tan T, et al. (2016) Novel morphological features for non-mass-like breast lesion classification on DCE-MRI. MICCAI Workshop on Machine Learning in Medical Imaging(MLMI), Lect Notes Comput Sci, 10019 LNCS:305–312
- Srikantha A, Harz M, **Wang L**, et al. (2012) Symmetry-based detection of ductal carcinoma in situ in breast MRI. Eur J Radiol, 81 Suppl 1:S158-9.
- Srikantha A, Harz M.T., Newstead G, **Wang L.**, et al. (2013) Symmetry-based detection and diagnosis of DCIS in breast MRI. Pattern Recognition: 35th German Conference (GCPR), In: Lect. Notes Comput. Sci, pp 255–260

4.1. Introduction

Dynamic contrast enhanced MRI has been widely used in breast cancer screening of high risk patients, preoperative staging, and post-treatment follow-up, for its high sensitivity. According to the BI-RADS lexicon, breast lesions are classified into mass, nonmass, and foci [105]. The detection and diagnosis of breast cancer in its intraductal stage might help to prevent from growing to invasive cancers [106]. DCE-MRI is increasingly used as an important new tool in the detection, diagnosis, staging and management of breast cancer [107]. The key benefits of breast MRI are its high sensitivity in detecting breast carcinoma and the ability of depicting cancers that are occult on mammography, ultrasound, and clinical breast examinations [108]. Compared to other modalities, DCE-MRI offers not only information on lesion morphology but also on functional features such as tissue perfusion and enhancement kinetics [109]. The breast cancer is diagnosed using DCE-MRI by interpreting the enhancement patterns of lesions and morphological characteristics [110, 111]. Despite possessing a very high sensitivity that usually exceeds 90%, the reported lower specificity of breast MRI limits its application only on specific patient groups, such as women with high risk or with suspected abnormalities [108, 110, 112, 113]. In recent years, breast MRI is recommended as an additional screening modality of breast cancer to mammography in selected population groups with elevated risk. Annual MRI screening is recommended for the women with a BRCA mutation, women who are untested first-degree relatives of a BRCA carrier, and women with a lifetime breast cancer risk between $20-25\%$ or greater [114, 115]. First results of various large prospective studies have shown that MRI appears to be about twice as sensitive as mammography in detecting tumors in women at high familial risk of breast cancer [116]. Other than screening, breast MRI has been shown to be advantageous for evaluating patients with a new breast cancer diagnosis, monitoring patients undergoing neoadjuvant chemotherapy, and evaluating patients with metastatic axillary findings [108].

The diagnosis of breast cancer in its intraductal stage might help to prevent it from becoming invasive cancer [103]. However, the delineation and diagnosis of non-masses, most notably DCIS, is challenging in breast MRI reading even for human observers [103, 104]. Clinical evidences show that the kinetic parameters have the potential to distinguish benign and malignant in masses more effectively, but fail to demonstrate usefulness in discriminating the non-masses [104]. Therefore, the computer-aided diagnosis tools strongly relying on kinetic features often fail in classifying non-masses. In terms of sensitivity and specificity in non-masses, no previous trials achieved a performance matching CAD approaches for solid masses [103]. To achieve better performance, there is a demand for prominent morphological features depicting the lesion shapes and distributions [102].

4.2. Related Works

A major limitation of breast MRI is its relatively lower specificity, which can result in many false positive findings, unnecessary recalls and biopsies [112, 117]. The lower specificity is attributed to many factors, such as the overlapping imaging features of benign and malignant lesions [108], lack of standardization regarding image acquisition and interpretation

guidelines [109], reader expertise in interpreting MRI sequences [118]. Meanwhile, multi-parametric MRI sequences generate a huge amount of data that increase the working load of radiologists. Recent studies showed that lesions are regularly overlooked or misinterpreted in breast cancer screening programs with MRI [119, 120]. Therefore, computer-aided diagnosis (CAD) systems are required. CAD systems are able to assist radiologists and physicians in analyzing a substantial amount of morphological, kinetic and texture features of breast suspicious findings, reducing the intra- and inter-observer reading variability and ultimately improving the diagnostic accuracy. Clinical evidences have shown that using CAD tools for breast MRI may help to reduce false positives [110, 121, 122]. Normally, a CAD system of breast MRI consists of two stages: detection and diagnosis, which are designed with different focus. The detection stage concentrates on detecting all suspicious lesions, while the diagnosis stage strives for classifying the suspicious lesions into benign and malignant types.

Recently, a few CAD systems focusing on detecting breast lesions in MRI have been reported [123–127]. A convolutional neural networks (CNNs) was employed by Ertas et al. to establish a knowledge-based lesion localization technique, which was applied on a 3D normalized maximum intensity-time ratio (nMITR) map [123]. The method developed by Vignati et al (2011) et al. used subtracted mean intensity projection images over time, which were normalized using the contrast uptake of the mammary vessel [124]. Renz et al. (2012) evaluated a fully automatic detection system that segmented lesions with a hierarchical 3D Gaussian pyramid approach [127]. More recently, Chang et al. (2014) combined kinetic and morphological features to identify focal tumor breast lesions [125]. Gubern-Merida et al. proposed a two-stage machine learning approach using both voxel and region features to locate the lesions and evaluate their malignancy degrees [126].

Compared to detection, more studies were published in the field of diagnosis [128–136]. These works assumed the lesions have been detected either manually or automatically. Features depicting morphologies, kinetic enhancement patterns and textures of the breast lesions were explored to discriminate benign and malignant tumors. Chen et al. used a fuzzy c-means (FCM) clustering-based technique to automatically identify characteristic kinetic curves (CKCs) from breast lesions and extracted the features from representative CKCs in the task of lesion classification [128]. The same group developed a subsequent diagnosis system by adding morphological and texture features that yield better diagnosis performance [129]. Levman et al. evaluated the effects of variations in temporal feature vectors and kernel functions on the the separation of malignant and benign DCE-MRI breast lesions by SVM [130]. Textural kinetic feature expressing the spatiotemporal changes in breast lesion texture was investigated for lesion discrimination in the work proposed by Agner et al. [131]. A new feature characterizing the lesion fractional volume of washout was proposed by Huang et al., and the study shows the washout volume fraction was significantly larger for malignant breast tumors than for benign lesions [132]. Agliozzo et al. developed a CAD system to diagnose mass lesions based on a support vector machine (SVM), which was trained using a combination of morphological, kinetic and spatiotemporal feature set [136]. Hoffmann et al. evaluated the discriminative power of a set of morphological and kinetic descriptors separately, and the Zernike velocity

moments capturing the joint spatiotemporal behaviors of the lesions, to diagnose a collection of nonmass breast lesions [133]. More recently, Wang et al. combined a broader range of characteristic features depicting 3D morphology, shape, texture, and pharmacokinetic model kinetics of breast lesions, resulting in a higher tumor classification accuracy of 91.67% [134]. Yang et al. investigated a new approach to improve diagnostic performance based on the automated detection and analysis of bilateral asymmetry of characteristic kinetic features between left and right breasts [135]. Goto et al. [111] directly compared the diagnostic performance of DCE-MRI (early enhancement) with that of high-spatial-resolution MRI (morphologic features) for the first time. They claimed that in the majority of cases breast lesions were correctly diagnosed merely based on certain morphologic features, which makes those features more important than early enhancement for differentiating malignant breast lesions from benign. The accuracy of 95% and 87% were achieved for masses and non-masses respectively.

In these previous detection and diagnosis CAD systems, most of them were developed and evaluated on relatively small datasets [124, 125] or on a dataset comprising only mass lesions, which does not cover the entire spectrum of malignant breast lesions such as nonmass and foci enhancing lesions [123, 127, 128, 132, 136]. Among the detection systems, the accuracies in term of free-response operating characteristic (FROC) were reported with a large variance. The best FROC value reported was 0.69 false positives (FP) per case at detection rate of 99% on 76 mass lesions [123]. Gubern-Merida et al. achieved a FROC value of 4 FP per case at detection rate of 89% on a larger data set comprising 219 lesions, whereas benign lesions were not included [126]. Most of the diagnosis systems did not integrate a detection stage and assumed that the lesions were identified in advance. A fully automated system incorporating both stages was present by Renz et al, yielding a diagnostic accuracy of 93.5% by testing 141 mass lesions [127]. The two-class classification performance reported in most diagnosis systems was measured by area under the curve (AUC) value, which ranged from 0.74 [133] to 0.96 [136]. The minimal AUC was obtained by testing 84 nonmass lesions, while the maximal AUC was achieved on a data set comprising 73 mass lesions. Discriminating nonmass lesions, most notably ductal carcinoma in situ (DCIS), is challenging in breast MRI reading. Clinical evidences show that the kinetic parameters were more effective in discriminating mass lesions, but failed to discriminate benign from malignant nonmass lesions [137]. Therefore, it is still an open issue but highly on demand to devise a fully automated CAD system that is:

- equipped with both detection and diagnosis stages.
- applicable on all lesion types: mass, nonmass and foci.
- capable of reaching higher detection and diagnosis accuracy with less computational efforts.

4.3. Materials and Methods

In this work, we propose three novel morphological features, describing lesion shapes based on the already existing sphere packing algorithm [138], in combination with Zernike descriptors

[27]. These features lead to a more precise shape based delineation of malignant and benign lesions and thus a higher discrimination accuracy. Beside introduction of novel morphological features, the contribution of this work lies in the feature extraction and selection of the features and the evaluation of their performance in discriminating benign and malignant non-mass-like lesions. All these feature types are integrated as modules into a CAD framework implemented on MeVisLab platform[2]. The processing pipeline depicting each individual module is shown in Fig.4.1. To test the performance of the introduced features, we conducted several experiments using a data set including 86 patients with 106 non-mass-like lesions, among which 68 were pathologically confirmed malignant, and 38 were benign findings. We evaluated the classifier performance using the mentioned features with a Random Forest (RF) classifier in a 10-fold cross-validation scheme, and we achieved an accuracy of 90.56%, precision of 90.3%, and the area under the ROC curve (AUC) value of 0.94.

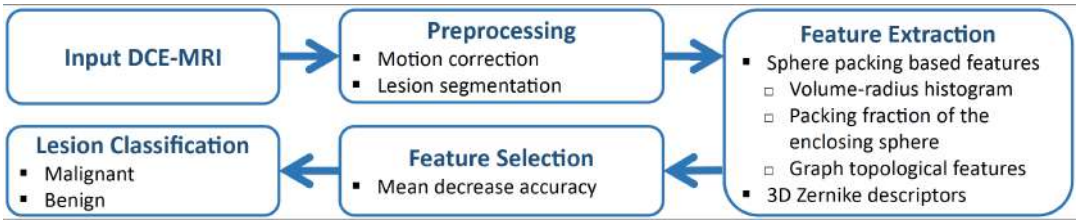

Figure 4.1: The integrated framework comprising preprocessing, feature extraction and selection, and lesion analysis modules.

4.3.1. Imaging Technique and Data Set

The DCE-MRI images were acquired on a 1.5 T scanner (Magnetom Vision, Siemens, Erlangen) in Nijmegen, Netherlands. A dedicated breast coil (CP Breast Array, Siemens, Erlangen) was used in prone patient placement. The pixel spacing differed between volumes with values ranging from 0.625 mm to 0.722 mm. The slice thickness was 1.3 mm, and the volume size was $512 \times 256 \times 120$ voxels. TR and TE were 6.80 s and 4.00 s, respectively, at a 20 degree flip angle. All patients were histologically confirmed by needle aspiration/excision biopsy or surgical removal. Subsequently, the amount of malignant lesions were 68, most of which were diagnosed as DCIS. The rest were diagnosed as invasive ductal carcinoma (IDC), invasive lobular carcinoma (ILC), lobular carcinoma in situ (LCIS) and metastasis. On the other hand, benign histologic findings were found in 38 lesions including fibrocystic changes (FCC), adenosis and hyperplasia. One experienced radiologist retrospectively reviewed the histologic reports and identified the reported lesions. All the lesions were manually segmented with a computer-assistant tool using region-growing and manual correction.

4.3.2. Feature Extraction

A total of four morphological features are proposed, including three novel shape descriptors based on the already existing data structure generated by sphere packing algorithm, plus the

[2]MeVisLab: Medical image processing and visualization platform: http://www.mevislab.de [Accessed on 16 March 2016]

Zernike descriptors. These features are able to efficiently describe the shape and distribution properties of the lesions.

Features Based on Sphere Packing

The morphological features that we explored are extracted using the data structures generated by the sphere packing technique [138], which is a new and promising data representation for several fundamental problems in computer graphics and virtual reality, such as collision detection and deformable object simulation. The algorithm iteratively fills the lesion with a fixed number of non-overlapping spheres starting with the one with the largest possible radius, under the condition that they should completely locate inside the lesion. Next, all the components of the spheres (3D coordinates and radius) are normalized by scaling down to unit length with respect to their minimum and maximum values of the components. Once each lesion is packed by the aforementioned spheres, the following morphological features are extracted.

a) Volume-radius histogram: A histogram in which the radius ranges of internal spheres lie on the x-axis with an arbitrary number of bins and the y-axis is the sum of the sphere volumes with the radius falling into a bin. The sphere packing initially occupies as much volume from the lesion as possible with the biggest possible sphere. Therefore, in benign lesions (with a more regular or round shape), the majority of the lesion space is occupied by a few number of sizable spheres and the rest by considerably smaller ones. In contrast, in malignant lesions, most of the volume is occupied with medium-sized spheres (Fig. 4.2). More detailed description about this feature is given in Sec. 1.2.4.

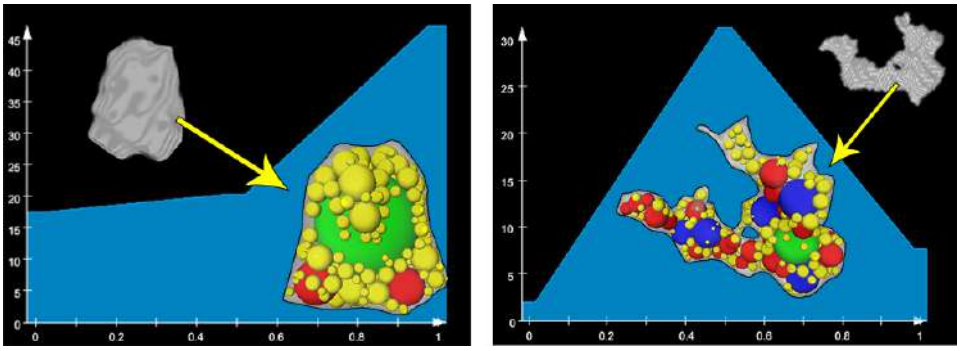

Figure 4.2: The volume-radius histogram (indicated by blue distribution) of two lesions packed with 200 spheres. In benign lesions (left) most of their space is filled with sizable spheres; in malignant lesions (right), medium-sized ones occupy most of the internal space.

b) Packing fraction of enclosing sphere: For each lesion, all the internal spheres generated by the sphere packing algorithm were enclosed by a bigger sphere or ball and the occupied fraction of that is calculated as a feature. It is dimensionless and always less in unit range. Several strategies can be applied to define the center point's location of the aforementioned sphere, such as mean centering of coordinates, placing it between the two most distant spheres, in the center of the largest internal sphere, and the center of the smallest

enclosing ball [139]. In benign lesions (which often have a regular and round shape) the enclosing sphere is more occupied and has less empty gaps than the malignant ones. This fraction is closer to one for benign and is near zero for malignant lesions.

c) Graph topological features: Graph analysis can assist characterizing the complex structures, leading to a better realization of relations that exist between their components [140]. In this work, it is adapted to characterize the spatial arrangement of the lesion's internal spheres. We constructed the graphs, in which the center points of embedded spheres are considered as nodes, and spatial relationship between them as edges with weights according to their distance. Several structures, including Prim's and Kruskal's minimum spanning trees, relative neighborhood, Gabriel, and β-skeleton graphs were examined to gain the best accuracy (Fig. 4.3). Finally, the Gabriel graph showed the highest [141]. Furthermore, spa-

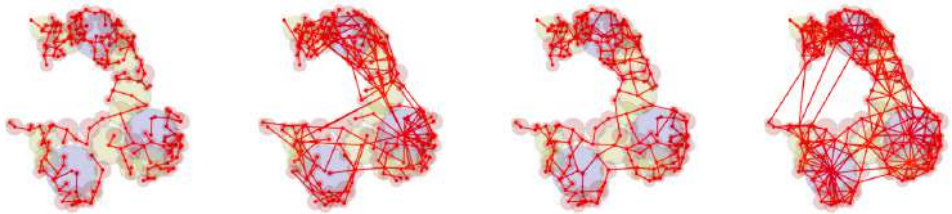

(a) (b) (c) (d)

Figure 4.3: Kruskal's (a) and Prim's (b) minimum spanning trees, relative neighborhood (c), and Gabriel (d) graph structures obtained by connecting 200 internal spheres.

tial constraints such as maximum neighbors (K-Max) were employed to form sub-graphs. We used several cluster validity indices, such as graph compactness indices, edge density, structure linearity [142], Dunn's Index, Davies Bouldin index, MinMaxCut, graph's cohesion [143], modularization quality, global silhouette index, Jaccard Coefficient, Folkes, Mallows, Hubert, and Arabie's indices [144] to extract the global and local graph-based geometrical features. The feature vector is formed by the values of all the aforementioned indices.

3D Zernike Descriptors

Moment-based descriptors have been broadly used for object recognition [27] and shape matching [28] to provide a compact numerical expression of the spatial features. We extracted 3D Zernike descriptors using an extension of spherical-harmonics-based descriptors, presented by Novotni and Klein [35], which captures object coherence in the radial direction. More detailed description about the Zernike features is given in Sec. 1.2.3.

4.4. Results and Evaluations

To evaluate the machine learning methods, the following metrics were used:

- **TP Rate** is the rate of *true positives* in results.
- **FP Rate** is the rate of resulted *false positives*.

- **Precision** is defined as the fraction of elements correctly classified as positive out of all the elements the algorithm classified as positive.
- **ROC Area** is the area under the curve (AUC), the evaluation for the classifier performance.

4.4.1. Classification Results without Feature Selection

To examine the performance of the proposed features, the first evaluation was conducted without applying any feature selection. We adopted all 106 findings comprising 68 malignant and 38 benign lesions. Each lesion was packed with 4000 spheres. The parameter tuning for the aforementioned features was performed by parameter sweeping of values in a multi-dimensional parameter space and applying the following classification on the feature vectors of each combination to get the best parameter values of the highest accuracy (see Table 4.1).

Feature extraction module	Parameters	Best value	No. Features
Volume-radius histogram	Number of bins	50	50
Packing fraction of the enclosing ball	Center point's location	Mean centering	1
Graph morphological features	K-Max, Graph type	No. nodes, Gabriel	19
Zernike descriptors	Maximum order	15	72

Table 4.1: Feature types and their parameter space, plus the optimized values and number of their output features.

For validation of the extracted features, binary classifiers - including Random Forest, Naive Bayes, AdaBoost, and Support Vector Machine (SVM) - were trained with a total of 142 features acquired from the above mentioned methods. For each classifier, a stratified 10-fold cross-validation scheme was applied on the lesions in the data set. The classification power, expressed as AUC is listed in Table 4.2. The best results were achieved with the RF classifier.

Classifier type	TP Rate		FP Rate		Precision		AUC	
	ben.	mal.	ben.	mal.	ben.	mal.	ben.	mal.
Random Forest	0.78	0.91	0.08	0.21	0.83	0.88	0.90	0.90
Naive Bayes	0.86	0.44	0.55	0.13	0.46	0.85	0.66	0.81
AdaBoost	0.65	0.89	0.10	0.34	0.78	0.82	0.83	0.83
Support Vector Machine	0.68	0.29	0.70	0.31	0.35	0.62	0.48	0.48

Table 4.2: The TP and FP rates, precision, and AUC values from classification results of different lesion types using four different classifiers (ben. is benign and mal. is malignant). Here the RF classifier outperforms the other three.

4.4.2. Classification Results with Feature Selection

For the machine learning algorithms, it is important to use feature reduction mechanisms to decrease over-fitting of the training data. Taking advantage of Mean Decrease in Accuracy (MDA) and Mean Decrease GINI (MDG) [145] as variable importance criteria, from a total of

142 features in features set, the top 30 most effective ones were selected for evaluation. Using the RF classifier, MDA ranking showed a higher accuracy than MDG. Among the top features rated by MDA, *volume-radius histogram*, *packed fraction of enclosing ball*, *graph features*, and *Zernike descriptors* features gained the highest order respectively. It should be mentioned that, among those features, only three graph features of *linear structure*, *new compactness index* Cp^*, and *Dunn's index* [144] (Eq. 4.1) appeared on the top 30 MDA features.

$$Dunn(C) = \frac{d(C_i, C_j)}{\mathrm{diam}(C_h)} \quad , \quad Cp^* = \frac{\sum_{i=1}^{N-1} \sum_{j=i+1}^{N} \mathrm{sim}(v_i, v_j)}{N(N-1)/2} \tag{4.1}$$

Figure 4.4 shows the variable importance plot obtained from RF. It can be seen that among the 30 most important features in both MDA and MDG rankings, the first place belongs to the features of *volume-radius histogram* method (black features). *Zernike moments* features are in the second place of importance, especially in MDA ranking. The third rank belongs to the *graph features*, including only three features of *New Compactness Index CP**, *linear structure* and *Dunn's Index*. As not many *spherical shape histogram* features can be seen among the most important features, they place fourth.

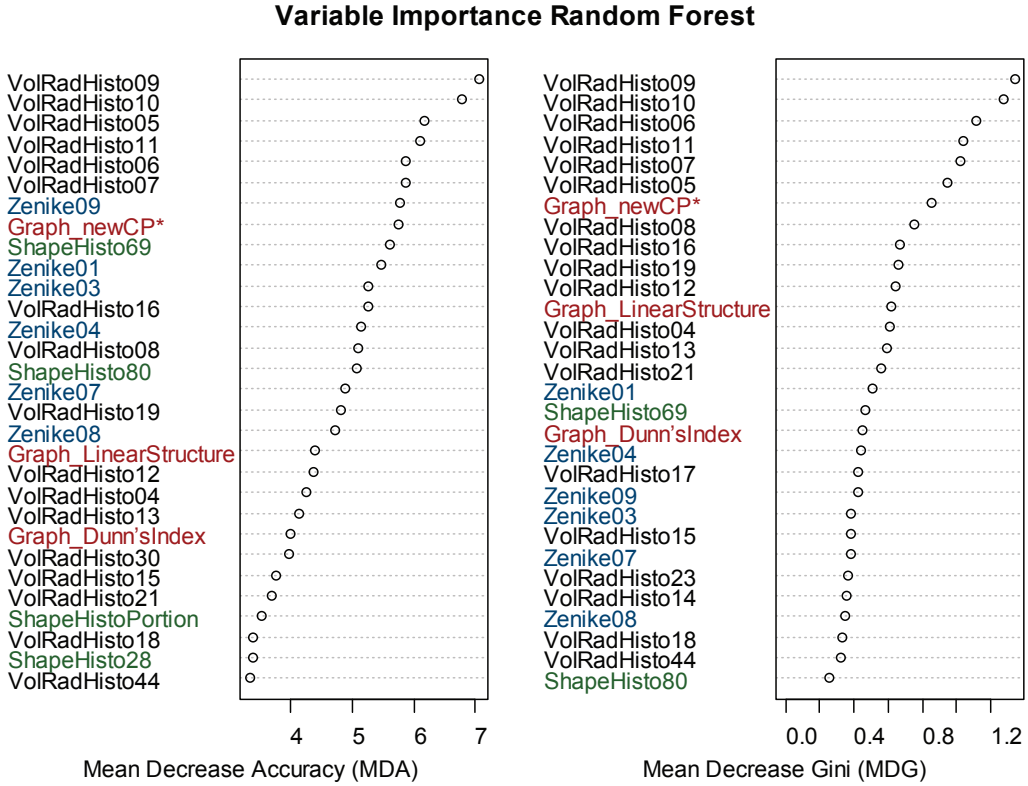

Figure 4.4: Variable importance in Random Forest evaluation. On left, the *Mean Decrease Accuracy* ranking depends on how well the model actually predicts. On right, the *Mean Decrease Gini* ranking reflects the overall goodness of fit. The two indices measure different things, but they are related.

Furthermore, applying the Principal Component Analysis (PCA) feature selection was investigated to reduce the dimensionality even more and find the best correlation between the

features. However, no improvement was seen in the evaluation results. Table 4.3 shows the classification results of the RF using 10-FCV before and after applying MDA, MDG, PCA over MDA, and PCA over MDG.

Feature selection	No. features	TP Rate		FP Rate		Precision		Accuracy		AUC	
		ben.	mal.	ben.	mal.	ben.	mal.	ben.	mal.	ben.	mal.
No selection	142	0.789	0.912	0.088	0.211	0.833	0.886	13.2%	86.79%	0.907	0.907
MDG	30	0.816	0.956	0.044	0.184	0.912	0.903	9.43%	90.56%	0.935	0.935
MDA	30	0.816	0.956	0.044	0.184	0.912	0.903	9.43%	90.56%	0.94	0.94
PCA on MDG	5	0.763	0.941	0.059	0.237	0.879	0.877	12.26%	87.73%	0.935	0.935
PCA on MDA	5	0.816	0.926	0.074	0.184	0.861	0.900	11.32%	88.67%	0.936	0.936

Table 4.3: The classification results of the RF using 10-FCV before and after applying MDA and MDG rankings, plus PCA on them (ben. is benign and mal. is malignant).

To sum up, the proposed method in differentiating between malignant and benign lesions, achieved the accuracy of area under the ROC curve of 0.936 using Random Forest classifier. The processing time for the trained classifier to provide the results is around 4.2 seconds using a 3.5 GHz Intel CPU and a GeForce GTX 680 graphics card.

Figure 4.5 shows some of samples in evaluation which are correctly classified ((a), (b), (c), (d)), along with the cases which are classified incorrectly ((e), (f)). Several illustrations can be seen in the figure which represent different steps of feature extraction process.

4.5. Discussion

This paper focuses on utilizing the sphere packing (non-overlapping and non-uniform radii) to develop a set of novel morphological features to classify breast non-mass-like lesions. Under the assumption that malignant lesions tend to have irregular shapes and margins compared to benign lesions (which have more regular and round shape), the sphere packing based features can effectively capture the shape differences and thus increase the discrimination accuracy. All the proposed features are translation, rotation, and scaling invariant, since they either are coordinate free features, or because we normalized the data at first.

To our knowledge, this is the first time that such an shape representation has been investigated for classifying non-mass lesions in MRI. One advantage of sphere packing is that it can describe volumetric shapes more concisely than a voxel representation or mesh surface. In addition, it allows for deriving additional meta-representations (e.g. proximity graphs and skeletons), which we investigated in this work too. Among many other insights, we discovered that the volume-radius histogram is a particularly efficient shape descriptor to classify non-mass breast lesions into benign and malignant.

To reduce the redundancy of the extracted features, we investigated the application of two feature selection techniques: MDA and PCA to decrease the over-fitting of the data. The classification performance of these features was tested with a data set of 106 non-mass-like lesions collected from 86 patients. Two experiments comparing the performance with and without feature selection were conducted. The classification accuracy, using different classifiers was

evaluated. The best AUC value of 0.94 was achieved when using MDA selected features with a RF classifier and 10-FCV scheme. The experiment demonstrated the discriminative power of our proposed features and their potential to increase the diagnostic accuracy of a CAD system. Reducing the number of features to 30 using MDA leads to very low over-fitting and unbiased results at the end. In the future, we will focus on further improving the calculation efficiency of these features and also investigate more features based on the sphere packing.

We acknowledge that there are limitations in our study. To the best of our knowledge, there is no validated data set for non-masses publicly available that we can perform a benchmark on and compare the results with others. Therefore, we used the aforementioned data set that was labeled meticulously by radiologists, which makes it the best-suited data set for our work. The result could differ from what we have achieved when a different dataset is given.

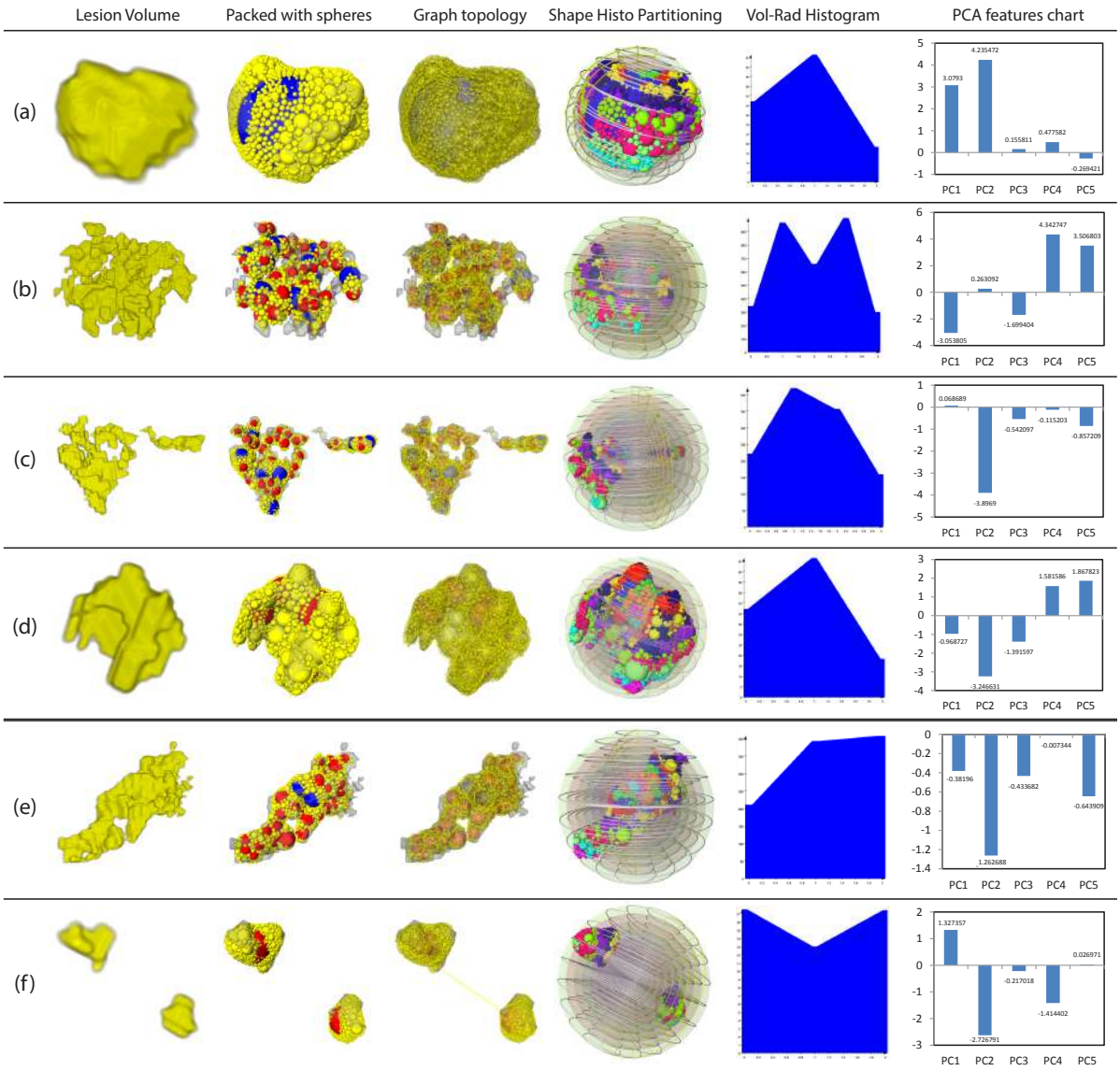

Figure 4.5: Classification evaluation sample data. In this figure several steps of feature extraction are illustrated for different benign and malignant cases. From left to right: the original lesion volume, the packed lesion geometry with spheres, the graph topology based on connecting the center points, enclosing spherical wire frame that partitions lesion's surrounding space to acquire elements (embedded spheres) distributions, volume-radius histogram, and the corresponding chart based on the Principal Components (PC) attributes of the lesion are represented. (a,b) show two examples of *true positive* cases which their types are benign and they are classified as benign too. (c,d) show two examples of *true negative* cases which their types are malignant and they are classified as malignant too. (e) shows an example of *false negative* case which its type is malignant but it is classified as benign. (f) shows an example of *false negative* case which its type is benign but it is classified as malignant.

5

Nipple Detection Using Tube-like Shape Descriptor

Acknowledgment

I would like to give my sincere gratitude to my colleagues in MEVIS: Fabian Zoehrer and Dr. Joachim Georgii, who are always good consultants for algorithm understanding and development. They have generously shared me with a lot of background knowledge about the 3D breast ultrasound, which is a relatively new imaging modality. Additionally, I am also grateful to the work of Dr. Albert Gubern-Merida (Nijmegen, Netherlands), Dr. Ritse Mann (Nijmegen, Netherlands) and Dr. Julia Müller (Mediri, Germany), who have kindly provided the medical image data with manual annotation and assisted me to evaluate the algorithm.

Publications

The algorithm description, implementation, and evaluation of breast nipple detection in 3D ultrasound were published in the following scientific papers:

- **Wang L**, Böhler T, Zöhrer F, et al. (2014) A hybrid method towards automated nipple detection in 3D breast ultrasound images. 36th Annual International Conference of the IEEE Engineering in Medicine and Biology Society (EMBC), pp. 2869-2872.

- **Wang L**, Böhler T, Zöhrer F, et al. (2014) Fully Automated Nipple Detection in 3D Breast Ultrasound Images. Breast Imaging: 12th International Workshop (IWDM), pp 64-71

- **Wang L**, Zöhrer F, Friman O, Hahn HK (2011) A fully automatic method for nipple detection in 3D breast ultrasound images. Comput Assist Radiol Surg (CARS) 6:S191–S192

5.1. Introduction

In complement to mammography, automated breast ultrasound (ABUS) emerges as an important imaging modality applied in breast cancer screening, especially on patients with dense breasts where the sensitivity of mammography is poor. Mammography suffers poor sensitivity in screening patients with dense breasts. Recent studies reported that supplemental ABUS increases detection rate of small and mammography occult breast cancers [146, 147]. In clinical diagnostic procedure, nipple position provides useful diagnostic informations in reading automated 3D breast ultrasound (ABUS) images. Hence, the interpretation of ABUS data has gained significant interests in computer-aided diagnosis (CAD) of breast cancer [148, 149].

In a CAD system, nipple position is an important reference marker which allows for localizing the quadrants of breast lesions. On the other hand, the nipple position can be used to measure the distance between the breast lesions and the nipple. Furthermore, given data acquired in other imaging modalities, such as mammography, MRI or tomosynthesis, registering images across multiple modalities requires nipple positions as effective reference landmarks to improve registration accuracy. However, the presence of speckle noises caused by the interference waves and variant imaging directions in ultrasonography challenge the task of automatic identification of the nipple position.

In this chapter, the application of Laplacian-based and Hessian-based shape descriptors is presented to demonstrate how these descriptors have been used in the task of automatic detection of nipple position in 3D ultrasound images. The algorithm description and performance evaluation are organized in the following sections: First, section 5.3.1 introduces a fast and automated algorithm to detect nipples in 3D breast ultrasound images. The method fully takes advantages of the consistent characteristics of ultrasonographic signals observed at nipples and employs a multi-scale Laplacian-based blob detector to eventually identify nipple positions. Second, to combine the power of Hessian and Laplacian shape descriptors, in section 5.3.2, a hybrid fully automatic method to detect nipple positions in ABUS images is presented. The method extends the multi-scale Laplacian-based method that we proposed previously, by integrating a specially designed Hessian-based method to locate the shadow area beneath the nipple and areola. Subsequently, the likelihood maps of nipple positions generated by both methods are combined to build a joint-likelihood map, where the final nipple position is extracted.

5.2. Related Works

Compared with other commonly used imaging modalities, such as mammography, 2D ultrasound, MRI or Ct, 3D breast ultrasound is a relatively new imaging sequence. Therefore, only a few groups are dedicated in the development of automated processing algorithms or tools, including nipple detection. After a rigorous literature review on this topic, to the extent of our knowledge, only one scientific publication was found, which is the work of Moghaddam et al. [150]. In their contribution, a machine learning based approach was proposed. First, all images were normalized to eliminate the intensity variation to improve the feature expression ability. Then, multi-scale blobness features were extracted and fed to a gentle boost classifier

for training. To assess the performance of the trained classifier, a total of 294 different 3D breast ultrasound images were used for testing. As a result, the method could accurately located the nipple in 90% of the anterior-posterior views and 79% of other views. It was noticed that the proposed method was sensitive to the image acquisition view. Additionally, attributed to trait of machine learning techniques, the training procedure has to be rebuilt when a new data set is collected.

5.3. Materials and Methods

5.3.1. Nipple Detection Based on Laplacian Shape Descriptor

The method is comprised of several pre-processing steps to find the region of interest (ROI) of the nipple and build a binary mask that excludes background. Then, a multi-scale blob detector is employed to detect the nipple tip point. A schematic overview of the entire detection workflow is illustrated in Fig. 5.1.

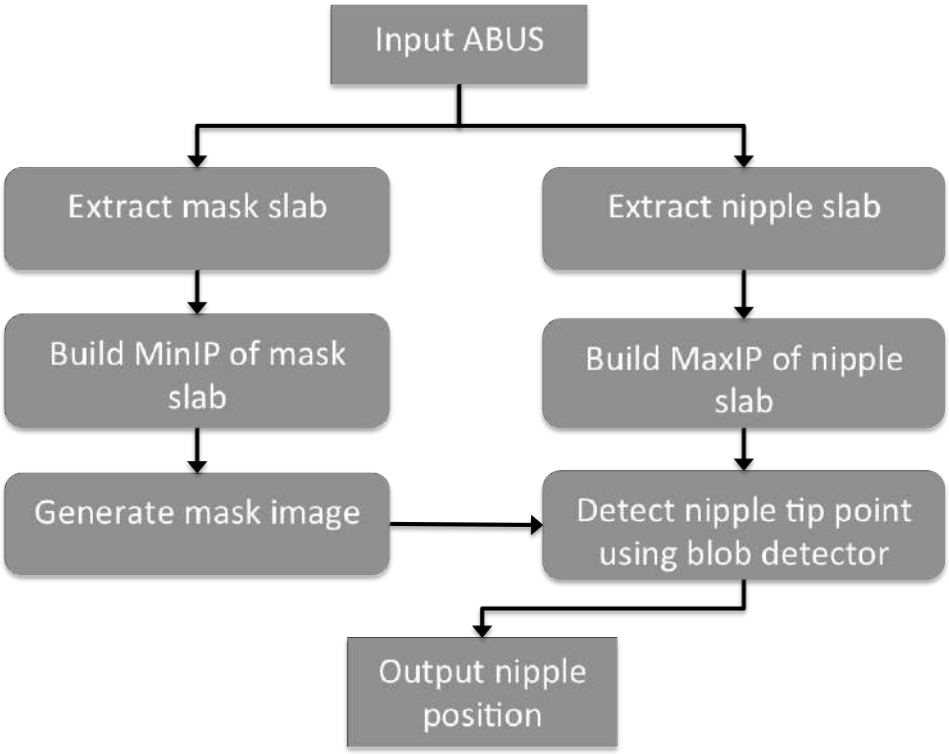

Figure 5.1: A schematic overview of the detection workflow.

Pre-processing

Normally, ABUS volumes are scanned in transversal planes. In pre-processing step, we re-formatted all images to coronal planes, because the features extracted from coronal planes will be analyzed in subsequent steps. Depending on different scanning views, the ultrasound transducer panel touches and compresses the target breast in different ways. Usually, in coronal planes, the nipple is imaged in the center of an ABUS volume scanned in AP view, whereas other views, such as MED or LAT, can push the nipple to peripheral imaging borders. One

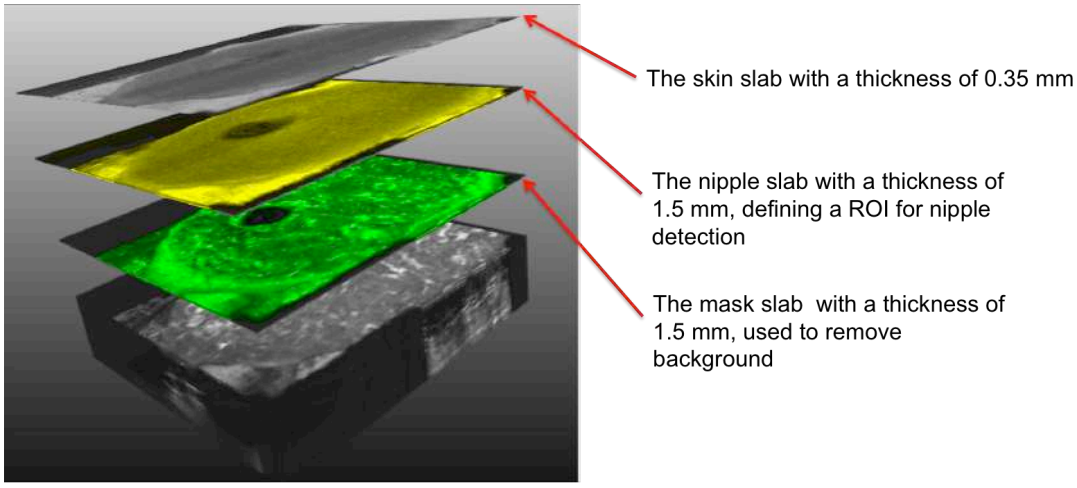

Figure 5.2: 3D visualization of the extracted nipple slab (yellow) and mask slab (green)

of the key anatomical observations is that the nipple is always near to the transducer panel, despite its centric or peripheral positions. Therefore, the nipple always appears in a bunch of anterior coronal slices that are not far away from transducer. Based on this observation, a nipple slab with the thickness of 1.5 mm enclosing a pile of anterior coronal slices is extracted, which starts with the slice with a distance of 0.35 mm to the transducer panel (see Fig. 5.2). The nipple slab defines a ROI, where subsequent nipple detection algorithms are applied to localize nipple tip points. In addition, to get rid of background, another mask slab with the same thickness following the nipple slab is extracted (see Fig. 5.2).

Then, the minimum intensity projection (MinIP) image over all slices of the mask slab is calculated, resulting in a 2D projected image where the intensities of background areas are almost zero (Fig. 5.3(b)(1)). By a simple thresholding process, a binary mask containing the pixels with intensities larger than 1 is obtained. Followed by a morphological closing operation with a kernel size 5×5, possible holes and gaps of the binary mask are filled (Fig. 5.3(b)(2)). Similarly, the maximum intensity projection (MaxIP) image of the nipple slab is computed, resulting in a 2D map, in which the nipple tip point will be searched for (Fig. 5.3(b)(3)). To reduce computational expense, the MaxIP image of the nipple slab and the mask image are down-sampled to a lower in-plane resolution defined by a fixed scale factor: 0.125×0.125. To eliminate disturbing structures, the MaxIP image is further smoothed by a Gaussian kernel with $\sigma = 3$ (Fig. 5.3(b)(4)).

Blob Detection

A key observation is that the nipple appears as a 2D dark blob structure in the MaxIP image of the nipple slab, which can be enhanced by a commonly used blob descriptor: Laplacian of Gaussian filter (LoG) [151]. Given a MaxIP image $I(x, y)$ and a Gaussian kernel at scale σ: $g(x, y, \sigma)$, the MaxIP image convolved with multiple Gaussian kernels with variant sizes leads to a scale-space representation: $L(x, y, \sigma) = I(x, y) \star g(x, y, \sigma)$ [152]. The Laplacian operator $\nabla^2 L = L_{xx} + L_{yy}$ is then calculated at each scale σ, which produces strong negative response in dark blob regions (Fig. 5.3(b)(5)). We adopted a multi-scale LoG filter with variant

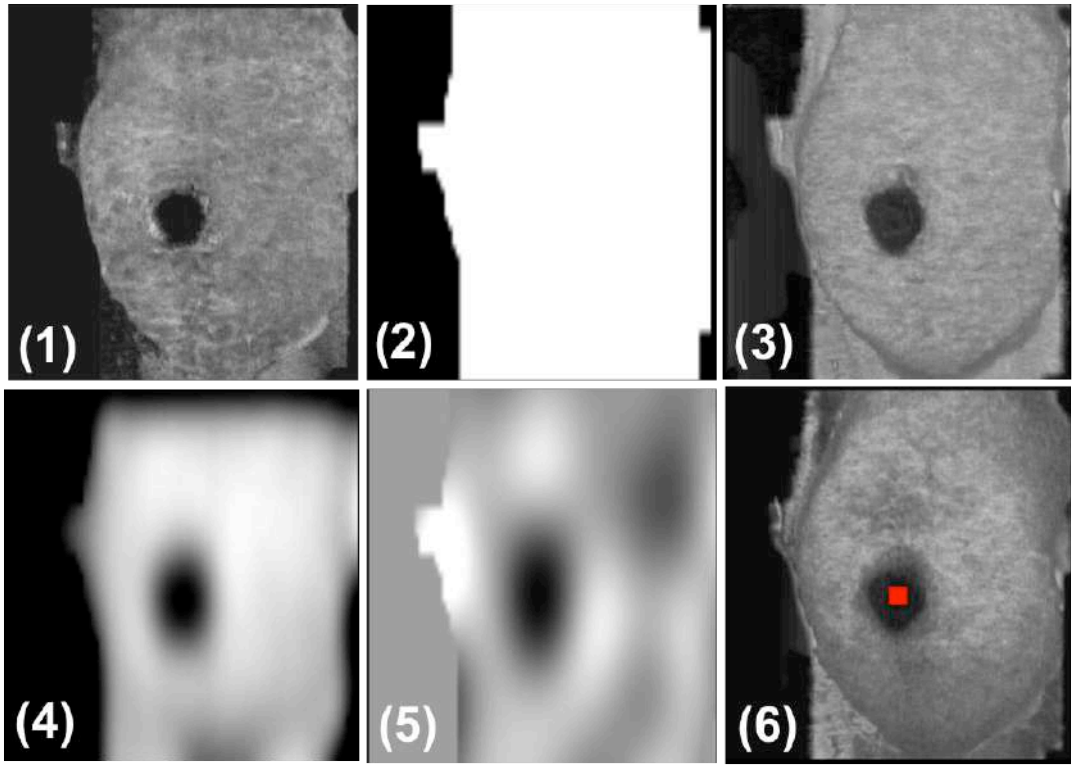

Figure 5.3: workflow of blob structure detection: (1) MinIP image of the mask slab; (2) generated binary mask; (3) MaxIP image of the nipple slab; (4) down-sampled and smoothed MaxIP image; (5) response of LoG filter at scale $\sigma = 6$; (6) extracted global minima and detected nipple position (red).

σ ranging from 1.5 to 15 mm with a step size of 1.5 mm. The optimal scale that delivers the global minimal response is selected, and the corresponding 2D coordinate in the MaxIP image is recorded as the nipple position in X and Y dimensions. To fetch the Z dimension, we projected the 2D point back to the middle slice of the nipple slab, which reconstructs the 3D position of the nipple (Fig. 5.3(b)(6)).

5.3.2. Nipple Detection Based on Hybrid Shape Descriptor

The hybrid method combines the detection power of both Hessian detector and Laplacian detector. The tube-like shadow observed beneath nipple and areola in ABUS data inspires the idea of applying a 3D Hessian-based tubular filter to enhance the shadowing region, resulting a Hessian-based likelihood map. Meanwhile, the multi-scale Laplacian blob detector builds a Laplacian-based likelihood map. Multiplying these two maps ends up with a joint probability distribution of nipple position, where the most probable nipple position can be estimated. A schematic overview of the proposed hybrid method is given in Fig. 5.4.

Hessian-based Nipple Detection

Due to the acoustic properties of the nipple and areola, the strength (amplitude) of echo signals received from tissues beneath nipple and areola is normally weak. Hence, a tube-like structured shadow beam is formulated beneath the nipple and areola. Normally, the shadow beam attached to the nipple and areola starts from the first several anterior slices and extends

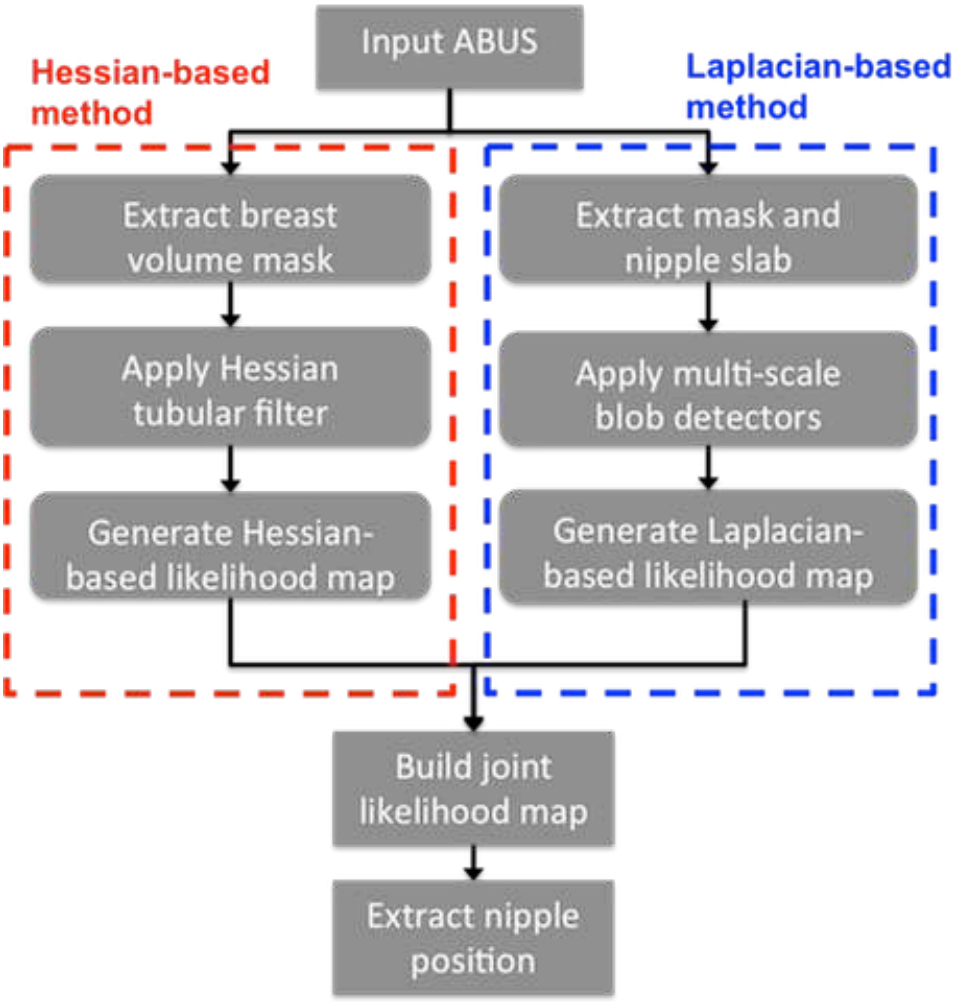

Figure 5.4: Schematic workflow of the hybrid detection method

to the posterior slices in coronal view (see Fig. 5.5). In comparison to other dark regions with variant lengths and shapes originated by other tissues and lesions, it almost traverses through the breast and reaches to chest wall. Based on these observations, a Hessian-based tubular filter is designed to locate the nipple shadow beam, from which the corresponding nipple position can be identified.

Hessian-based filters have been widely employed to analyze local structures of 3D images. Eigen values of the Hessian matrix present different patterns for various geometrical structures, such as blob-like, tube-like or sheet-like objects [153]. Assuming the Eigen values ordered in $\lambda_1 \geq \lambda_2 \geq \lambda_3$, a dark tube-like structure conforms to a pattern of $\lambda_3 \approx 0, \lambda_1 \approx \lambda_2 \gg 0$, where the first and second Eigen values are positive and larger than 0 (see Fig. 5.5). For other geometrical structures, the second Eigen values of sheet-like and noise structures are approximately close to 0, and all the Eigen values of blob-like structures are equally larger than 0 [17].

To exclude background, a mask volume is built by analyzing the intensity histogram of the input ABUS volume. The quantile of $25th$ percent is chosen as the minimal intensity to eliminate background air (see Fig. 5.6(b)). Then, the Eigen values of each voxel is computed

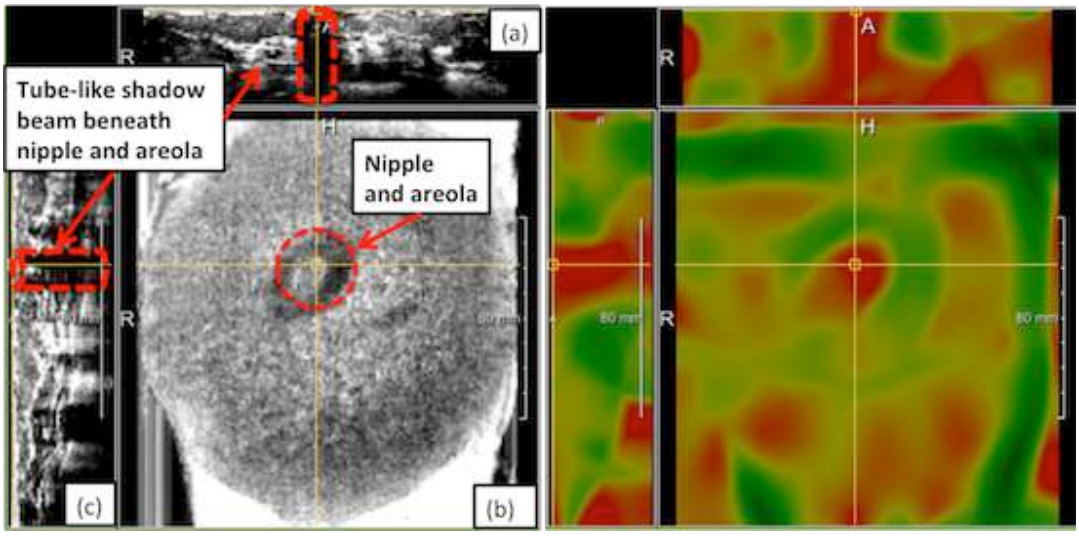

Figure 5.5: (Left) Shadow beam beneath nipple and areola in orthogonal views: (a) axial (b) coronal and (c) sagittal; (Right) A heat map visualized the computed second largest Eigen value λ_2 (red represents larger values)

(see Fig. 5.6(c)). To build a fast and efficient tubular filter to enhance nipple shadow beam, we chose a simplified measure S that accumulates all the second larger Eigen values along the depth direction in coronal view: $S = \Sigma_1^n \lambda_2$ (Fig. 5.6(d)), where n is the depth dimension. After integral over the depth dimension, a 2D likelihood map scaled between 0 and 1 is built, from which the maxima is extracted which expresses the projected 2D position of the center line of the nipple shadow beam. Ideally, this position represents the nipple position as well, as the center of the nipple correlates with the center line of shadow beam. Finally, the position of the maxima is projected back to the top anterior location which is 0.75 mm to the first coronal slice, and recognized as the final detected 3D nipple position. It is noticed that blob-like structures also yield a larger λ_2. However, due to the limited amounts and scales of the blob-like structures presented in volumes, they do not produce significant larger accumulation on the likelihood map after integrating over the depth dimension.

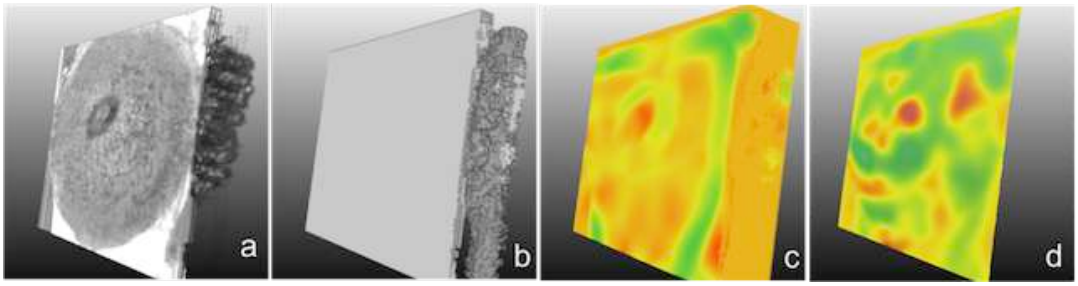

Figure 5.6: Workflow illustration of Hessian-based method: (a) a 3D input ABUS volume; (b) the mask volume; (c) the heat map of λ_2 (red represents larger values); (d) the accumulated response of Hessian tubular filter: S.

Hybrid Detection Method

Both Hessian-based and Laplacian-based methods yield two likelihood maps indicating the probability distribution of nipple position. Therefore, it is natural to combine them to estimate

a hybrid joint distribution, which is potentially able to improve detection accuracy. Since the original Laplacian response conveys negative values to the dark blob region, the sign of its value is inverted. Then, both response images are scaled in the range of $[0, 1]$ to estimate probability distribution (Fig. 5.7(a,b)). Eventually, the two likelihood maps are multiplied, resulting in a joint map (Fig. 5.7(c)), where the most probable nipple position is extracted (Fig. 5.7(d)).

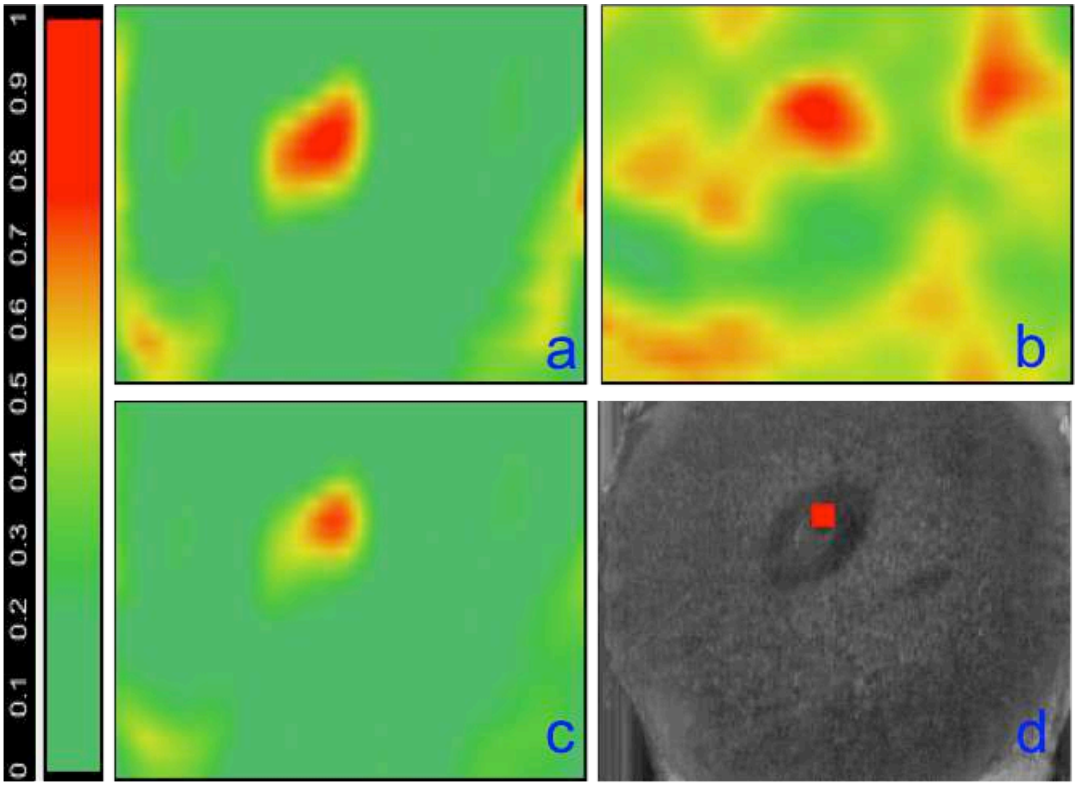

Figure 5.7: (a) the likelihood map built by Laplacian method; (b) the likelihood map built by Hessian method; (c) the hybrid likelihood map; (d) the maxima extracted from hybrid map, indicating most probable nipple position.

5.4. Results and Evaluations

5.4.1. Dataset

Compared with our previous study [154], we enhanced the data set with more collected scans, including 926 ABUS image sequences acquired by Siemens S2000 ABVS systems as part of the iMODE-B (imaging and molecular detection for breast cancers) study at the University Breast Center Franconia, University Hospital Erlangen, Germany. The study was approved by the Ethics Committee of the Medical Faculty, Friedrich-Alexander University Erlangen Nuremberg and all patients gave written informed consent. Breasts were scanned in five possible imaging views: anterior-posterior (AP), medial (MED), lateral (LAT), superior (SUP) and inferior (INF) (as shown in Fig. 5.8). Acquisitions in different views involve different compressions of breasts, which leads to variant imaging characteristics of nipples. The presence of nipples varies according to different acquisition views. The locations of nipples were clearly identified

in AP views and distributed in peripheral regions in other views. For several extreme cases where the nipples were pushed to the image borders, a portion of the nipples were still visible. The in-plane image resolution of the collected ABUS volumes is 719×565 with a slice number of 318, associated with in-plane voxel spacing of 0.2×0.07 mm and slice thickness of 0.525 mm. To validate the performance of our method, an experienced radiologist annotated all images by pinpointing the tip points of nipples (a tip point is the most anterior point of a nipple in coronal planes), serving as the ground truth.

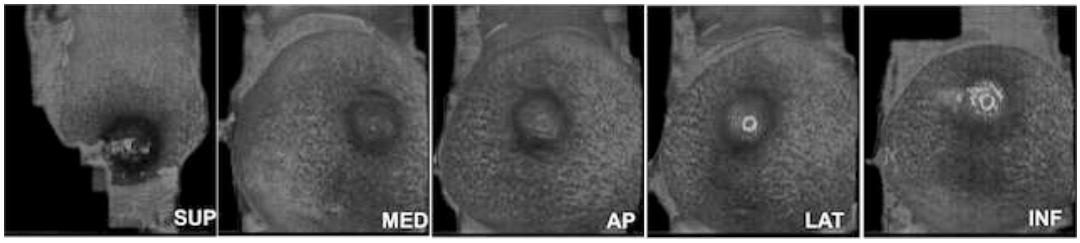

Figure 5.8: ABUS scans for the left breast of a patient, illustrating nipple positions in different imaging views: AP, MED, LAT, SUP and INF.

5.4.2. Evaluation of Laplacian Filter

We ran the algorithm on 113 ABUS volumes in the testing data set. The average computation time per ABUS volume was 0.6 seconds on a machine with a 3.7GHz CPU. The detection accuracy was quantitatively measured by calculating the root-mean-square distance in mm (RMSD) between detected nipple positions and annotated ground truth in 3D. Statistical analysis of the distance error was conducted, obtaining a result of 6.6 ± 8.9mm ($mean \pm std$). Figure 5.9 demonstrates the histogram analysis of RMSD, showing the majority of distance deviation falls in the interval of $(0, 15)$ mm. Moreover, the distribution of detection rates against variant tolerant thresholds of distance errors is depicted in Fig. 5.9. It is noticed that nearly half of the test images achieved a distance error less than 4 mm, and more specifically when setting tolerance as 8 mm, where is the average size of the nipples in our database, nearly 78% of test images were correctly detected. Nevertheless, the method might fail when nipples were pushed to image borders during acquisition and imaged partially in extracted nipple slabs (see Fig. 5.10). The LoG filter was proved to perform stably in detecting global minimal response that is supposed to associate with the target nipple position.

5.4.3. Evaluation of Hybrid Filter

The proposed method was tested on 926 healthy and pathological ABUS volumes. The average computation time per ABUS volume was 5 seconds on a machine with a 3.7GHz CPU. The detection accuracy was quantitatively measured by calculating the root-mean-square distance in mm (RMSD) between detected nipple positions and annotated ground truth in 3D. Statistical analysis of the distance error were conducted, obtaining a result of 7.08 ± 10.96 mm for the hybrid method. To demonstrate the improvement of combining both methods, the performance of each single method was tested separately, resulting in 8.18 ± 15.64 mm for Laplacian-based

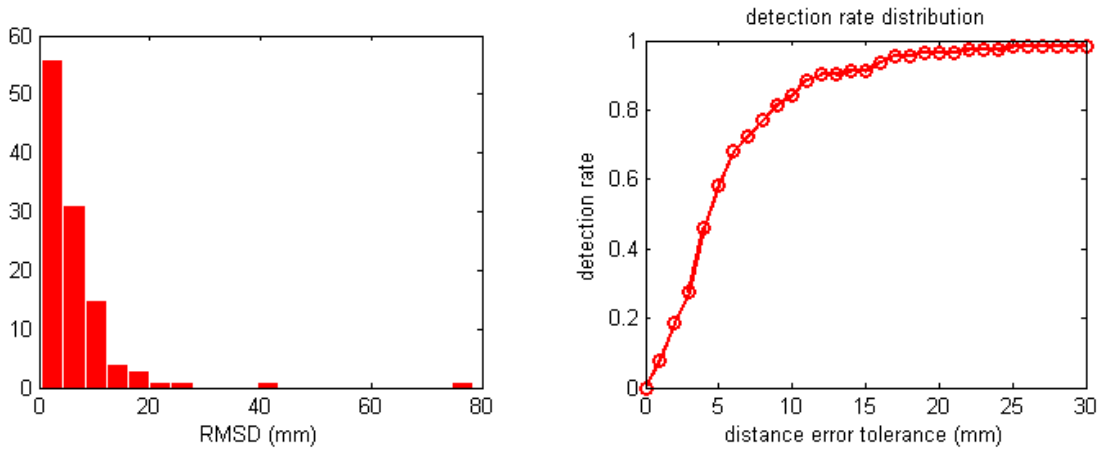

Figure 5.9: Histogram analysis of RMSD (left). Detection rates against variant tolerant distance errors (right).

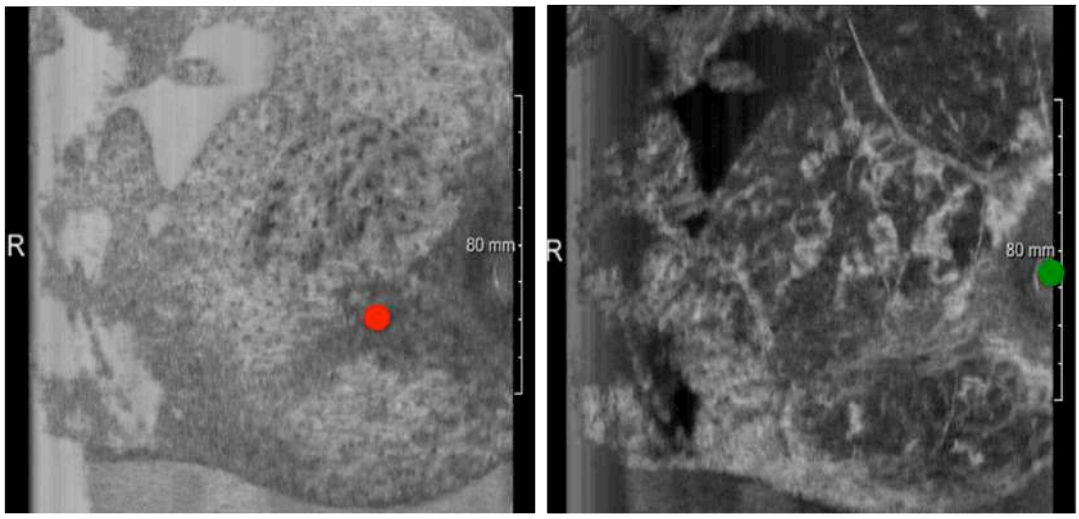

Figure 5.10: A failed example overlaid with the annotated marker (green) and the detected nipple (red), notice the nipple is imaged partially and very close to borders.

method and 13.67 ± 20.73 mm for Hessian-based method (see Fig. 5.11). Figure 5.12 demonstrates the histogram analysis of RMSD, showing the majority of distance errors of all methods fall in the interval of $(0, 10)$ mm. The hybrid method outperforms each single method. Moreover, the distribution of detection rates against variant tolerant thresholds of distance errors is depicted in Fig. 5.13. It is noticed that the hybrid method obtains higher detection rate when tolerant error is larger than 7 mm. More specifically, when setting tolerance as 10 mm, which is the average size of nipples in our database, nearly 88% of test images were correctly detected by hybrid method, which again exceeds 85% of Laplacian-based method and 74% of Hessian-based method.

By investigating the outliers with large errors, we find that the method might fail when nipples were pushed to image borders during acquisition and imaged partially in extracted nipple slabs. Besides, both the LoG and Hessian filters were proved to perform stably in detecting target nipple position. However, when the breast mask extracted from mask slab is

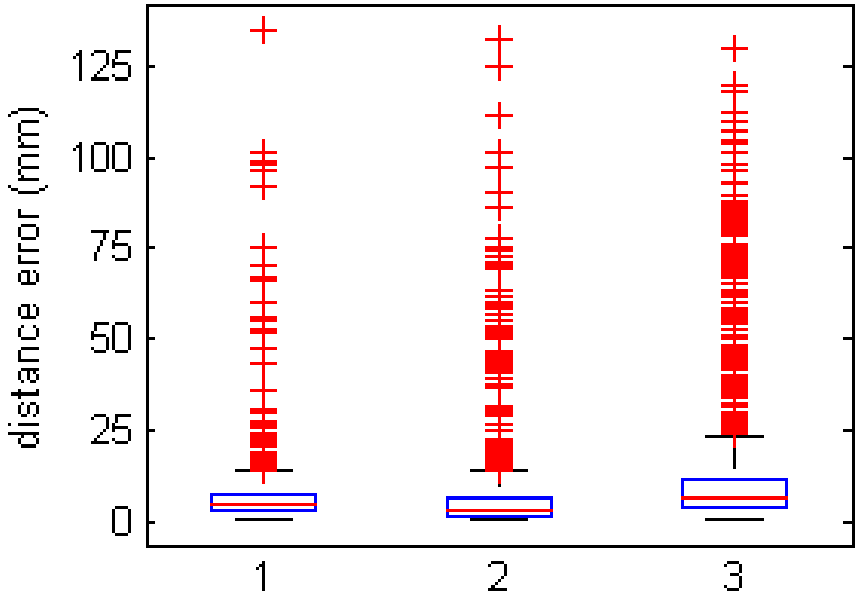

Figure 5.11: Boxplot of distance errors associated with hybrid (1), Laplacian-based (2) and Hessian-based (3) methods.

not sufficiently accurate, or a lesion that mimics the features of the nipple appears in the nipple slab, they might be attracted by spurious structures and recognize them as nipple positions.

5.4.4. Performance Comparison with Other Methods

As introduced in Section 5.2, Moghaddam et al. proposed an automatic nipple detection algorithm based on machine learning technique [150]. We have established a comparison study to validate the performance of both methods.

Test Data Set

The comparison study independently collected 345 ABUS volumes, which were not used in the previous evaluations for all the methods. The reference nipple positions were annotated by an experienced technician, but finally validated or corrected by expert radiologists.

Evaluation and Results

In [150], the classifier was trained using a set of blobness features and finally generated a likelihood map indicating the probability map of the nipple position. There are two strategies to extract the nipple position out of the likelihood map:

- Smooth the likelihood map and pick the global maximum (denoted as "LocalMax").
- Threshold the likelihood map at 0.7 and take the gravity center of the largest connected component as the nipple position (denoted as "CCA")

Since our method is based on the Laplacian and Hessian filters, it was denoted as "LapHess". The nipple position of each ABUS volume was detected by these three methods. The distance

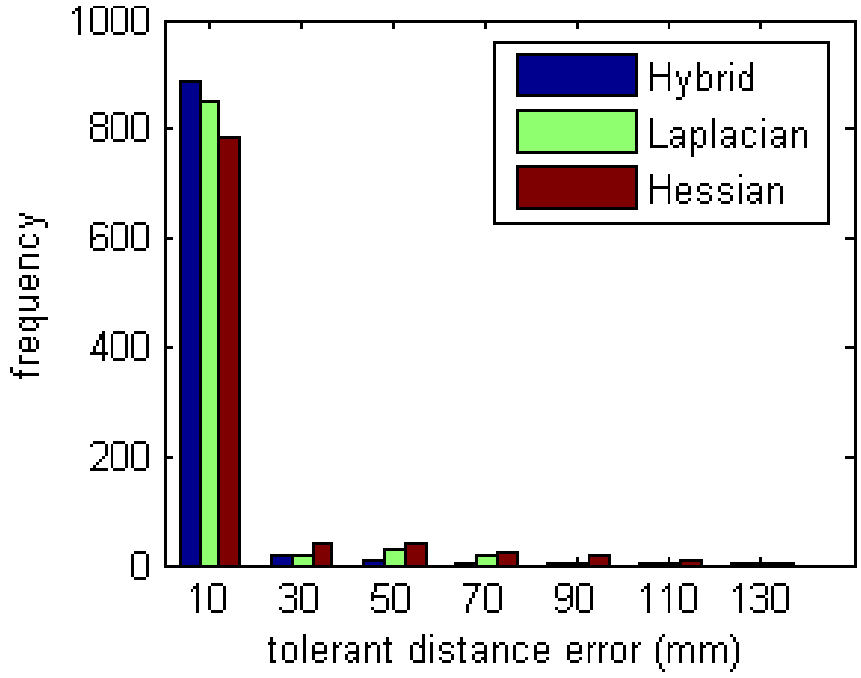

Figure 5.12: Histogram distribution of RMSD calculated for each method.

Table 5.1: Detection rates of the methods

Method	**Number of Correct Detection (total 345)**	**Detection Rate (%)**
LapHess	253	73
LocalMax	183	53
CCA	220	64

error between the detected and reference nipple positions was computed. The tolerance of distance error was set to 8 mm, which is the mean nipple radius. The detection accuracy of the three methods was listed in Table 5.1, based on which it was shown that the LapHess method outperformed other two methods in terms of the detection accuracy.

Since two different searching strategies were used for the nipple position based on Moghaddam's approach, it is necessary to test if there two strategies have correlated performance, i.e., if the distance error of LocalMax correlates with that of CCA. Figure 5.14 plotted the distance error of all test cases for both methods, from which we can see these two detection strategies correlate quite tightly. The same type of correlation plots of LapHess against CCA and LapHess against LocalMax were also drawn in Fig. 5.15 and in Fig. 5.16, respectively. It is observed that the LapHess method does not correlate with other two methods, which means they could potentially compensate the performance of each other. To further prove this observation, we plotted the cases which have at least 20 mm distance error derived at least by one algorithm in Fig. 5.17, which has shown that the errors differ strongly for the different algorithms as shown in the histogram. Many cases with a small error with LapHess approach (high blue bar) have quite large errors with the LocalMax or CCA approaches and

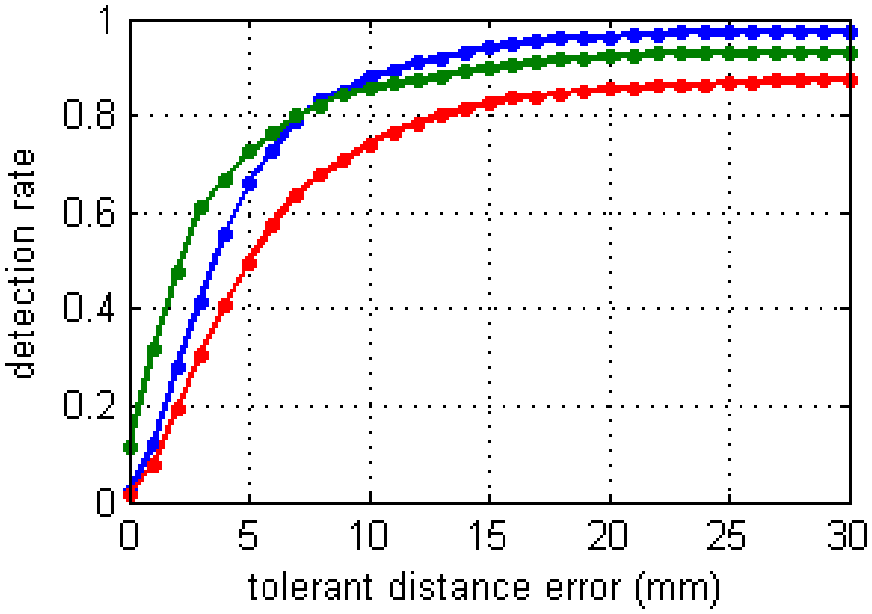

Figure 5.13: Detection rates against variant tolerant distance errors drawn for each method.

vice versa, which means the detection performance has a great potential to be increased by combining the LapHess with LocalMax or CCA methods.

Confidence Index

One common property of these methods is that they finally yield a probability map. The local maximum with the highest probability value v_1 in range $[0, 1]$ is recognized as the nipple position. To quantify the confidence level of the result, we defined an index called "confidence index", which indicates quantitatively the reliability of the detected nipple position. The basic assumption behind it is that the second local maximum v_2 should be much smaller than v_1 in case v_1 has a larger confidence level to be closer to the ground truth position. The confidence index (CI) is defined in the following equation:

$$CI = \left(\frac{v_1}{v_1 + v_2} - 0.5 \right) \times 2 \tag{5.1}$$

From the equation, it is noted that CI is a value in the range of $[0, 1]$. Index 0 indicates the result is almost like a random guess, while index 1 indicates the result is quite reliable that is very likely to be the real nipple position. To investigate the reliability of the LapHess method, we have plotted the distribution of confidence rates against distance error for LapHess (in Fig. 5.18), CCA (in Fig. 5.19), and LocalMax (in Fig. 5.20). The Pearson's correlation coefficients were computed for each of them. As a result, the LapHess method achieved the most negative correlation coefficient value -0.51. It proved that the cases for which LapHess had higher distance error had lower confidence index. In other words, the LapHess method can not only detect the nipple position in a relatively higher detection rate, but also can predict the reliability of the result.

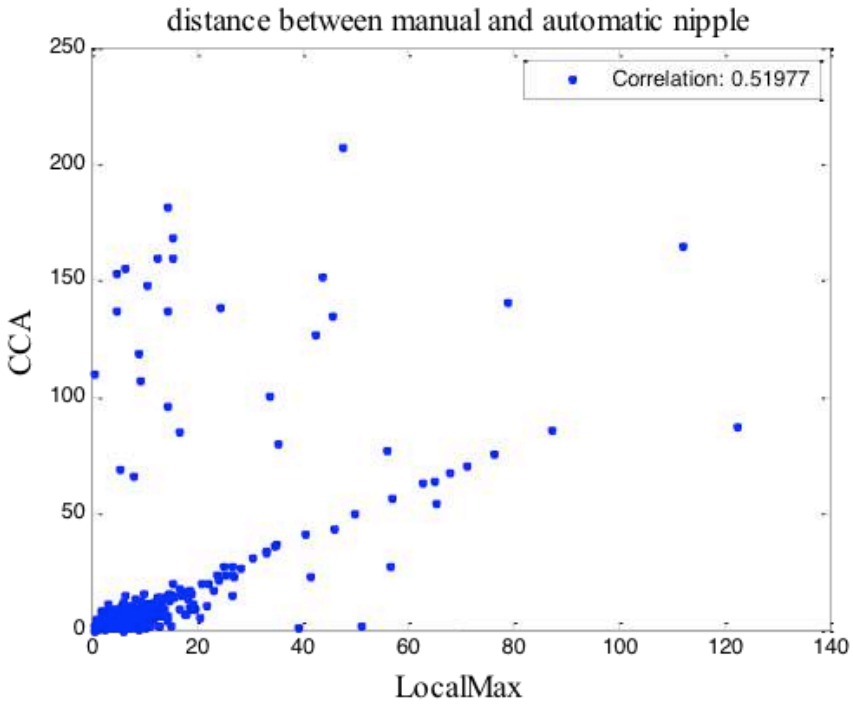

Figure 5.14: Distance error correlation between LocalMax and CCA methods.

5.5. Discussion

In this work, we first presented a fast and automated method to detect nipple positions in ABUS scans. The method fully investigates the anatomical and ultrasonographic properties of nipples in coronal planes. A multi-scale blob detector based on Laplacian filters permits the detection of nipples with variant sizes and signal strengths. A test on 113 ABUS volumes shows its capability of precisely detecting nipples, resulting in a distance error of 6.6 ± 8.9 mm $(mean \pm std)$.

Then, we further investigate the capability of the Hessian-based shape descriptor for nipple detection. In ultrasound images, the shadow areas associated with solid tissues in breast are commonly. The acoustic properties of the nipple and areola result in a tube-like shadow area beneath them. The identification of this associated shadow area helps to locate the nipple position based on their spatial relationship. The presented method performs a simplified Hessian-based measure to enhance and locate the dark shadow area correlated with the nipple and areola. Then, a 2D measure map is generated from which the first maxima is extracted that indicates the location of the center line of the shadow area. Finally, the nipple position is achieved by projecting the maxima to the first anterior slice. The proposed method was tested intensively with a large number of data sets, and the experimental results showed that a detection rate of 88.9% was reached.

The Hessian-based method could be improved by considering multi-scales Laplacian filter to adapt with variant nipple sizes and investigating more features of the nipple in the first several anterior slices, which leads to a hybrid shape descriptor that combines the power of both. The Laplacian-based method is designed to detect nipple in an extract nipple slab,

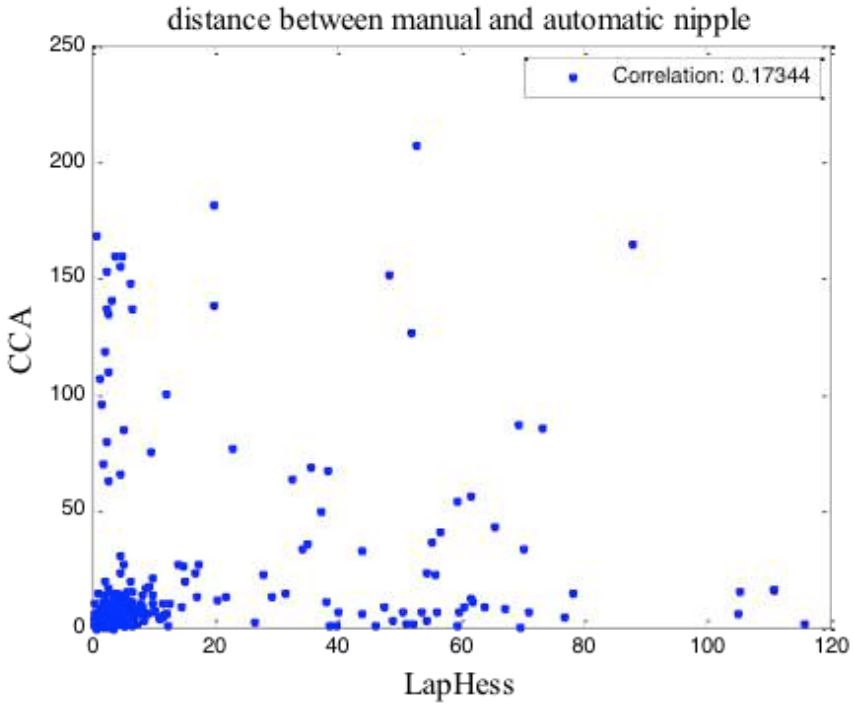

Figure 5.15: Distance error correlation between LapHess and CCA methods.

using a 2D Laplacian-based blob detector, whereas, Hessian-based method explores the entire ABUS volume and seeks for the location of shadow beam associated with nipple and areola. By combining these two detectors, a joint likelihood map is built, providing more accurate estimation of nipple position. A test on 926 ABUS volumes shows the capability of the hybrid method to precisely detect nipples, resulting in a distance error of 7.08 ± 10.96 mm ($mean \pm standard\ deviation$).

Both Laplacian and Hessian methods are designed under different assumptions: Laplacian method assumes the nipple appears near to transducer and exhibits as a dark blob structure, which could be mimicked by other type of lesions; Hessian method assumes the presence of shadow beam beneath nipple and areola, which is robust against the presence of lesions that normally exhibit weaker shadowing strength than nipple and areola. The idea of combining both methods is inspired by the fact that the hybrid method could overcome the shortcomings of each individual. However, in case the nipple is not sufficiently scanned in the field of view, or the structures, such as lesions, which mimic the properties of nipples, the hybrid method might fail.

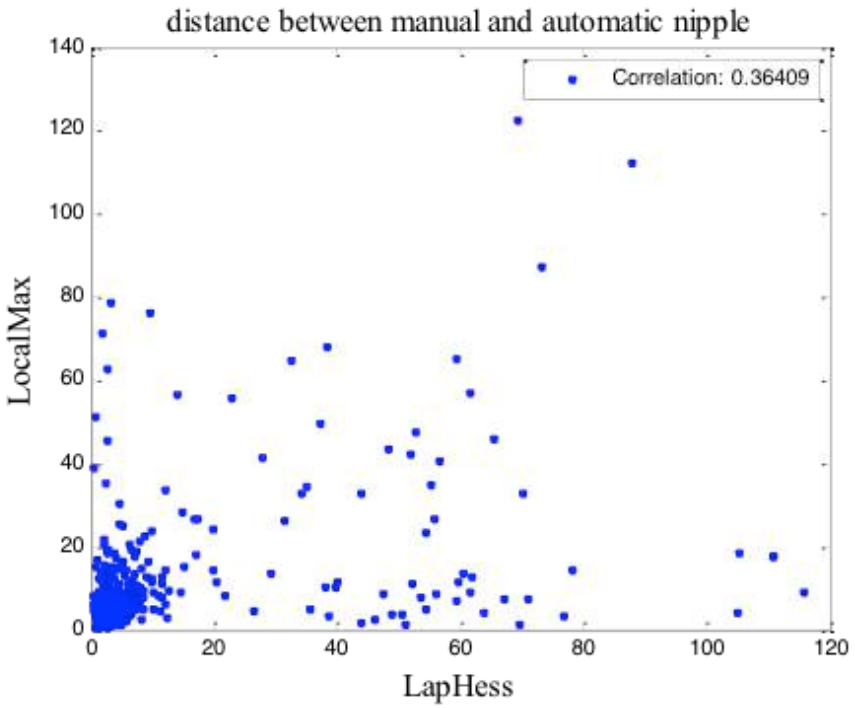

Figure 5.16: Distance error correlation between LapHess and LocalMax methods.

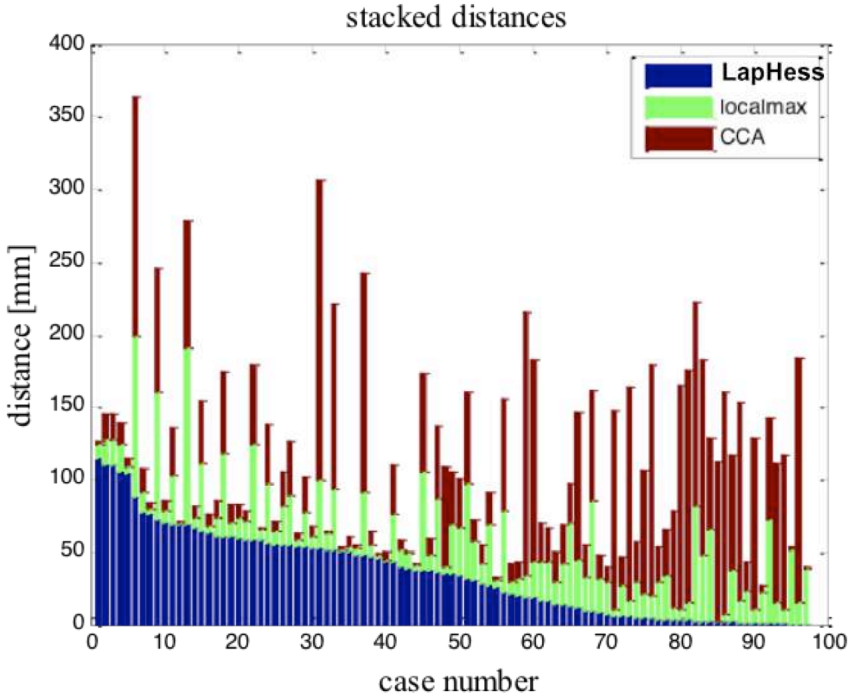

Figure 5.17: Stacked plot of the cases which have the distance error larger than 20 mm obtained at least from one method.

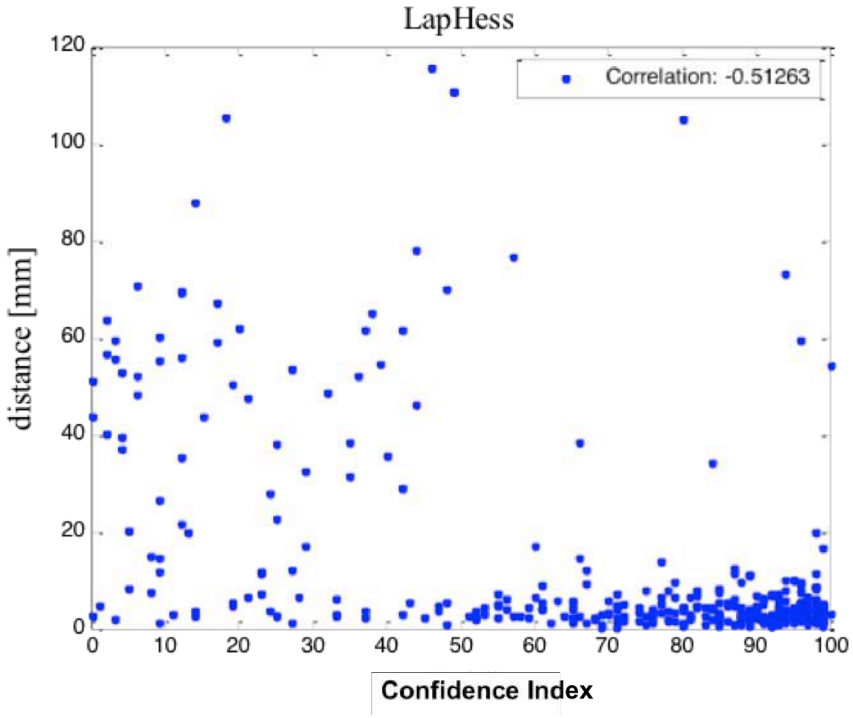

Figure 5.18: Plot of confidence index value against the distance error of LapHess method

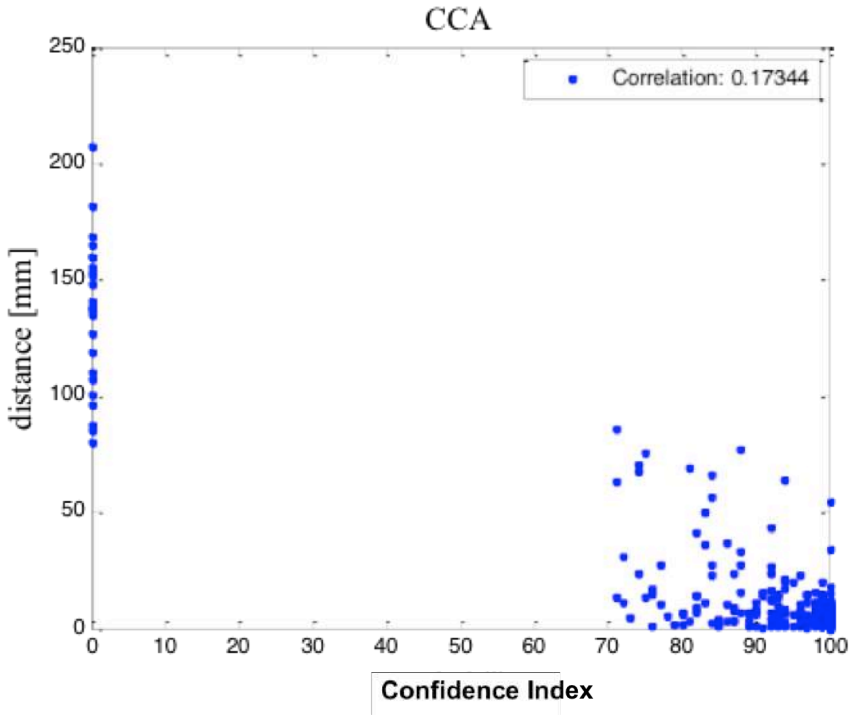

Figure 5.19: Plot of confidence index value against the distance error of CCA method

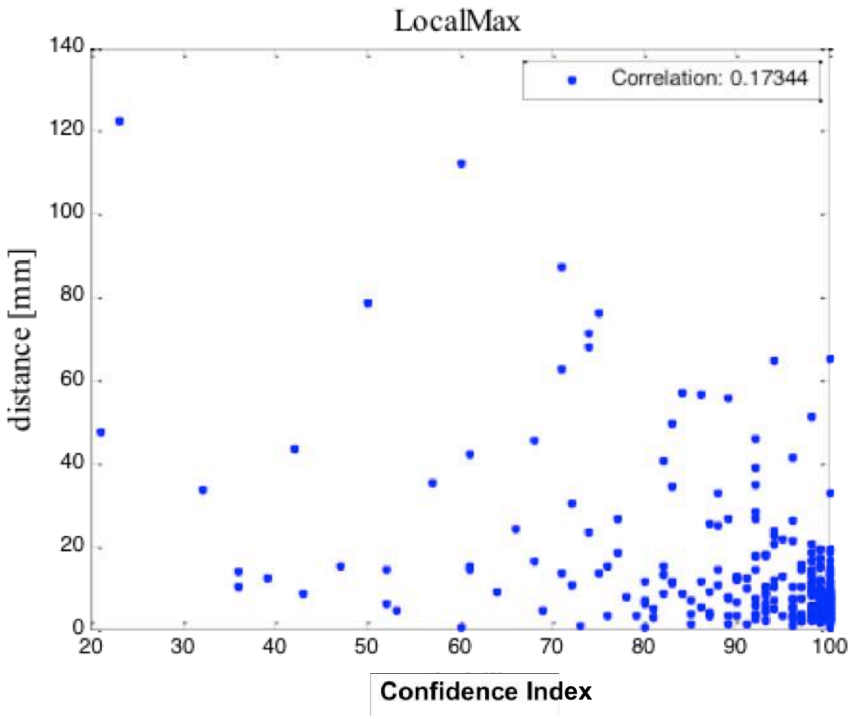

Figure 5.20: Plot of confidence index value against the distance error of LocalMax method

6

Liver Vessel Segmentation Using Vesselness Shape Descriptor

Acknowledgment

I would like to give my sincere gratitude to my colleagues in MEVIS: Dr. Stephan Zidowitz and Dr. Jan Moltz, who has supported with many inspirations and ideas during the development and optimization of this method. Additionally, I am also grateful to the work of Dr. Andrea Schenk who has kindly provided the medical image data with manual annotation and assisted me to evaluate the algorithm.

Publications

The algorithm description, implementation, and evaluation of liver vessel segmentation in multi-phase CT plus the applications that used this method were published in the following scientific papers:

- **Wang L**, Hansen C, Zidowitz S, Hahn HK (2014) Segmentation and Separation of Venous Vasculatures in Liver CT Images. In: SPIE Med imaging.
- **Wang L**, Schnurr A, Zidowitz S, et al. (2016) Segmentation of hepatic arteries in multi-phase liver CT using directional dilation and connectivity analysis. In: SPIE Med. Imaging. pp. 97851P–97851P.
- **Wang L**, Hansen C, Zidowitz S, Hahn HK (2013) Interactive Segmentation of Vascular Structures in CT Images for Liver Surgery Planning. Dtsch. Gesellschaft für Comput. und Robot. Chir. (CURAC).
- Sänger, C., Schenk, A., Schwen, L. O., **Wang, L.**, Gremse, F., Zafarnia, S., … Dahmen, U. (2015). Intrahepatic Vascular Anatomy in Rats and Mice-Variations and Surgical Implications. PLoS ONE, 10(11), e0141798.

6.1. Introduction

According to the data from the GLOBOCAN project, liver cancer is the sixth most common cancer worldwide in 2012 [155] and is ranked the second most common cause of cancer deaths. To ensure the sufficient function and survival of the remaining liver tissue after therapy, the supply and drainage of blood as well as the connection to the bile ducts have to be secured. Detailed models of hepatic vein (HV), portal vein (PV), hepatic artery (HA) and bile duct (BD) are necessary to integrate these conditions into the liver surgery planning process. In clinical routine, liver venous vasculatures can be enhanced by contrast agents administrated in multi-phase computer tomography images of livers. During the acquisition of multi-phase CT images, venous and arterial vessels are enhanced by injecting contrast agent. Along with the wash-in and wash-out procedures of contrast agent in different vascular branches, CT volumes are acquired in different time points to extract the phases where each individual vessel is maximally enhanced. The analysis of these enhanced vascular structures in different phases is required to explore patient-individual branching patterns. Segmentation of these vascular structures is the prerequisite for model construction and computer-assisted surgery planning. Combined with tumor segmentation, spatial relations between vessels and tumors can be quantitatively analyzed. Moreover, the segmentation of vessels builds the basis for vascular risk analyses [156] and virtual resection planning [157]. In addition, labeling vessels helps identify vascular territories.

The segmentation of these tree structures is a non-trivial task. The enhanced signals established by contrast agent are often not stably acquired due to non-optimal acquisition time. Inadequate contrast and the presence of large lesions in oncological patients, make the segmentation task quite challenging.

In this chapter, a novel framework and efficient workflow with minimal user interactions to analyze liver vasculature in multi-phase CT images are introduced. To ensure segmentation quality and efficiency, a set of semi-automatic algorithms are applied to initially segment different vascular structures in different phases. A fully automatic vessel separation procedure runs parallel to separately connected hepatic and portal veins. In addition, an interactive editing method is integrated into the framework to refine the segmentation of each individual structure. Quantitative evaluations of segmented vessels were conducted, for which three metrics, including skeleton distance, branch coverage and boundary surface distance, are defined to quantitatively and objectively assess the misalignment between segmented and reference vessels.

6.2. Related Works

Even though a substantial amount of research has been conducted on the analysis of vascular structures, it is still considered as an open problem (see [158–160]). Hessian-based filters are the major methods used in these efforts so as to enhance tube-like structures but suppress others. Specifically, enhancing tube-like structures is normally based on the analysis of eigenvalues and eigenvectors of the Hessian matrix. A variety of tubular filters have been defined using the ratio of eigenvalues to distinguish tubes from planes and blobs [16, 17, 161] .

Manniesing [162] employed the eigenvalues to define the diffusion tensor of anisotropic filters to enhance vascular structures. Addition to eigenvalues, the eigenvectors were also used to develop medialness functions to extract the vascular centerlines [163, 164]. To handle vessels of different radii, a multi-scale framework is usually incorporated in the Hessian-based analysis. The other methods such as the model-based approaches and the level-set techniques were also explored. A directional filter bank was presented by Truc et al. to enhance tubular structures and used 2D images for evaluation [165]. Qian et al. defined an enhancement filter based on the probability density function in a polar coordinate [166]. Agam et al. proposed an enhancement filter using the eigenvalues of the correlation matrix of gradient vectors [167], while Aylward et al. traced the intensity ridges as the medial axis of tubes [168]. A statistical framework, attempting to estimate a solution vector including the next point on the medial axis, the tangent vector to the next point, and the scale of the tube, was reported by Wong et al. [169]. Gulsun et al. proposed a medialness function to look for the medial axis through the minimum-path-cost algorithm [170]. Wörz et al. improved a vascular model for small and large vessels and employed an optimization algorithm to fit the model, find the medial axis, and estimate the radius [171]. Gooya devised a new formulation of level-sets to evolve the front in the longitudinal direction of a tube [172]. In [160], a new filter that enhances medial axis of tubes with a symmetric cross-section was proposed. Normally, performance comparison of these methods is not applicable, due to different test data sets and variant measurements for evaluation were used.

6.3. Materials and Methods

6.3.1. Segmentation and Separation of Hepatic Vein and Portal Vein

In this section, a framework with minimal user interactions to analyze venous vasculatures including HV and PV in multi-phase CT images will be introduced. Firstly, presented vasculatures are automatically segmented adopting an efficient multi-scale Hessian-based vesselness filter. The initially segmented vessel trees are then converted to a graph representation, on which a series of graph filters are applied in post-processing steps to rule out irrelevant structures. Eventually, we develop a semi-automatic workflow to refine the segmentation in the areas of inferior vena cava and entrance of portal veins, and to simultaneously separate hepatic veins from portal veins. In multi-phase liver CT, contrast enhanced images of HV and PV can be either acquired in a common phase or two individual phases. The proposed method is capable of handling both cases to segment HV and PV simultaneously or individually. Figure 6.1 illustrates the processing pipeline.

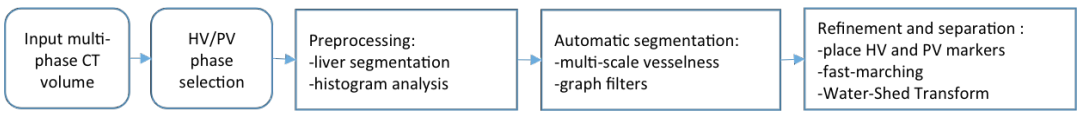

Figure 6.1: Schematic overview of the work flow.

Preprocessing

In preprocessing, we segment the liver on the selected venous phase (see Fig 6.2(a)). The liver mask confines the calculation of vesselness response within the liver to reduce computational expense. Due to the enhancement by contrast agent, venous structures appear as hyperdense. To preclude the extreme hypodense voxels that definitely don't belong to HV and PV, we analyze the histogram of the liver CT image and determine a minimum threshold L_{min}, corresponding to the peak of the histogram distribution. We assume that the venous voxels should not appear with the highest frequency in the liver, which means that any voxels below L_{min} are assumed not belonging to venous vessels and will be excluded from subsequent steps.

Automatic Initial Segmentation of HV and PV

Hessian-based filters have been widely employed to enhance tube-like structures in 3D images. There are several vesselness filters published in previous works [17, 153]. Because the contrast of venous vessels in different input images are quite heterogeneous, we choose the multi-scale, Hessian-based vesselness filter introduced by Frangi et al. to enhance the vessels in a CT volume [17]. The major benefits of Frangi's vesselness filter include the integration of information from all three Eigenvalues and the independence from their absolute values, which are associated with contrast levels of vessels. The outputs of the filter are scaled within the range between 0 and 1. Assuming the Eigenvalues of Hessian matrix are sorted in order: $|\lambda_1| \leq |\lambda_2| \leq |\lambda_3|$, Frangi's vesselness filter is defined as follows:

$$f(\sigma) = \begin{cases} 0 & \text{if} \quad \lambda_2 > 0 \;\; or \;\; \lambda_3 > 0 \\ \left(1 - \exp\left(\frac{-R_A^2}{2\alpha^2}\right)\right) \exp\left(\frac{-R_B^2}{2\beta^2}\right) \left(1 - \exp\left(\frac{-S^2}{2c^2}\right)\right) & \text{otherwise} \end{cases} \tag{6.1}$$

where

$$R_A = |\lambda_2|/|\lambda_3|, \qquad R_B = \frac{|\lambda_1}{\sqrt{|\lambda_2 \lambda_3|}}$$

and

$$S = \sqrt{\lambda_1^2 + \lambda_2^2 + \lambda_3^2}.$$

The ratio R_A is designed to differentiate vessels from sheet-like structures, whereas R_B is used to distinguish vessels from blob-like structures. The term S aims to suppress noise structures. The scale parameter σ indicates the size of Gaussian kernel used for calculating Hessian matrix. The parameters used in this filter, α, β and c are set to $0.5, 0.5$ and 10. Considering the radius range of HV and PV, we choose three optimized scales for σ: 1.5 mm, 2.25 mm, and 3 mm based on our experimental tests, which are able to capture vessels with thin, medium, and thick radii (see Fig. 6.2(b)). The ultimate vesselness response is obtained by extracting the maximum across all scales. Normally, calculating the Hessian matrix is quite expensive when increasing the size of Gaussian kernel. To speed up, we adopt an inverse multi-scale strategy which keeps the kernel size constant at 1.5 mm, but down-samples input volumes to larger voxel spacing.

On the basis of vesselness response, we initially segment HV and PV utilizing an automatic region-growing algorithm. The seeds of region-growing are automatically found by analyzing

the histogram of vesselness outputs. All voxels with a vesselness value between 90_{th} and 99_{th} percentiles are taken as seed points. The lower and upper thresholds of region growing are chosen as 75_{th} and 99.9 percentiles, respectively. If the HV and PV possess high contrast against their surrounding structures, the initial segmentation normally yields satisfactory results (see Fig. 6.2(c)).

Nevertheless, for the cases where HV and PV exhibit extremely low contrast or where large hypodense lesion areas with internal hyperdense structures are present, many irrelevant structures will be enhanced by the vesselness filter and captured in region-growing step. Therefore, we first transform the segmented vessel tree structure into a graph representation [173] and validate the graph tree using two criteria:

1. The volume of each independent graph tree should exceed a lower limit Tmin.

2. The edge length of branches should be longer than a minimum threshold Emin .

These two graph filters can rule out most irrelevant tree structures and prune disturbing branches. Other issues lie in the areas of inferior vena cava and entrance of PV, which are normally not enclosed by the segmented liver mask. Moreover, the inferior vena cava can be hypodense or hyperdense depending on the contrast agent density. We propose a robust interactive solution to recover the segmentation in both regions. Two markers need to be placed in the regions where main branches of HV and PV are joined (see Fig. 6.2(e)). Then, a fast marching algorithm is applied in the predefined neighborhoods of these two markers [174]. The efficient computation of the algorithm permits instant display of segmented regions when marker positions are adjusted until optimal positions are reached.

Refinement of HV and PV Segmentations

In case the HV and PV exhibit extremely low contrast, or large hypodense lesions with internal hyperdense structures are present, many irrelevant structures will be enhanced as well by the vesselness filter and captured in the region-growing step. For refinement, we first transform the segmented vessel trees into a graph representation [173] and validate the graph tree using two graph filters. Unconnected components of the segmented vessels will be transformed into different graph trees. Each graph tree has three basic elements: root, node, and edge. One of the attributes of a graph tree is volume size. The first filter introduces a lower limit to the volume size of each individual graph tree. The graph trees with volume less than 0.5 ml are filtered out. Hence, unconnected components can be removed by this filter. Additionally, we measure the edge length of all branches in a graph tree and assign a minimum threshold to truncate small branches shorter than 10 mm. From our experiments, these two graph filters are able to rule out isolated trees and prune spurious branches (see Fig. 6.2(d)).

Other issues lie in the areas of inferior vena cava and entrance of PV, which are normally not enclosed by the liver mask and thus not segmented. Moreover, the inferior vena cava can be hypodense or hyperdense depending on the density of contrast agent. We propose a robust interactive solution to recover the segmentation in both regions. Two markers need to be placed in the regions of inferior vena cava and entrance of PV (see Fig. 6.2(e)). Then, a fast

marching algorithm is applied in the predefined neighborhoods of these two markers [174]. The speed map of fast marching is determined by commonly used Sigmoid filter which applies Sigmoid function on intensities [175]. A local spherical neighborhood region with a radius of 20 mm is defined for each marker. The parameters α_{sig} and β_{sig} of the Sigmoid function are set as 10 and the mean intensity of the voxels in defined spherical neighborhoods, respectively. The stop value of propagation is set to 50. The efficient computation of the algorithm permits instant display of the segmented region when each marker is adjusted, until the optimal position is reached.

Separation of HV and PV

The HV and PV will be simultaneously segmented when they present in a common phase. For liver surgical planning, it is demanding to separate and analyze them individually. The separation process is triggered when HV and PV markers are placed. To meet time constraints, we employ an interactive watershed transform algorithm that takes the HV and PV markers as the seed points of two different classes [176]. The cost image of the watershed transform is the original intensity image, smoothed with an edge-preserving diffusion filter. The entire volume is classified into two classes associated with the HV and PV markers. Eventually, the segmented HV and PV can be separated by applying the class labels on the segmentation results (see Fig. 6.2(f)).

6.3.2. Segmentation of Hepatic Artery

Segmentation of hepatic arteries in multi-phase computed tomography (CT) images is indispensable in liver surgery planning. The branching patterns of HA are suffered with several types of variations. To get a clear picture of each individual HA branching pattern is critical before the administration of surgery, since unusual HA branch can be erroneously resected which completely fail the therapy.

During image acquisition, the hepatic artery is enhanced by the injection of contrast agent. The enhanced signals are often not stably acquired due to non-optimal contrast timing. Other vascular structure, such as hepatic vein or portal vein, can be enhanced as well in the arterial phase, which can adversely affect the segmentation results. Furthermore, the arteries might suffer from partial volume effects due to their small diameter. To overcome these difficulties, we propose a framework for robust hepatic artery segmentation requiring a minimal amount of user interaction. First, an efficient multi-scale Hessian-based *vesselness* filter is applied on the artery phase CT image, aiming to enhance vessel structures with specified diameter range. Second, the *vesselness* response is processed using a Bayesian classifier to identify the most probable vessel structures. Considering the *vesselness* filter normally performs not ideally on the vessel bifurcations or the segments corrupted by noise, two vessel-reconnection techniques are proposed. The first technique uses a directional morphological operator to dilate vessel segments along their centerline directions, attempting to fill the gap between broken vascular segments. The second technique analyzes the connectivity of vessel segments and reconnects disconnected segments and branches. Finally, a 3D vessel tree is reconstructed. A schematic overview of the entire workflow is illustrated in Fig. 6.4.

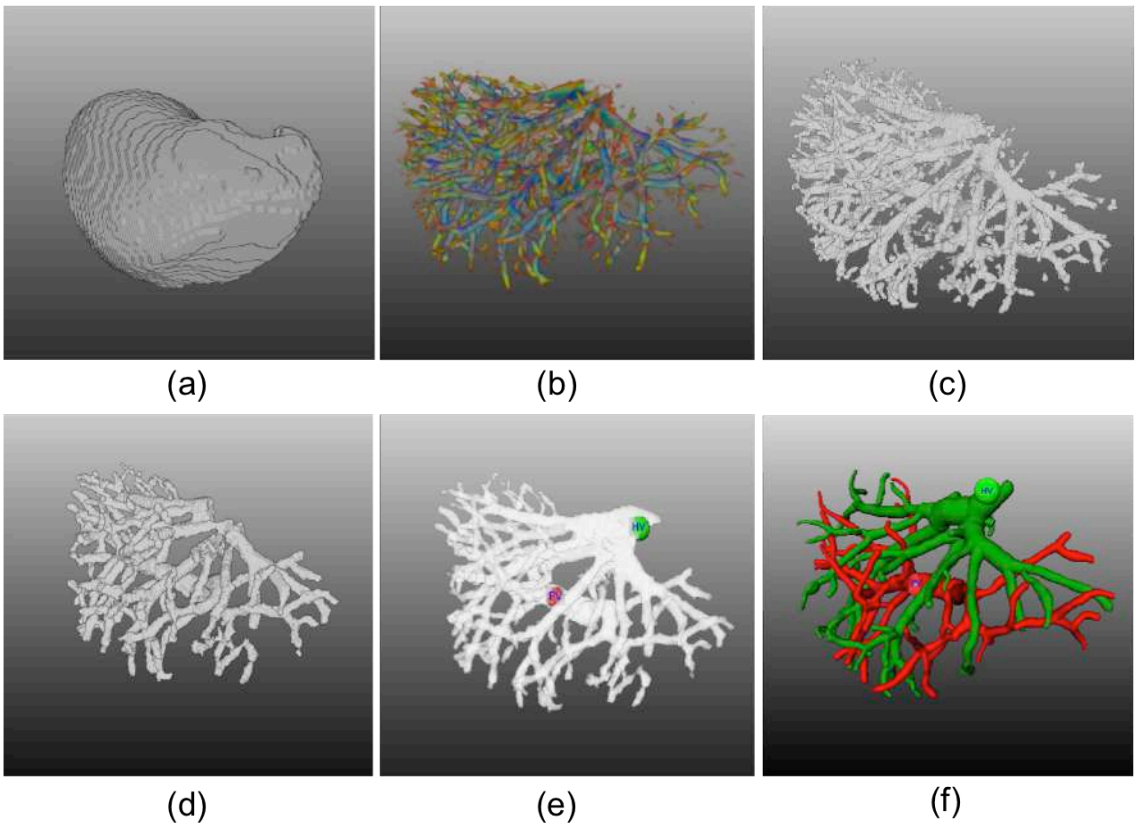

Figure 6.2: HV/PV segmentation and separation: (a) segmented liver mask; (b) response of multi-scale vesselness filter represented with color map: red, green and blue indicates response of small, medium and large scales, respectively; (c) initial segmentation of HV/PV; (d) HV/PV segmentation after graph filters; (e) interactive refinement of HV/PV segmentation: HV and PV markers displayed with green and red dots; (f) result of separating HV and PV.

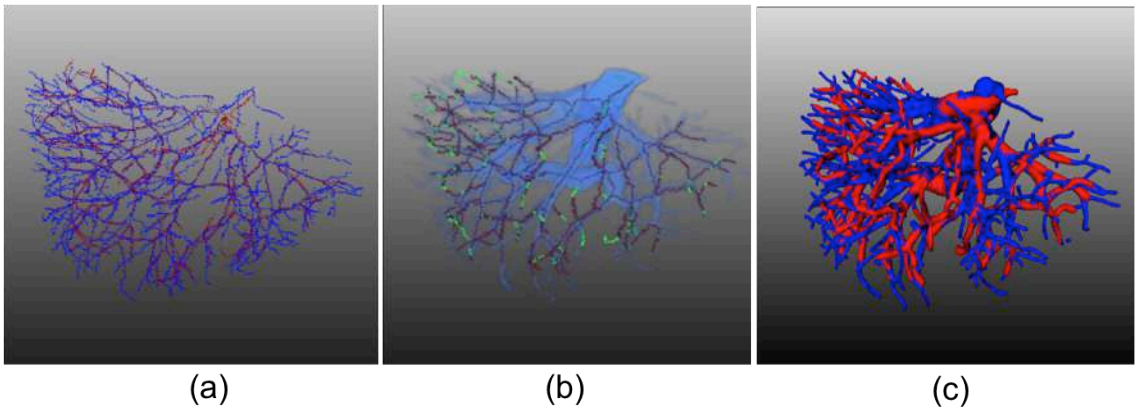

Figure 6.3: Depiction of evaluation metrics: (a) computation of distance between reference skeleton (blue) and segmented skeleton (red); (b) calculating proportion of segmented skeleton (red) covered by reference volume (light blue), and the uncovered skeletons are indicated in green; (c) surface distance between segmented volume (red) and reference volume (blue).

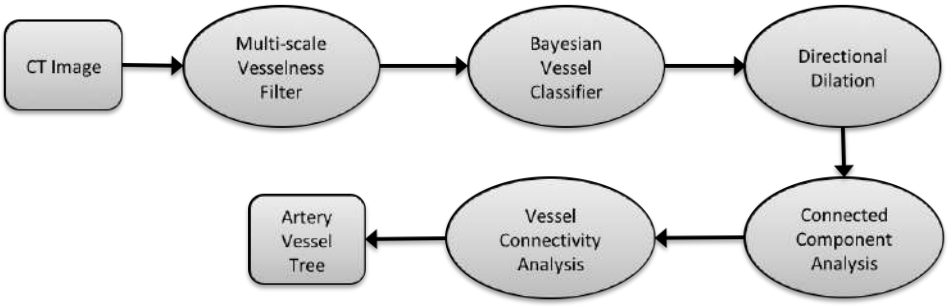

Figure 6.4: Schematic overview of the entire segmentation workflow.

Multi-scale Vessel Enhancement Filter

Because the contrast level of HA in different input images is quite heterogeneous, we used the multi-scale, Hessian-based vesselness filter defined in equation 6.1 with different parameter settings. The scale parameter σ indicates the size of Gaussian kernel used for calculating Hessian matrix. The parameters used in this filter, α, β and c are set to $0.5, 0.5$ and 10. Considering the radius range of HA, we choose three optimized scales for σ: 1 mm, 1.2 mm, and 1.4 mm based on our experimental tests, which are able to capture vessels with thin, medium, and thick radii. The ultimate *vesselness* response is obtained by extracting the maximum across all scales.

Bayesian Vessel Classifier

The *vesselness* outputs of three scales are individually assessed with a Bayesian vessel classifier that uses a Gaussian mixture model (GMM), assuming that the image is a mixture of a finite number of Gaussian distributions with unknown parameters. The Bayesian vessel classifier is supposed to differentiate the vasculature from non-vasculature based on the *vesselness* response. Therefore, the number of Gaussian distributions in the GMM is assumed as two. The expectation maximization (EM) algorithm is exploited to estimate the mean and the variance of each Gaussian distribution. Since the EM algorithm requires initializing all parameters, mean, variance and probability for both classes have to be estimated. The Frangi's *vesselness* measurement is comparable across scales and images, which makes it possible to determine a set of initial parameters. To further simplify the process, a minimal *vesselness* threshold was used to discard background voxels with close to zero *vesselness* response. Using the parameters calculated by the EM algorithm, the probability distribution of vasculature and non-vasculature classes are achieved. Thus, a voxel belonging to a class c based on it's *vesselness* value x can be obtained using Bayesian formula: .

$$p(c|x) = (p(x|c) \times p(c))/p(x) \tag{6.2}$$

Each voxel is then assigned to the class with higher probability. This classification is conducted for all three *vesselness* outputs. A voxel is marked as vessel in a binary output image (as shown in Fig. 6.5 (b)), if it is classified as vessel in one of the three scales.

Directional Morphological Dilation

The binary output of the Bayesian vessel classifier depicts the most probable vessel segments with gaps and holes. To close small gaps in between and also fill holes, a directional morphological dilation along the vessel orientation is applied.

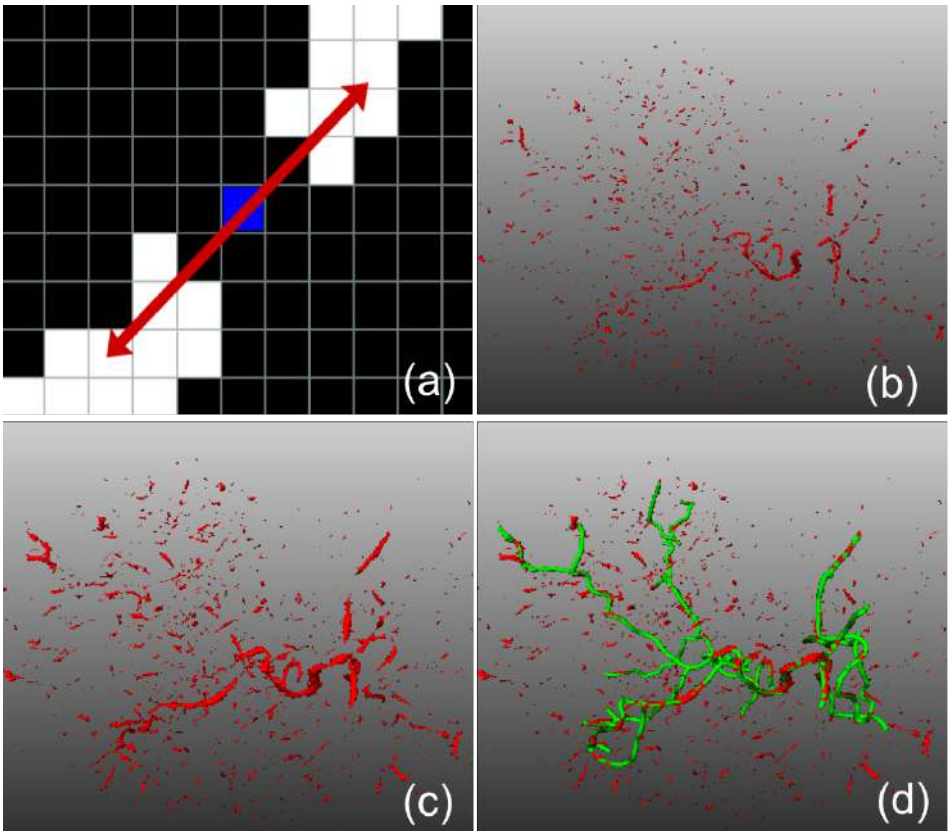

Figure 6.5: (a) directional dilation kernel (red line) applied in a background voxel (blue); (b) vessel segments resulted from Bayesian classifier; (c) vessel segments resulted from directional dilation; (d) the reconstructed HA vessel tree (green) obtained by connecting and merging vessel segments.

Although dilation is a common used morphological operator to fill the gap in binary images, it often merges irrelevant neighboring structures. To overcome this problem, the orientation of a vessel segment, which is derived from the eigenvector of the hessian matrix that correlates to the smallest eigenvalue, is incorporated in the dilation process. The structure element is defined as a line with a fixed length along the local vessel orientation (see Fig. 6.5(a)). The directional dilation performs only on the background voxels near to the detected vessel segments. The voxel values of the line element are interpolated. The percentage of foreground voxels is computed and compared to a percentage threshold. If the percentage exceeds the threshold, the currently processed background voxel is labeled as foreground in the output image. To achieve a higher level of connectivity, this dilation procedure is performed twice. The second round utilizes the result of the first round as the input. Compared with the vessel segments identified by Bayesian classifier (see Fig. 6.5(b)), the dilated vessel segments as depicted in Fig. 6.5(c) tend to be more connected with fewer gaps.

Vessel Connectivity Analysis

To some extent, the directional dilation shows its ability to bridge the gaps between vessel segments, but still does not work well enough to build a complete HA vessel tree. Particularly, the bifurcations connecting different level of branches can be missing, due to the inherent weakness of the *vesselness* filter, which normally performs imperfectly in joint regions. To build a complete vessel tree, a root is required to be identified, and the connectivity of all vessel segments to their parent branches, and ultimately to the root needs to be analyzed. We analyze the vessel connectivity by computing the cost of the path connecting a vessel segment to the root, which consists of several steps.

Skeleton Components Extraction

First, a connected component analysis is performed on the skeletons of the dilated vessel segments. The skeleton, representing the centerline voxels of a vessel segment, is extracted by a thinning operation. A component is defined as a group of skeleton voxels and has a unique index. The size of a component is the number of its skeleton voxels. The radius and the 3D position of each skeleton voxel are saved. All vessel segments are traversed, and their corresponding components are constructed. Not all components will be fed to the subsequent steps, and a valid component should fulfill two conditions:

- its size should be larger than a minimum threshold.
- it should not form a ring structure.

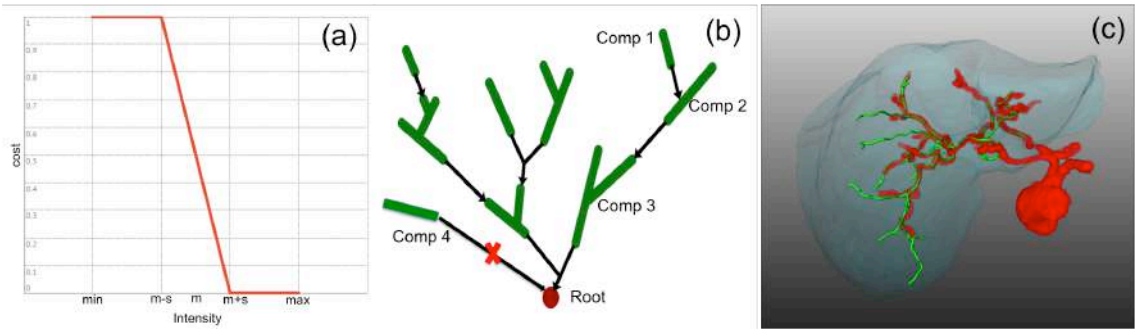

Figure 6.6: (a) Mapping function to compute the cost image; (b) illustration of optimal path from components to the root and the connection cost (arrow length is proportional to the cost strength) between primary component (such as Comp 1) to its follower (Comp 2). Comp 4 will not be reconnected to the root due to the cost exceeding the threshold; (c) 3D visualization of reference HA volume (red) and segmented HA skeleton (green).

Connection Cost Computation

The HA vessel system is assumed to be a tree structure with a root node that can be selected as any point on the main HA branch, before it further splits to small branches in the liver. Considering the HA anatomy, the root may be defined either inside or outside the liver. To ensure the accuracy of the root position, it was decided to place the root by the user interactively. To calculate the connection cost from a skeleton component to the root, a cost image has to

be built. We generate a cost image by applying a transfer function on the intensities of the original CT image as depicted in Fig. 6.6(a). First, the mean (m) and standard deviation (s) of the intensities are calculated. The function maps all the intensities smaller than $m - s$ to 1 and all the ones larger than $m + s$ to 0. The intensities in between will be mapped linearly to the range of $(0, 1)$. Additionally, the cost value of all skeleton voxels in each component is set to 0. Then, the Dijkstra algorithm is applied on the cost image, and the optimal path with the minimal cost from any voxel to the root can be found. Because the cost traveling from one skeleton voxel to another within a component is 0, the voxels belonging to the same component will result in the same optimal path. This path is then defined as the optimal path for the component to reach the root, and the corresponding connection cost is the sum of the cost values along the path.

Vessel Component Connecting

After the optimal paths to the root for all the components have been found, the component connecting process is triggered. First of all, two additional attributes are assigned to each component: the follower and the cost to the follower. For a primary component, its optimal path is traced towards the root. If another component is found on the path, the tracing process stops. The found component is assigned as the follower for the primary one, and the cost between them is the subtraction of their costs to the root. Certainly, it is possible that no other component is found on the optimal path till the root, and then the follower for the primary component is set as the root and the cost to the follower is identical as the cost to the root. Afterwards, the costs to the follower for all components are sorted in ascending order. The component connecting and merging process is started with the one with the minimal cost and iterate through all the components based on the cost order. To avoid unreliable connecting, the primary component and its follower will be connected and merged only if the cost is under a threshold. For the components of which the followers are the root, the cost threshold is doubled, because the root might be placed a little bit far from the liver arising higher cost. The entire process is illustrated in Fig. 6.6(b). The gap between a primary component and its follower is filled with the skeleton voxels on the optimal path. The radii of these skeleton voxels are interpolated with the radii of the primary and the follower component voxels. Finally, all connected and merged components that can reach the root are selected to build the complete HA vessel tree, which serves as the segmentation results as shown in Fig. 6.6(c).

6.4. Results and Evaluations

6.4.1. Evaluation Metrics

Evaluating the alignment of two vessel trees is not as easy as other mass objects. Two major features characterizing a tree structure are branching patterns and radii. To measure the consistency of branching patterns and radii more specifically, besides the widely used overlap metric: Dice Coefficient (DC), we introduce three additional metrics: skeleton distance, branch coverage, and boundary surface distance. First of all, the skeletons (indicated as SK_{seg} and SK_{ref}) of the segmented and reference vessel volumes (indicated as V_{seg} and V_{ref}) are

extracted, and similarly the boundary surfaces (indicated as BS_{seg} and BS_{ref}) of both volumes are automatically derived as well.

Dice Coefficient

Dice Coefficient (DC) is computed to measure the overlap between V_{seg} and V_{ref}. Generally, it is able to reflect both misalignment of branches and errors of radii to some extent. The results obtained for the calculation of DC were 0.52 ± 0.11 ($mean \pm stdev$)

Skeleton distance

Skeleton distance metric aims to particularly measure the alignment of branching patterns by computing the distance between two skeletons: SK_{seg} and SK_{ref} (see Fig. 6.3(a)). It is a bi-directional distance measure. The average distance from SK_{seg} to SK_{ref} is calculated as following: for each point of SK_{seg}, its paired point on SK_{ref} was defined as the one with the least distance to it. The sum distance was computed over all these point pairs. Ultimately, the average distance $D_{seg2ref}$ was calculated by dividing the sum distance with the count of point pairs. Inversely, the average distance $D_{ref2seg}$ from SK_{ref} to SK_{seg} can be obtained in the same way. Ultimately, the average distance between SK_{seg} and SK_{ref} is defined as $D = (D_{seg2ref} + D_{ref2seg})/2$. Experiments showed that the mean of D was 7.82 mm with a standard deviation of 2.96 mm. In Fig. 6.7, the distributions of Dice Coefficient and skeleton distance illustrated by box-and-whisker plots were given.

Branch coverage

Branch coverage metric $P_{seg2ref}$ reports the percentage of SK_{seg} covered by the corresponding reference volume V_{ref} (see Fig. 6.3(b)), and the same percentage $P_{ref2seg}$ is computed inversely for the skeleton of reference SK_{ref}. The average P of the two percentages depicts branching consistency of both vessel trees from another perspective. More specifically, it is able to reflect two typical types of errors arose in segmentation problems: under-segmentation or over-segmentation. Under-segmentation correlates with the relation that $P_{seg2ref}$ is greatly larger than $P_{ref2seg}$, and over-segmentation behaves in opposite way. The experimental results of the average branch coverage P achieved a mean of 0.64 with a standard deviation of 0.11.

Boundary surface distance

The metric of boundary surface distance investigates the deviation of both branching patterns and radii. It evaluates the distance between BS_{seg} and BS_{ref} (see Fig. 6.3(c)). Similar to the computation of skeleton distance, it is again a bi-directional distance. The distance from BS_{seg} to BS_{ref} is indicated as $SD_{seg2ref}$, and $SD_{ref2seg}$ represents the inverse distance. The average surface distance SD is derived by $SD = (SD_{seg2ref} + SD_{ref2seg})/2$. The mean and standard deviation of SD were 4.74 mm and 2.16 mm, respectively. Additionally, to fetch an overview of the distributions of branch coverage and surface distance, the box plots of these two measures were demonstrated in Fig. 6.8.

6.4.2. Evaluation of HV and PV Segmentation

To evaluate the performance of the proposed method, a test set enclosing 60 multi-phase hepatic CT scans acquired from 30 liver donors and 30 oncological patients was collected. HV/PV phases were taken for all scans. The volumes of HV/PV were manually segmented by an experienced radiologist, serving as reference for quantitative evaluation. In addition, the markers used to refine and separate the HV and PV were placed manually and saved prior to automatic testing. Image resolution of HV/PV phases in test images ranges from $512 \times 512 \times 189$ to $512 \times 512 \times 310$. Calculation of the multi-scale vesselness filter takes 15 to 40 seconds depending on different image resolutions. The initial segmentation and subsequent refinement of HV/PV take maximally 3 seconds using a 3.07 GHz Intel CPU.

Table 6.1: Metrics and if they express a specific type of misalignment error.

	Dice Coefficient DC	skeleton distance D	branch coverage P	surface distance SD
branching pattern errors	Yes	Yes	Yes	Yes
radii errors	Yes	No	No	Yes

Table 6.2 lists the statistical results of all proposed metrics for the entire test cases. It is easy to observe that branch coverage from segmentation to reference is better than inverse direction on average. The reason is that our radiologists tend to delineate the complete reference vessels including very thin vasculatures whose radii are less than 1 mm, which are normally not detected by the method and of less interest for liver surgical planning in clinical practice.

Table 6.2: The statistical analysis results of the volumetric difference and surface distance measurements.

	DC	$D_{seg2ref}$ (mm)	$D_{ref2seg}$ (mm)	D (mm)	$P_{seg2ref}$	$P_{ref2seg}$	P	$SD_{seg2ref}$ (mm)	$SD_{ref2seg}$ (mm)	SD (mm)
Mean	0.52	4.92	10.72	7.82	0.78	0.51	0.64	3.30	6.18	4.74
Stdev	0.11	5.29	3.26	2.96	0.19	0.13	0.11	3.97	2.18	2.16
Min	0.25	1.02	5.12	4.81	0.23	0.18	0.28	0.55	3.44	2.38
Max	0.68	30.70	24.15	20.37	0.99	0.77	0.79	23.37	14.31	14.11

To better correlate visual inspection with the proposed quantitative metrics, four exemplary segmented and corresponding reference masks of HV and PV are visualized in Fig. 6.9, where the values of associated metrics for each case were attached. Notice that branch coverage P manifests the same trend with Dice Coefficient. However, skeleton distance D and boundary surface distance SD behave slightly differently compared to DC in the first two cases, where case 2 has a larger DC, but larger distance errors expressed by D and SD. The reason is that they basically measure the distances in different dimensions. D tries to measure the distance between lines, and SD measures the distance between surfaces, whereas DC measures the distance between volumes. Therefore, they reflect the two types of errors, branching patterns and radii, with different strength and focus. Table 6.1 lists the focus of each metric in measuring misalignment of two vessel trees. In case 2, a larger DC value indicates a better alignment in the parts with larger volume sizes, such as vena cava, whereas its alignment with

respect to branching patterns is actually worse than case 1 slightly, because a larger SD is observed. In this sense, SD is a more reliable metric than DC in reflecting both errors brought by branching patterns and radii in comparison of vessel trees.

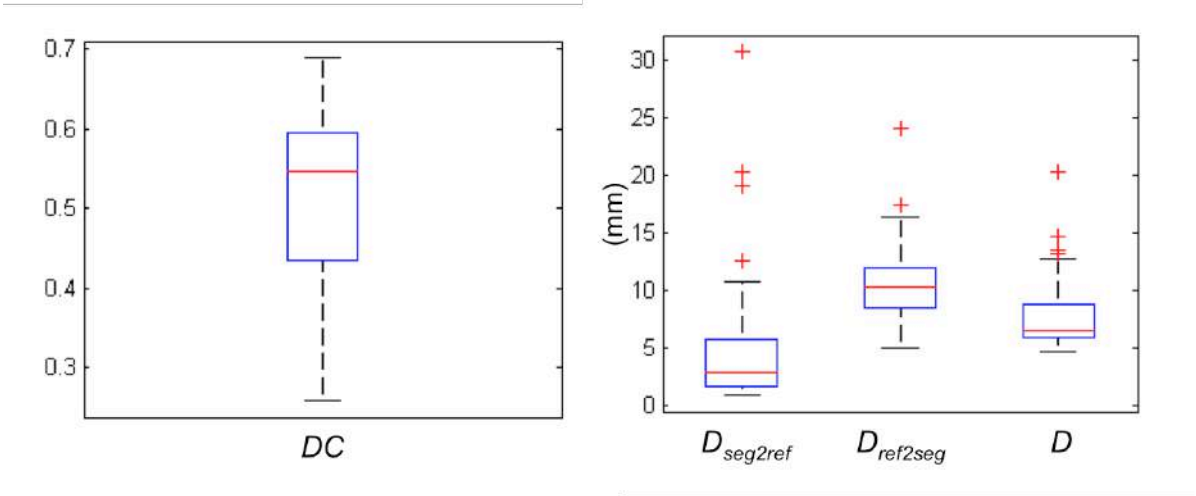

Figure 6.7: Distribution of Dice coefficient and skeleton distance: box plot of DC (left); box plots of $D_{seg2ref}$, $D_{ref2seg}$ and D (right).

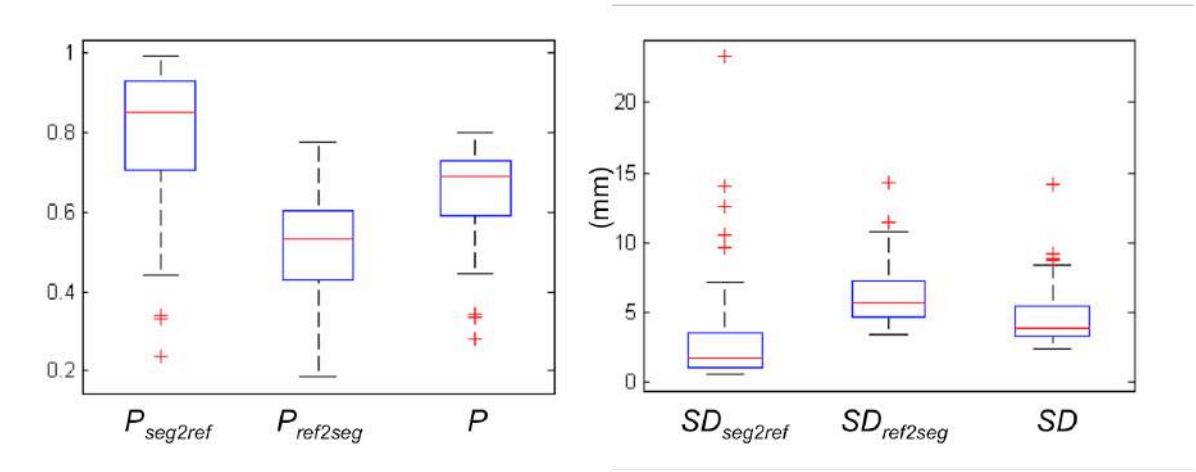

Figure 6.8: Distribution of brach coverage and boundary surface distance: box plots of $P_{seg2ref}$, $P_{ref2seg}$ and P (left); box plots of $SD_{seg2ref}$, $SD_{ref2seg}$ and SD (right).

6.4.3. Evaluation of HA Segmentation

We collected 18 hepatic multi-phase CT datasets with tumors for the evaluation of our approach. All data sets have a voxel spacing of 0.7mm × 0.7mm × 0.8mm. For each dataset, the liver was imaged once in the venous phase and once in the arterial phase. The liver mask and HA vessel were segmented manually by a medical professional (MeVis Distant Service, Bremen, Germany), and the latter serves as the reference for evaluation. The similarity of two vessel trees is difficult to express with a single measurement. Regarding the time efficiency, processing one dataset overall took about 1 minute on average on a machine with a 6-Core

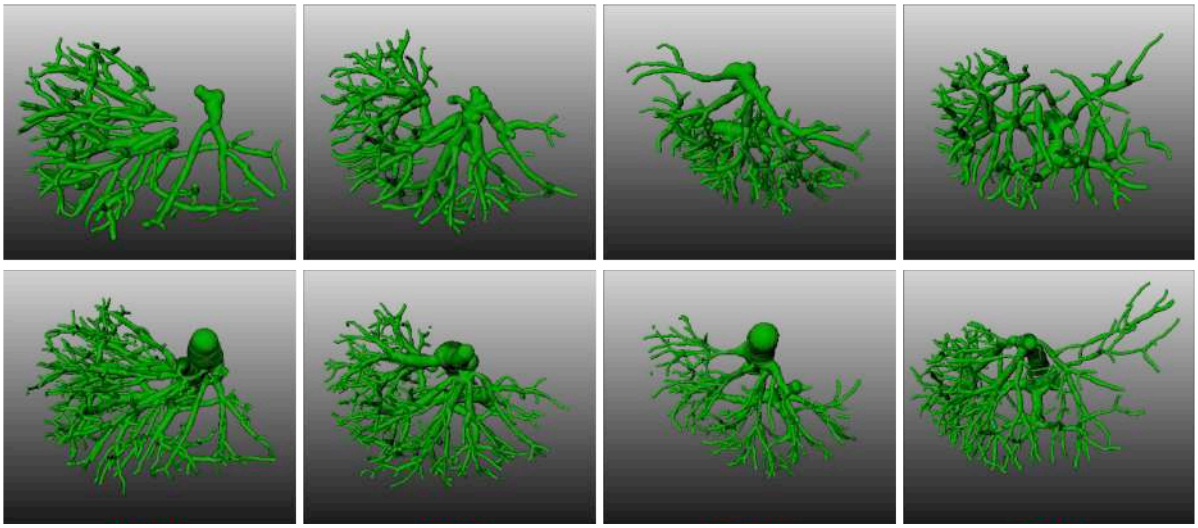

Case 1:	Case 2:	Case 3:	Case 4:
DC = 0.65	**DC = 0.68**	**DC = 0.38**	**DC = 0.44**
$D_{seg2ref}$ = 1.55	$D_{seg2ref}$ = 1.48	$D_{seg2ref}$ = 7.60	$D_{seg2ref}$ = 3.18
$D_{ref2seg}$ = 8.14	$D_{ref2seg}$ = 8.74	$D_{ref2seg}$ = 10.93	$D_{ref2seg}$ = 9.26
D = 4.84	**D = 5.11**	**D = 9.27**	**D = 6.22**
$P_{seg2ref}$ = 0.94	$P_{seg2ref}$ = 0.96	$P_{seg2ref}$ = 0.49	$P_{seg2ref}$ = 0.82
$P_{ref2seg}$ = 0.59	$P_{ref2seg}$ = 0.62	$P_{ref2seg}$ = 0.45	$P_{ref2seg}$ = 0.47
P = 0.77	**P = 0.79**	**P = 0.47**	**P = 0.65**
$SD_{seg2ref}$ = 0.74	$SD_{seg2ref}$ = 0.85	$SD_{seg2ref}$ = 5.48	$SD_{seg2ref}$ = 1.90
$SD_{ref2seg}$ = 4.02	$SD_{ref2seg}$ = 4.52	$SD_{ref2seg}$ = 6.66	$SD_{ref2seg}$ = 5.45
SD = 2.38	**SD = 2.68**	**SD = 6.07**	**SD = 3.68**

Figure 6.9: Four examples of segmentation results and their associated metric values: segmented HV and PV (top row); reference segmentation of HV and PV (middle row); corresponding values of the metrics used for evaluation (bottom row). Each column relates with one particular case.

3.5 GHz CPU, in which about 5 seconds were taken to place the root interactively.

The error of misalignment can result from two sources: branching pattern and radius, which need to be addressed with different measurements. To assess the quantitative segmentation quality, the following metrics were used:

- Skeleton coverage (SC): percentage of the segmented skeleton covered by the reference vessel volume
- Mean symmetrical distance (MSD): mean distance between the segmented and reference skeletons

If the branching pattern of the segmentation is accurate, its skeleton should be completely covered by the reference volume, resulting in a higher SC value. MSD is even more sensitive to the error of branching patterns. These metrics were computed inside the liver mask. The mean and standard deviation values of SC and MSD were 0.55 ± 0.27 and 12.7 ± 7.9mm, respectively. Figure 6.10 demonstrates two example cases with relatively high and low SC values. It can be observed that the algorithm is capable of capturing the majority of enhanced HA vessels which are enhanced properly with a significant contrast with surroundings. On the other hand, in the cases where the segmentation performs not well, normally HV and PV vasculatures are substantially enhanced as well, due to imperfect imaging time during the acquisition. If the HA phase is taken imperfectly with enormous enhancement of other vasculatures such as HV and PV, the algorithm can be misled and generate a substantial amount of false positive segmentation. Additionally, as shown in Fig. 6.6(c), the manually annotated reference often did not reach the small HA branches deep inside the liver. Some more examples visually depicting the performance are given in Fig. 6.11.

6.5. Discussion

In this work, we developed a semi-automatic approach which is dedicated to precisely segmenting and separating venous and arterial vasculatures in liver CT images, which is a crucial task for liver surgery planning. An extensive assessment for the proposed method was conducted with a large scale of test images, for which manual annotations by radiologists were built as the ground truth. Three new quantitative measurements: skeleton distance, branch coverage, and boundary surface distance, were proposed to review the performance from different perspectives.

For the segmentation of HV and PV, multi-scale vesselness filter is sensitive in detecting vascular structures in different contrast levels. Considering the balance between performance and computational expense, we choose three scales in this work, which consumes the time in acceptable range. In practice, the disturbing structures resembling vasculatures locally will be enhanced as well, especially in the patients with oncological lesions. The graph filters and manual editing tool in post-processing step are capable of ruling out these false positives. The optimal parameter settings for the graph filters used in post-processing were obtained through a brutal test iterating through all possible combinations. The success of Water-Shed transform

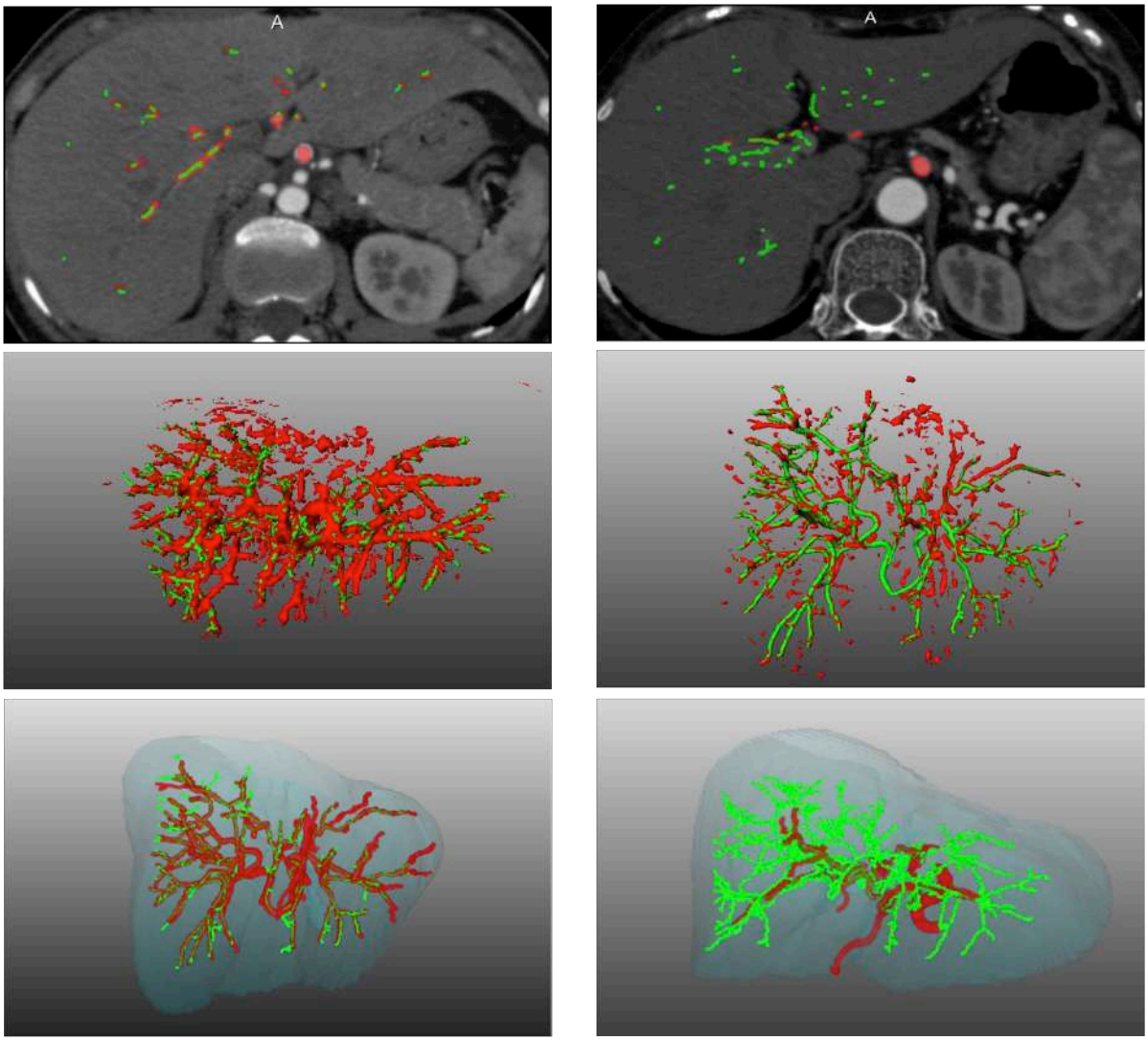

Figure 6.10: Examples showing two cases with high (left column) and low (right column) SC values. (Top row) the 2D view of ground truth (red) and segmentation (green); (Middle row) the vessel segments (red) and the reconnected vessel branches (green); (Bottom row) the 3D visualization of ground truth (red) and segmentation (green).

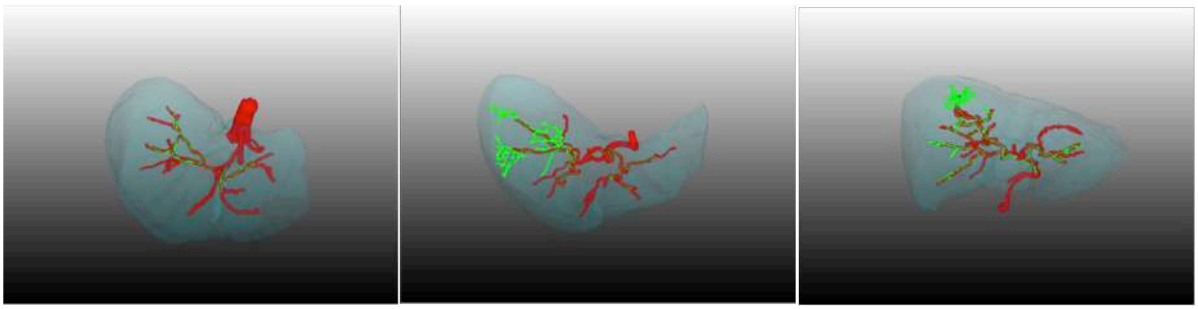

Figure 6.11: Visual demonstration of the reference (red) and segmented (green) HA vessels.

algorithm used in separation of HV and PV depends on the marker positions. We search for the local maxima in the near of two placed seed markers and extend number of seeds by adding neighboring points. The correction of seed markers helps to improve the robustness and reliability of the separation method. The proposed semi-automatic segmentation framework is capable of capturing venous vasculatures in both healthy and oncological livers. The latter case normally consists of lesions with varied sizes and incomplete vasculatures. The extensive quantitative test proves the applicability in the application of computer-aided surgery planning. A user study, aiming to measure the performance gain, is planned for the further work.

For the segmentation of HA, the proposed directional dilation morphological operator along the vessel centerline orientation is capable of bridging the gap between the broken vessel segments to some extent. The subsequent Dijkstra-based vessel connectivity algorithm has a great potential to reliably reconstruct the complete vessel tree, and thus to improve the workflow of liver surgery planning. To guarantee the performance of the algorithm, the HA phase CT should be taken with a satisfactory quality where no substantial amount of other vasculatures are enhanced.

The segmentation of vasculatures has been one of the most popular and challenging tasks in clinical routines. Many imaging modalities dedicated to delineating vessel structures are applied, such as 2D or 3D angiography based on CT, MRI or ultrasound [161, 167, 177]. Therefore, many contributions related to vessel segmentation have been reported with various focus. A large portion of these works focuses on the extraction of the center line of a vessel in 2D or 3D [163, 169, 178], where no reliable radius estimation is investigated. Among the works proposed to segment complete vessel in 3D, there are two main categories of approaches, Hessian- or model-based methods [171, 177]. As mentioned in previous sections, no standard metrics have been proposed to evaluate the segmentation quality with respect to both center line and radius accuracy, which makes a horizontal performance comparison between different studies quite difficult. Moreover, the scale and quality of test images used in different contributions are very inhomogeneous. Many works only reported the results based on either synthetic images or a data set with very limited number of cases [163, 165, 171]. Our approach was developed with an intention to fulfill the standard of commercial usage. Compared to other solutions, our approach is computational efficient, robust against bad image qualities suffering low signal to noise ratio, and applicable for various input images without any assumptions of prior knowledge. Certainly, a few drawbacks of our approach have been explored. For instance, it attempts to over-segment rather than under-segment the vasculatures, considering the fact that deleting unwanted branches is easier than adding missing branches in subsequent interactive editing mode. Furthermore, the error inherited from Hessian vesselness filter, such as the enhancement error of branch bifurcation, was not completely avoided, which might lead to broken branches, especially for thin vessels.

7

Conclusions

The theoretical principles and practical applications of various shape descriptors have demonstrated their efficiency and efficacy on several fundamental image processing tasks, ranging from segmentation, registration to detection and classification. Shape information of the target objects to be analyzed plays an important role in computer vision and image processing. Particularly in the field of medical image processing, due to the fact that specified organs or body structures normally sustain solid shapes, a prominent descriptor that is dedicated to a specific shape can dramatically simplify the task of object extraction. A shape filter can not only enhance the structures possessing a particular shape but also suppress other structures with different or none (such as noise) shapes. Therefore, shape filters are more favored when handling an object with a relatively stable 2D or 3D morphology compared to other basic edge or line filters, which are sensitive to only intensity change. In this thesis, we have demonstrated a series of typical applications that leverage the discrimination power of shape descriptors. These filters are selected by considering both performance and efficiency, because time constraints have to be fulfilled in practical clinical routines.

In Chapter 2, we investigated the usage of a modified version of Hough transform, aiming to locate and segment the boundary of femur heads in 2D fluoroscopic images. Hough transform has been commonly adopted in describing regular shapes that can be expressed analytically by mathematical equations, such as a circle, eclipse or line [40]. It can be also extended to identify arbitrary shapes by building a map encoding the shape characteristics. The task of femur head identification in fluoroscopic images is full of challenges, for instance, the intensity inhomogeneity, low signal to noise ratio, varying imaging views and so on. To overcome these obstacles, we have designed a dedicated framework based on Gabor-based Hough transform. First of all, the prominent edge pixels were detected by Gabor filters that capture the gratitude and orientation of the gradient direction. Considering the discontinuity of femur head boundary, we extended the Gabor filter by introducing a curve operator that bends the Gabor filter into an arc shape, to better fit with the curved boundary of femur head. Our experiments shown the curved Gabor filter outperformed the traditionally used

Canny edge detector. Then, the Hough transform is applied only to the detected edge pixels, such that the accumulation map will not be influenced by irrelevant pixels other than femur head boundary. To cope with the false positive results appeared in the acetabular region, we enforced scanning procedure to search for the circle pairs representing both acetabular and femoral boundaries. The quantitative experiments, using a test data set comprising 1184 fluoroscopic images with 719 AP views and 465 ML views, were carried out. From the statistical results, the detection rate for all test images was 80%, and for normal and moderate categories it was 91.4%. Note that the high detection rate of 98.5% was achieved in the normal category, which proved its capability in normal clinical practice. Moreover, the method was implemented in C++ using OpenMP based parallelization for the computationally expensive parts. The average computational time per case was 2.04 seconds in an Intel Core2 Duo 2.2GHz CPU, such that the efficiency is guaranteed for practical usage.

In Chapter 3, a Hessian-based shape descriptor has proven its applicability to enhance sheet-like structures [75]. The boundary surface of many human organs exhibit as sheet-like plane. A typical example is the pectoral muscle in 3D breast MR images. The segmentation of pectoral muscle is the most challenging step in the whole breast segmentation work flow, attributed to the bias field artifacts which lead to the intensity variation even for the same type of tissue. This type of non-uniformity can fail many segmentation techniques that assume the intensity in-homogeneity is not severe. However, normally the quality of breast MRI suffers a lot from this artifact. The sheetness filter we designed has shown its potential to cope with this problem. Since the Hessian-based shape descriptor is quite invariant to continuous intensity variation caused by bias field artifact, it is able to enhance and capture the structures with sheet-like shapes, as long as the local contrast to neighboring tissue of an object still preserves the shape appearance. We have designed the sheetness filter in a way that its response is always positive and normalized from 0 to 1. It acts like a probability map that indicates the likelihood of each voxel lying on a sheet. The response normalization is a very important feature that allows for comparison across different data sets. Dislike CT images, the gray value of MRI is not standardized and can vary a lot between different image sequences. Therefore, it is quite beneficial to develop a filter whose response is normalized and comparable when applying on MR images. Furthermore, the computational efficiency is taken into account as a key property. We have optimized the filter to minimize its computational expense when processing 3D MR volumes with high resolution. To prove the performance of the filter and the entire segmentation framework, two major experiments were conducted to evaluate pectoral muscle segmentation and the breast segmentation. The method of pectoral muscle segmentation was evaluated quantitatively with a test data set which includes 30 breast MR images by measuring the average distances between the segmented boundary and the annotated surfaces in two ground truth sets, and the statistics showed that the mean distance was 1.434 mm with the standard deviation of 0.4661 mm. In the second experiment, the segmented breast boundaries of 84 breast MR images, acquired in five different sites with variant imaging protocols, were compared to the manual segmentation. An average distance of 2.56mm with a standard deviation of 3.26mm was achieved.

Since the breast segmentation method was developed, it has been integrated as a key preprocessing procedure in many applications, for instance, the registration of breast current and prior MRI studies (see Section 3.2), the construction of breast deformation models[179, 180], the segmentation of breast fibroglandular tissue [181], bias field correction in breast MRI [182], breast density estimation based on MRI [71] or the computer-aided diagnostic tools such as lesion classification (see Chapter 4).

In Chapter 4, a computer-aided diagnostic system dedicated to automating the breast lesion interpretation is introduced. In the clinical routine of reading breast MRI, the delineation and diagnosis of nonmass breast lesions such as ductal carcinoma in situ are among the most challenging tasks. Recent studies show that kinetic features derived from dynamic contrast enhanced MRI are less effective in discriminating malignant nonmasses against benign ones due to their similar kinetic characteristics [104]. Adding shape descriptors can improve the differentiation accuracy. From another aspect, based on the standard BI-RADS guideline of interpreting breast MRI lesion, shape characteristics are recommended as very important factors to adjudge the malignancy of the lesions [105]. A mass lesion with round or oval shapes tends to be benign compared to irregular shapes with spiculated margins. In this work, we proposed a set of novel morphological features using the sphere packing technique, aiming to discriminate breast lesions based on their shapes. Among the features that we have introduced, it is found that the volume-radius histogram feature is the most prominent one. Meanwhile, other features like packing fraction index, graph topological features, and 3D Zernike descriptors have shown their potential to discriminate the lesion types. As many of our previous work, to test the performance of this system, we have collected 106 findings comprising 68 malignant and 38 benign lesions extracted from 86 patients. As a result, we achieved an accuracy of 89.62%, precision of 90.1% and area under the ROC curve of 0.972 for the differentiation of benign and malignant types. Our study using the volume-radius shape descriptor achieved very high discrimination accuracy.

In Chapter 5, Laplacian and Hessian-based shape descriptors used for automatic nipple detection in 3D breast ultrasound sequences are proposed. Three dimensional breast ultrasound emerged as a new imaging modality for breast cancer screening and diagnosis, especially for the high-risk group of women [146, 147]. Since this imaging technique has not been widely exploited in clinical routine, there are a few groups focusing on the development of computer assisted tools for this modality. Nipple position provides useful diagnostic information in reading automated 3D breast ultrasound images. The identification of nipples is required to localize and determine the quadrants of breast lesions. Nevertheless, the presence of speckle noise induced by interference waves and variant imaging directions in ultrasonography poses challenges to the task. In this work, we first propose a fast and automated algorithm to detect nipples in 3D breast ultrasound images. The method fully takes advantages of the consistent characteristics of ultrasonographic signals observed at nipples and employs a multi-scale Laplacian-based blob detector to eventually identify nipple positions. Then, we extend the multi-scale Laplacian-based method, by integrating a specially designed Hessian-based method to locate the shadow area beneath the nipple and areola. Subsequently, the likelihood

maps of nipple positions generated by both methods are combined to build a joint-likelihood map, where the final nipple position is extracted. To validate the efficiency and robustness, the extended hybrid method was tested on 926 ABUS images, resulting in a distance error of 7.08 ± 10.96 mm (mean $\pm$ standard deviation). To the extent of our knowledge, none of the published works have used such a scale of test data for evaluation. Therefore, we have much confidence in the performance and efficiency of this hybrid method, which has a potential to commercial usage.

In Chapter 6, we propose a framework based on a novel vesselness shape descriptor to analyze liver vasculatures in multi-phase CT images. The major vessels of liver are critical for liver surgical planning and diagnosis of liver disease, which are hepatic vein (HV), portal vein (PV), and hepatic artery (HA). First of all, we focus on the venous vasculatures: HV and PV. During the acquisition of multi-phase CT images, both of the venous vessels are enhanced by injected contrast agent and acquired either in a common phase or in two individual phases. Therefore, the analysis normally consists of two important preprocessing tasks: segmenting both vasculatures and separating them from each other by assigning different labels. The enhanced signals established by contrast agent are often not stably acquired due to non-optimal acquisition time. Inadequate contrast and the presence of large lesions in oncological patients, make the segmentation task quite challenging. Firstly, presented vasculatures are automatically segmented by adopting an efficient multi-scale Hessian-based vesselness filter. The initially segmented vessel trees are then converted to a graph representation, on which a series of graph filters are applied in post-processing steps to rule out irrelevant structures. Eventually, we develop a semi-automatic workflow to refine the segmentation in the areas of inferior vena cava and entrance of portal veins, and to simultaneously separate hepatic veins from portal veins.

The segmentation of hepatic artery is not an easy task, because HA is normally very thin inside liver. However, segmentation of hepatic arteries in multi-phase computed tomography images is indispensable in liver surgery planning, since the distribution of HA has many variations. If these variations were not observed before surgery, vessel damage might occur during the surgery. During image acquisition, the hepatic artery is enhanced by the injection of contrast agent. The enhanced signals are often not stably acquired due to non-optimal contrast timing. Other vascular structure, such as hepatic vein or portal vein, can be enhanced as well in the arterial phase, which can adversely affect the segmentation results. Furthermore, the arteries might suffer from partial volume effects due to their small diameter. To overcome these difficulties, first, an efficient multi-scale Hessian-based *vesselness* filter is applied on the artery phase CT image, aiming to enhance vessel structures with specified diameter range. Second, the *vesselness* response is processed using a Bayesian classifier to identify the most probable vessel structures. Considering the *vesselness* filter normally performs not ideally on the vessel bifurcations or the segments corrupted by noise, two vessel-reconnection techniques are proposed. The first technique uses a directional morphological operator to dilate vessel segments along their center line directions, attempting to fill the gap between broken vascular segments. The second technique analyzes the connectivity of vessel segments and

reconnects disconnected branches. Finally, a 3D vessel tree is reconstructed.

To evaluate the segmentation method, intensive tests enclosing 60 CT images from both healthy liver donors and oncological patients was conducted. To quantitatively measure the similarities between segmented and reference vessel trees, we propose three additional metrics: skeleton distance, branch coverage, and boundary surface distance, which are dedicated to quantifying the misalignment induced by both branching patterns and radii of two vessel trees. These proposed metrics could be helpful to measure the similarity between two tree-like structures.

By reviewing these five application challenges chosen in this dissertation, all of them aim at a fully automated image processing solution, each for a clinically relevant problem, and always applied to routine clinical image data. In many instances, a comparison to existing methods was performed and the suitability of the achieved solutions was demonstrated. Due to the real-world orientation of these five experiments, the development of these solutions was facing a highly challenging situation in each of them due to variability in image acquisition, anatomical and pathological variability, numerous imaging artifacts, and the lack of a valid and complete geometric model for the structure to be detected. It should be noted that in the chosen area, publications exist with higher accuracy values, but often those contributions are based on much less problematic cases as compared to the presented solutions.

The latest trend in medical image computing is that the methods based on deep learning techniques have shown their huge potential in dealing with the challenges in segmentation, registration, detection and classification. Tremendous contributions using deep learning have been published in recent years, after their great success in the applications of computer vision. Many tasks including the applications introduced in this dissertation are reported to be handled well with higher accuracy [183, 184]. Deep learning approaches have their inherit advantages in detection and classification tasks if a large scale of training samples were given. In computer vision, 2D images serve as the most common input for training and testing. However, in medical image computing, 3D or even 4D images are the most common input for algorithms. Therefore, deep learning might encounter some difficulties in interpreting 3D data. Smart strategies of partitioning 3D images and parallel training have to be considered. Deep learning techniques are suitable for analyzing gray level images, while the shape analysis can be applied on binary images containing shape information. Another bottle neck limiting the performance of deep learning in medical image computing is the scale and quality of the training samples. It has been proved that deep learning performs worse than traditional techniques when no sufficient training samples with annotation can be provided [185]. Hence, to build a ”MedImageNet” data set that is equivalent to the scale and quality of the ”ImageNet” for computer vision is the most urgent task [186]. Once this medical data set is built, it will boost the performance of many deep learning solutions for medical imaging tasks.

In summary, in this thesis, we have explored several versatile and cost-effective shape descriptors and their typical applications in basic medical image processing procedures. The extensive tests have shown that the shape descriptors are of great value in solving practical challenges due to their advantages in accuracy, efficiency, and effectiveness.

Publications by Lei Wang

1. **Wang L**, Schnurr A, Zidowitz S, et al. (2016) Segmentation of hepatic arteries in multi-phase liver CT using directional dilation and connectivity analysis. SPIE Med. Imaging. pp. 97851P-97851P-8.

2. **Wang L**, Chitiboi T, Meine H, et al. (2016) Principles and methods for automatic and semi-automatic tissue segmentation in MRI data. Magn Reson Mater Physics, Biol Med 29, pp. 95-110.

3. **Wang L**, Strehlow J, Rühaak J, et al. (2015) A fast alignment method for breast MRI follow-up studies using automated breast segmentation and current-prior registration. SPIE Med. imaging. 9413, pp. 941334-941334-8.

4. **Wang L**, Gubern-merida A, Diekmann S, et al. (2015) Automatic spatial linking of lesions in breast MRI follow-up images. RSNA.

5. **Wang L**, Gubern-Merida A, Diaz O, et al. (2015) Automated assessment of motion in breast MRI to assess study quality and prevent unnecessary call-backs. ECR 1-10.

6. **Wang L**, Harz M, Böhler T, et al. (2014) A robust and extendable framework towards fully automated diagnosis of nonmass lesions in breast DCE-MRI. IEEE Int Symp Biomed Imaging (ISBI).

7. **Wang L**, Böhler T, Zöhrer F, et al. (2014) A hybrid method towards automated nipple detection in 3D breast ultrasound images. 36th Annual International Conference of the IEEE Engineering in Medicine and Biology Society, pp. 2869-2872.

8. **Wang L**, Böhler T, Zöhrer F, et al. (2014) Fully Automated Nipple Detection in 3D Breast Ultrasound Images. Breast Imaging: 12th International Workshop, IWDM, pp. 64-71.

9. **Wang L**, Hansen C, Zidowitz S, Hahn HK (2014) Segmentation and separation of venous vasculatures in liver CT images. SPIE Med Imaging, pp. 90350Q-90350Q-8.

10. **Wang L**, Hansen C, Zidowitz S, Hahn HK (2013) Interactive Segmentation of Vascular Structures in CT Images for Liver Surgery Planning. Dtsch. Gesellschaft für Comput. und Robot. Chir (CURAC).

11. **Wang L**, Platel B, Ivanovskaya T, et al. (2012) Fully automatic breast segmentation in 3D breast MRI. IEEE Int Symp Biomed Imaging(ISBI), pp. 1024-1027.

12. **Wang L**, Kohnen M, Friman O, Hahn HK (2011) Fast automated segmentation of femoral heads in fluoroscopic X-ray images. IEEE Int. Symp. Biomed. Imaging (ISBI), pp. 984-988.

13. **Wang L**, Hendrik J, Bornemann L, Hahn HK (2012) A Minimally-interactive Method to Segment Enlarged Lymph Nodes in 3D Thoracic CT Images Using a Rotatable Spiral-Scanning Technique. SPIE Med imaging 8315, pp. 83150D-83150D-8.

14. **Wang L**, Filippatos K, Friman O, Hahn HK (2011) Fully automated segmentation of the pectoralis muscle boundary in breast MR images. SPIE Med. imaging. pp. 796309-796309-8.

15. **Wang L**, Zöhrer F, Friman O, Hahn HK (2011) A fully automatic method for nipple detection in 3D breast ultrasound images. Comput Assist Radiol Surg (CARS) , pp. S191-S192.

16. Tan T, Gubern-Merida A, Borelli C, **Wang L**, et al. (2016) Segmentation of malignant lesions in 3D breast ultrasound using a depth-dependent model. Med Phys 43, pp. 4074-4084.

17. Srikantha, A.; Harz, M.T.; Newstead, G.; **Wang, L**; Platel, B.; Hegenscheid, K.; Mann, R.M.; Hahn, H.K.; Peitgen H-O (2013) Symmetry-based detection and diagnosis of DCIS in breast MRI. Pattern Recognition: 35th German Conference (GCPR), In: Lect. Notes Comput. Sci, pp. 255-260.

18. Razavi M, **Wang L**, Tan T, et al. (2016) Novel morphological features for non-mass-like breast lesion classification on DCE-MRI. MICCAI Workshop on Machine Learning in Medical Imaging(MLMI), Lect Notes Comput Sci, pp. 305-312.

19. Schwen LO, Wei W, Gremse F, **Wang L**, et al. (2015) Algorithmically generated rodent hepatic vascular trees in arbitrary detail. J Theor Biol 365, pp. 289-300.

20. Schwaab J, Merida AG, **Wang L**, Günther M (2015) Automatic Assessment of the Nipple Position in 3D Breast Ultrasound Images. MICCAI BIA 1-8.

21. Razavi M, **Wang L**, Gubern-Merida A, et al. (2015) Towards accurate segmentation of fibroglandular tissue in breast MRI using fuzzy c-means and skin-folds removal. Image Anal Process, ICIAP.

22. Ivanovskaya T, **Wang L**, Hegenscheid K, Völzke H (2015) Sliding Level Set-Based Boundary : Fully Automated Dense Breast Segmentation in Native MR Mammograms. Miccai Bia 1-8.

23. Pätz T, Harz M, **Wang L**, et al. (2015) Sliding Motion in Breast Deformation Modeling. MICCAI-BIA 2015, Proc 3rd MICCAI Work Breast Image Anal 1-8.

24. Diez Y, Gubern-Merida A, **Wang L**, et al. (2014) Comparison of methods for current-to-prior registration of breast DCE-MRI. Breast Imaging: 12th International Workshop, IWDM, pp. 689-695.

25. Sänger, C., Schenk, A., Schwen, L. O., **Wang, L.**, Gremse, F., Zafarnia, S., Dahmen, U. (2015). Intrahepatic Vascular Anatomy in Rats and Mice-Variations and Surgical Implications. PLoS ONE, 10(11).

26. Ivanovska T, Laqua R, **Wang L**, et al. (2014) A level set based framework for quantitative evaluation of breast tissue density from MRI data. PLoS One 9:e112709.

27. Ivanovska T, Laqua R, **Wang L**, et al. (2014) An Efficient Level Set Method for Simultaneous Intensity Inhomogeneity Correction and Segmentation for MR Images. IEEE Trans. Med. Imaging.

28. Ivanovska T, **Wang L**, Laqua R, et al. (2013) A fast global variational bias field correction method for MR images. In: 8th Int. Symp. Image Signal Processing.

29. Gubern-Merida A, **Wang L**, Kallenberg M, et al. (2013) Breast segmentation in MRI: quantitative evaluation of three methods. SPIE Med. imaging, pp. 86693G-86693G-7.

30. Ivanovska T, Laqua R, **Wang L**, et al. (2013) Fast implementations of the levelset segmentation method with bias field correction in MR images: Full domain and mask-based versions. IbPRIA, pp. 674-681.

31. Srikantha A, Harz M, **Wang L**, et al. (2012) Symmetry-based detection of ductal carcinoma in situ in breast MRI. Eur J Radiol 81 Suppl 1, pp. S158-9.

32. Harz MT, Georgii J, **Wang L**, et al. (2012) Efficient Breast Deformation Simulation. Work Virtual Real Interact Phys Simul, pp. 117-126.

33. Hahn HK, Harz MT, Seyffarth H, **Wang L**, et al. (2010) Concepts for efficient and reliable multi-modal breast image reading. Int. Work. Breast Imaging (IWDM). In Lect. Notes Comput. Sci. , pp. 121-128.

Bibliography

[1] M. Kass, a. P. Witkin, D. Terzopoulos, and Snakes, *Active contour models,* Int. J. Comput. Vis. **1**, 133 (1987).

[2] F. Heckel, H. Meine, J. H. Moltz, J.-M. Kuhnigk, J. T. Heverhagen, A. Kiessling, B. Buerke, and H. K. Hahn, *Segmentation-Based Partial Volume Correction for Volume Estimation of Solid Lesions in CT,* IEEE Transactions on Medical Imaging **33**, 462 (2014).

[3] S. Osher and J. Sethian, *Fronts Propagating with Curvature Dependent Speed: Algorithms Based on Hamilton-Jacobi Formulations,* Journal of Computational Physics **79**, 12 (1988).

[4] J. Sethian, *Level set methods and fast marching methods : evolving interfaces in computational geometry, fluid mechanics, computer vision, and materials science* (Cambridge University Press, 1999).

[5] Y. Boykov and V. Kolmogorov, *An experimental comparison of min-cut/max- flow algorithms for energy minimization in vision,* Pattern Analysis and Machine Intelligence, IEEE Transactions on **26**, 1124 (2004).

[6] V. Kolmogorov and R. Zabin, *What energy functions can be minimized via graph cuts?* Pattern Analysis and Machine Intelligence, IEEE Transactions on **26**, 147 (2004).

[7] J. Talairach and P. Tournoux, *Co-planar stereotaxic atlas of the human brain. 3-Dimensional proportional system: an approach to cerebral imaging* (Thieme; 1st Edition edition, 1988).

[8] R. Kikinis, M. Shenton, D. Iosifescu, R. McCarley, P. Saiviroonporn, H. Hokama, A. Robatino, D. Metcalf, C. Wible, C. Portas, R. Donnino, and F. Jolesz, *A digital brain atlas for surgical planning, model-driven segmentation, and teaching,* IEEE Transactions on Visualization and Computer Graphics **2**, 232 (1996).

[9] T. Rohlfing, R. Brandt, R. Menzel, D. B. Russakoff, and C. R. Maurer, *Quo Vadis, Atlas-Based Segmentation?* in *Handbook of Biomedical Image Analysis* (Springer US, Boston, MA, 2005) pp. 435–486.

[10] T. Rohlfing, R. Brandt, R. Menzel, and C. R. Maurer, *Evaluation of atlas selection strategies for atlas-based image segmentation with application to confocal microscopy images of bee brains.* NeuroImage **21**, 1428 (2004).

[11] T. Heimann and H. P. Meinzer, *Statistical shape models for 3D medical image segmentation: A review,* Medical Image Analysis **13**, 543 (2009).

[12] N. Otsu, *A Threshold Selection Method from Gray-Level Histograms,* IEEE Trans. Syst., Man, Cybern., Syst. **9**, 62 (1979).

[13] D. Comaniciu and P. Meer, *Mean shift: A robust approach toward feature space analysis,* IEEE trans. Analysis and Machine Intelligence **24**, 603 (2002).

[14] S. Z. Li, *Markov Random Field Modeling in Image Analysis* (Springer Science & Business Media, 2009) p. 362.

[15] L. Wang, K. Filippatos, O. Friman, and H. Hahn, *Fully automated segmentation of the pectoralis muscle boundary in breast MR images,* SPIE medical imaging **7963**, 796309 (2011).

[16] Y. Sato, S. Nakajima, N. Shiraga, H. Atsumi, S. Yoshida, T. Koller, G. Gerig, and R. Kikinis, *Three-dimensional multi-scale line filter for segmentation and visualization of curvilinear structures in medical images,* Med Image Anal LECTURE NOTES IN COMPUTER SCIENCE, **2**, 143 (1998).

[17] A. F. Frangi, W. J. Niessen, K. L. Vincken, and M. a. Viergever, *Multiscale vessel enhancement filtering,* in *Medial Image Computing and Computer-Assisted Invervention - MICCAI'98. Lecture Notes in Computer Science, vol 1496*, Vol. 1496 (Springer, 1998) pp. 130–137.

[18] L. M. J. Florack, J. J. Koenderink, and M. Viergever, *Scale and the differential structure of images,* Image and Vision Computing **10**, 376388 (1992).

[19] L. Wang, F. Zoehrer, O. Friman, and H. K. Hahn, *A fully automatic method for nipple detection in 3D breast ultrasound images,* Computer Assisted Radiology and Surgery **6**, S191 (2011).

[20] J. J. Koenderink and A. J. van Doorn, *Surface shape and curvature scales,* Image and Vision Computing **10**, 557 (1992).

[21] H. Yoshida and J. Näppi, *Three-dimensional computer-aided diagnosis scheme for detection of colonic polyps.* IEEE transactions on medical imaging **20**, 1261 (2001).

[22] X. Zhang, G. McLennan, E. a. Hoffman, and M. Sonka, *Automated detection of small-size pulmonary nodules based on helical CT images.* Information processing in medical imaging **19**, 664 (2005).

[23] M. Wang and Z. Song, *Automatic Detection of Fiducial Marker Center Based on Shape Index and Curvedness,* Image (Rochester, N.Y.) , 81 (2008).

[24] F. Phillips and J. T. Todd, *Perception of local three-dimensional shape,* Journal of Experimental Psychology: Human Perception and Performance **22**, 930 (1996).

[25] W.-Y. Kim and Y.-S. Kim, *A region-based shape descriptor using Zernike moments,* Signal Processing: Image Communication **16**, 95 (2000).

[26] V. Venkatraman, L. Sael, and D. Kihara, *Potential for protein surface shape analysis using spherical harmonics and 3D Zernike descriptors,* Cell biochemistry and biophysics **54**, 23 (2009).

[27] Z. Chen and S. K. Sun, *A zernike moment phase-based descriptor for local image representation and matching,* IEEE Transactions on Image Processing **19**, 205 (2010).

[28] J. Ricard, D. Coeurjolly, and A. Baskurt, *Generalizations of angular radial transform for 2D and 3D shape retrieval,* Pattern Recognition Letters **26**, 2174 (2005).

[29] M. R. Teague, *Image analysis via the general theory of moments*,* JOSA **70**, 920 (1980).

[30] C.-H. Teh and R. T. Chin, *On image analysis by the methods of moments,* Pattern Analysis and Machine Intelligence, IEEE Transactions on **10**, 496 (1988).

[31] Z. von F, *Beugungstheorie des schneidenver-fahrens und seiner verbesserten form, der phasenkontrastmethode,* Physica **1**, 689 (1934).

[32] M. S. Al-Rawi, *3D (pseudo) Zernike moments: Fast computation via symmetry properties of spherical harmonics and recursive radial polynomials,* in *Image Processing (ICIP), 2012 19th IEEE International Conference on* (IEEE, 2012) pp. 2353–2356.

[33] P. G. Callahan and M. D. Graef, *Precipitate shape fitting and reconstruction by means of 3D Zernike functions,* Modelling and Simulation in Materials Science and Engineering **20**, 15003 (2012).

[34] N. Canterakis, *3D Zernike moments and Zernike affine invariants for 3D image analysis and recognition,* in *In 11th Scandinavian Conf. on Image Analysis* (Citeseer, 1999).

[35] M. Novotni and R. Klein, *Shape retrieval using {3D} {Zernike} descriptors,* Computer-Aided Design **36**, 1047 (2004).

[36] J. Teuber, R. Weller, G. Zachmann, and S. Guthe, *Fast Sphere Packings with Adaptive Grids on the GPU,* In GI AR VRWorkshop , 181 (2013).

[37] R. Weller and G. Zachmann, *ProtoSphere: a GPU-assisted prototype guided sphere packing algorithm for arbitrary objects,* ACM SIGGRAPH ASIA 2010 Sketches , 1 (2010).

[38] S. Belongie, J. Malik, and J. Puzicha, *Shape context: A new descriptor for shape matching and object recognition,* Advances in Neural Information Processing Systems **546**, 831 (2000), arXiv:arXiv:1011.1669v3 .

[39] R. Veltkamp and M. Hagedoorn, *State of the Art in Shape Matching,* Principles of Visual Information Retrieval , 87 (2001).

[40] S. C. Pei and J. H. Horng, *Circular-arc Detection Based On Hough Transform,* Pattern Recognition Letters **16**, 615 (1995).

[41] S.-h. Chiu, C. Wen, J. Lee, K. Lin, and H. Chen, *A FAST RANDOMIZED GENERALIZED HOUGH TRANSFORM FOR ARBITRARY SHAPE DETECTION,* International Journal of ... **8**, 1103 (2012).

[42] R. A. Zoroofi, Y. Sato, T. Sasama, T. Nishii, N. Sugano, K. Yonenobu, H. Yoshikawa, T. Ochi, and S. Tamura, *Automated Segmentation of Acetabulum and Femoral Head from 3-D CT Images,* IEEE Transactions on Information Technology in Biomedicine **7**, 329 (2003).

[43] Y. Cheng, S. Zhou, Y. Wang, C. Guo, J. Bai, and S. Tamura, *Automatic segmentation technique for acetabulum and femoral head in {CT} images,* Pattern Recognition **46**, 2969 (2013).

[44] F. Yokota, T. Okada, M. Takao, N. Sugano, Y. Tada, and Y. Sato, *Automated segmentation of the femur and pelvis from 3D CT data of diseased hip using hierarchical statistical shape model of joint structure,* in *Lecture Notes in Computer Science*, Vol. 5762 LNCS (2009) pp. 811–818.

[45] R. A. Zoroofi, Y. Sato, T. Nishii, N. Sugano, H. Yoshikawa, and S. Tamura, *Automated segmentation of necrotic femoral head from 3D MR data,* Computerized Medical Imaging and Graphics **28**, 267 (2004).

[46] Y. Chen, X. Ee, W. K. Leow, and T. S. Howe, *Automatic extraction of femur contours from hip x-ray images,* Computer Vision for Biomedical Image Applications: First International Workshop, CVBIA , 200 (2005).

[47] F. Ding, W. K. Leow, and T. S. Howe, *Automatic segmentation of femur bones in anterior-posterior pelvis X-ray images,* Lecture Notes in Computer Science (including subseries Lecture Notes in Artificial Intelligence and Lecture Notes in Bioinformatics) **4673 LNCS**, 205 (2007).

[48] X. Dong, M. A. G. Ballester, and G. Zheng, *Automatic extraction of femur contours from calibrated x-ray images using statistical information,* Journal of Multimedia **2**, 46 (2007).

[49] R. Chav, T. Cresson, C. Kauffmann, and J. a. de Guise, *Method for fast and accurate segmentation processing from prior shape: application to femoral head segmentation on x-ray images,* SPIE Medical Imaging 2009: Image Processing **7259**, 72594Y (2009).

[50] P. Gamage, S. Q. Xie, P. Delmas, and W. L. Xu, *Segmentation of radiographic images under topological constraints: Application to the femur,* International Journal of Computer Assisted Radiology and Surgery **5**, 425 (2010).

[51] B. T. Hammond and J. Charnley, *The sphericity of the femoral head,* Medical & Biological Engineering **5**, 445 (1967).

[52] M. a. Fischler and R. C. Bolles, *Random sample consensus: a paradigm for model fitting with applications to image analysis and automated cartography,* Communications of the ACM **24**, 381 (1981).

[53] R. Chandra, L. Dagum, D. Kohr, D. Maydan, J. McDonald, and R. Menon, *Review Literature And Arts Of The Americas*, Vol. 129 (Morgan Kaufmann, 2001) p. 230, arXiv:arXiv:1011.1669v3 .

[54] S. Sinha and U. Sinha, *Recent advances in Breast MRI and MRS,* NMR in Biomedicine **22**, 3 (2009).

[55] S. G. Orel and M. D. Schnall, *MR imaging of the breast for the detection, diagnosis, and staging of breast cancer.* Radiology **220**, 13 (2001).

[56] J. G. M. Klijn, *Early diagnosis of hereditary breast cancer by magnetic resonance imaging: What is realistic?* Journal of Clinical Oncology **28**, 1441 (2010).

[57] W. DeMartini and C. Lehman, *A Review of Current Evidence-Based Clinical Applications for Breast Magnetic Resonance Imaging,* Topics in Magnetic Resonance Imaging **19**, 143 (2008).

[58] A. J. Rijnsburger, I. M. Obdeijn, R. Kaas, M. M. A. Tilanus-Linthorst, C. Boetes, C. E. Loo, M. N. J. M. Wasser, E. Bergers, T. Kok, S. H. Muller, H. Peterse, R. A. E. M. Tollenaar, N. Hoogerbrugge, S. Meijer, C. C. M. Bartels, C. Seynaeve, M. J. Hooning, M. Kriege, P. I. M. Schmitz, J. C. Oosterwijk, H. J. De Koning, E. J. T. Rutgers, and J. G. M. Klijn, *BRCA1-associated breast cancers present differently from BRCA2-associated and familial cases: Long-term follow-up of the Dutch MRISC screening study,* Journal of Clinical Oncology **28**, 5265 (2010).

[59] C. Balleyguier, S. Ayadi, K. Van Nguyen, D. Vanel, C. Dromain, and R. Sigal, *BIRADS classification in mammography,* European Journal of Radiology **61**, 192 (2007).

[60] E. a. Morris, L. H. Schwartz, M. B. Drotman, S. J. Kim, L. K. Tan, L. Liberman, a. F. Abramson, K. J. Van Zee, and D. D. Dershaw, *Evaluation of pectoralis major muscle in patients with posterior breast tumors on breast MR images: early experience.* Radiology **214**, 67 (2000).

[61] A. Gubern-Merida, R. Marti, J. Melendez, J. L. Hauth, R. M. Mann, N. Karssemeijer, and B. Platel, *Automated localization of breast cancer in DCE-MRI,* Medical Image Analysis **20**, 265 (2015).

[62] Z. Pang, D. Zhu, D. Chen, L. Li, and Y. Shao, *A Computer-Aided Diagnosis System for Dynamic Contrast-Enhanced MR Images Based on Level Set Segmentation and ReliefF Feature Selection,* Computational and Mathematical Methods in Medicine **2015**, 1 (2015).

[63] G. Ertaş, H. Gülçür, O. Osman, O. N. Uçan, M. Tunacı, and M. Dursun, *Breast MR segmentation and lesion detection with cellular neural networks and 3D template matching,* Computers in Biology and Medicine **38**, 116 (2008).

[64] S. Wu, S. P. Weinstein, E. F. Conant, a. R. Localio, M. D. Schnall, and D. Kontos, *Fully automated chest wall line segmentation in breast MRI by using context information,* Imaging **8315**, 831507 (2012).

[65] J. Milenković, O. Chambers, M. Marolt Mušič, and J. F. Tasič, *Automated breast-region segmentation in the axial breast MR images,* Computers in Biology and Medicine **62**, 55 (2015).

[66] V. Giannini, A. Vignati, L. Morra, D. Persano, D. Brizzi, L. Carbonaro, A. Bert, F. Sardanelli, and D. Regge, *A fully automatic algorithm for segmentation of the breasts in DCE-MR images,* 2010 Annual International Conference of the IEEE Engineering in Medicine and Biology Society, EMBC'10 **2010**, 3146 (2010).

[67] M. Koenig, H. Laue, T. Boehler, H.-O. Peitgen, and M. K. Et al., *Automatic segmentation of relevant structures in DCE MR mammograms,* in *Medical Imaging*, edited by M. L. Giger and N. Karssemeijer (International Society for Optics and Photonics, 2007) pp. 65141S–65141S–6.

[68] K. Nie, J.-H. Chen, S. Chan, M.-K. I. Chau, H. J. Yu, S. Bahri, T. Tseng, O. Nalcioglu, and M.-Y. Su, *Development of a quantitative method for analysis of breast density based on three-dimensional breast MRI.* Medical physics **35**, 5253 (2008).

[69] M. Lin, J.-H. Chen, X. Wang, S. Chan, S. Chen, and M.-Y. Su, *Template-based automatic breast segmentation on MRI by excluding the chest region.* Medical physics **40**, 122301 (2013).

[70] T. Ivanovska, L. Wang, R. Laqua, K. Hegenscheid, H. Volzke, and V. Liebscher, *A fast global variational bias field correction method for MR images,* in *2013 8th International Symposium on Image and Signal Processing and Analysis (ISPA)* (2013) pp. 667–671.

[71] T. Ivanovska, R. Laqua, L. Wang, V. Liebscher, H. Völzke, and K. Hegenscheid, *A level set based framework for quantitative evaluation of breast tissue density from MRI data,* PLoS ONE **9**, e112709 (2014).

[72] C. G. Ortiz and a. L. Martel, *Automatic atlas-based segmentation of the breast in MRI for 3D breast volume computation,* Medical Physics **39**, 5835 (2012).

[73] F. Khalvati, C. Gallego-Ortiz, S. Balasingham, and A. L. Martel, *Automated Segmentation of Breast in 3-D MR Images Using a Robust Atlas,* IEEE Transactions on Medical Imaging **34**, 116 (2015).

[74] A. Gubern-Merida, M. Kallenberg, R. Mann, R. Marti, and N. Karssemeijer, *Breast segmentation and density estimation in breast MRI: a fully automatic framework,* IEEE Journal of Biomedical and Health Informatics **2194**, 2168 (2013).

[75] M. Descoteaux, L. Collins, and K. Siddiqi, *Geometric flows for segmenting vasculature in MRI: Theory and validation,* in *Medical Image Computing and …*, Vol. 3216 (2004) pp. 500–507.

[76] M. Descoteaux, M. Audette, K. Chinzei, and K. Siddiqi, *Bone enhancement filtering: Application to sinus bone segmentation and simulation of pituitary surgery,* in *Lecture Notes in Computer Science (including subseries Lecture Notes in Artificial Intelligence and Lecture Notes in Bioinformatics)*, Vol. 3749 LNCS (2005) pp. 9–16.

[77] F. Prêteux, C. I. Fetita, and P. Grenier, *Modeling, segmentation, and caliber estimation of bronchi in high resolution computerized tomography,* Journal of Electronic Imaging **8**, 36 (1999).

[78] A. Gubern-Mérida, L. Wang, M. Kallenberg, R. Martí, H. K. Hahn, and N. Karssemeijer, *Breast segmentation in MRI: quantitative evaluation of three methods,* in *SPIE medical imaging*, Vol. 8669 (2013) pp. 86693G–86693G–7.

[79] A. Gubern-Mérida, M. Kallenberg, R. Martí, and N. Karssemeijer, *Fully automatic fibroglandular tissue segmentation in breast mri: an atlas-based approach,* MICCAI Workshop: breast image analysis (2011).

[80] A. Gubern-Mérida, M. Kallenberg, R. Martí, and N. Karssemeijer, *Segmentation of the Pectoral Muscle in Breast MRI Using Atlas-Based Approaches,* Medical image computing and computer-assisted intervention : MICCAI **15**, 371 (2012).

[81] C. K. Kuhl, S. Schrading, C. C. Leutner, N. Morakkabati-Spitz, E. Wardelmann, R. Fimmers, W. Kuhn, and H. H. Schild, *Mammography, breast ultrasound, and magnetic resonance imaging for surveillance of women at high familial risk for breast cancer.* Journal of clinical oncology : official journal of the American Society of Clinical Oncology **23**, 8469 (2005).

[82] G. Abramovici and M. B. Mainiero, *Screening breast MR imaging: comparison of interpretation of baseline and annual follow-up studies.* Radiology **259**, 85 (2011).

[83] T. Boehler, K. Schilling, U. Bick, and H. K. Hahn, *Deformable Image Registration of Follow-Up Breast Magnetic Resonance Images BT - Biomedical Image Registration: 4th International Workshop, WBIR 2010, Lübeck, Germany, July 11-13, 2010. Proceedings,* Biomedical Image Registration SE - 2 **6204**, 13 (2010).

[84] L. Roose, D. Loeckx, W. Mollemans, F. Maest, and P. Suetens, *Adaptive boundary conditions for physically based follow-up breast MR image registration.A,* Medical image computing and computer-assisted intervention : MICCAI ... International Conference on Medical Image Computing and Computer-Assisted Intervention **11**, 839 (2008).

[85] Y. Diez, L. Wang, A. Gubern, J. Marti, and R. Marti, *Comparison of Methods for Current-to-Prior Registration of Breast DCE-MRI,* in *International Workshop on Breast Imaging* (2014) pp. 689–695.

[86] J. Rühaak, S. Heldmann, T. Kipshagen, and B. Fischer, *{H}ighly {A}ccurate {F}ast {L}ung {CT} {R}egistration,* in *SPIE Medical Imaging, Image Processing* (2013) pp. 86690Y–86690Y–9.

[87] J. Modersitzki, *FAIR: Flexible Algorithms for Image Registration* (SIAM, 2009) p. 189.

[88] J. Modersitzki, *Numerical Methods for Image Registration* (Oxford University Press, 2003) p. 212.

[89] E. Haber and J. Modersitzki, *Intensity gradient based registration and fusion of multi-modal images,* Methods of Information in Medicine **46**, 292 (2007).

[90] B. Fischer and J. Modersitzki, *Curvature based image registration,* Journal of Mathematical Imaging and Vision **18**, 81 (2003).

[91] J. Nocedal and S. J. Wright, *{N}umerical optimization* (Springer, 1999).

[92] L. König and J. Rühaak, *{A} {F}ast and {A}ccurate {P}arallel {A}lgorithm for {N}on-{L}inear {I}mage {R}egistration using {N}ormalized {G}radient {F}ields,* in *IEEE International Symposium on Biomedical Imaging: From Nano to Macro* (2014) pp. 580–583.

[93] T. Sorensen, *Det. Kong. Danske Vidensk, Selesk Biology Skr*, Vol. 5 (I kommission hos E. Munksgaard, 1948) pp. 1–34.

[94] Y. Díez, A. Oliver, X. Lladó, J. Freixenet, J. Martí, J. C. Vilanova, and R. Martí, *Revisiting intensity-based image registration applied to mammography,* IEEE Transactions on Information Technology in Biomedicine **15**, 716 (2011).

[95] Y. Diez, A. Oliver, M. Cabezas, S. Valverde, R. Martí, J. C. Vilanova, L. Ramió-Torrentà, À. Rovira, and X. Lladó, *Intensity based methods for brain MRI longitudinal registration. A study on multiple sclerosis patients,* Neuroinformatics **12**, 365 (2014).

[96] B. AVANTS, C. EPSTEIN, M. GROSSMAN, and J. GEE, *Symmetric diffeomorphic image registration with cross-correlation: Evaluating automated labeling of elderly and neurodegenerative brain,* Medical Image Analysis **12**, 26 (2008).

[97] D. Rueckert, L. I. Sonoda, C. Hayes, D. L. Hill, M. O. Leach, and D. J. Hawkes, *Non-rigid registration using free-form deformations: application to breast MR images.* IEEE Transactions on Medical Imaging **18**, 712 (1999).

[98] M. Modat, G. R. Ridgway, Z. A. Taylor, M. Lehmann, J. Barnes, D. J. Hawkes, N. C. Fox, and S. Ourselin, *Fast free-form deformation using graphics processing units,* Computer Methods and Programs in Biomedicine **98**, 278 (2010).

[99] J.-P. Thirion, *Non-rigid matching using demons,* Proceedings CVPR IEEE Computer Society Conference on Computer Vision and Pattern Recognition , 245 (1996).

[100] Y. Ou, A. Sotiras, N. Paragios, and C. Davatzikos, *DRAMMS: Deformable registration via attribute matching and mutual-saliency weighting,* Medical Image Analysis **15**, 622 (2011).

[101] L. Breiman, *Random forests,* Mach. Learn. **45**, 5 (2001).

[102] S. A. Jansen, A. Shimauchi, L. Zak, X. Fan, G. S. Karczmar, and G. M. Newstead, *The diverse pathology and kinetics of mass, nonmass, and focus enhancement on MR imaging of the breast,* Journal of Magnetic Resonance Imaging **33**, 1382 (2011).

[103] C. Kuhl, S. Schrading, H. Bieling, E. Wardelmann, C. Leutner, R. Koenig, W. Kuhn, and H. Schild, *MRI for diagnosis of pure ductal carcinoma in situ: A prospective observational study,* Lancet **370**, 485 (2007).

[104] S. A. Jansen, X. Fan, G. S. Karczmar, H. Abe, R. A. Schmidt, M. Giger, and G. M. Newstead, *DCEMRI of breast lesions: is kinetic analysis equally effective for both mass and nonmass-like enhancement?* Medical physics **35**, 3102 (2008).

[105] A. A. Tardivon, A. Athanasiou, F. Thibault, and C. El Khoury, *Breast imaging and reporting data system (birads): magnetic resonance imaging,* European journal of radiology **61**, 212 (2007).

[106] C. K. Kuhl, S. Schrading, H. B. Bieling, E. Wardelmann, C. C. Leutner, R. Koenig, W. Kuhn, and H. H. Schild, *Mri for diagnosis of pure ductal carcinoma in situ: a prospective observational study,* The Lancet **370**, 485 (2007).

[107] S. G. Orel and M. D. Schnall, *Mr imaging of the breast for the detection, diagnosis, and staging of breast cancer 1,* Radiology **220**, 13 (2001).

[108] W. DeMartini and C. Lehman, *A review of current evidence-based clinical applications for breast magnetic resonance imaging,* Topics in magnetic resonance imaging **19**, 143 (2008).

[109] C. Kuhl, *The current status of breast mr imaging part i. choice of technique, image interpretation, diagnostic accuracy, and transfer to clinical practice 1,* Radiology **244**, 356 (2007).

[110] C. D. Lehman, S. Peacock, W. B. DeMartini, and X. Chen, *A new automated software system to evaluate breast mr examinations: improved specificity without decreased sensitivity,* American Journal of Roentgenology **187**, 51 (2006).

[111] M. Goto, H. Ito, K. Akazawa, T. Kubota, O. Kizu, K. Yamada, and T. Nishimura, *Diagnosis of breast tumors by contrast-enhanced MR imaging: comparison between the diagnostic performance of dynamic enhancement patterns and morphologic features,* Journal of magnetic resonance imaging : JMRI **25**, 104 (2007).

[112] N. H. Peters, I. H. Borel Rinkes, N. P. Zuithoff, W. P. Mali, K. G. Moons, and P. H. Peeters, *Meta-analysis of mr imaging in the diagnosis of breast lesions 1,* Radiology **246**, 116 (2008).

[113] C. K. Kuhl, S. Schrading, C. C. Leutner, N. Morakkabati-Spitz, E. Wardelmann, R. Fimmers, W. Kuhn, and H. H. Schild, *Mammography, breast ultrasound, and magnetic resonance imaging for surveillance of women at high familial risk for breast cancer,* Journal of clinical oncology **23**, 8469 (2005).

[114] D. Saslow, C. Boetes, W. Burke, S. Harms, M. O. Leach, C. D. Lehman, E. Morris, E. Pisano, M. Schnall, S. Sener, *et al.*, *American cancer society guidelines for breast screening with mri as an adjunct to mammography,* CA: a cancer journal for clinicians **57**, 75 (2007).

[115] M. Kriege, C. T. Brekelmans, C. Boetes, P. E. Besnard, H. M. Zonderland, I. M. Obdeijn, R. A. Manoliu, T. Kok, H. Peterse, M. M. Tilanus-Linthorst, *et al.*, *Efficacy of mri and mammography for breast-cancer screening in women with a familial or genetic predisposition,* New England Journal of Medicine **351**, 427 (2004).

[116] M. O. Leach, *Breast cancer screening in women at high risk using mri,* NMR in biomedicine **22**, 17 (2009).

[117] C. D. Lehman, J. D. Blume, D. Thickman, D. A. Bluemke, E. Pisano, C. Kuhl, T. B. Julian, N. Hylton, P. Weatherall, M. O'Loughlin, *et al.*, *Added cancer yield of mri in screening the contralateral breast of women recently diagnosed with breast cancer: results from the international breast magnetic resonance consortium (ibmc) trial,* Journal of surgical oncology **92**, 9 (2005).

[118] M. D. Dorrius, M. C. Jansen-van der Weide, P. M. van Ooijen, R. M. Pijnappel, and M. Oudkerk, *Computer-aided detection in breast mri: a systematic review and meta-analysis,* European radiology **21**, 1600 (2011).

[119] E. B. Pages, I. Millet, D. Hoa, F. C. Doyon, and P. Taourel, *Undiagnosed breast cancer at mr imaging: analysis of causes,* Radiology **264**, 40 (2012).

[120] K. Yamaguchi, D. Schacht, G. M. Newstead, A. R. Bradbury, M. S. Verp, O. I. Olopade, and H. Abe, *Breast cancer detected on an incident (second or subsequent) round of screening mri: Mri features of false-negative cases,* American Journal of Roentgenology **201**, 1155 (2013).

[121] T. C. Williams, W. B. DeMartini, S. C. Partridge, S. Peacock, and C. D. Lehman, *Breast mr imaging: computer-aided evaluation program for discriminating benign from malignant lesions 1,* Radiology **244**, 94 (2007).

[122] L. C. Wang, W. B. DeMartini, S. C. Partridge, S. Peacock, and C. D. Lehman, *Mri-detected suspicious breast lesions: predictive values of kinetic features measured by computer-aided evaluation,* American Journal of Roentgenology **193**, 826 (2009).

[123] G. Ertas, H. O. Gulcur, M. Tunaci, O. Osman, and O. N. Ucan, *A preliminary study on computerized lesion localization in mr mammography using 3d nmitr maps, multilayer cellular neural networks, and fuzzy c-partitioning,* Medical physics **35**, 195 (2008).

[124] A. Vignati, V. Giannini, M. De Luca, L. Morra, D. Persano, L. A. Carbonaro, I. Bertotto, L. Martincich, D. Regge, A. Bert, *et al.*, *Performance of a fully automatic lesion detection system for breast dce-mri,* Journal of Magnetic Resonance Imaging **34**, 1341 (2011).

[125] Y.-C. Chang, Y.-H. Huang, C.-S. Huang, J.-H. Chen, and R.-F. Chang, *Computerized breast lesions detection using kinetic and morphologic analysis for dynamic contrast-enhanced mri,* Magnetic resonance imaging **32**, 514 (2014).

[126] A. Gubern-Mérida, R. Martí, J. Melendez, J. L. Hauth, R. M. Mann, N. Karssemeijer, and B. Platel, *Automated localization of breast cancer in dce-mri,* Medical image analysis **20**, 265 (2015).

[127] D. M. Renz, J. Böttcher, F. Diekmann, A. Poellinger, M. H. Maurer, A. Pfeil, F. Streitparth, F. Collettini, U. Bick, B. Hamm, *et al.*, *Detection and classification of contrast-enhancing masses by a fully automatic computer-assisted diagnosis system for breast mri,* Journal of Magnetic Resonance Imaging **35**, 1077 (2012).

[128] W. Chen, M. L. Giger, L. Lan, and U. Bick, *Computerized interpretation of breast mri: investigation of enhancement-variance dynamics,* Medical physics **31**, 1076 (2004).

[129] W. Chen, M. L. Giger, G. M. Newstead, U. Bick, S. A. Jansen, H. Li, and L. Lan, *Computerized assessment of breast lesion malignancy using dce-mri: robustness study on two independent clinical datasets from two manufacturers,* Academic radiology **17**, 822 (2010).

[130] J. Levman, T. Leung, P. Causer, D. Plewes, and A. L. Martel, *Classification of dynamic contrast-enhanced magnetic resonance breast lesions by support vector machines,* Medical Imaging, IEEE Transactions on **27**, 688 (2008).

[131] S. C. Agner, S. Soman, E. Libfeld, M. McDonald, K. Thomas, S. Englander, M. A. Rosen, D. Chin, J. Nosher, and A. Madabhushi, *Textural kinetics: a novel dynamic contrast-enhanced (dce)-mri feature for breast lesion classification,* Journal of Digital Imaging **24**, 446 (2011).

[132] J. Huang, T. Hahn, L. Hoisington, S. Schafer, X. Zong, and K. Berger, *Improving suspicious breast lesion characterization using semi-automatic lesion fractional volume washout kinetic analysis,* Medical physics **38**, 5998 (2011).

[133] S. Hoffmann, J. D. Shutler, M. Lobbes, B. Burgeth, and A. Meyer-Bäse, *Automated analysis of non-mass-enhancing lesions in breast mri based on morphological, kinetic, and spatio-temporal moments and joint segmentation-motion compensation technique,* EURASIP Journal on Advances in Signal Processing **2013**, 1 (2013).

[134] T.-C. Wang, Y.-H. Huang, C.-S. Huang, J.-H. Chen, G.-Y. Huang, Y.-C. Chang, and R.-F. Chang, *Computer-aided diagnosis of breast dce-mri using pharmacokinetic model and 3-d morphology analysis,* Magnetic resonance imaging **32**, 197 (2014).

[135] Q. Yang, L. Li, J. Zhang, G. Shao, C. Zhang, and B. Zheng, *Computer-aided diagnosis of breast dce-mri images using bilateral asymmetry of contrast enhancement between two breasts,* Journal of digital imaging **27**, 152 (2014).

[136] S. Agliozzo, M. De Luca, C. Bracco, A. Vignati, V. Giannini, L. Martincich, L. Carbonaro, A. Bert, F. Sardanelli, and D. Regge, *Computer-aided diagnosis for dynamic contrast-enhanced breast mri of mass-like lesions using a multiparametric model combining a selection of morphological, kinetic, and spatiotemporal features,* Medical physics **39**, 1704 (2012).

[137] S. A. Jansen, X. Fan, G. S. Karczmar, H. Abe, R. A. Schmidt, M. Giger, and G. M. Newstead, *Dcemri of breast lesions: Is kinetic analysis equally effective for both mass and nonmass-like enhancement?* Medical physics **35**, 3102 (2008).

[138] R. Weller and G. Zachmann, *ProtoSphere: a GPU-assisted prototype guided sphere packing algorithm for arbitrary objects,* ACM SIGGRAPH ASIA 2010 Sketches , 1 (2010).

[139] B. Gartner, *Smallest Enclosing Balls A Fast and Robust C ++ Implementation,* in *European Symposium on Algorithms* (Springer, 1999) pp. 325–338.

[140] S. Ali, R. Veltri, J. a. Epstein, C. Christudass, and A. Madabhushi, *Cell cluster graph for prediction of biochemical recurrence in prostate cancer patients from tissue microarrays,* in *SPIE Medical Imaging* (International Society for Optics and Photonics, 2013) pp. 86760H—-86760H.

[141] K. R. Gabriel and R. R. Sokal, *A new statistical approach to geographic variation analysis,* Systematic Biology **18**, 259 (1969).

[142] R. a. Botafogo, E. Rivlin, and B. Shneiderman, *Structural analysis of hypertexts: identifying hierarchies and useful metrics,* ACM Transactions on Information Systems **10**, 142 (1992).

[143] R. Raidou, U. Van Der Heide, C. Dinh, G. Ghobadi, J. Kallehauge, M. d. Breeuwer, and A. Vilanova, *Visual Analytics for the Exploration of Tumor Tissue Characterization,* in *Computer Graphics Forum*, Vol. 34 (Wiley Online Library, 2015) pp. 11–20.

[144] F. Boutin and M. Hascoet, *Cluster validity indices for graph partitioning,* in *Proceedings. Eighth International Conference on Information Visualisation, 2004. IV 2004.* (IEEE, 2004) pp. 376–381.

[145] M. L. Calle and V. Urrea, *Letter to the editor: Stability of Random Forest importance measures,* Briefings in Bioinformatics **12**, 86 (2011).

[146] V. Giuliano and C. Giuliano, *Improved breast cancer detection in asymptomatic women using 3D-automated breast ultrasound in mammographically dense breasts,* (2013).

[147] M. Nothacker, V. Duda, M. Hahn, M. Warm, F. Degenhardt, H. Madjar, S. Weinbrenner, and U.-S. Albert, *Early detection of breast cancer: benefits and risks of supplemental breast ultrasound in asymptomatic women with mammographically dense breast tissue. A systematic review,* BMC Cancer **9**, 1 (2009).

[148] T. Tan, B. Platel, R. Mus, L. Tabar, R. M. Mann, and N. Karssemeijer, *Computer-aided detection of cancer in automated 3-D breast ultrasound,* IEEE Transactions on Medical Imaging **32**, 1698 (2013).

[149] T. Tan, B. Platel, T. Twellmann, G. van Schie, R. Mus, A. Grivegnée, R. M. Mann, and N. Karssemeijer, *Evaluation of the effect ofcomputer-aided classification ofbenign and malignant lesions onreader performance in automated three-dimensional breast ultrasound,* Academic Radiology **20**, 1381 (2013).

[150] M. J. Moghaddam, T. Tan, N. Karssemeijer, and B. Platel, *Automatic Nipple Detection on 3D Images of an Automated Breast Ultrasound System (ABUS),* SPIE medical imaging **9034**, 1 (2014).

[151] a. Huertas and G. Medioni, *Detection of intensity changes with subpixel accuracy using laplacian-gaussian masks.* IEEE transactions on pattern analysis and machine intelligence **8**, 651 (1986).

[152] T. Lindeberg, *Feature detection with automatic scale selection,* International Journal of Computer Vision **30**, 79 (1998).

[153] M. Descoteaux, D. L. Collins, and K. Siddiqi, *A geometric flow for segmenting vasculature in proton-density weighted MRI,* Medical Image Analysis **12**, 497 (2008).

[154] L. Wang, T. Böhler, F. Zöhrer, J. Georgii, C. Rauh, P. a. Fasching, B. Brehm, R. Schulz-Wendtland, M. W. Beckmann, M. Uder, and H. K. Hahn, *Fully Automated Nipple Detection in 3D Breast Ultrasound Images,* International Workshop on Breast Imaging (2014).

[155] J. Ferlay, I. Soerjomataram, R. Dikshit, S. Eser, C. Mathers, M. Rebelo, D. M. Parkin, D. Forman, and F. Bray, *Cancer incidence and mortality worldwide: Sources, methods and major patterns in GLOBOCAN 2012,* International Journal of Cancer **136**, E359 (2015), arXiv:arXiv:1011.1669v3 .

[156] C. Hansen, S. Zidowitz, M. Hindennach, A. Schenk, H. Hahn, and H. O. Peitgen, *Interactive determination of robust safety margins for oncologic liver surgery,* International Journal of Computer Assisted Radiology and Surgery **4**, 469 (2009).

[157] O. Konrad-Verse, B. Preim, and A. Littmann, *Virtual Resection with a Deformable Cutting Plane.* SimVis , 203 (2004).

[158] F. Kirbas, C. Quek, *A review of vessel extraction techniques and algorithms,* Computing Surveys **36**, 81 (2004).

[159] D. Lesage, E. D. Angelini, I. Bloch, and G. Funka-Lea, *A review of 3D vessel lumen segmentation techniques: Models, features and extraction schemes,* Medical Image Analysis **13**, 819 (2009).

[160] A. H. Foruzan, R. A. Zoroofi, Y. Sato, and M. Hori, *A Hessian-based filter for vascular segmentation of noisy hepatic CT scans,* International Journal of Computer Assisted Radiology and Surgery **7**, 199 (2012).

[161] S. Kawajiri, X. Zhou, X. Zhang, T. Hara, H. Fujita, R. Yokoyama, H. Kondo, M. Kanematsu, and H. Hoshi, *Automated segmentation of hepatic vessel trees in non-contrast X-ray {CT} images,* Progress in Biomedical Optics and Imaging - Proceedings of SPIE **6512**, 65123A (2007).

[162] R. Manniesing, M. A. Viergever, and W. J. Niessen, *Vessel enhancing diffusion. A scale space representation of vessel structures,* Medical Image Analysis **10**, 815 (2006).

[163] K. Krissian, N. A. Epidaure, S. A. France, Y. Trousset, G. Electric, M. Systems, and B. Cedex, *Model Based Multiscale Detection of 3D Vessels,* Cvpr , 1 (1998).

[164] T. Pock, C. Janko, R. Beichel, and H. Bischof, *Multiscale Medialness for Robust Segmentation of {3D} Tubular Structures,* in *CVWW 2005: Proceedings of the 10th Computer Vision Winter Workshop* (2005) pp. 93–102.

[165] P. T. H. Truc, M. A. U. Khan, Y. K. Lee, S. Lee, and T. S. Kim, *Vessel enhancement filter using directional filter bank,* Computer Vision and Image Understanding **113**, 101 (2009).

[166] X. Qian, M. P. Brennan, D. P. Dione, W. L. Dobrucki, M. P. Jackowski, C. K. Breuer, A. J. Sinusas, and X. Papademetris, *A non-parametric vessel detection method for complex vascular structures,* Medical Image Analysis **13**, 49 (2009).

[167] G. Agam, S. G. Armato, and C. Wu, *Vessel tree reconstruction in thoracic CT scans with application to nodule detection,* IEEE Transactions on Medical Imaging **24**, 486 (2005).

[168] S. R. Aylward and E. Bullitt, *Initialization, noise, singularities, and scale in height ridge traversal for tubular object centerline extraction,* IEEE Transactions on Medical Imaging **21**, 61 (2002).

[169] W. C. K. Wong and A. C. S. Chung, *Probabilistic vessel axis tracing and its application to vessel segmentation with stream surfaces and minimum cost paths,* Medical Image Analysis **11**, 567 (2007).

[170] M. A. Gulsun and H. T. H. Tek, *Geometric modeling of tubular structures,* 2008 IEEE Computer Society Conference on Computer Vision and Pattern Recognition Workshops (2008), 10.1109/CVPRW.2008.4562994.

[171] S. Wörz and K. Rohr, *Segmentation and quantification of human vessels using a 3-D cylindrical intensity model,* IEEE Transactions on Image Processing **16**, 1994 (2007).

[172] A. Gooya, H. Liao, K. Matsumiya, K. Masamune, Y. Masutani, and T. Dohi, *A variational method for geometric regularization of vascular segmentation in medical images,* IEEE Transactions on Image Processing **17**, 1295 (2008).

[173] D. Selle, B. Preim, A. Schenk, and H. O. Peitgen, *Analysis of vasculature for liver surgical planning,* IEEE Transactions on Medical Imaging **21**, 1344 (2002).

[174] J. a. Sethian, *A fast marching level set method for monotonically advancing fronts.* Proceedings of the National Academy of Sciences of the United States of America **93**, 1591 (1996).

[175] J. Han and C. Moraga, *The influence of the sigmoid function parameters on the speed of backpropagation learning,* From Natural to Artificial Neural Computation Lecture Notes in Computer Science, **930**, 195 (1995).

[176] H. Hahn and H.-O. Peitgen, *The Skull Stripping Problem in MRI Solved by a Single 3D Watershed Transform,* Medical Image Computing and Computer-Assisted Intervention – MICCAI 2000 **1935**, 129 (2000).

[177] B. E. Chapman and D. L. Parker, *3D multi-scale vessel enhancement filtering based on curvature measurements: Application to time-of-flight MRA,* in *Medical Image Analysis*, Vol. 9 (2005) pp. 191–208.

[178] O. Friman, M. Hindennach, and H. O. Peitgen, *Template-based multiple hypotheses tracking of small vessels,* in *2008 5th IEEE International Symposium on Biomedical Imaging: From Nano to Macro, Proceedings, ISBI*, Vol. 2 (IEEE, 2008) pp. 1047–1050.

[179] M. T. Harz, J. Georgii, L. Wang, K. Schilling, and H.-O. Peitgen, *Efficient Breast Deformation Simulation,* Workshop on Virtual Reality Interaction and Physical Simulation , 117 (2012).

[180] T. Pätz, M. Harz, L. Wang, C. Stöcker, K. Schilling, J. Colletta, M. Schlooz-Vries, H. K. Hahn, and J. Georgii, *Sliding Motion in Breast Deformation Modeling,* MICCAI-BIA 2015, Proceedings of the 3rd MICCAI Workshop on Breast Image Analysis , 1 (2015).

[181] M. Razavi, L. Wang, A. Gubern-Merida, T. Ivanovska, H. Laue, N. Karssemeijer, and H. K. Hahn, *Towards accurate segmentation of broglandular tissue in breast MRI using fuzzy c-means and skin-folds removal,* in *Image Analysis and Processing — ICIAP 2015*, Vol. 9279 (2015).

[182] T. Ivanovska, L. Wang, R. Laqua, K. Hegenscheid, H. Volzke, and V. Liebscher, *A fast global variational bias field correction method for MR images,* in *8th International Symposium on Image and Signal Processing and Analysis (ISPA)* (2013) pp. 667–671.

[183] H. Greenspan, B. van Ginneken, and R. M. Summers, *Guest editorial deep learning in medical imaging: Overview and future promise of an exciting new technique,* IEEE Transactions on Medical Imaging **35**, 1153 (2016).

[184] G. J. S. Litjens, T. Kooi, B. E. Bejnordi, A. A. A. Setio, F. Ciompi, M. Ghafoorian, J. A. W. M. van der Laak, B. van Ginneken, and C. I. Sánchez, *A survey on deep learning in medical image analysis,* CoRR **abs/1702.05747** (2017).

[185] M. Bianchini and F. Scarselli, *On the complexity of neural network classifiers: A comparison between shallow and deep architectures,* IEEE Transactions on Neural Networks and Learning Systems **25**, 1553 (2014).

[186] J. Deng, W. Dong, R. Socher, L.-J. Li, K. Li, and L. Fei-Fei, *ImageNet: A Large-Scale Hierarchical Image Database,* (2009).

List of Figures

List of Tables